Development of Analytical Techniques to Monitor Bone Penetration in 3D via Computer Tomography Analysis

THESIS SUBMITTED TO THE UNIVERSITY OF LONDON FOR THE DEGREE OF DOCTOR OF PHILOSOPHY

December 2013

BY

Alan Joseph Buchan Parish

Supervisors: Dr Graham R Davis & Dr Karin A Hing

SCHOOL OF ENGINEERING AND MATERIAL SCIENCE QUEEN MARY UNIVERSITY OF LONDON MILE END ROAD, LONDON, E1 4NS

Abstract

There has been much work into getting clear and precise images of bone growing within different osteoconductive and osteoinductive scaffolds for the aim of investigating and quantifying the effect the different grafts have on the bone that forms within the graft. Before the bone structure and volume can be quantified, the images produced need to segmented into their different regions.

Using images produced from x-ray computed tomography, the samples can be segmented based on their densities. As the voxels have distinct size, if just the density is used to segment out the regions, there will be some miss-identification at the edges of the regions (ghosting). To overcome this problem of misidentification, automated segmentation methods were developed which take not only the intensity of the voxels in the images (which are related to the density) into account for the segmentation but also the local properties.

With correct segmentation the volume and surface area are better represented and methods for structure measurement can and were developed. These methods allow for not only the structure of the bone and implants to be quantified, but for the change in structures between the different implants to be compared. This allows for the different structures caused by the different graft materials to be seen and compared. This comparison when used on its own or with other methods such as histology not only allows for the different structures to be identified but all the change in structures due to factors such as remodelling to be identified.

Table of Contents

Table of Figures

Table of Tables

Declaration

I declare that the work performed is entirely my own, conducted during the course of my Ph.D. Studies at the Queen Mary University of London and has not been previously submitted for a degree at this or any other university.

Alan Joseph Buchan Parish

Acknowledgements

I would first like to thank my supervisors Karin and Graham, for their constant support and letting me follow my crazy ideas in this thesis.
EPSRC and ApaTech for their financial support and grants.

A huge thanks to my parents and family who without their constant support none of this would have been possible. A special thanks to my colleagues and former bay mates Vivi, Nav and Krystelle, who were always there for me. A musical thanks to Rob, Lewis and Russell who provided a great distraction from the stress of work.
Also a big thanks to Zofia for her advice and imaging expertise.
For support in the office from, Filipe, Danielle, Ben, Clare, Amin and Erica who helped stop me going mad after all the years.
Thank you the former members of the Hof including Alban for their support and crash space and to icsf for being a mad group of people.
Also to Jen for helping me get through my last summer of the PhD
Humongous thanks to Ines for bouncing ideas off proof reading and being a great dinner companion and the best possible friend.
A big thanks to Tom my former house mate who persuaded me to use python.
And a thank you to my science buddy Pyria, who has been invaluable during the last couple of months of the thesis.
Also thanks to the GOG community for their crazy distracting and generous ways which has been a great help to me throughout the years.
A thank you to Noreen for helping me with biology, Bee for stats, John for his insights and to Mark and Donal for their support.
And to the funny people of Nottingham, including Mayte, Carolina, Laura, Pepe, José and Jake.
Also to Paco for just being himself.
And finally the biggest thanks and the dedication of this thesis to my friend Krysia, without her support none of this would have been possible and I probably would have given up.

Introduction

Autologous bone grafting, literally taking bone from one part of a patient to graft into another site, has been an internationally recognised technique since 1919. However because of the limited supply of autograft bone within a patient, since the advent of this technique there has been a rapid introduction of alternative synthetic bone graft (SBG) materials.

Traditionally the success of the grafting materials was assessed via two dimensional histology slices. In order to make scientific comparisons, stereographic techniques were used to quantify the volume of new bone formed after the treatment. While these methods can provide information about the bone growth and distribution in the SBGs, it is limited in providing quantifiable three dimensional measurements of connectivity and distribution of the bone. This makes it hard to determine whether or not the bone has penetrated the whole way through the defect or is just restricted to the periphery, as well as the shape of the bone within the SBGs.

With the increasing availability and quality of X-ray computed tomography, a three dimensional image can be created of the SBG and the bone forming within it, thus allowing the quantification of the bone growth by its three dimensional position and structure in a time efficient manner.

In order to do this accurately, there is a need for good quality imaging coupled with accurate segmentation. Up to this point, segmentation techniques were based around operator dependant selection of a “cut off” grey scale, which represents the density of the samples; leaving the analysis subject to the skill level of the operator. Also, because of the limitations of using absolute grey scale levels to define regions, ghosting of thin layers of bone around the SBG were seen where there was none.

Therefore there is a need for the development of novel segmentation methods to overcome these limitations with the acquisition of “good” segmentation data.

In this thesis novel methods of image segmentation will be investigated and created, focusing on correctly representing the shape and the edges of the samples for the different regions.

Once the methods are created, novel quantification methods can be developed and performed on test samples of hydroxyapatites with differing total and strut porosities as well as the effect of silicon substitutions. This allows for the SBGs to be compared by not only the amount of bone formed in the implants, but also by the shape and

connectivity of the bone within the grafts.

1 Literature Review

1.1 Bone

Bone has been studied since ancient times, with the earliest surviving text book on human anatomy being from about 180 AD by the Greek, Galen (Singer, 1952). Even over 1800 years later bone is still an active topic of research with over 50,000 bone articles published between 2012 and 2013 (US National Library of Medicine, 2013). Bone is one of the major organs in the body, it provides multiple functions and as such is of great interest to many scientific and medical disciplines (Hall, 2005).
The mechanical properties of the bone provide the body with its overall support as well as sites for attachment of both ligaments and muscles as well as protection for the internal organs (Hall, 2005). The bone also is important biologically, providing an environment for bone marrow, with the red bone marrow producing multiple cell types, most importantly blood cells (Mehta & Hoffbrand, 2013). Furthermore, its chemical properties allows it to act as a store for calcium and phosphorus as well as being a major contributor to mineral homeostasis (Hall, 2005). Bone also provides a defence against acidosis (Lemann, Litzow, & Lennon, 1966) and has been shown to preferentially store lead that contaminates the body (>90 % of the total lead in the body) (Barry, 1975).
It is therefore not unreasonable to assume that to provide these important functions bone is not a simple structure, or necessarily a static one.

1.1.1 Structure of Bone

Bone is a composite material, comprised of a mixture of organic and inorganic materials as Gray stated “an animal and an earthy part intimately combined together” (Gray, 1977). The structure can be more accurately described as being comprised principally of the fibrous protein collagen, which is impregnated with a mineral (Currey, 2002).
The overall structure of bone is hierarchical with each level exhibiting its own complex structure (Weiner & Traub, 1992) and as such when it is described it is often split into levels determined by size (Rho, Kuhn-Spearing, & Zioupos, 1998). The different levels that the bone will be viewed at (and their related sizes) are listed below:

- Ultra: Molecular structures of the constituent elements (<100's of nanometres).
- Nanostructure: Collagen fibres comprised of fibrils with embedded bone mineral (100's of nanometers-1 μm).

- Sub-Microstructure: Lamellar and woven bone (1-10 μm).
- Microstructure: Haversian systems, osteons and single trabeculae (10-500 μm).
- Macrostructure: Distinct bone tissues, the Cortical and Trabecular bone (>500 μm).

1.1.1.1 Ultra Structure

At the lowest level bone is comprised of fibrous proteins (collagen), calcium phosphate crystals, water, proteins and polysaccharides as well as cells and blood vessels in some types of the bone (Currey, 2002).
In humans the organic matter (collagen, proteins and polysaccharides) makes up 24 % of weight (39 % of volume), while the inorganic matter (calcium phosphate which is generally referred to as the bone mineral) makes up 70 % of the weight (50 % of the volume) and the water in the bone makes up 6 % of the weight (11 % of the volume) (Snyder, Cook, & Nasset, 1974).

1.1.1.1.A Collagen

Collagen is comprised of three polypeptide chains wrapped around each other into a triple helix which have been described as “wound around each other like a piece of rope” (Merrett, Kozak Ljunggren, Mondal, Griffith, & Rafat, 2012). Each of the three chains must have glycine, the smallest amino acid, at every third position, but can have any other two amino acids in the other two positions in the collagen chain (normally Proline and Hydroxyproline) (Figure 1-1) (Kadler, Holmes, Trotter, & Chapman, 1996). The different constituent chains determine the type of the collagen, for example type I collagen (which is the type found in bone) has two α1(I) chains and a α2(I) chain, while type II which is found in cartilage is comprised of three α1(II) chains (Kadler *et al.*, 1996).

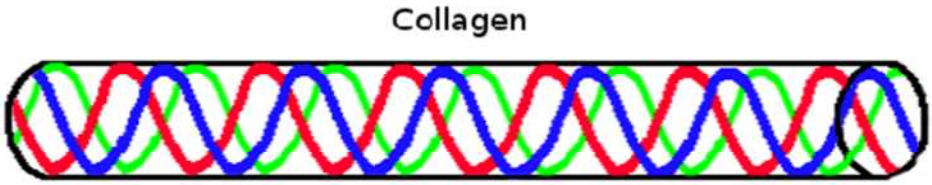

Figure 1-1 Structure of collagen comprised of three polypeptide chains (Based on the descriptions by (Merrett *et al*., 2012) *and* (Kadler *et al*., 1996) *).*

Mechanically collagen is an elastic material with a Young's modulus which has been recorded in the range of 3.7-11.5 GPa (at Room Temperature via AFM)(Wenger, Bozec, Horton, & Mesquida, 2007).

1.1.1.1.B Non-Collagenous Proteins

10 % of the organic proteins in bone are non-collagenous proteins (Roach, 1994). These proteins are important in the structure, growth and maintenance of the bone.
There are five key non-collagenous proteins which have been identified to date:

- Osteocalcin which limits bone formation without impairing bone reabsorption or mineralization (Ducy, Desbois, Boyce, & Pinero, 1996).
- Osteopontin which is a cell-binding protein which anchors osteoclasts (bone reabsorbing cells) to the mineralized matrix (Reinholt, Hultenby, Oldberg, & Heinegård, 1990).
- Osteonectin which anchors the mineral components of bone to collagen (Termine *et al*., 1981).
- Sialoprotein has an unclear purpose but has been suggested to be important in how cells attach to the bone matrix (Oldberg, Franzén, & Heinegård, 1988) as well as acting as a possible nucleation site for the bone mineral (Hunter & Goldberg, 1993).
- Thrombospondin which supports cell attachment and is mediated by calcium (Lawler, Weinstein, & Hynes, 1988).

1.1.1.1.C Bone Mineral

The mineral part of bone has been known to be a form of calcium phosphate for some time and it was referred to as “phosphate and carbonate of lime” by Ward in 1838 (Ward, 1838). However, it was only with early X-ray diffraction work by researchers

such as DeJong, Kay, Hendick and Hill that the similarities between the mineral part of bone and hydroxyapatite were realized and it is now generally accepted that the mineral in bone is comprised of a non-pure version of hydroxyapatite
(Currey, 2011; Hendricks & Hill, 1950; Posner, 1969). Hydroxyapatite has the stoichiometric chemical formula of $Ca_{10}(PO_4)_6(OH)_2$ and has a hexagonal crystal structure (Figure 1-2) (X. Lu *et al*., 2011).

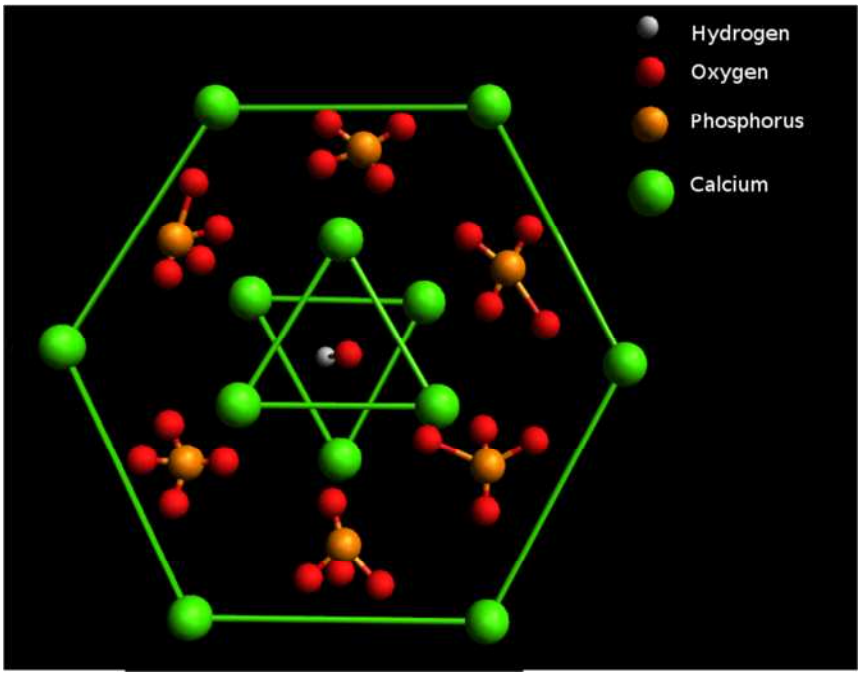

Figure 1-2 Structure of Hydroxyapatite when viewed down the C axis (Drawn in the program Avogardo) (based on the image by (X. Lu *et al*., 2011) *).*

The mineral in bone however is not purely stoichiometric hydroxyapatite and exhibits multiple elemental substitutions, at both the cationic calcium sites and the anionic phosphate sites, these substitutions include Na, Mg, Cl, F, K, Zn, SiO_4, Fe, Sr, Pb and CO_3 (McConnell, 1962; Posner, 1985; Young, 1975). The substitutions within hydroxyapatite have been shown to change both its structure and properties (Gibson, Best, & Bonfield, 2002; Hing, Revell, Smith, & Buckland, 2006; Miyaji, Kono, & Suyama, 2005; Porter *et al*., 2005; Verberckmoes *et al*., 2004).
Interestingly for at least one of the substitutions, namely silicate, it is seen in higher concentrations in areas of early bone calcification than in mature bone; thus implying that there might be a change in composition of the bone mineral during the bone formation process (Carlisle, 1970, 1986).
The bone mineral also functions as a store of elements used for biological processes including calcium and sodium and can be released to neutralise acidosis in the body;

with sodium and carbonate being removed during acidosis and gained during alkalosis (Burnell, 1971).

1.1.1.1.D Water

Water plays an important role in bone's structure and properties, with water in the bone at the sub-nano scale providing stability to the collagen via hydrogen bonds, which in turn adds to its mechanical properties (Ramachandran & Chandrasekharan, 1968). Water is also present as “bound” water in the bone mineral as a hydrated shell (Neuman, Toribara, & Mulryan, 1953).
At the higher structural levels water makes up ~12 % of the total bone volume and an increase in bone stiffness with loss of water has been noted (Nyman *et al*., 2006).

1.1.1.2 Nano Structure

The nano structure of the bone is comprised of collagen and bone mineral crystals which combine together in fibrils to form a composite material with the bone mineral crystals arranged periodically (~67 nm) along the surface of the fibrils of collagen in platelets (Landis, Hodgens, Arena, Song, & McEwen, 1996; Landis, Hodgens, Song, *et al*., 1996) (Figure 1-3).

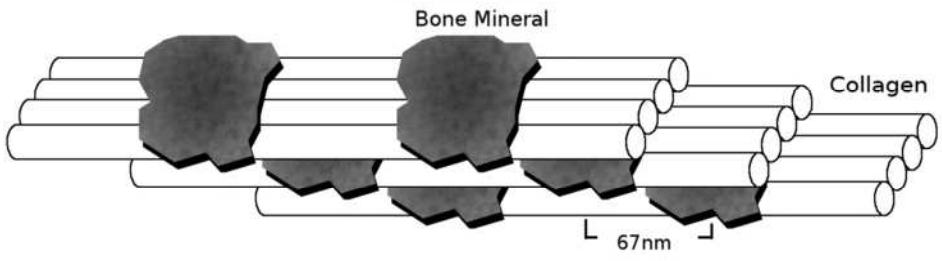

Figure 1-3 Close up structure of a bone fibril, comprised out of collagen and bone mineral showing the 67 nm spacing of the bone mineral based on the diagram by (Landis, Hodgens, Arena, *et al*., 1996).

The collagen (type I) joins together into fibrils via an entropy driven reaction which is proceeded by a loss of solvent molecules from the surface of the protein molecules, which results in assemblies with a circular cross-section (Figure 1-4) (Kadler *et al*., 1996).
The fibrils in the bone form together into fibres as shown in Figure 1-4 (Landis, Hodgens, Song, *et al*., 1996), which then makes up the larger bone structures (Liu & Thomopoulos, 2014)

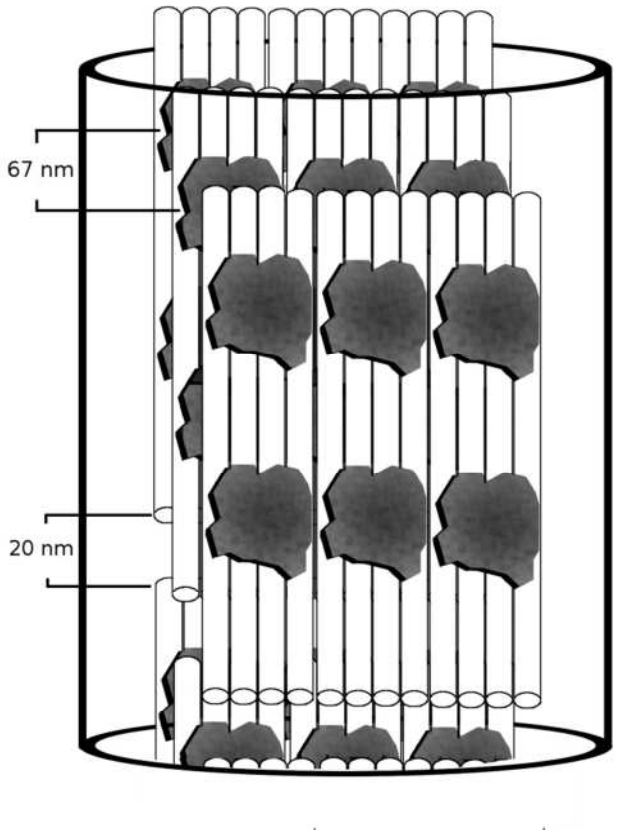

Figure 1-4 Structure of bone fibrils, in a bone fibre based on the diagram by (Landis, Hodgens, Song, *et al*., 1996).

1.1.1.3 Sub-micro Structure

The fibres of bone mineral and collagen generally form two different kinds of bone, depending upon their organisation, these are termed woven and lamellar bone *(*Table 1-1*)* (Currey, 2002).

The woven bone is deposited in small disorganised portions, which are formed quicker than the highly organised lamellar bone (Weiner & Wagner, 1998)

Table 1-1 Information about size and shape of the woven and lamellar type of bone (Currey, 2002).

	Woven	Lamellar
Diameter of Fibres	0.1-3 microns	2-3 microns
Arrangement of Fibres	Random	Sheets of 2-6 micron thickness
Shape and Size of Bone Cells	Roughly isodiametric ~ 20 microns	Oblate spheroids 5:1 ratio of major and minor axis of 20 microns
Higher Level Organisation	Found in lumps	Found in circumferential lamellae

1.1.1.3.A Woven Bone

Woven bone is formed from a disorganised mix of bone fibres (Figure 1-5), and is laid down first during bone formation and some forms of bone healing and then is remodelled into lamellar bone (Weiner & Wagner, 1998). As such it is only seen in mammals in their embryonic state and in fracture healing sites (Hall, 2005).

Figure 1-5 Structure of the fibres in woven bone (based off a diagram by (Weiner & Wagner, 1998).

Not only does its structure differ from lamellar bone but it also possesses smaller bone mineral crystals than those seen in mature lamellar bone (Su, Sun, Cui, & Landis, 2003).

1.1.1.3.B Lamellar Bone

The Lamellar bone is formed in organised layers (Figure 1-6) which are arranged in a "plywood" structure with each layer differing in rotation (average of 30 degrees) (Weiner, Arad, Sabanay, & Traub, 1997; Weiner & Wagner, 1998; Ziv, Sabanay, Arad, Traub, & Weiner, 1996). The Lamellar bone is stiffer than the collagen fibrils on their own with a recorded stiffness of interstitial cortical lamellae of 25.8±:0.7 GPa compared

to 3.7-11.5 GPa for collagen on its own (Rho, Tsui, & Pharr, 1997; Wenger, Horton, & Mesquida, 2008).

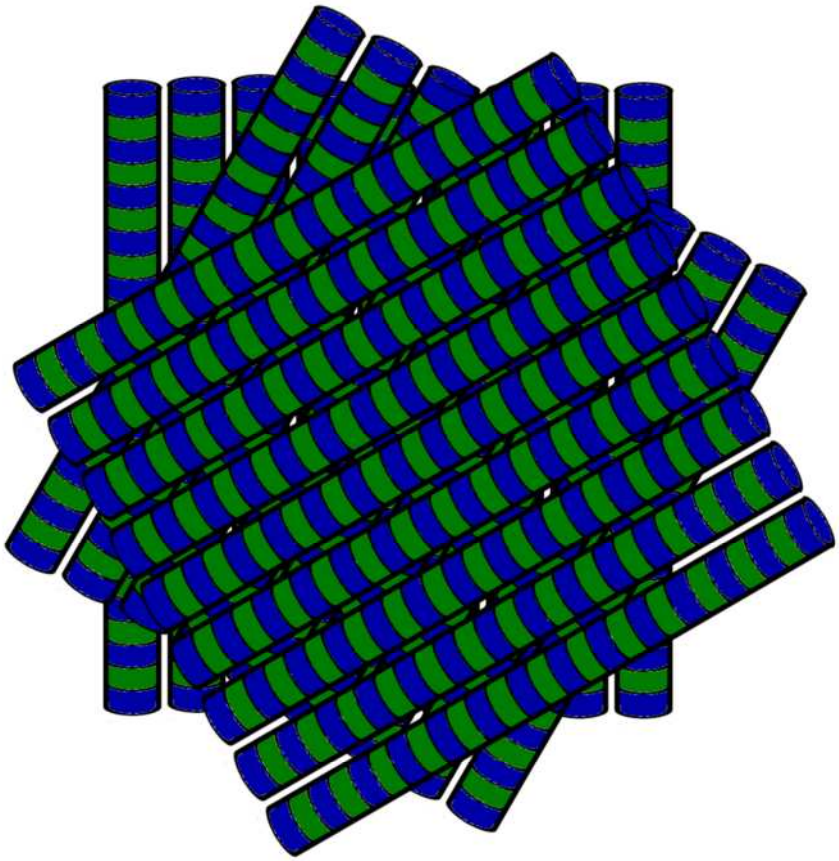

Figure 1-6 Structure of layers of bone lamellar, comprised of rotated bone fibres (at 30 degrees) based on a diagram by (Weiner & Wagner, 1998).

The lamellar bone supports the osteocyte bone cells between the individual lamella in gaps called lacuna which are connected via small channels called a canaliculus which allow the osteocytes to communicate with each other via their branches (Bonewald, 2007). The canaliculi are found throughout the lamellar with a number density of 0.18 ± 0.03/μm^2 (L. Wang *et al.*, 2005).

1.1.1.4 Micro Structure

At the micro structure the lamellar bone and woven bone form into the structural units of the larger bone tissue types (Rho *et al.*, 1998).
These structural units are osteons found in the cortical bone and individual trabeculae found in trabecular bone (van Oers, Ruimerman, Tanck, Hilbers, & Huiskes, 2008).

1.1.1.4.A Osteons

The osteon is formed out of sheets of lamellar bone which in turn are formed in

cylindrical structures with a 3D screw shape (Figure 1-7); with a gradual change in the lamellar orientation at each layer (Wagermaier *et al*., 2006). The osteons surround haversian canals which contain blood vessels, nerves, and some connective tissue and in some of the larger canals, lymphatic vessels (Snyder *et al.*, 1974).

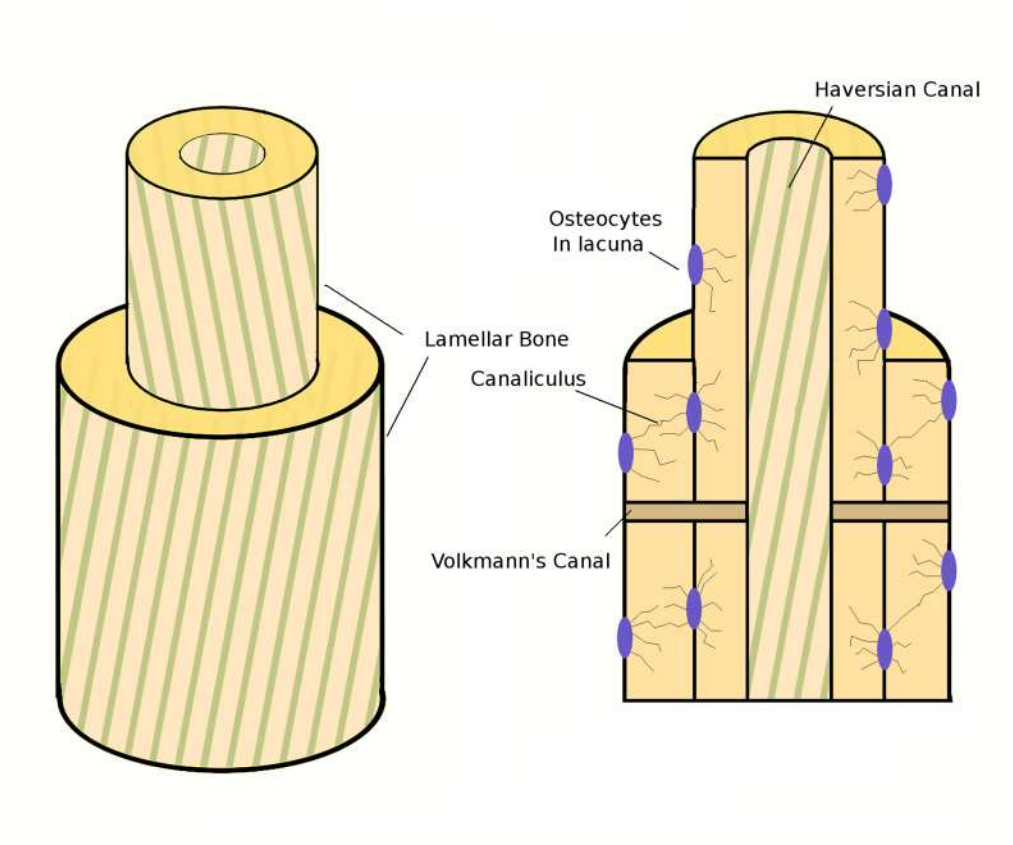

*Figure 1-7 Structure of osteons comprised of lamellar bone (based on a diagram of lamellar orientation (*Bromage *et al.*, 2003*) and diagram of lacuna (*L. Wang *et al.*, 2005*).*

Adjacent haversian canals are connected by volkmann's canals which run at 90 degree angles to the central canal of the bone (Kalfas, 2001).

There are two kinds of osteons, primary and secondary, the primary are formed directly in bone formation while the secondary are formed via remodelling; structurally the secondary osteons have a surrounding “cement line” and are “weaker” than the primary osteons (Currey, 2002). The “cement line” is devoid of canaliculi and has a higher calcium to phosphorus (Ca:P) ratio than the lamellar bone (Burr, Schaffler, & Frederickson, 1988; Skedros, Holmes, Vajda, & Bloebaum, 2005).

The properties of the lamellar bone are not constant within the individual osteons with the stiffness reducing from the inner-most ring to the outer-most ring of the lamellar bone (Rho, Zioupos, Currey, & Pharr, 1999).

1.1.1.4.B Trabeculae

The trabecula is the structural unit of the trabecular bone. It is comprised of a “hemi-osteon” (Stout & Crowder, 2012) which in turn is comprised of “irregular, sinuous convolutions of lamellae” (Rho *et al*., 1998) with lacuna and canaliculi (Figure 1-8*)*.

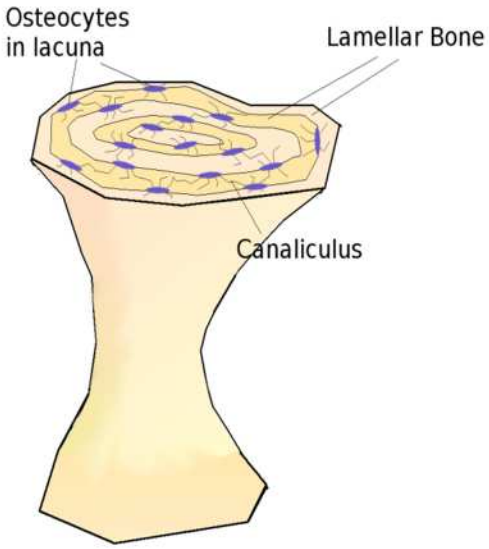

Figure 1-8 Structure of trabeculae comprised of lamellar bone based on the photograph by (Townsend, Rose, & Radin, 1975) *and description by* (Rho *et al*., 1998).

The size of the trabeculae are in the order of 0.08-0.14 mm in diameter and 1 mm in length (Singh, 1978).

1.1.1.5 Macro Structure

The two major types of bone tissue that have long been recognised, are cortical (also known as compact) and trabecular (also known as cancellous) bone (Figure 1-9) (Strong, 1919). There are also two types of non-bone tissues which line the bone, the periosteum which covers the outside of the bone and the endosteum which lines the surface of the bone around the marrow cavity (Currey, 2002). When there is trabecular bone in the body it is encompassed by between the cortical bone (Currey, 2002). Mechanically, the cortical bone has anisotropic mechanical properties, being stiffer in the longitudinal direction than in the transverse direction (Turner, Rho, Takano, Tsui, & Pharr, 1999).

On the other hand the trabecular bone displays isotropic properties within its individual trabeculae with their Young's Modulus being in-between the cortical bone's longitudinal and transverse values (Turner *et al*., 1999).

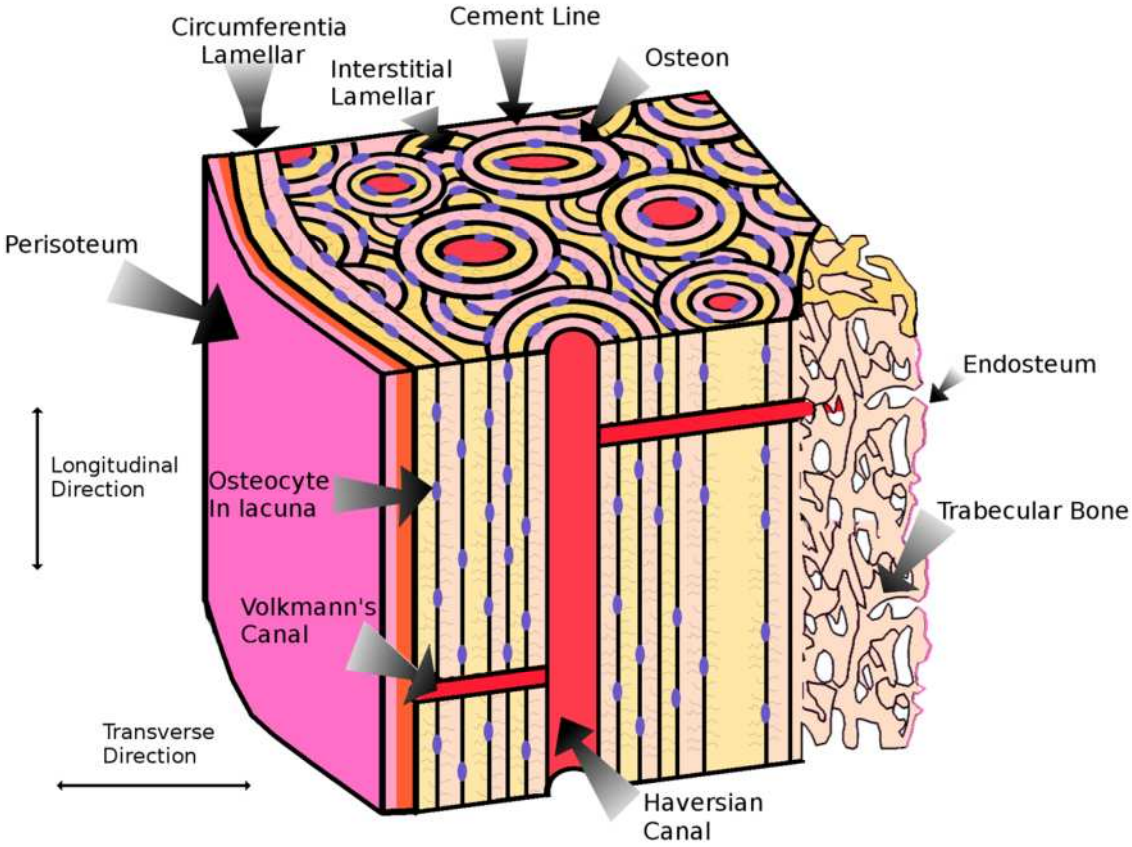

Figure 1-9 Macro structure of bone including cortical and trabecular bone tissue (based on 3D bone image (Le Meng Bao *et al*., 2013), *histology slice of cortical bone* (Tomkinson, Reeve, Shaw, & Noble, 1997) *and 2D schematic of cortical bone* (Skedros *et al*., 2005).

1.1.1.5.A Cortical Bone Tissue

The cortical bone is a strong and dense structure which is comprised of ordered osteons and lamellar of bone (Currey, 2002; Skedros *et al*., 2005).

There are three patterns of bone found in cortical bone tissue, concentric, circumferential and interstitial (Tomes & Morgan, 1853).

- The concentric pattern consists of osteons including their haversian canals.
- Interstitial is the lamellar in-between the osteons, which don't have full rings or haversian canals (the interstitials do not necessarily form circular structures).
- Circumferential is the lamellar bone which forms the surface of the bone.

1.1.1.5.B Trabecular Bone Tissue

The trabecular bone is an open network of bone tissue which has a high strength-to -weight ratio which is present in the inner sections of larger bones and can contain bone

marrow (Holden, 1887).
Structurally it is comprised in varying degrees of rods and plates which form a (sometimes directional) connective matrix (Singh, 1978) which has been identified as appearing in the form of “needle-like rays” (Holden, 1887).

1.1.1.5.C Periosteum and Endosteum

The periosteum and the endosteum are the cell layer intermediates around the outer and inner surfaces of the bone and bone canals respectively (the term periosteum can also be used to include the collagenous sheet covering the bone) (Currey, 2002).
They both consist of two layers; an outer-fibrous layer and an inner-cellular layer (Mckibbin, 1978). The periosteum allows for transfer of nutrients into the bone and acts as a site for appositional bone growth (Holden, 1887; Scheuer & Black, 2004). The cellular layer has been shown to be an important part of bone healing with the removal of the periosteum causing compromised callus formation during bone lengthening in rabbits (Kojimoto, Yasui, Goto, Matsuda, & Shimomura, 1988).
The periosteum is also a source of pluripotent cells (in the form of mesenchymal stem cells) and as such it is of interest in the field of tissue engineering (Stevens, Qanadilo, Langer, & Shastri, 2004).

1.1.1.5.D Bone Marrow

There are two major types of bone marrow; the red bone marrow, which produces cells such as red blood cells (Mehta & Hoffbrand, 2013) and the yellow bone marrow which acts as a fat store (Table 1-2) (Snyder *et al*., 1974).

Table 1-2 Chemical composition of adult bone marrow (Snyder *et al*., 1974).

Marrow Type	Chemical Composition
Yellow Marrow (50 %)	80 % Fat 15 % Water 5 % Proteins
Red Marrow (50 %)	40 % Fat 40 % Water 20 % Proteins

The red bone marrow contains mesenchymal stem cells (Kern, Eichler, Stoeve, Klüter, & Bieback, 2006) which can differentiate into osteoblasts (bone forming cells) and chondrocytes (cartilage formation and maintaining cell) (Caplan, 1991). The red bone marrow also contains the hematopoietic precursor cells which can form into osteoclasts (bone removal cells) (Lacey *et al*., 1998).

The yellow marrow appears to have little physiological function and acts as a fat store as well as providing function as a packing material (Currey, 2002).

1.1.2 Cells Involved In Bone Biology

Bone is not just a complex multi-scale composite material, it also possesses the ability to regenerate and repair itself (Sela & Bab, 2012).

This is accomplished by four specialised bone cells which are involved with bone growth (Figure 1-10) these are the osteoblasts, osteocytes, bone lining cells and the osteoclasts (Currey, 2002).

In bone formation the chondrocyte, which is the cell which forms and maintains cartilage, is also important (Caplan, 1991).

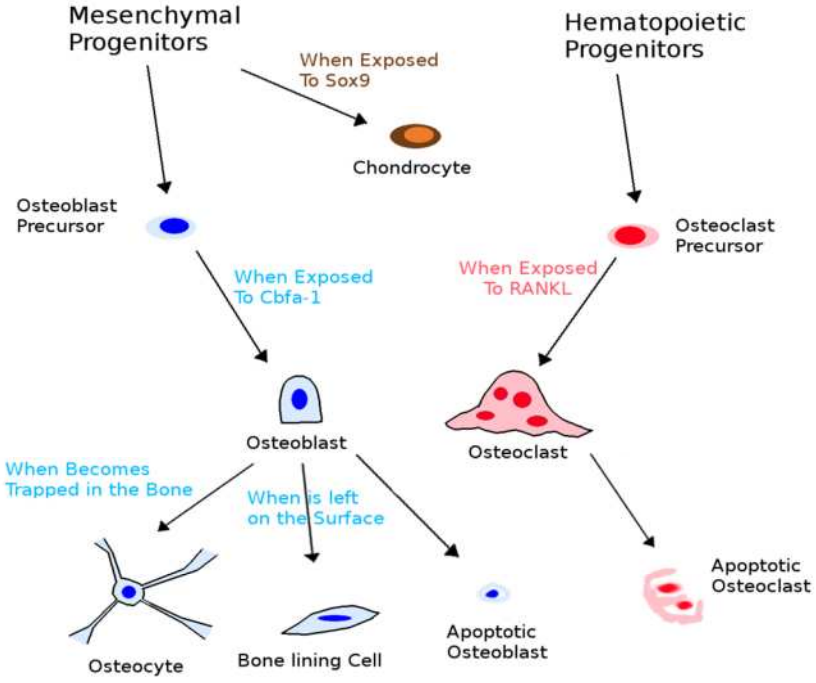

Figure 1-10 The cells involved in bone formation and remodelling, and their differentiation routes (based on a diagram from (Oursler *et al*., 2014) *and information from*(R. Smith, Wordsworth, *et al*, 2005)*).*

1.1.2.1.A Osteoblasts

The function of the osteoblasts is to synthesize and mineralize the bone (R. Smith *et al*., 2005).

Osteoblasts are cuboidal and columnar in shape with a single central nucleus (Athanasou, 1996). They arise from mesenchymal stem cells (Sela & Bab, 2012) which differentiate into osteoblasts when exposed to the factor Cbfa-1 (this can be seen by the lack of bone formation in Cbfa1-deprived mice embryos) (Komori *et al*., 1997; Otto *et al*., 1997). The Wnt signalling pathway has also been shown to regulate the number and activity of osteoblasts (R. Smith *et al*., 2005).

The osteoblasts communicate with neighbouring osteoblasts and osteocytes via gap junctions (transmembrane channels) (Civitelli, 2008).

In bone formation osteoblasts mineralises cartilage, either in primary mineral apposition (which occurs at 5-10 days after soft tissue deposition) or secondary mineral apposition (which occurs after the basic structural unit of bone has been fully formed) (Boivin & Meunier, 2003). In the mineralisation process inorganic phosphate (Pi) joins with calcium ($Ca^{2+)}$ to form the hydroxyapatite (HA) (Hessle *et al*., 2002).

The inorganic phosphate (P_i) can either be formed from nucleoside triphosphates (NTPs) or inorganic pyrophosphate (PP_i) under the effect of the osteoblast protein tissue-nonspecific alkaline phosphatase (TNAP) or is obtained from the rest of the body (most likely by intestinal absorption).

The NTPs can be converted to PP_i under the influence of the protein plasma cell membrane glycoprotein-1 (PC-1), this then acts as a feedback mechanism on the formation of HA as PP_i inhibits HA formation (Figure 1-11) (Hessle *et al*., 2002).

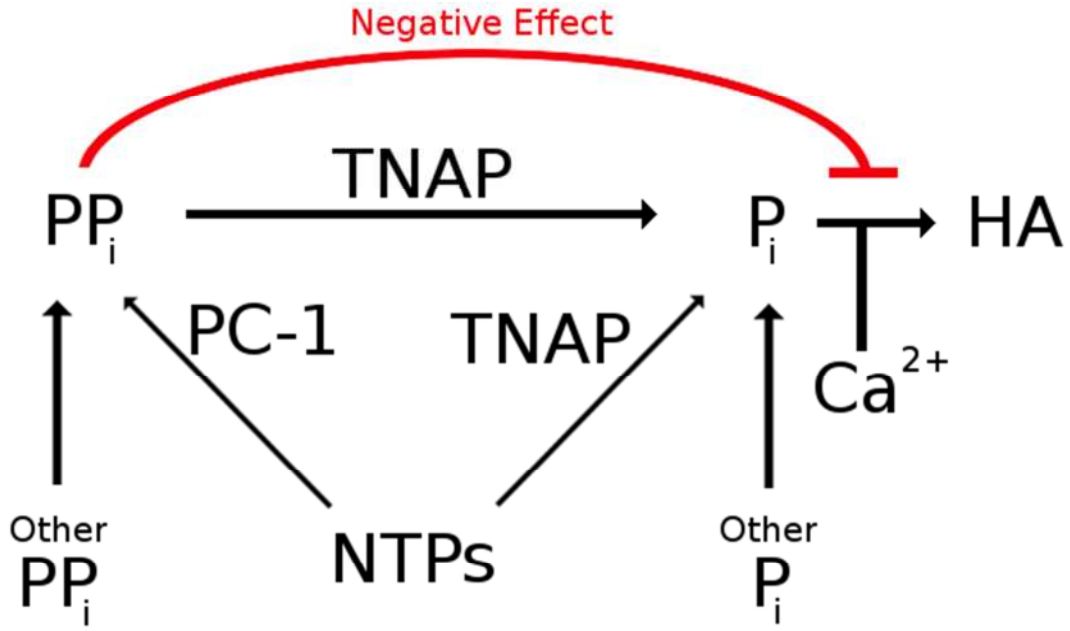

Figure 1-11 The effect of inorganic pyrophosphate, inorganic phosphate, nucleoside triphosphates, calcium and the proteins tissue- nonspecific alkaline phosphatase and plasma cell membrane glycoprotein-1 on hydroxyapatite formation (Based on a diagram by (Hessle *et al*., 2002)*).*

Vitamin D is important in both the homeostasis of calcium and phosphorous and increases the mineralisation of the bone (Athanasou, 2001; Bronner & Farach-Carson, 2004). The amount of vitamin D in the body is controlled by a feedback loop with Parathyroid hormone (PTH), with PTH stimulating vitamin D formation (in the form of 1,25-dihydroxyvitamin D) and vitamin D in turn reduces the secretion of PTH (Athanasou, 2001).

Other factors have been shown to be involved with this process; for example the Bone morphogenic protein (BMP-2) has been shown to induce alkaline phosphatase under Wnt signalling (Rawadi, Vayssière, Dunn, Baron, & Roman-Roman, 2003).

When the osteoblasts finish forming bone, some (around 15 %) are surrounded (trapped) by the matrix and become osteocytes (Hadjidakis & Androulakis, 2006). Some of the other osteoblasts remain on the surface and become bone lining cells and the rest undergo apoptosis (also known as controlled cell death) (Stout & Crowder, 2012).

1.1.2.1.B Osteocytes

Osteocytes are formed from osteoblasts that become trapped in the bone matrix. They exist inside the bone and communicate with each other and bone lining cells via long branches (Van Der Plas & Nijweide, 1992).

It is believed that osteocytes monitor internal stresses and strains in the body and control the remodelling process by communication with the lining cells and or osteoblasts via gap junctions on their branches (Civitelli, 2008; Klein-Nulend & Plas, 1995; Mullender & Huiskes, 1997).

1.1.2.1.C Bone lining Cells

Bone lining cells are formed from osteoblasts which remain on the surface of the bone after bone formation. They are attached flatly onto the surface of the bone (Korper, Jansen, Saftig, Everts, & Delaisse, 2002) and line the entire surface (Eriksen, 2010).
In bone remodelling the bone lining cells clean out any de-mineralised collagen from the resorption pits created by osteoclasts and replace it with proline-rich protein (Korper *et al*., 2002).

1.1.2.1.D Osteoclasts

Osteoclasts are large multinucleated cells which are involved with reabsorbing the bone for remodelling (Stout & Crowder, 2012; Teitelbaum, 2000).
They share a lineage with blood cells (from hematopoietic/blood origin) and are formed after the “receptor activator of nuclear factor ligand” (RANKL also known as osteoprotegerin ligand (OPGL)) activates the osteoclast precursors that exist in the bone marrow and blood (Athanasou, 1996; Lacey *et al*., 1998). This activation is regulated by osteoprotegerin (OPG) (Simonet *et al*., 1997) which is a factor in the marrow which also binds to the RANKL (Lacey *et al*., 1998; Yasuda, Shima, Nakagawa, Mochizuki, *et al*., 1998; Yasuda, Shima, Nakagawa, Yamaguchi, *et al*., 1998).
Osteoclasts reabsorb the bone in pits beneath themselves (Chambers & Revell, 1984) with the pits being of the order of 1-3 μm for mice (Boyce, Yoneda, Lowe, Soriano, & Mundy, 1992). This is achieved by forming sealed compartments next to the bone's surface and then secreting acids and enzymes which degrades the minerals and proteins in the bone respectively (Väänänen *et al*., 1990; Werb, 1997).
Osteoclasts have a life span of approximately four weeks and are known to undergo apoptosis (Athanasou, 2001).

1.1.2.1.E Chondrocytes

Chondrocytes form and maintain cartilage cells; they are derived from mesenchymal stem cells (the same as osteoblasts) and require the transcription factor SOX9 for

formation (Bi, Deng, Zhang, Behringer, & de Crombrugghe, 1999; R. Smith *et al*., 2005). Other factors which have been shown to control the chondrocytes's differentiation (into perhypertrophic and hypertrophic chondrocytes) include Indian Hedgehog (IHH), Bone Morphogenic Proteins (BMPs), Patathyroid hormone-related protein PTHrP and WNT5a (Wuelling & Vortkamp, 2011). Chondrocytes are important in endochondral ossification as they act as an intermediate structure before the bone is formed (Mackie, Ahmed, Tatarczuch, Chen, & Mirams, 2008).

1.1.3 Bone Growth and Remodelling

1.1.3.1 Ossification

Mammalian bone formation (ossification) can happen in two generalised processes; either being formed from hyaline (transparent) cartilage, which is referred to as endochondral ossification or as a direct transformation from a highly vascular membrane, which is referred to as intramembranous ossification (Scheuer & Black, 2004).

Endochondral ossification involves mesenchymal cells and forms trabecular bone while intramembranous ossification itself has two distinct forms, namely the formation of dermal and perichondral bone; which are formed from neural crest and mesenchymal cells respectively and are related to diploic (as seen in the skull) and cortical(and trabecular) bone formation respectively (Scheuer & Black, 2004).

Endochondral formation first starts with the mineralisation of pre-existing cartilage which has been formed by from chondrocyte, this starts first with the cartilage being invaded with blood vessels and osteoclasts and then followed by osteoblasts (Mackie *et al*., 2008). As bones continue to grow after birth, first cartilage is formed to allow for expansion; this cartilage is referred to as the growth plate which separates the bone into the primary and secondary centres of ossification; in bones with articular cartilage there is also a growth plate called the Articular-epiphyseal growth cartilage (Figure 1-12) (Mackie *et al*., 2008).

The longitudinal growth in the endochondral bone formation all happens at the growth plate, which contains chondrocytes at various stages of differentiation and is regulated by the factors PTHrP, IHH, BMPs and FGFs (Spath, Andrade, Chau, & Nilsson, 2011). In the centre of the cartilage matrix chondrocytes differentiate into prehypertropic and hypertrophic chondrocytes; these then produce a mineralised extracellular cartilage

matrix which acts as a medium for the following bone deposition (Wuelling & Vortkamp, 2011).

When the pre-bone is only a cartilage matrix it is surrounded by a layer of fibroblast-like cells called the perichondrium which differentiates into osteoblasts and forms the periosteum, at the stage when the chondrocytes become hypertrophic; the blood vessels invade the bone from the periosteum (Wuelling & Vortkamp, 2011).

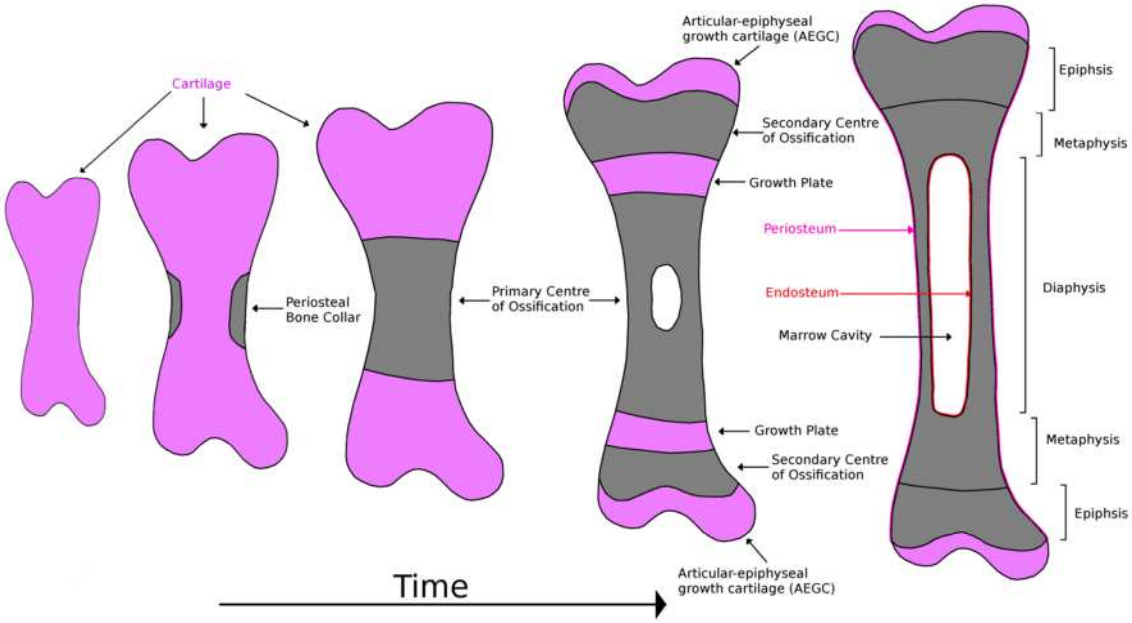

Figure 1-12 Endochondral ossification over time, based on the diagram by (Mackie *et al*., 2008).

Intermebranous ossification can also be seen in the formation of long bones with the formation of concentric bone layers under the periosteum which provides the growth of the thickness of the bone (Simkiss, 1975). As the bone grows it is also being continuously remodelled.

1.1.3.2 Remodelling of Bone

There are three general reasons why the bone in the body remodels (Burr, 2002):

- Firstly it provides a way for the body to alter its balance of minerals.
- Secondly it provides a mechanism for the skeleton to adapt to its mechanical environment.
- Thirdly it provides a mechanism to repair damage caused by repetitive cyclic loading.

1.1.3.2.A A Brief History on the Ideas of Bone remodelling

There has always been clear interest in the interrelationship between the structure and the function of bone within bone research (Roesler, 1987). In the early 19th century this research investigated the differences between the mechanics of the inner architecture of the bone, namely why there was a difference in structure between cortical and trabecular bone (Koch, 1917; Roesler, 1987). The early work in this field was by Bourgery in the (with highly praised drawings by Jacob as shown in Figure 1-13) with it being considered the first work describing the inner structure of the trabecular bone and the relation to the forces acting on it (Roesler, 1987; Wyman, 1857). Bourgery suggested that the bone's structure is an optimization of strength to weight, stating "The simplest of examination of the differences in density or of rarity of bone tissue in certain parts shows that bones unite all three conditions of maximum solidity and lightness for a volume determined by the use of the parts." (Bourgery, 1832) (Thanks to A.Cadu at Uppsala University for the kind translation).

Figure 1-13 Jacob's representation of the internal structure (in a coronal section) of the head of the femur (Bourgery, 1832).

While the interpretation of the inner architecture of bone by Bourgery was later described as being in “error” his was still one of the first works devoted to understanding the reason for the architecture of bone (Koch, 1917). Another prominent anatomist at the time, Charles Bell touched on the idea of the structure fitting the forces upon it, stating “But it is pertinent to our purpose to notice, that this minute lattice-work, or the cancelli which constitute the interior structure of bone, have still reference

to the forces acting on the bone;" (Bell & Wyman, 1902) (in a collection of his earlier work first published in 1828). Bell again touched upon the effect on structure of the bone by external forces in a collection of supplementary dissertations published with Paley's Natural Theology in 1838; in which he stated "That the bones which form the interior of animal bodies should have the most perfect shape, combining strength and lightness,..." (Paley, Brougham, & Bell, 1836). This work on understanding the internal structure of bone was continued on by others, such as Ward, Quain, Wyman and Humphry, who all made steps forward in the understanding of the structure of bone (Koch, 1917).

Quain connected the structure of the bone to the external pressures, stating that "it may usually be observed that the strongest laminae run through the structure in those directions in which the bone has naturally to sustain the greatest pressure." (Quain, 1849).

Ward in his book *The Outlines of Human Osteology* published in 1838, provided a diagram of the femur relating it's mechanical principles to a "bracket" (Figure 1-14) (Ward, 1838).

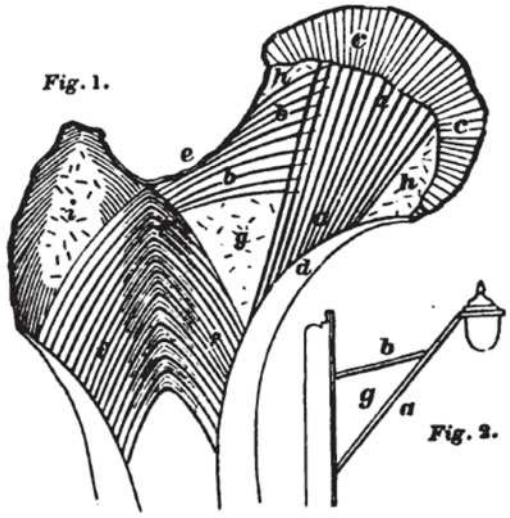

Figure 1-14 Ward's representation of the internal structure of the femur (in a coronal section) comparing it to a lamp bracket (Ward, 1838).

Wyman writing on the subject in 1849, commended the work that had gone before (citing in particular Bourgery & Jacob, Ward, Quain and Bell); however he points out their short comings of both the knowledge of the internal structure of the trabecular bone and the lack of descriptions of its "mechanical arrangements", providing his own improvement over Ward's diagram of the femur (Figure 1-15) (Wyman, 1857).

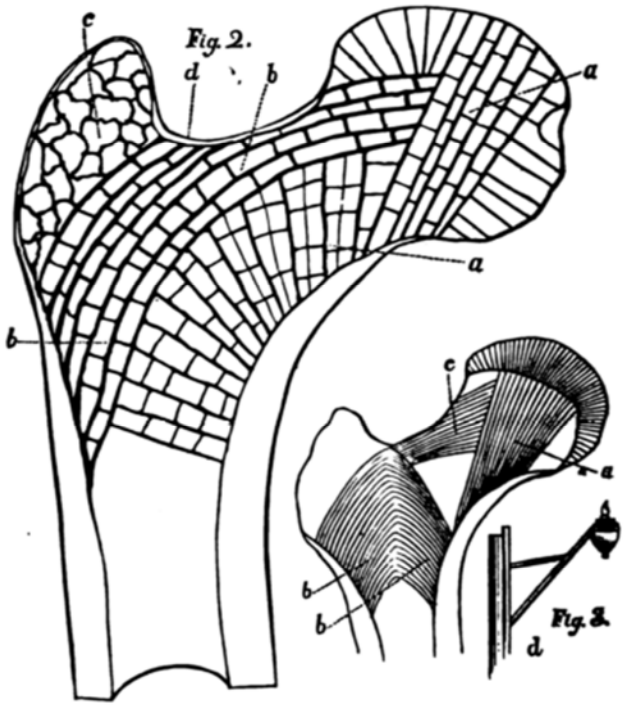

Figure 1-15 Wyman's representation of the internal structure of the femur (in a coronal section), including his representation of Ward's representation for comparison and critique (Wyman, 1857).

However it was a collaboration between the anatomist Von Meyer and the engineer Culmann in 1867 which influenced one of the most famous names in the science of bone remodelling, the German anatomist Julius Wolff (Skedros & Brand, 2011). The work by Von Meyer and Culmann combined the mechanical crane structure drawn by Culmann and the anatomic analysis of the trabecular bone by Von Meyer, which Von Meyer reference to as having a “unmistakable resemblance” (Figure 1-16) (von Meyer, 2011) (Translation of the 1867 work *Die Architectur der Spongiosa*).

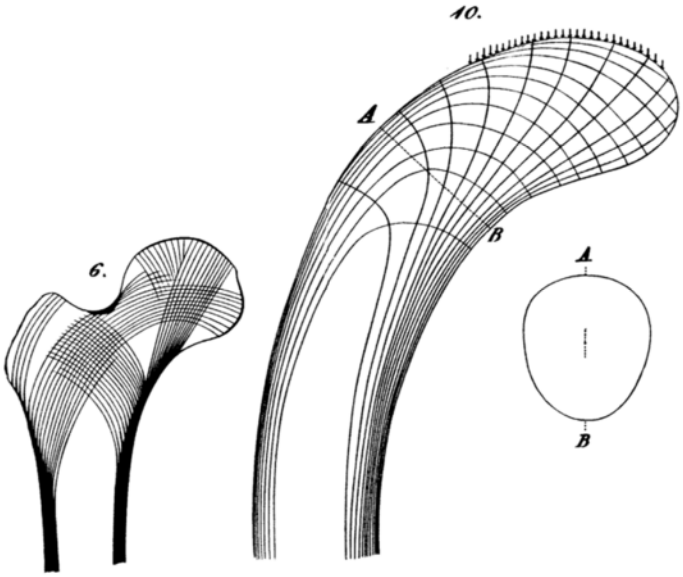

Figure 1-16 Von Meyer's and Culmanns representation of the forces in a femur (in a coronal section) and its similarity to a Culmann crane (von Meyer, 2011). *Reprint of the original 1867 paper, image cropped and rearranged but not modified).*

Wolff's paper in 1869 commends Von Meyer's and Culmann's work though stating that Von Meyer's illustrations do not match the crane as well as his own dissections did (Wolff, 2011) (Translation of the 1869 work *Ueber die Bedeutung der Architectur der Spongiösen Sunstanz für de Frage Vom Knochenwachsthu Vorläufge Mettheilung*). Wolff's next two papers in 1870 and 1873 on the structure of bone would later form his magnum opus *Da Gesetz der Transfromation der Knochen* (The Law of Bone Remodelling) published in 1892 (Brand, 2010). In Wolff's 1870 paper on the structure of the trabecular (in which it is worth noting that he states that it was only through Von Meyer's paper that he became convinced of the well-motivated architecture of the bone, and that it was not a widely accepted idea) he presents not only his own diagrams on the structure of the trabecular compared to Culmann's crane, but also photographs to back up his representation of the internal structure of the bone (Wolff, 2010) (Figure 1-17). (Translation from the 1870 work *Ueber die innere Architectur der Knochen und ihre Bedeutung für die Frage vom Knochenwachsthum*).

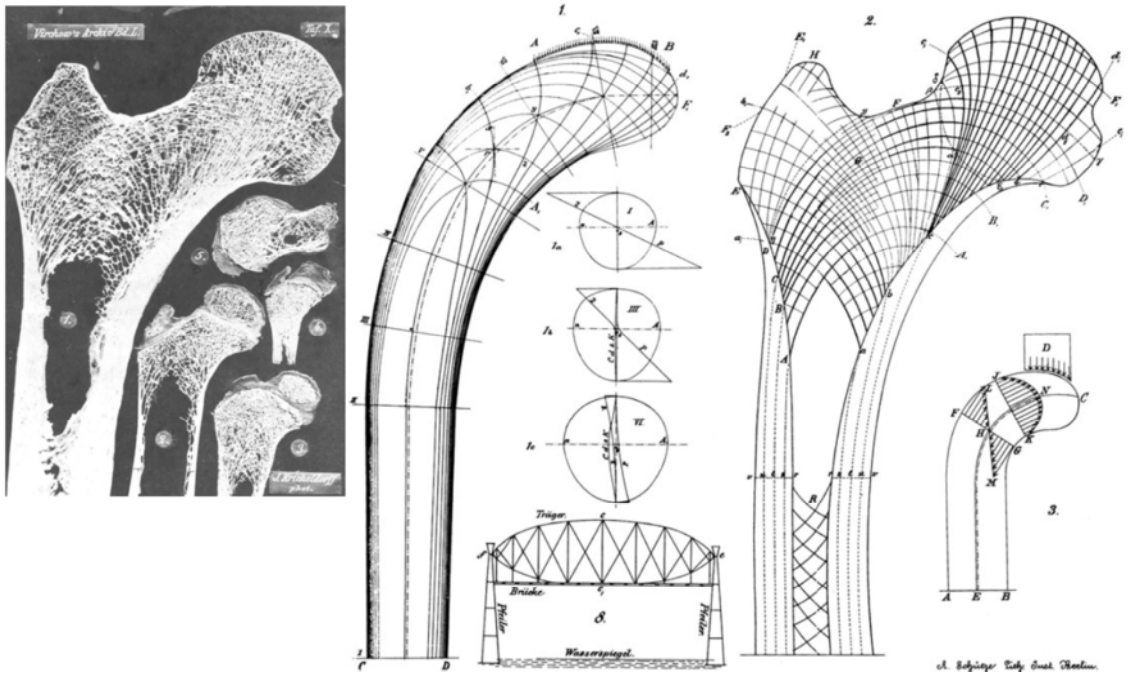

Figure 1-17 Wolff's representation of the forces in a femur (in a coronal section) and its similarity to a Culmann crane and slices of femur (Wolff, 2010) *.(Reprinted from the original paper in 1870).*

It is important at this point to talk about Roux and his work in 1881 which discussed bone remodelling as a quantitative self-regulating mechanism (Roesler, 1987). Roux's 1881 work entitled *Der Kampf Der Theili Im Organimus* (Roux, 1881) was considered to be an important work in both the field of evolution (Darwin called the book “the most important book on Evolution which has appeared for some time” (Darwin, 1887)) and the field of bone biology, with Wolff referring to Roux's work multiple times in his opus *Das Gesetz der Transformation der Knochen* (The law of Bone Remodelling) (Wolff, 1986). The fact that Roux's work is not as wide spread in the field of bone remodelling as Wolff's could be due to either the lack of an official translation of his major work or simply that “his writing is not easy to understand” (Hamburger, 1997).

In Wolff's opus *Das Gesetz der Transformation der Knochen* (The law of Bone Remodelling) he presents detailed photographs of the cross sectional slices of bones (which are in fact “Fourier” sections of the bone which allow for the internal architecture of the bone to be seen through each slice) of both healthy and diseased and damaged bone and connects them to the external forces (it is the examination of these slices which he cites as the reason that his conclusions hold more merit than the other research that came before him, as they lacked clear insight into the structure of the bone) (Wolff, 1986) (translated from the 1892 work). In this work he states the “rule” of

remodelling to be “the law of remodelling is the law according to which alterations of the internal architecture, clearly observed and following mathematical rules, as well as secondary alterations of the external form of the bones following the same mathematical rules, occur as a consequence of primary changes in the shape and stressing or in the stressing of the bones.” (Wolff, 1986). It is important to note at this point that Maquet (who with Furlong translated *Das Gesetz der Transformation der Knochen* for the 1986 English version) pointed out that Wolff never did develop his rule mathematically nor did he “elucidate” it (Maquet, 1992).

Though it should be noted that Wolff does also refer back to his preliminary thinking on the subject and his previous statement “It seems almost doubtless that the bone trabeculae disappear where, as a result of a curvature, they are no longer stressed. New bony elements must develop where the material is stressed as a result of bony regeneration or of curvature of the bone” this statement is similar to the optimisation ideas of both Bell and Bourgery (Wolff, 1986).

An important point that should be noted is that the term “Wolff's law” has become so attached to bone remodelling that it has become not only the general term for bone remodelling to fit its mechanical factors but also has become an umbrella term for the thoughts and statements of other scientists such as Bourgery and Bell in their maximum-minimum ideas of bone as well as Pauwel and Roux (Maquet, 1992; Ruff, Holt, & Trinkaus, 2006). Wolff's law has been rephrased by others such as Keith in 1919 who put the law in terms of osteoblasts stating “The law is simply this: Osteoblasts at all times build and unbuild according to the stresses to which they are subjected.” (Keith, 1919). Thus it is important to check the definitions of Wolff's law when reading past (and current) research and it is not being used “like a *Deus ex machina”* to the problem of bone remodelling (Attributed to Kummer's laudatio on the occasion of what would have been Pauwel's 100th birthday (Roesler, 1987)).

The ideas put forward by Wolff (and those who influenced him) while causing controversy (which lasted until the 1940s) were the basis of the views of those who studied the mechanical effects on bone architecture up until the spread of interdisciplinary science in the field (such as the work into the piezoelectric effect of bone by Fukada and Yasuda in 1957 (Fukada & Yasuda, 1957)) (Frost, 1998b).

In 1960 the paradigm for the research of bone remodelling (named the 1960 paradigm by Frost) refocused on the cells and their non-mechanical influences in the bone as both the cause and cure of skeletal health as well as disease and not the reaction to the

external mechanical forces (Frost, 1998a, 1998b).

The 1960 paradigm with its omissions combined with the limitation of interdisciplinary communication at the time created a pressing need to combine the different branches of bone research and rethink the state of the art, which happened at a series of hard tissues workshops at Utah university hosted by Professor Jee, which by 1995 formed the ideas for what is now referred to as the Utah paradigm (Frost, 1998a, 1998b).

A theory which attempts to connect the mechanical and cell effects is the mechanostat mechanism proposed by Frost that implies there is a feedback loop which monitors the mechanical usage (MU) of the bone and connects it to the biological mechanism of controlling the bone mass, thus correcting any serious mismatches between the two (Frost, 1987) which can be seen as an extension of Roux's paradigm (Huiskes, 2000).

The Frost's mechanostat theory was built on how strain was connected to bone remodelling even going as far as giving the ranges of strain where there would be extra bone formation (1500-2000 micro strain in his 1987 paper) and where there would be bone die-back (100-300 micro strain in his 1987 paper) (Frost, 1987).

While there have been criticisms of the specifics of the mechanostat theory (Including the fact that it makes predictions as to the behaviour of bone under disuse (Turner, 1999)), much like the theories before it, it has evolved with time as new scientific information have come to light which in turn lead to new discussions (Such as that between Frost and Turner (Frost & Turner, 2000)). It is thus that in one Frost's last papers, which was a review on the Mechanostat, the theory can be clearly seen to have evolved from the idea in 1987 now separating out the remodelling from modelling; even presenting values for the Remodelling threshold (50-100 micro strain), Modelling threshold (1000-1500 micro strain) and Pathologic threshold (~3000 micro strain) (Frost, 2003).

(A diagram of how the mechanostat relates to bone remodelling and modelling is shown as Figure 1-18).

Much like Wolff's law before it, the mechanostat theory has been built upon (and been subject to verification (Mahnama, Tafazzoli-Shadpour, Geramipanah, & Mehdi Dehghan, 2013) with some of the most recent work being on connecting the mechanical and bone remodelling response with the biology of the bone such as the osteocyte and its possible function as the sensor in the mechanostat model (Hughes & Petit, 2010).

To summarise, in the past, bone remodelling has been connected exclusively to the external forces that the bone is exposed to and also exclusively to the cellular factors,

but with the connection between the osteocyte and the mechanical forces a concise picture of bone remodelling can be seen which appears to answer how and why remodelling of bone occurs.

1.1.3.3 The Basic Multicellular Unit

The collection of cells which form and maintain the bone (Osteoblast, Osteocyte, bone lining cells and Osteoclasts) are referred to as a Basic Multicellular Unit (BMU) when they are *in situ* (Kular, Tickner, Chim, & Xu, 2012).
The remodelling of bone cellular units can be viewed as having six distinct stages (Schett, 2004) (Figure 1-18):

- Resting State: The resting state is the bone's natural fully formed healthy state, with osteocytes inside the bone and bone lining cells on top.
- Activation: Osteocytes continuously send signals that inhibit the activation of new remodelling BMUs, thus osteocyte apoptosis or micro fracture stops this signalling and activates the new remodelling cycle.(R. B. Martin, 2000; Stout & Crowder, 2012).
- Resorption: The bone is reabsorbed by the activation of osteoclasts which collect on the remodelling site.
- Migration: After the osteoclasts undergo apoptosis, bone lining cells migrate to the site to “clean” it and lay down proline-rich protein (Korper *et al*., 2002).
- Formation: The new bone in the form of un-mineralised osteoid is laid down by osteoblasts, with some osteoblasts becoming trapped and becoming osteocytes.
- Mineralization: Finally the osteoid is mineralised and the bone returns to its resting state.

These remodelling steps can be connected to overall bone remodelling (and modelling) via the implementation of the mechanostat theory thus showing when the amount of bone will increase, decrease or stay the same (Frost, 2003).
These stages are related to differing amounts of strain that the bone is subject to, which can be referred to as the minimally effective strains (MES) for each process (Frost, 2003).

- MESr: Bone's disuse based bone remodelling threshold range, which is the point at which a decrease in the bone mass starts to occur (Frost states it as 50-100

micro strain).

- MESm: Bone's modelling threshold range, which is the point at which an increase in the bone mass starts to occur (Frost states it as 1000-1500 micro strain).
- MESp: Bone's operational micro damage threshold, above this point woven bone formation “usually” replaces lamellar bone formation (Frost, 2001) (Frost states it as ~3000 micro strain).
- Fx: Bone's fracture strength, which is the point at which the bone fractures and modelling cannot occur (Frost states it as ~25,000 micro strain in young adults).

These strain amounts segment the bones into four different stages of bone remodelling (Frost, 1987, 2003).

- Disuse: Bone dies back.
- Adapted: No change in total bone mass.
- Mild Overload: Formation of lamellar bone.
- Pathological Overload: Formation of Woven bone.

It is also important to note that multiple processes of remodelling and modelling happen at the same time, such that the change in bone mass is a combined function of both (Figure 1-18) (Frost, 1987, 2003; Schett, 2004).

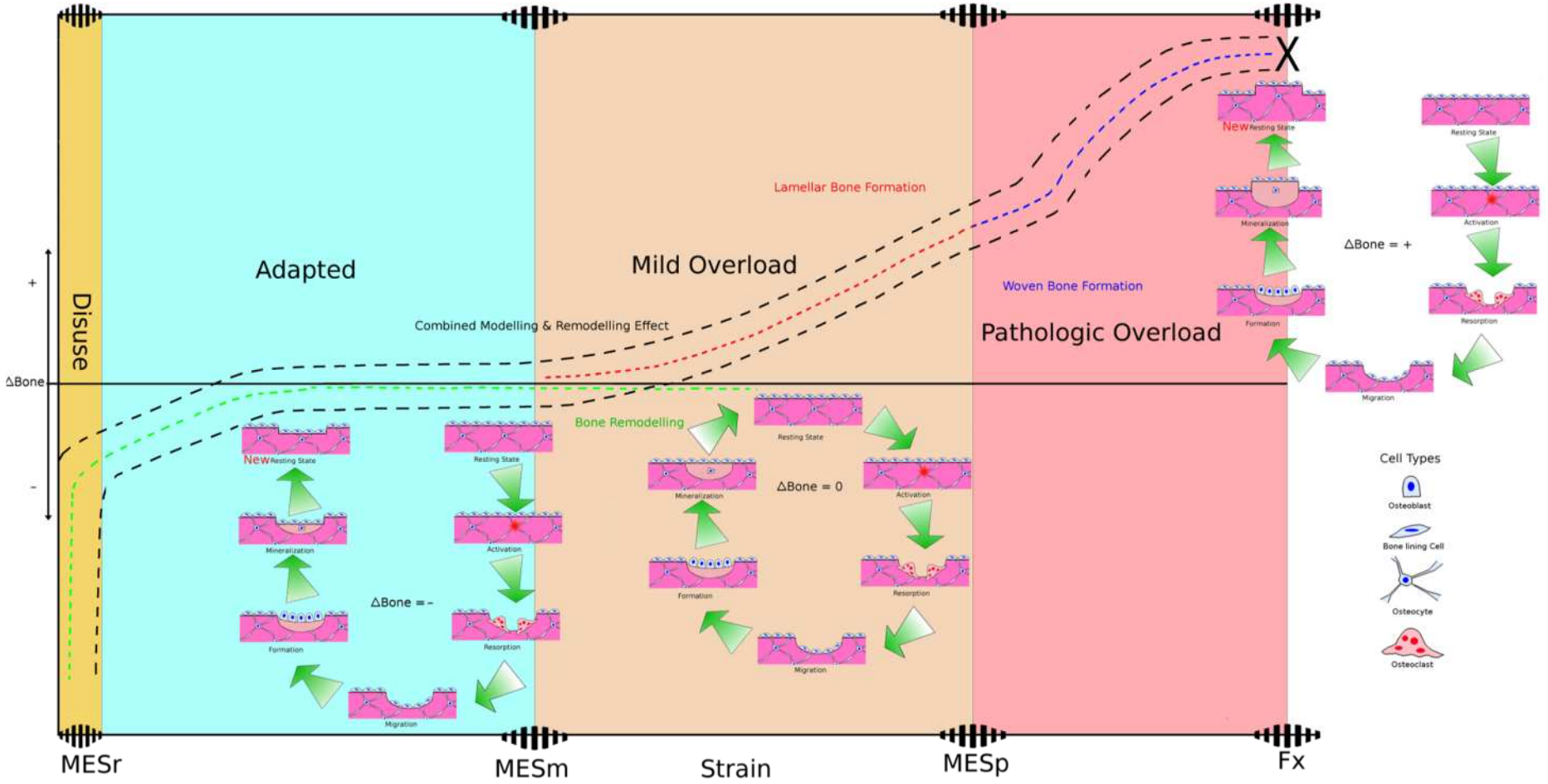

Figure 1-18Diagram of the different regions of bone modelling and remodelling showing the combined modelling and remodelling effect on the bone (black line) with related BMU diagrams for bone remodelling and modelling. (Based on the BMU diagram by (Schett, 2004) *the modelling and remodelling effect mechanostat diagram by* (Frost, 2003) *and the remodelling and modelling diagrams by* (Frost, 1987)*).*

1.1.4 Bone Healing and Diseases

1.1.4.1 Fracture Healing

Fracture healing of bone is a complex process involving both intracellular and extracellular molecular signalling (Dimitriou, Tsiridis, & Giannoudis, 2005).
In classical histological terms fracture healing can be divided into primary fracture healing (also referred to as direct or cortical fracture healing) and secondary fracture healing, with primary involving a direct attempt by the cortex of the bone to repair any interruption it has suffered, while secondary involves responses in both the periosteum and external soft tissue and the formation of a callus (Einhorn, 1998).
Primary fracture healing can be viewed as being another form of the continuous bone turnover (remodelling) which is occurring all the time in bone, this process can be attempted to be forced in surgery by putting the fracture in compression such that the surfaces of the bone are in contact (Mckibbin, 1978).
Secondary fracture healing process involves both intramembranous and endochondral ossification (Figure 1-19), these combine in at least six healing steps (Einhorn states five, while Dimitriou *et al*, adds the calcification stage) (Dimitriou *et al*., 2005; Einhorn, 1998) including:

- Hematoma formation and inflammation
- Cartilage formation
- Cartilage calcification
- Cartilage removal
- Bone formation
- Bone remodelling

Following trauma, proinflammatory cytokines, (interleukin-1 (IL-1), interleukin-6 (IL-6), and tumour necrosis factor-a (TNF-a)) are expressed first in the inflammatory phase and later in the remodelling phase with BMP-2 signalling (Sela & Bab, 2012; Tsuji *et al*., 2006).
During the first 7-10 days the periosteum initiates intramembranous ossification causing the formation of woven bone millimetres from the fracture site, at the same time the

callus overlaying the fracture starts to take on the appearance of cartilage (Einhorn, 1998).

The calcification of the fracture callus happens after approximately nine days and follows almost the same mechanisms as seen in the growth plate during ossification, once the fracture gap is closed, the callus, which is now fully formed out of woven bone, starts to remodel into lamellar bone (Einhorn, 1998).

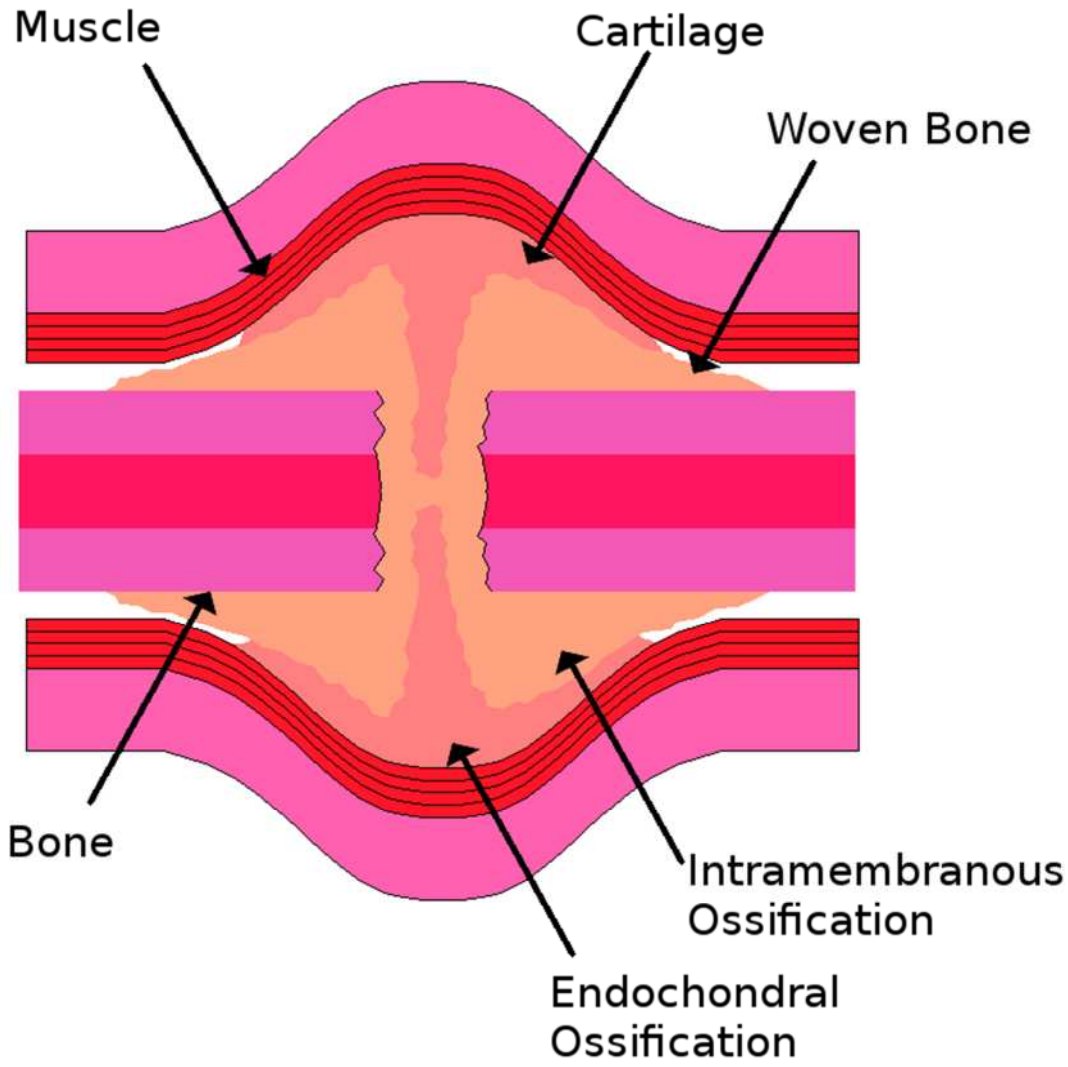

Figure 1-19 Diagram of bone fracture and the positions of intramembranous and endochondral ossification based on the diagram by (Bostrom *et al*., 1995).

1.1.4.1.A Critical Defect Size

There are situations when the defect created during fracture is too large for the bone to heal which is referred to as the critical defect size, in these situations, a graft would be required to either fully or partially bridge the defect site, so that the bone can heal (Sela & Bab, 2012).

It is important to note that because of the time constrains in studies the term critical size defect in animal research has come to mean the size of defect that will not heal on its own during the duration of the study (Gosain, Song, & Yu, 2000). While clinically determined to be twice the diameter of the injured bone (Sela & Bab, 2012), there is still an experimental need for the critical defect sizes to be measured for the different animal models, as in this thesis both ovine (sheep) and lapin (rabbit) models will be used the critical defect sizes for each need to be considered (Campion, Chander, Buckland, & Hing, 2011; Fini *et al*., 2005) (Table 1-3).

Table 1-3 Table of different animal models and their respective "critical defect" size.

Animal Model (Site: Length of Study)	Size and shape of Critical defect	Source
Ovine (Distal femur: 12 Weeks)	8mm diameter and 15mm deep cylindrical defect	(Campion *et al*., 2011)
Lapine (distal femoral condyle: 12 weeks)	6mm diameter and 10mm(+-0.5) deep cylindrical defect	(Fini *et al*., 2005)

It should be noted that there are factors which can affect the ability of critical defects to heal, for example BMP-4 has been shown to heal 7 mm diameter defects (larger than a critical defect) in the femoral shaft in a rat model after 12 week (Shen *et al*., 2004).

1.1.4.2 Aging

As bone is constantly remodelling, it could be thought that the bone would remain in perfect condition for its entire lifetime.

There is evidence however that the bone's mineral composition changes as it undergoes micro damage, with evidence of the carbonate groups being preferentially removed from the mineral (Ruppel, Burr, & Miller, 2006). This would leave bone with a different mineral structure to that with which it began with.

As well as this as the bone ages it loses bone density, which results in bone which suffers more fractures (Riggs *et al*., 1982; D. M. Smith, Khairi, & Johnston, 1975). The collagen is also shown to decrease in mechanical integrity with age, which would also increase the frequency of fractures (X. Wang, Shen, Li, & Agrawal, 2002). This increase in fractures could be the cause of the change in the bone network in the elderly, namely

the shift from a continuous trabecular network in the young to the disconnected network in the elderly, which can be viewed as a loss of distinct trabeculae from the bone, and not an overall degradation of its structure (though there is a slight reduction of thickness of the remaining bone) (Parfitt *et al.*, 1983).

1.1.4.3 Bone Disease

The disorders of the bones and skeleton have been often referred to as “metabolic bone diseases” of which the “classic” metabolic bone diseases can be considered to be related to the mineral in the bone while the disease related to the organic parts of the bone can be identified as the “new”, with the two groups being divided as shown below (R. Smith *et al.*, 2005) (Table 1-4 & Table 1-5).

Table 1-4 Table of the “classic” metabolic bone diseases and their symptoms (R. Smith *et al.*, 2005).

Disorder (Classic Metabolic)	Symptoms
Osteoporosis	Reduction in thickness and number of trabecular
Osteomalacia (& rickets)	Low mineralisation
Parathyroid Bone Disorders	Cysts in long bones
Paget Disease	Uncontrolled osteoclast activity
Skeleton and Malignant Disease	Cancer

Table 1-5 Table of the "new" metabolic bone diseases and their symptoms (R. Smith *et al*., 2005).

Disorder (New Metabolic)	Symptoms
Osteogenesis Imperfecta	Brittle bone syndrome
Chondrodysplasias	Short limbed as reduction in collagen?
Osteopetroses & Osteoscleroses	Dense bones
Marfan Syndrome	Extraskeletal bone growth (including extra height)
Ehlers-Danlos Syndrome	Hyperextensible skin and excessive joint laxity
Enzyme Defects	Various
Fibrous Dysplasia	Cranio-facial deformities, thin weak bone
Fibrogenesis imperfecta ossium &Related Disorders	Failure to mineralize/mineralization disruption
Ectopic Mineralization	Extraskeleton ossification

Osteoporosis is the most common metabolic bone disease and a major cause of fractures in bone (Favus, 2010; R. Smith *et al*., 2005). Osteoporosis is defined by the reduction in bone over a set volume with a measure of either bone mineral density or bone mineral content if there is shift of more than 2.5 standard deviations below the mean peak bone mass (R. Smith *et al*., 2005). Osteoporosis is an important factor in the increasing amount of fractures in the ageing populations as studies have shown that the risk of fracture increases with a decreasing bone mass density (National Osteoporosis Guideline Group, 2014). From a cellular point of view osteoporosis can be seen as an imbalance between the osteoblast and osteoclast activity and the causes can range from menopause (Primary causes) to nutritional (Secondary) (R. Smith *et al*., 2005). Osteomalacia (& rickets) is caused by the lack of vitamin D or by the inability to metabolise it and as such the body has defective mineralization causing deformed and painful bones (R. Smith *et al*., 2005).While the treatment for rickets is vitamin D,

patients with healthy amounts of vitamin D but lacking in calcium in their diet exhibit similar symptoms and need to be treated with calcium or calcium and vitamin D and not just vitamin D (Thacher *et al*., 1999).

Parathyroid Bone Disorders involve the parathyroid hormone (PTH) and include both the effects of hyperactive parathyroid as well as parathyroid hormone resistance (or deficiency) (R. Smith *et al*., 2005). Hyperparathyroisism can result in hypercalcaemia, (though not always seen constantly in the patient) bone resorption and ectopic calcification while efficiency and resistance can also result in hypercalcaemia as well as hyperphoshatemia and other physiological conditions in the body (Bilezikian *et al*., 2002; R. Smith *et al*., 2005).

Paget's Disease is the second most common metabolic bone disease (effecting 2-3% of the population over 60) it is characterised by increased remodelling rate of the bone, which causes deformations (Reddy, Kurihara, Menaa, & Roodman, 2001). The increase in remodelling rate is connected with increased osteoclasts activity, which are increased in both number and size and with up to 100 nuclei (compared to the normal 5-10) and as an increase in osteoblast number and activity which produces “exuberant” new woven bone formation (Reddy *et al*., 2001; Roodman, 1995). It is currently thought that the osteoclasts are hyperesponisive to the RANK ligand and this is caused in some way by the Measles virus nucleocapsid (MVNP) (Reddy *et al*., 2001; Sundaram, Senn, & Reddy, 2013). Current treatments for Paget's disease include drugs such as biophosphates and Clodronates (R. Smith *et al*., 2005). There are surgical interventions which can be performed on patients with Paget's disease to reduce pain but because of the nature of the diseases they have extra complications and as such it is preferable that the disease activity be decreased first before surgery is attempted (Kaplan, 1999).

Skeleton and Malignant Disease includes primary tumours, which are uncommon, and the rare malignant primary tumours as well malignant cells from other parts of the body (Athanasou, 2001; R. Smith *et al*., 2005). The tumours in bone can either be benign or malignant and can cause a variety of problems in the bone for the patient (Table 1-6) (Athanasou, 2001).

Table 1-6 Features of benign and malignant bone tumours (Athanasou, 2001).

Feature	Benign	Malignant
Pain	May be absent or present	Frequently Present
Soft Tissue Mass	Not Present	Often Present
Periosteal Reaction	Variable	Common
Margin of Lasion/Zone of Transition	Well-defined ± sclerotic	Poorly-Defined
Trabeculation	May Be Present	Unusual
Cortical Destruction	Rare	Unusual
Pattern of Osteolysis	Geographic	Moth-eaten or Permeative

The treatments for these conditions can range from surgery, radiotherapy and chemotherapy to endocrine manipulation (R. Smith *et al*., 2005).

Osteogenesis Imperfecta is caused by dominant mutations in the genes for type I collagen, which causes fragility in the bone (R. Smith *et al*., 2005).

Chondriodysplasias are inherent disorders which cause disruptions of skeletal development via disrupting cartilage growth and the growth plate in endochondral ossification, with over a hundred distinct forms of the condition having been observed in humans (Horton & Hecht, 2002). The disruption in the growth and formation of the long bones can present itself in the short or disproportionate stature of the affected patient (R. Smith *et al*., 2005)

Osteopetroses and Osteoscleroses are inherited dense bone disorders either from lack of bone resorption or excess bone formation (R. Smith *et al*., 2005). As the suppression of RANK (Receptor Activator of Nuclear Factor) in mice has been shown to cause osteopetroses either a mutation to the RANK or its receptors has been considered as a cause for the disorder (Li *et al*., 2000).

Marfan Syndrome is a disorder of the connective tissue which affects 1-3 per 10,000, and is thought to be caused by a mutation in the fibrillin-1 gene, (which produces fibrillin-1 which is associated with elastin). In the skeleton it results in elongation (including the limbs and skull) and deformity of the bones (Pyeritz & Dietz, 2002; R. Smith *et al*., 2005).

Ehlers-Danlos Syndrome presents with multiple types with the common features being hyper extensible skin and excessive joint mobility, the syndrome causes mutations in collagen as well as defects in the collagen metabolism (R. Smith *et al*., 2005). Patients suffering from Ehlers-Danlos syndrome have been shown to exhibit lower bone density with a resultant higher fracture chance (Dolan, Arden, Grahame, & Spector, 1998).
There are many potential enzyme defects which can affect the skeleton, all of them rare which leads them to commonly being mistaken for more common disorders (R. Smith *et al*., 2005). It includes such disorders as hypophosphatasia, which causes defective bone mineralisation due to mutations in Tissue Non-Specific Alkaline Phosphatase (TNSALP), as well as Alkaptonuria which causes increased pigmentation in connective tissue (caused by the deficiency or lack of the enzyme homogentisc acid oxidase) this pigmentation can cause stiffness and pain within the skeletal system (La Du, 2002; R. Smith *et al*., 2005; Zurutuza *et al*., 1999).
Fibrous dysplasia is caused by a mutation in the G-protein signalling system, and it presents in bone (sometimes in a mosaic fashion) by producing lesions with disorganised woven bone formation, which leads to deformation and weakness which in turn leads to fracture (Bianco *et al*., 2000; R. Smith *et al*., 2005).
Fibrogenesis imperfecta ossium causes the mineralisation of bone to become defective via the production of type I collagen deficient tissue which does not mineralise correctly (R. Smith *et al*., 2005).
Ectopic Mineralization is either the ossification or deposition of mineral outside the skeleton, in some cases the cause can be identified as abnormal local biochemistry which relates to bone formation, but in most cases the causes are unknown (R. Smith *et al*., 2005).

1.1.5 Summary

In summary, bone is a complex organ at not only multiple scales of structure but also in the cells and factors which control them. This complex system is able to remodel in response to the changes in its environment as well as to heal and repair fractures below a certain size. However for large fractures and bone disease outside assistance is required to allow the bone to become “whole” again which can come in the shape of drugs or in the case of a significant amount of bone loss, a piece of bone or other material which can be grafted into place.

1.2 Bone Grafts

In the field of orthopaedics there is a clear need for materials to fill critical sized defects and for the use in rebuilding bones damaged by injury and disease. These materials are now known as bone grafts and have changed significantly over time since their first usage in both the materials and the philosophy behind their selection.

1.2.1 Bridging the Gap

The earliest evidence of the use of grafting in bone comes from cranioplasty (which can be seen as the sister procedure to trephination), with gaps in Inca skulls from 2000 BC being filled either with a precious metal, or a gourd (the selection thought to depend on status) with the graft showing evidence of post-implantation healing (Sanan & Haines, 1997).

Since then many different materials had been used to fill the gaps within bone with the list of recognised materials at the end of the 1800s compiled by Curtis listed below (Curtis, 1893):

Curtis referred to them as materials for dealing with cavities and also states that all the materials had “all been made to heal-in in bone cavities”

Foreign substances:

- *Non-absorbable, such as various metals, celluloid, plaster-of-Paris*
- *Absorbable, such as catgut, Halstead's "fibre," sponge, decalcified bone, simple dead bone, ivory.*

Living bone:

- *From another species.*
- *From the same species or the same individual.*

These materials were selected on the criteria that the gap in the bone needed to be filled, either to allow for healing or to just to fix the bone in place. It was in the late 1800s that the knowledge and science of bone biology had reached a point where a scientific approach could be applied to the selection of grafting material.

1.2.2 Bone To Bone

As seen in Curtis's list, bone itself was a recognised material to fill defects in bone, the first report of a successful bone graft was reported by the Dutch surgeon Job Van

Meekeren which involved a dog xenograft (from a different species) for a cranioplasty in 1668 (Boer, 1988; Meekeren, 1668).

This lead onto the first clinical autograft (bone taken from the patient) which was performed in 1820 by Philips Von Walter (cranioplasty) and the first clinical allograft (bone taken from another patient, dead or alive) which was performed by William Macewen (humerus reconstruction) in 1880 (Blitch & Ricotta, 1996; Boer, 1988).

However, it was earlier during the 1700s, that the biological qualities of bone healing started to be "understood" and as such using bone as a grafting material gathered considerable interest.

This first research has been attributed to Duhamelon with his work on the periosteum of the bone and its importance in bone growth, which was closely followed by the work of Hunter (also in the 1700s) who put the same periosteal theory of bone healing into question (Haldeman, 1933; Keith, 1917).

It was these opposite ideas that lead to the work by the French Surgeon Ollier, who incidentally first published the term bone graft in 1861 (*"greffe osseuse"*), his work showed "conclusively" that compact bone could live apart from both the periosteum and marrow which was further confirmed by Macewen thus implying that the living bone cells could be transferred from one site to another (such as in a bone graft) (Donati, Zolezzi, Tomba, & Viganò, 2007; Groves, 1917). However in 1893 Barth demonstrated that a great majority of the cells in the bone graft die, which was later confirmed by Axhausen in 1898 (Groves, 1917).

This research while not showing how the living part of bone survives when it is transplanted showed that there was a clear interest in understanding how bone reacts to being extracted and transplanted from one site to another.

However, it was not until the publication of Albee's work in 1915 (Albee, 1915) on bone graft surgery that the procedure of bone transplantation started to become wide spread (Boer, 1988). Only a year later Davison published his work on "Autoplastic Bone Surgery" (Davison, 1916) with both books mentioning the importance of the periosteum in bone grafting and defining clearly the importance of the field (Warbasse, 1916). By 1919 Albee was able to report on 1600 successful bone grafts showing how far the procedure had come in a relatively short time (Meeder & Eggers, 1994).

By the early 1920s it was generally accepted that the autograft died once implanted and as such acted as a scaffold for bone growth and by the 1930s the accepted idea was that the periosteum was the most important part of the graft, with the rest of the graft dying

and being reabsorbed. (Haldeman, 1933; S. Smith, 1921). This interest in the periosteum has carried on into the present day with now the interest in being to remove the cells from the periosteum to implant into a separate graft (Ball, Bonzani, Bovis, Williams, & Stevens, 2011).

This constant investigation and continuing interest shows the complexity of understanding bone cells in bone grafting.

1.2.2.1 Autograft and Allograft Performance

Autografts while providing the "best healing rate" are not without their limitations. These limitations include the size and shape of graft available from the patient taking into account that "large" autografts will also increase surgery time, blood loss of the patient and increased postoperative morbidity (of 8 %) which also results in an increased risk of infection and post-op pain (Burchardt, 1983; Malinin & Brown, 1981; Thordarson, 1995).

It is because of these limitations of the autograft that allografts became an attractive alternative, but they are also not without their own drawbacks, including eliciting an immunological response in the host as well as a 50% rejection rate when taken from a live donor (Burchardt, 1983; Zimmermann & Moghaddam, 2011).

Some of the disadvantages and hazards of allografts over autograft are shown below (Thordarson, 1995):

- Fracture (>10 %)
- Infection (15% to 20 %)
- HIV (0.0001 %)

The transmission of infectious agents in allografts (especially of concern from cadaver transplantation) can be virtually eliminated via the processing and sterilisation of the allograft but the process can also weaken both the mechanical and biological properties of the graft (Zimmermann & Moghaddam, 2011).

In a direct comparison with allograft from a reliable source(n=99, from femoral heads from hip replacements no post processing) and autografts (n=83) in scoliosis surgery showed a significant decrease in surgery time for the allografts and no significant difference in the quality of surgery after a year (Fabry, 1991).

As of the start of the 21st century autogenous and allogenous bone were still the main sources for bone grafting procedures (Moore, Graves, & Bain, 2001).

The use of autografts and allografts was a significant step in the science of bone grafts, but while these each have their advantages, as demand grows there are not enough grafts of either type to fulfil demand, and as such a synthetic graft with similar properties became an attractive alternative.

1.2.3 Engineering a Solution

With the limited supply of bone for grafts and the continuing breakthroughs in material science, creating an artificial graft became an attractive and feasible alternative.

1.2.3.1 Materials

The materials that were first investigated for synthetic bone grafts were each created under a different ethos, with three of the most investigated grafts, tri-calcium phosphate (TCP), hydroxyapatite (HA) and bioglass, having distinctly different origins.
The early work on TCP (referred to as triple calcium phosphate and does not state which type) was performed by Albee who investigated if a synthetic material could stimulate bone growth, his study in dogs injecting a 5% solution of tri calcium phosphate into fractures showed a reduction in the average healing time from 42 to 31 days (Albee, 1920). TCP has two forms, alpha and beta, where alpha degrades faster than beta but does not induced the formation of nay more bone than the Beta form (Kamitakahara, Ohtsuki, & Miyazaki, 2008; Rojbani, Nyan, Ohya, & Kasugai, 2011).
Synthetic HA was first developed during the second world war as a substitute for bone char in sugar refining (Barrett, Brown, & Oleck, 1951). The first tests on HA bone regeneration were carried out by Ray in 1952 (Ray, Degge, Gloyd, & Mooney, 1952).
Bioactive glasses were first developed in 1969 by Hench while attempting to develop a material which could bond with the body and entered clinical use in 1985(Hench, 2006). Interestingly the common form of bioglass, 45S5 bonds to the bone via a calcium phosphate layer and not a silicon based one (Clark, Hench, & Paschall, 1976).
HA was also studied in another route by the hydrothermal conversion of coral, which came to fruition from the work by Weber and White in the early 1970s into copying the porosity of natural structure (Including Coral) using the process of replaminform for the purpose of creating new biomaterials (Weber, White, & Lebiedzik, 1971; White, Weber, & White, 1972). Work inspired by that of Weber and White took the idea in a different direction by using the coral directly by converting it into a form of HA via hydrothermal exchange (Roy & Linnehan, 1974). This coral based HA implant has been

shown to integrate at similar rate to an autograft in distal diaphysis in foxhounds (Holmes, Mooney, Bucholz, & Tencer, 1984). There also has been success in producing Phase pure HA directly from bovine bone (Ooi, Hamdi, & Ramesh, 2007).
Some of the other materials which have been developed include Glass ioniomer cements first developed in 1971 injectable calcium phosphate and calcium carbonate based biological cements which were introduced in 1998 (Moore *et al*., 2001).

1.2.3.2 The Requirements of a bone graft

Since the first synthetic bone grafts were developed there has been an increasing interest in determining how bone interacted with the grafts and how these reactions could be characterised.
It was in this environment that Urist in the 1950s set out a definition of the effect of induction of the graft on the host bone (Boer, 1988). Urist stated the definition of induction (based on Spemann's previous work) as “the physical-chemical effect which one tissue exerts upon another in contact with it.” (Urist, 1953).
Since Urist's first definition terms for the positive effects (prefixed with either osteo or osseo) of the graft on the host bone have been defined and are now generally accepted with the common ones being osteoinduction, osteoconduction, osteogenesis and osseointegration (Albrektsson & Johansson, 2001; Giannoudis, Dinopoulos, & Tsiridis, 2005; Ilan & Ladd, 2003):

- Osteoinduction: Undifferentiated and pluripotent cells are stimulated to develop cells in the bone-forming cell lineage (Albrektsson & Johansson, 2001).
- Osteoconduction: Bone cells form bone on the surface of the graft material, also referred to as the material providing a scaffold for the bone to grow on to (Albrektsson & Johansson, 2001; Ilan & Ladd, 2003).
- Osseointegration: .The formation of a bond between host bone and grafting material (the term first coined by Brånemark (Albrektsson & Johansson, 2001)) (Giannoudis *et al*., 2005).
- Osteogenesis: The process of direct bone formation from within the graft from osteoblasts and osteoblast precursors (so far only autograft has true osteogenic properties) (Ilan & Ladd, 2003).

The grafts can also be defined by the type of attachment that they form with pre-existing bone (Table 1-7).

Table 1-7: Types of Tissue Attachment of Bioceramic Prostheses (Hench & Wilson, 1993).

Type of Implant	Type of Attachment	Example
(1) Nearly inert	Mechanical interlock (Morphological Fixation)	Al_2O_3, Zirconia
(2) Porous	Ingrowth of tissues into pores (Biological Fixation)	Hydroxyapatite (HA) HA coated porous metals
(3) Bioactive	Interfacial bonding with tissues (Bioactive Fixation)	Bioactive glasses Bioactive glass-ceramics HA
(4) Resorbable	Replacement with tissues	Tricalcium phosphate Bioactive glasses

There is also the more general and common term “biocompatibility” which is defined by the oxford dictionary as “not harmful or toxic to living tissue” (Stevenson, 2010). From a surgical point of view the ideal graft is biocompatible, bioresorbable, osteoconductive, osteoinductive and allows osteogenesis, while being structurally similar to bone, easy to use, cost-effective and provides structural support (Greenwald *et al*., 2001; Ilan & Ladd, 2003).
With these definitions, there was created a common language for which to define and compare the different grafts that were being created.

1.2.4 Improving Grafts by Structure, Chemistry and Biology

1.2.4.1 Structure

For the structure of a graft, both the pore structure and micro structure can be altered to affect how the graft preforms.

1.2.4.1.A Pore Structure

In the 1970s Klawitter and Hulbert pioneered studies investigating the required pore size for bone ingrowth (Moore *et al*., 2001).

The work by Hulbert's states that after a four week study using calcium aluminate (defined in the work as inert) pores below 75 μm diameter produced only connective tissue, diameters between 75 μm, 100 μm produced both connective tissue and unmineralised bone, pores above 100μm diameter exhibited fully mineralised bone and pores larger than 150μm diameter were needed for the formation of osteons (Hulbert *et al*., 1970).

The work by Klawitter in porous high density polyethylene showed that bone growth was seen in pores as small as 40μm diameter (which was the smallest pore tested) but with optimal growth into pores of 100-135 μm diameter, in which the bone showed typical cell shapes and vascularisation (Klawitter, Bagwell, Weinstein, & Sauer, 1976).

A contemporary study using Cobalt alloy coated screws with pores of diameters between 20-100 microns bone was seen penetrating into the porous coating after four weeks implantation (even with a 4.5 mm gap between the coating and the bone) (Cameron, Pilliar, & Macnab, 1976).

From the review by Karageorgiou (Karageorgiou & Kaplan, 2005) it appears to be commonly accepted that a 100μm diameter (Quoting both Klawitter's and Hulbert's) is the smallest pore size for bone in growth *in vivo* this has been mirrored in other reviews such as by Jones (J. Jones, 2005) but with the 100μm being defined as minimum aperture diameter for angiogenesis.

These minimum pore sizes do not take into account the effect of the different materials, taking the pore measurements from bioinert materials to determine the pore size effect in bioactive materials. In fact it has been shown that a pore size of under 100 microns does result in bone growth in at least an unloaded structure (in a titanium implant in a rabbit model) (Itälä, Ylänen, Ekholm, Karlsson, & Aro, 2001).

It has also been shown that the pore structure influences the pattern of the bone growth, this implies that the shape of the bone within the pores should be investigated, not just the volume (Hing, Best, Tanner, Bonfield, & Revell, 2004).

The interconnections between the pores have also been shown to be important if not more so than the pore sizes, with relatively large values appearing to guarantee bone ingrowth (interconnect size the range of 250-300μm diameters) (Kolk *et al*., 2012). The minimum interconnect size required for bone ingrowth appears to be 20μm diameter with 50μm diameter assuring mineralisation formation (within beta TCP and HA models) (J. X. Lu *et al*., 1999). High levels of interconnects osteoconduction have been observed in pores of 50μm with large capillary running through the pores, which

appears to put into the question the idea that the pore diameter determines the bone growth (Chang *et al*., 2000).It has also been shown that as the interconnect size is increased in Porous HA sample with constant pore size there is an increase in bone growth of ~47 % to ~67 % with an increase of interconnect from 30μm to 130μm diameter (Flautre, Descamps, Delecourt, Blary, & Hardouin, 2001).

1.2.4.1.B Micro Structure

Not only can the porosity be changed on the macro scale, but the material of the graft in the struts between the pores can be porous in its own right on the micro (defined as <10μm diameter) or even nano scale.

In both hydroxyapatite and tricalcium phosphate, with similar sized pores there is a significant change in both growth when the specific surface area is changed (caused by micro porosity) with more bone growth occurring in general with the higher micro porosity, because of the higher surface area (Habibovic *et al*., 2005). In hydroxyapatite grafts this has been shown to have a significant effect on the osseointegration of the bone with the graft with a higher rate of micro porosity resulting in a higher rate of Hydroxycarbonate apatite formation (Campion, Ball, Clarke, & Hing, 2013; Hing, Annaz, Saeed, Revell, & Buckland, 2005).

It is worth noting that if the micro-porosity and material both affect the way that osteoblasts interact with it, it is a logical conclusion that the pore size that is required for bone ingrowth would not be the same for all materials and all micro porosities.

1.2.4.2 Chemistry

Not only have different materials been used to improve the graft's properties but also chemical substitutions have been performed to known synthetic bone graft materials. HA has had many different substitutions (Section 1.1.1.1.C) which have be shown to improve the grafting properties, with silicon being used to positive effect (Hing *et al*., 2006). Bioglass chemistry can also be modified for better results by adding extra elements to the mix such as strontium, which can change their reaction in the body, with enhanced cell proliferation (Hesaraki, Alizadeh, Nazarian, & Sharifi, 2010).

1.2.4.3 Biology

There has also been work into combining biological factors into the synthetic grafts, to attempt to recreate the effects of autografts and allografts.

This has been attempted by combining of TCP and BMP (study does not state which BMP was used) which showed an increase in bone bridging (from <10 % without BMP to 35-100 % with BMP) (Urist & Nilsson, 1987). BMP-7 has also been produced on its own under the trade name OP-1 (Osteogenic Protein-1, Stryker Biotech, Hopkinton, MA) for direct addition to grafts (Ilan & Ladd, 2003) .
The cells in the periosteum have also been extracted to be placed into grafts in another attempt to recreate the properties of the autograft (Stevens *et al*., 2004).

1.2.5 Future of Bone Grafting

There are now many different artificial bone grafting materials, with research being carried out into not only creating new materials but modifying the currently available materials with elemental substitutions, the addition of biological factors and the change of their structures. With these different factors that can be changed and combined there is the need to directly quantify the bone within the grafts. Especially since these factors such as chemical substitution and porosity cannot be considered as being mutually exclusive, with the change in one factor could well change how the body reacts to another factor. Therefore methods which can quantify the bone's growth in three dimensions provide a measure for the how the bone reacts and changes to different synthetic bone graft.

1.3 X ray Imaging and Computed Tomography

To analyse the 3D structure of the bone and bone graft, as well as the relationships between them, it is first required to scan the sample of bone and graft and produce 3D images of it. Because of the nature of the samples (varying densities between regions in samples) X-ray Computed Tomography is the ideal method to image them. But it is important to first understand the limitations and sources of errors for X-ray imaging.

1.3.1 X-rays

X-rays are high frequency electromagnetic waves and were discovered by Roentgen in 1895 (Roentgen, 2005). X-rays transmit energy in the form of photons which display properties of both waves and particles (Bushberg, Seibert, Leidholdt, & Boone, 2012). The wave-length and frequency of the X-ray are determined by the classic wave equation (c: Speed through the medium they are travelling, λ: Wave length, ν: Frequency) as shown in Equation 1-1.

Equation 1-1

$$c = \lambda \nu$$

The energy of the photon can be calculated from its wave properties and Planck's constant (6.626×10^{-34}) as shown in Equation 1-2.

Equation 1-2

$$E = h\nu = \frac{hc}{\lambda}$$

Because most X-ray systems work in the energy range of keV (Where eV is an Electron Volt which is approximately 1.6×10^{-19} Joules) the equation can be rearrange to give the energy in keV from the wave length (Assuming speed of light in a vacuum as 2.998×10^{8} m/s) as shown in Equation 1-3.

Equation 1-3

$$E(keV) = \frac{1.24}{\lambda(nm)}$$

X-rays can be produced from electrons transitioning between different atomic shells. The energy of these X-rays depends on the difference in binding energies in the atomic shells as shown in Equation 1-4 (Bushberg *et al*., 2012).

Equation 1-4

$$E_{Xray} = E_{bVacant\ Shell} - E_{bTransition\ Shell}$$

As well as being produced by electrons transitioning between different energy levels, X-rays are produced when electrons undergo deceleration (often due to interaction with a target material), which is referred to as bremsstrahlung (breaking) radiation (Bushberg *et al*., 2012; Wehr, Richards, & Adair, 1984). The electrons are first accelerated by charging an anode and a cathode, and this charge determines the maximum energy of the X-rays that can be produced (Bushberg *et al*., 2012). The number of X-rays produced at each energy via bremsstrahlung is linearly inverse to the energy of the electrons and thus produces a multi energy X-ray beam, in X-ray scanners the output X-rays are often filtered to remove the lower energy photons which would attenuate in too short a distance of the sample to be useful for imaging (Figure 1-20) (Bushberg *et al*., 2012).

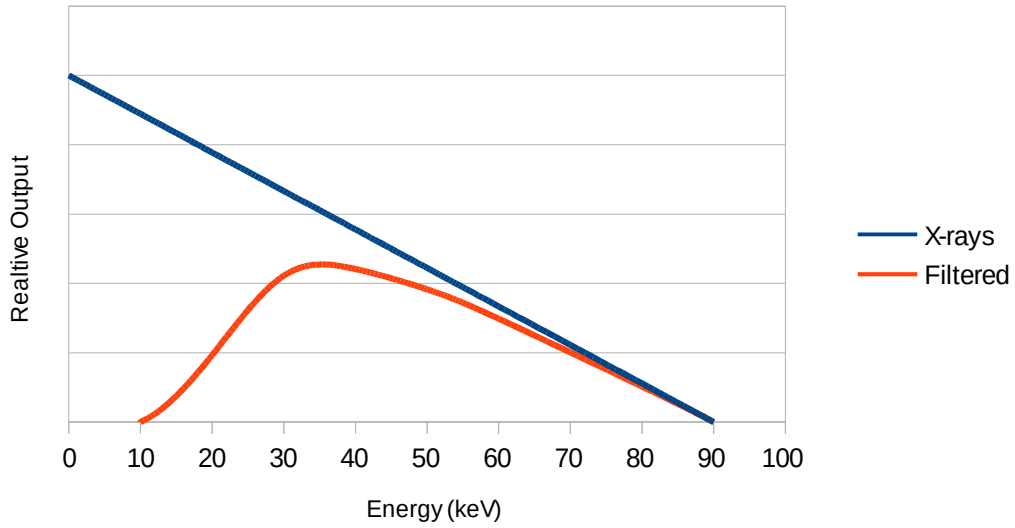

Figure 1-20 The X-rays produced via bremsstrahlung radiation and with a 1.5 mm aluminium filter(Based on an image by (Bushberg *et al*., 2012) *and data from* (Hubbell & Seltzer, 1996)*).*

The characteristic X-rays are also present in the X-rays produced in an accelerating X-ray source, produced from where the electrons interact atomically with the target. (Figure 1-21) (Bushberg *et al*., 2012; Hubbell & Seltzer, 1996).

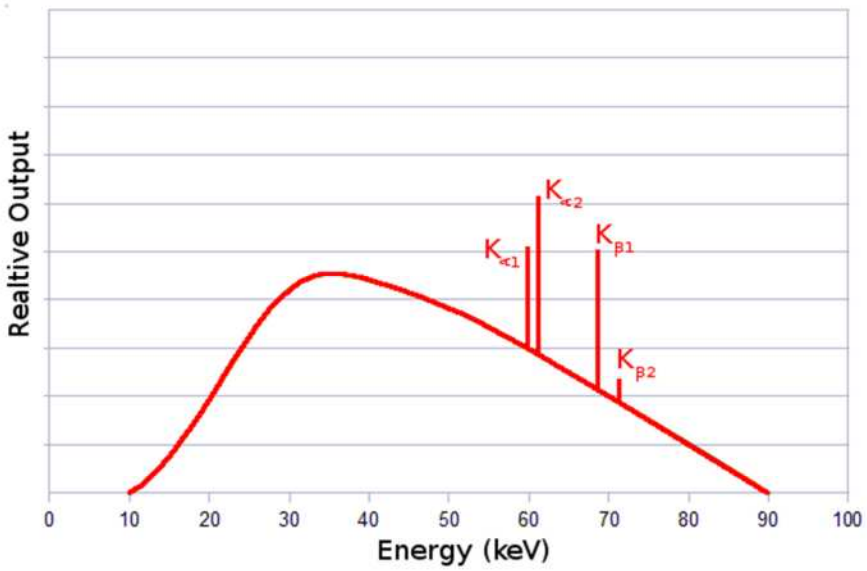

Figure 1-21 Diagram of the X-rays produced via bremsstrahlung radiation and then filtered with a 1.5 mm aluminium filter, with characteristic X-rays formed from a tungsten target(Based on an image by (Bushberg *et al*., 2012) *and data from* (Hubbell & Seltzer, 1996)*).*

Even with a mono-energy X-ray beam, the X-ray's photon frequency's fluctuate, in this case obeying the Poisson distribution (Equation 1-5), where *m* is the mean and *x* is the independent variable as shown in Equation 1-5 (Bushberg *et al*., 2012).

Equation 1-5

$$p(x) = \frac{m^x}{x!} e^{-m}$$

This means that when measuring the number of photons detected, the standard deviation (noise) is equivalent to the square root of the mean of the number of X-ray photons.

1.3.1.1 X-ray Interactions with Matter

When X-rays interact with matter, they attenuate either by being scattered or absorbed.

1.3.1.1.A Rayleigh scattering

When an electron undergoes Rayleigh scattering it interacts with an atom and excites it, resulting in the production of a new X-ray with the same energy but propagating in a different direction (Bushberg *et al*., 2012).

1.3.1.1.B Compton Scattering

When an X-ray undergoes Compton scattering the X-ray interacts with an electron in a

shell of the atom (most likely the outer shell) causing it to be ejected and a scattered X-ray to be produced. The energy of this resultant X-ray can be calculated from the energy of the incident X-ray (E_0) and the energy of the ejected electron as shown in Equation 1-6 (Bushberg *et al*., 2012).

Equation 1-6

$$E_0 = E_{Scattered} - E_{Ejected}$$

The Energy of the scattered X-ray can also be calculated by its angle of deflection from the incident X-ray as shown in Equation 1-7 (Bushberg *et al*., 2012).

Equation 1-7

$$E_{Scattered} = \frac{E_0}{1 + \frac{E_0}{511\ keV}(1 - cos\theta)}$$

1.3.1.1.C Photoelectric Effect

When an electron undergoes the photoelectric effect all the energy is transferred to an electron which is ejected from the atom, the energy of the electron emitted can therefore be calculated from the energy of the incident X-ray (E_0) and its binding energy (E_b) as shown in Equation 1-8 (Bushberg *et al*., 2012).

Equation 1-8

$$E_{Photoelectron} = E_0 - E_b$$

The probability of an electron undergoing photoelectric absorption, per unit of its mass can be determined from the atomic number (Z) and the energy of the incident X-ray (E) as shown in Equation 1-9 (Bushberg *et al*., 2012).

Equation 1-9

$$Probablity \approx \frac{Z^3}{E_0^3}$$

This can cause a cascade as higher energy electrons transition to fill the gap in the inner orbit, releasing X-rays as they change orbits.

At energies below 25keV the majority of X-ray photons interact with matter via the photoelectric effect (Ritman, 2004).

1.3.1.1.D Pair Production

When the energy of the X-rays exceed 1.022 MeV, they can interact with the nucleus and produce an electron positron pair (each of which 0.511 MeV) (Bethge, Kraft, Kreisler, & Walter, 2010).

1.3.1.1.E Attenuation

The proportion of X-rays attenuated (removed) when passing through a material is related to not only the material but also the energy of the X-rays, this attenuation (defined by the linear attenuation coefficient μ) is the combined attenuations caused by Rayleigh scattering, Compton scattering, Photoelectric absorption and Pair Production effects as shown in Equation 1-10.

Equation 1-10

$$\mu = \mu_{Rayleigh} + \mu_{Compton} + \mu_{Photoelectric} + \mu_{Pair\ Production}$$

For a "thin" layer of material the attenuation can be considered linear as shown in Equation 1-11 (Bushberg *et al*., 2012).

Equation 1-11

$$n = \mu N \Delta x$$

However for thicker materials there is an exponential relationship between the number of photons attenuated and the linear attenuation coefficient as shown in Equation 1-12. (Compton & Allison, 1935).

Equation 1-12

$$N = N_0 e^{-\mu x}$$

As attenuation is dependent on the atomic weight of the elements of the material as well as its density, it can be presented by dividing the attenuation by the density of the material, thus allowing for the density of the materials to also be taken into consideration as shown in Equation 1-13 (Hubbell & Seltzer, 1996).

Equation 1-13

$$N = N_0 e^{\frac{-\mu}{\rho}\rho x}$$

Beam attenuation can also be determined by using the Half Value Layer (HVL) which is the thickness of a material which reduces the number of X-rays by a half as shown in Equation 1-14 (Bushberg *et al*., 2012). This is also used to determine the effective energy of a poly-energetic beam, for example if a poly-energetic beam has the same HVL as a mono-energetic beam of energy 100 keV, it would be considered to have an effective energy of 100 keV (Bushberg *et al*., 2012).

Equation 1-14

$$\frac{N_0}{2} = N_0 e^{-\mu(HVL)}$$

The HVL can also be calculated from the linear attenuation coefficient as shown in Equation 1-15.

Equation 1-15

$$HVL = \frac{0.693}{\mu}$$

It is also possible to determine the Mean Free Path (MFP) of the photons, which is the average distant travelled by an X-ray in the beam inside the material as shown in Equation 1-16 (Bushberg *et al*., 2012).

Equation 1-16

$$MFP = \frac{HVL}{0.693}$$

1.3.1.1.F Beam Hardening

A poly-energetic X-ray beam does not attenuate in the same way as a mono-energetic beam of its effective energy, as each X-ray attenuates according to its own energy, and as such the number of X-rays attenuated relates to all the different energies of the X-rays as shown in Equation 1-17.

Equation 1-17

$$N = N_{E1}e^{-\mu_{E1}x} + N_{E2}e^{-\mu_{E2}x} + \cdots + N_{En}e^{-\mu_{En}x}$$

This means that as the X-ray beam travels through the materials, lower energy X-rays in the beam attenuate at a faster rate than higher energies causing the average energy in the beam to increase (harden) which complicates the reconstruction equations.

1.3.1.2 X-ray Phase Contrast Imaging

Another way to use X-rays to image an object is by measuring how the "phase" of the X-rays changes when passing through the different part of the object.
This can be achieved by using gratings to polarise the X-ray beams before they interact with the object and then using another grating before the detector so that the phase change of the X-rays can be measured and from this material properties can be discerned (Momose, 2005).

1.3.2 Image Quality and definitions

Before discussing how the X-rays can be used to create images it is first important to discuss what determines the quality (and usability) of an image.

1.3.2.1 Image Files

The data collected from either radiography or computed tomography (the creation of 3D datasets from X-rays) needs to be displayed so it can be interpreted. An image is split into square pixels which "display" different intensities, either as a single values (such as a greyscale) or as a combination of colour channels (for example, Red, Green, and Blue). The information for the intensities is stored in the form of bits (b), which is a switch with two states, on (value equals 1) and off (values equals 0). The number of possible states that a collection of bits can represent is equal to 2^n where n is the number of bits. Eight bits (which is called a byte (B)) can therefore hold 256 distinct states, or the values from 0-255 (as zero is a state), this is the number of states that a standard computer monitor can display in each of its three colour channels.
Other images files (such as medically used Dicoms, which commonly use 16 bits (Horii, Bidgood, & Horii, 1992)) use more than 8 bits per pixel as this gives a larger amount of recorded states and as such more information can be recorded.

1.3.2.2 Resolution

The smallest distinct part that can be resolved in an image is defined as the spatial resolution (Bushberg *et al*., 2012). Thus if the image of a cross section of an object can be used to identify 1000 distinct values in both the x and y direction of the image (width and height) and the object is a 10 cm square in real life, the spatial resolution is 10 microns.

The limitation of the spatial resolution comes from various sources such as the size and quality of the detector and the beam.

It is important at this point to note that spatial resolution and the colloquial term "resolution" are not the same, the often used "resolution" is a measure of the amount of pixels over a length, or area (1080 pixels over a height for example). Thus as the spatial resolution of an image of the entire cross section of an image decreases (improves), the resulting image will require a higher number of pixels and as such a higher "resolution".

1.3.2.3 Contrast

The contrast of an image is measure of the difference in intensity (brightness) between the different "objects" in the image and the background. The contrast can be limited by either the intensity of the transmitted X-rays or the detector's sensitivity.

1.3.2.4 Noise

Noise is defined as information that appears in the image but is not representative of the object that the images have been taken of.

The sources of noise include (Bushberg *et al*., 2012):

- Electronic: Caused by the system itself and any other electronics in close proximity.
- Structure: Caused by limitations and non-uniformity of the detector's output, as well as the limited number and size of "pixels" in the detectors.
- Quantum: Caused by any electrons and photons not from the desired source (e.g. the X-ray beam), including the effect of the Poisson distribution of the X-rays.

1.3.2.4.A Signal to Noise

The ratio between signal and the noise(Signal to Noise Ratio, SNR) can be calculated for an image by using the background as a reference state (Bushberg *et al*., 2012).The

SNR can be calculated by taking the sum of difference between the intensity of an object in a region of interest and the average intensity of the background over the standard deviation of the background intensity as shown in Equation 1-18.

Equation 1-18

$$SNR = \frac{\sum_i (x_i - \bar{x}_{BG})}{\sigma_{BG}}$$

The Rose criterion states that a SNR of 5 or larger is required for the objects to be discerned in an image of approximate size of $3.3x10^6$ pixels (which is approximately a 1825 pixel sided square) (Rose, 1973).

1.3.2.4.B Contrast to Noise

The contrast to noise ratio (CNR) is a size-independent measurement of noise, but it does require the compared object scanned to be homogeneous (Bushberg *et al.*, 2012). The CNR can be calculated by taking the average intensity of an object of interest minus the average intensity of the background divided by the standard deviation of the intensity of the background as shown in Equation 1-19.

Equation 1-19

$$CNR = \frac{\bar{x}_S - \bar{x}_{BG}}{\sigma_{BG}}$$

1.3.3 Radiography Imaging

When taking a radiograph (2D X-ray image) the magnification (M) and blur (L_g) relates to relative position of the object to both the X-ray source and the detector as well as the width of the detector as shown in Equation 1-20, Equation 1-21 & Equation 1-22 (Figure 1-22) (Bushberg *et al.*, 2012).

Equation 1-20

$$M = \frac{L_{Image}}{L_{Object}}$$

Equation 1-21

$$M = \frac{a + b}{a}$$

Equation 1-22

$$L_g = L_f \frac{b}{a}$$

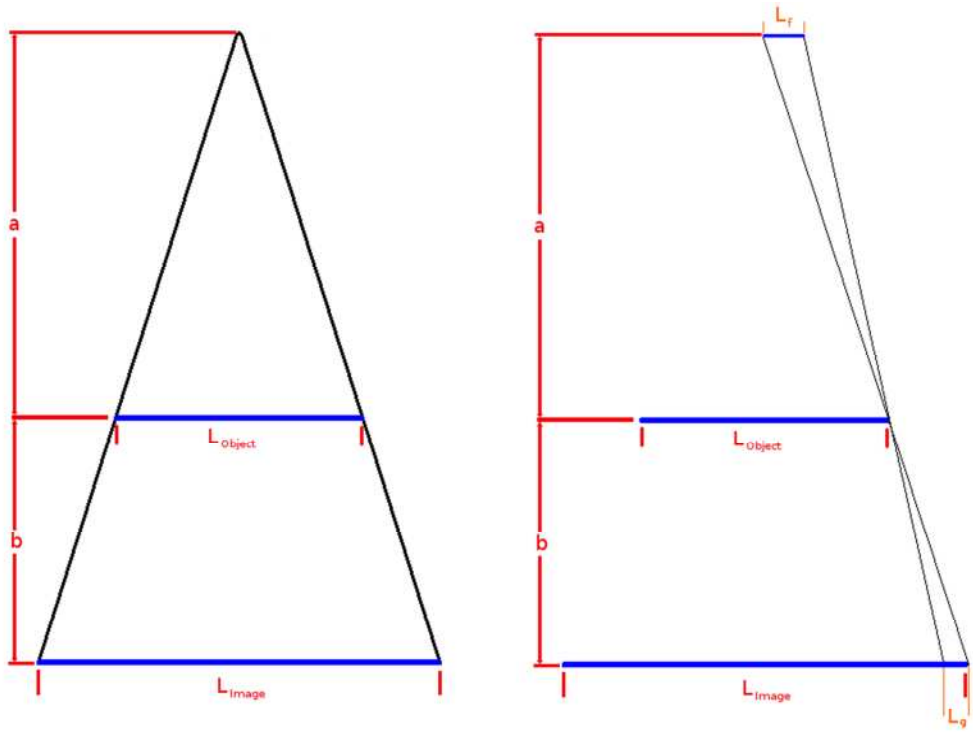

Figure 1-22 A diagram showing the magnification (M) of the radiographic projection and associated blurring (L_g) (based on a diagram by (Bushberg et al., 2012)).

By knowing the magnification of the system, the intensity of the X-rays and the distance that the shortest distance the X-rays could have travelled, a 2D reconstruction of the object can be created.

1.3.4 Computed Tomography

The same basic theory of radiographs can be applied to create a 3D reconstruction of the

object via X-ray interactions; this requires either the source of the beam to move around the object or for the object to rotate in a fixed beam. Computer Tomography (CT) has been used widely in medicine for scanning patients since the 1970s; the X-ray source typically moves around the patient and the quality of the scan is limited by the desire to minimize the X-ray dose (Hounsfield, 1980). Micro Computer Tomography is a form of CT which is used to investigates smaller samples which are rotated in a fixed X-ray beam, as the sample is not alive (in most cases), the limitation of reducing the dose is not applicable and as such long scans can be used to provide the smallest spatial resolution with the higher signal to noise.

1.3.4.1 Backprojection reconstructions

Backprojection reconstruction of CT data can be achieved via the Radon equation (Radon, 1917). (The derivation is shown clearly in English by Herman (Hermann, 1980), which is a mathematical representation of how a point on a two dimensional plane can be calculated by integration (where q defines the position along the beam) which is shown in Equation 1-23.

Equation 1-23

$$\sigma_{\bar{e}}(x,y) = -\frac{1}{2\pi^2}\lim_{\epsilon\to 0}\int_{\epsilon}^{\infty}\frac{1}{q}\int_{0}^{2\pi} m_1(x\cos\theta + y\cos\theta + q,\theta)d\theta\, dq$$

However there are limitations to the equation (Hermann, 1980):

- It creates a picture from all its line integrals not a finite number of beams intersecting with the sample.
- It does not take into account inaccuracies such as width of beam, scatter and beam hardening.
- It is a mathematical formula, not an algorithm.

The number of projections required for a reconstruction based on this equation is the amount such that the angles from zero to π radians are covered (though normally a full rotation is recorded (2π)) and as such the number of projections required to create a reconstruction is related to the beam geometry, with resolution and accuracy increasing with a higher number of projections (Epstein, 2003; Feldkamp, Davis, & Kress, 1984).

1.3.4.2 Backprojection Filtering

One of the problems with backprojection is that with a large number of measurements there is an inherent blur function of *1/r* (where r is the radial portion of the features) (Bushberg *et al*., 2012).

This blur can be "corrected" by the use of a convolution function (to combine one or more image or function) as shown by Equation 1-24 and a deconvolution kernel (a function which "reverses" a convolution function) (*h*) (Bushberg *et al*., 2012).

Equation 1-24

$$p'(x) = \int_{x'=-\infty}^{\infty} p(x)h(x - x')dx'$$

This can be processed faster by the use of a Fourier transformation (Bushberg *et al*., 2012).

1.3.4.3 Fan Beam Geometry

As mentioned earlier the back projection methodology is based on the geometry of the beam, one of the common used beam geometries is a 2D fan beam (Figure 1-23).

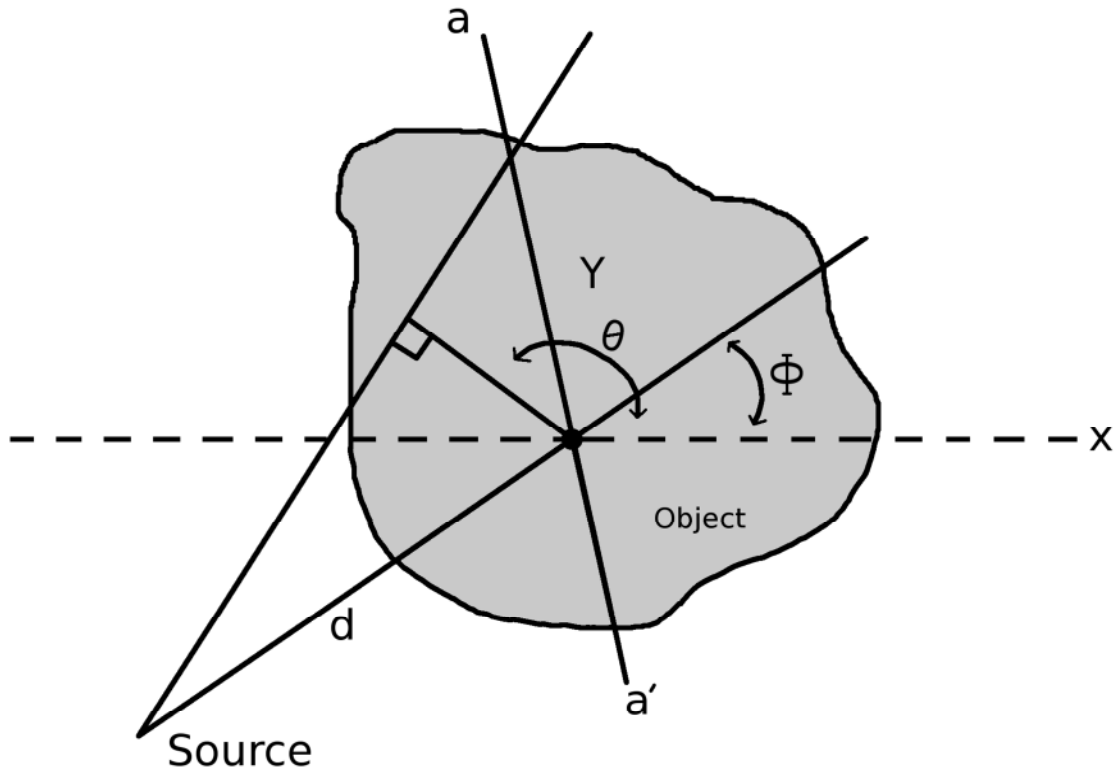

Figure 1-23 Geometry of a fan beam, intersection with object Y (based on a diagram by (Feldkamp *et al*., 1984).

Mathematically for a fan beam the reconstruction can be achieved by combining the integration along the beam line with the Radon transformation and using a Fourier transformation to apply a filter (g) as shown by Equation 1-25& Equation 1-26 (Feldkamp *et al*., 1984).

Equation 1-25

$$\bar{P}_{\varphi(i)}(Y_j) = \sum_{j'} P_{\varphi(i)}(Y_{j'}) \cos\theta_{j'} \int_{Y_{j'}+\Delta\frac{Y}{2}}^{Y_{j'}+\Delta\frac{Y}{2}} g_y\left(Y_j - Y'\right) dY'$$

Equation 1-26

$$g_y(Y) = Re \int_0^{\omega y_0} expi\omega Y \omega d\omega$$

1.3.4.4 Cone Beam Geometry

Another common geometry is the 3D cone beam (Figure 1-24).

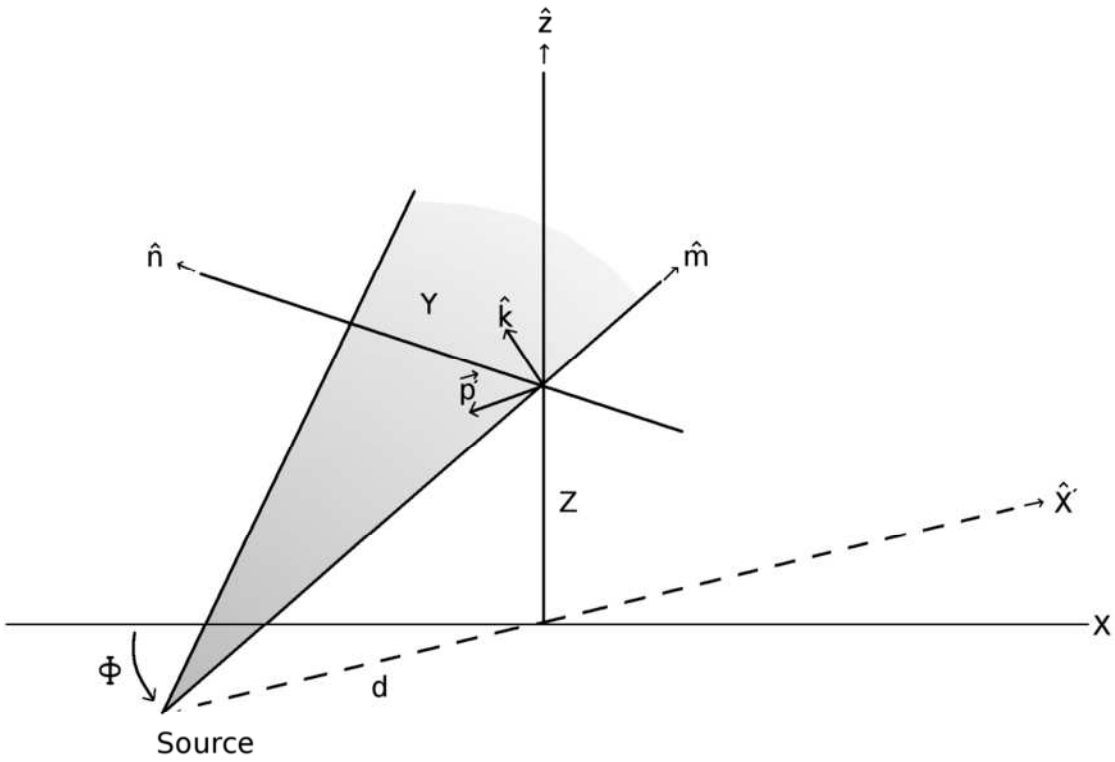

Figure 1-24 Geometry of a cone beam, intersection with object Y (based on a diagram by (Feldkamp *et al*., 1984)*).*

For a cone beam a similar process is followed as for the fan beam but in three dimension not just two, using cross products to combine the 3 dimensions as shown by Equation 1-26, Equation 1-27 & Equation 1-28 (Feldkamp *et al*., 1984).

Equation 1-27

$$\bar{P}_{\varphi(i)}(Y_j, Z_k) = \sum_{j'k'} P_{\varphi(i)}(Y_j, Z_k) \times cos\,\theta_{j'k'} \int_{Y_{j'}+\Delta\frac{Y}{2}}^{Y_{j'}+\Delta\frac{Y}{2}} g_y\left(Y_j - Y'\right)dY' \times \int_{Z_{j'}+\Delta\frac{Z}{2}}^{Z_{j'}+\Delta\frac{Z}{2}} g_z\left(Z_j - Z'\right)dZ'$$

Equation 1-28

$$g_z(Z) = sin\,\omega_{z0Z/\pi Z}$$

1.3.4.5 Algebraic reconstruction methods

Algebraic reconstruction methods (ART) (it is important to note the name is historical more than descriptive as they are not more algebraic than other methods) are another set of methods for reconstructing images from X-rays based around series expansion and not the Radon inversion formula directly (Epstein, 2003; Hermann, 1980).
ART is a process that uses multiple scans to produce a 3D image via iteratively reconstruction (or 2D slice) (Bushberg *et al*., 2012; Hermann, 1980). The number of

equations that are required to solve the reconstruction iteratively can be calculated by taking the total number of sub-regions of interest (pixels/voxels 3D pixels) and multiplying them by the number of Radon transformations at the spacing (one side of the sample), for a sample of 128 by 128 pixels this would require ~$3.15x10^8$ equations to solve (Epstein, 2003).
Mathematically ART uses the Kaczmarz's method, which is a iterative method for solving linear systems of equations (Natterer, 1986).

1.3.4.6 Detectors

There are two general ways to detect X-rays, either an indirect method where the X-rays are converted to photons within the visible portion of the spectrum with a scintillator for example a Gd_2O_2S ceramic, which then interacts with an imaging sensor; or by an direct method where the X-rays are converted directly into a charge and then measured (Bushberg *et al*., 2012; Yaffe & Rowlands, 1997).
Two common imaging sensors are the Charged Couple Device (CCD) and Complementary Metal-Oxide-Semiconductor (CMOS) which are found in both digital photography and radiography (Trussell & Vrhel, 2008).
In these systems a charge created by a photon's interaction with a sensor is converted into a voltage, the main difference between a CCD and a CMOS is that in a CCD, the charge is “shifted” from each of the sensors into a single charge converter and in a CMOS the conversion happens at each individual sensor. This difference leads to a larger sensor non-uniformity in the CMOS than in the CCD thus the CCD is preferred in higher end applications (Trussell & Vrhel, 2008) (Figure 1-25 & Figure 1-26).

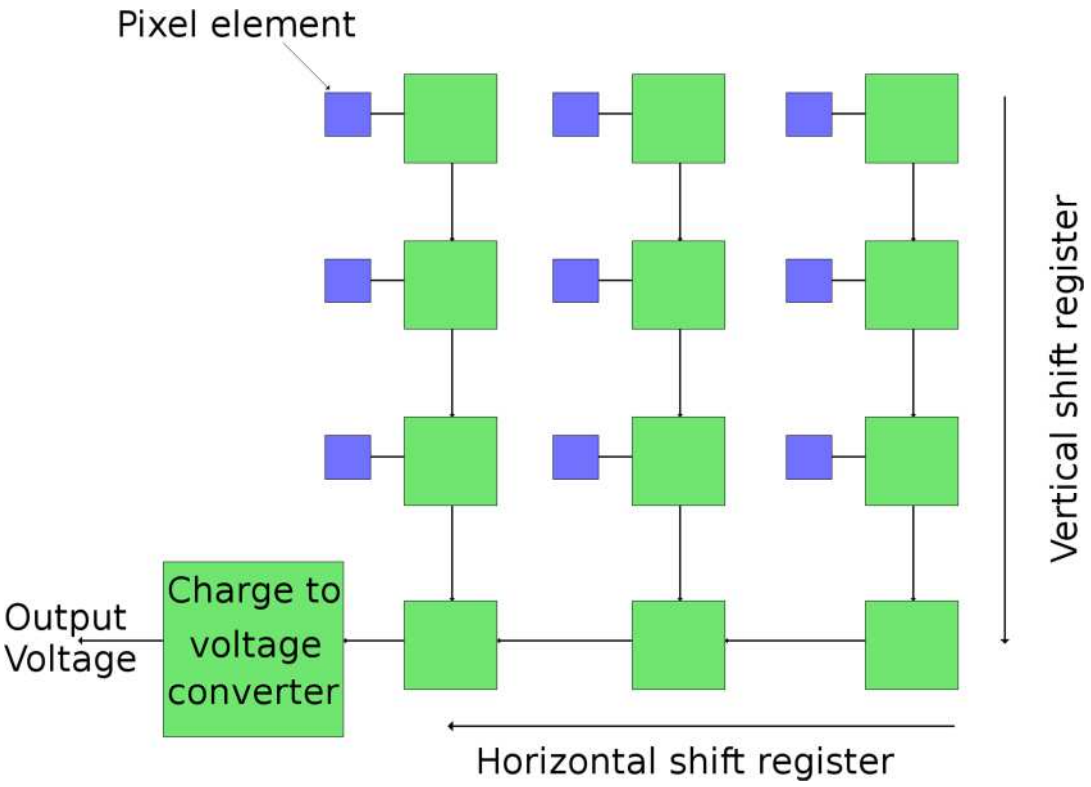

Figure 1-25 Diagram of a CCD (based on a diagram by (Trussell & Vrhel, 2008)*).*

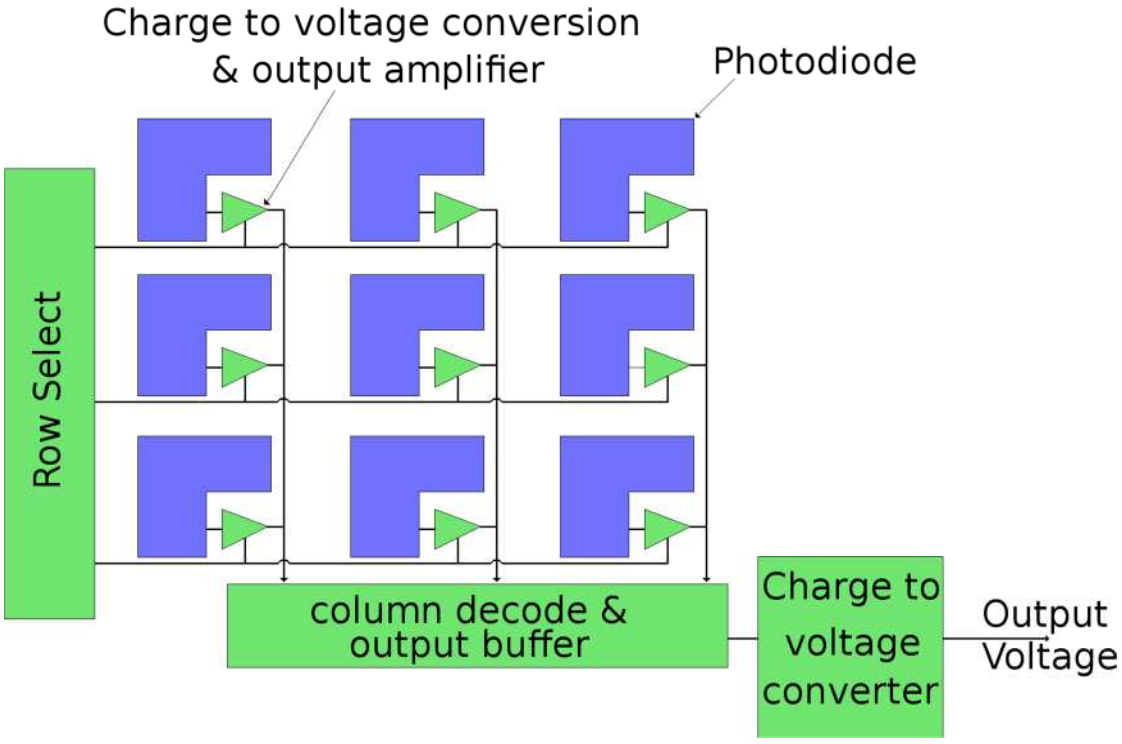

Figure 1-26 Diagram of a CMOS (based on a diagram by (Trussell & Vrhel, 2008)*).*

Amorphous flat panel detectors (specifically selenium (a-Se)) are the most developed of the photoconductors (indirectly converts X-rays into visual light photons) for X-ray

applications, in these detectors the X-rays are attenuated to create free electron-hole pairs which can be directly measured; its amorphous nature also provides a uniform sensing of the X-ray data (Yaffe & Rowlands, 1997).

1.3.5 Radiography and CT artefacts

As expected there are inherent limitations with both radiographs and CT X-ray reconstruction.

1.3.5.1 Beam Width

The beam is not a one dimensional line and has both a width and thickness, and is often approximated to have a rectangle profile, with a variable beam intensity within the beam (Epstein, 2003).This can be countered by performing an integration over the width of the beam or by using a X-ray beam which is detected in 3D i.e. cone instead of fan.

1.3.5.2 Partial Volume Effect

As the beam has width if there are two or more regions of different material, pixels which contain multiple attenuations will result in a value which is an average of the attenuations within (Figure 1-27) (Epstein, 2003). This can be reduced but not removed by increasing the resolution of the system.

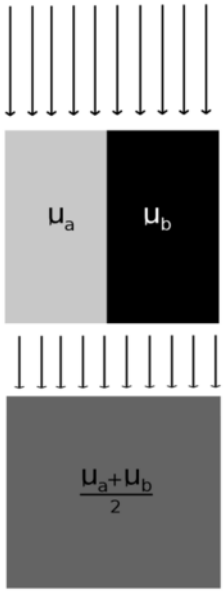

Figure 1-27 Example of a partial volume effect (Based on a diagram by (Epstein, 2003)*).*

1.3.5.3 Point spread

The X-ray data has an inherent spread function which is caused by the X-ray spot size as well as the light scatter caused by the scintillator (Figure 1-28).

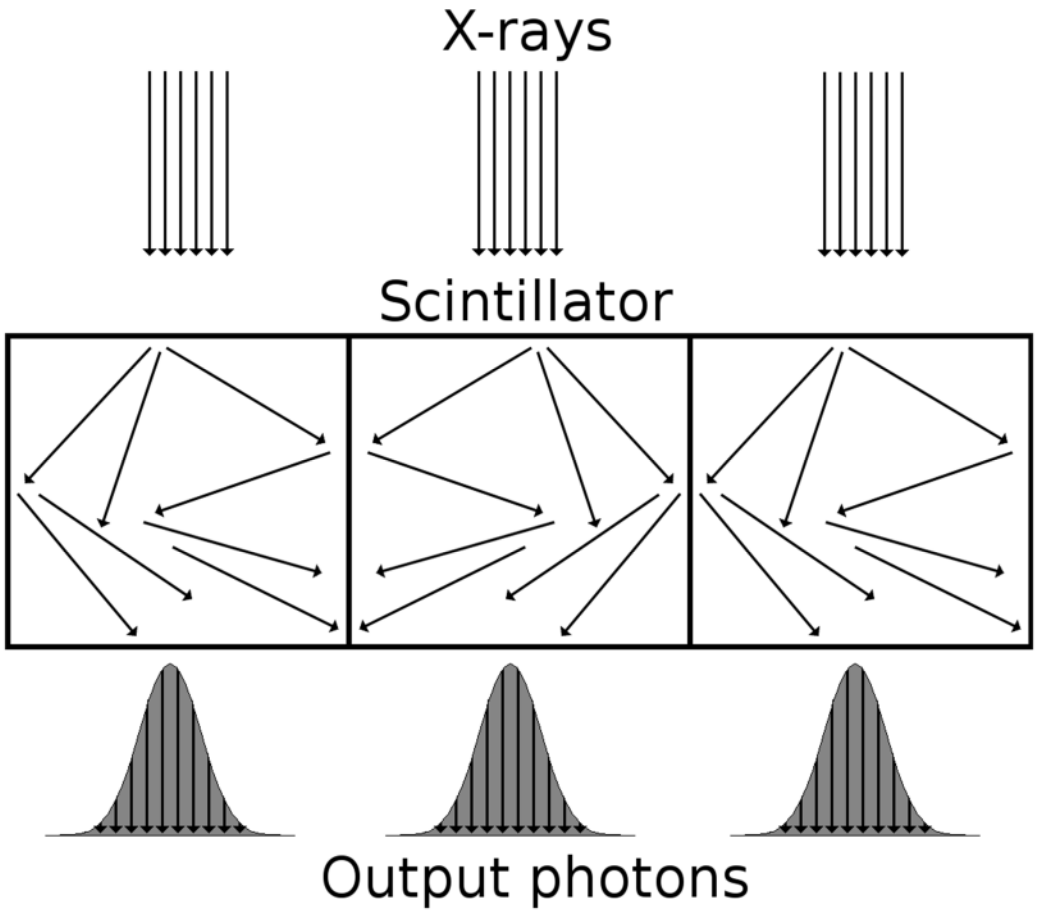

Figure 1-28 Effect of a scintillator on the distribution of the photons.

1.3.5.4 Beam-Hardening

Beam hardening (Section 1.3.1.1.F) causes reconstruction errors as properties of the material which the X-rays have passed through cannot be objectively determined. To compensate for beam hardening pre-filtering can be applied, during which the beam is pre-hardened before going into the sample, thus removing the lower energy X-rays but also decreasing the signal to noise (as less of the energy of the beam gets through) (Figure 1-29) (Jovanovi, Khan, Enzmann, & Kersten, 2013).

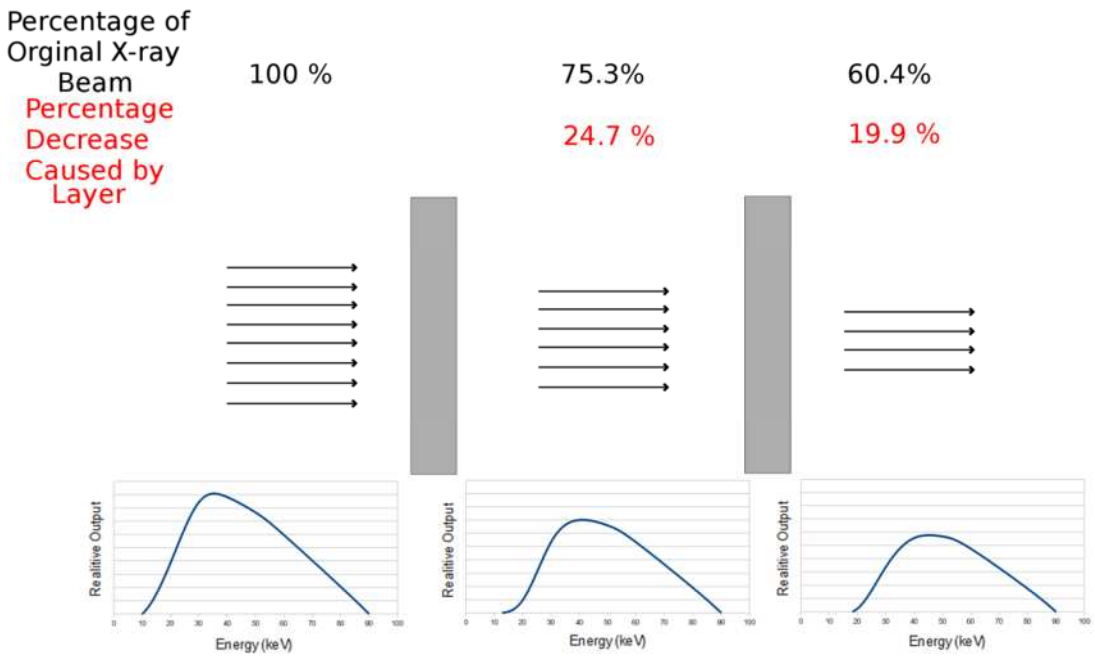

Figure 1-29 The hardening of a filtered beam when passing through two 1.5mm layers of aluminium.

By knowing the material properties before scanning, assumptions can be made and used to compensate for the beam hardening, such as remapping the attenuation curve for bone (by assuming a linear relationship) (Brooks & Di Chiro, 1976).
If the shape of the sample is known and the sample is a solid the beam hardening at each point can be deduced from its position in the sample (Jovanovi *et al*., 2013).
Also if the beam is of "high quality" (close to single energy) it will be affected less by beam hardening, however this requires expensive large equipment such as a synchrotron (Borah *et al*., 2005).

1.3.5.5 Ring Artefacts

Differences in the detector element sensitivities can result in ring artefacts (as the sample is rotated) as shown in Figure 1-30, this can be compensated for by using Time Delay Integration (TDI) which is where the detector is moved independently of the beam, collecting the X-ray data across multiple sensors and then integrating the results from all the sensors (Davis & Elliott, 2006).

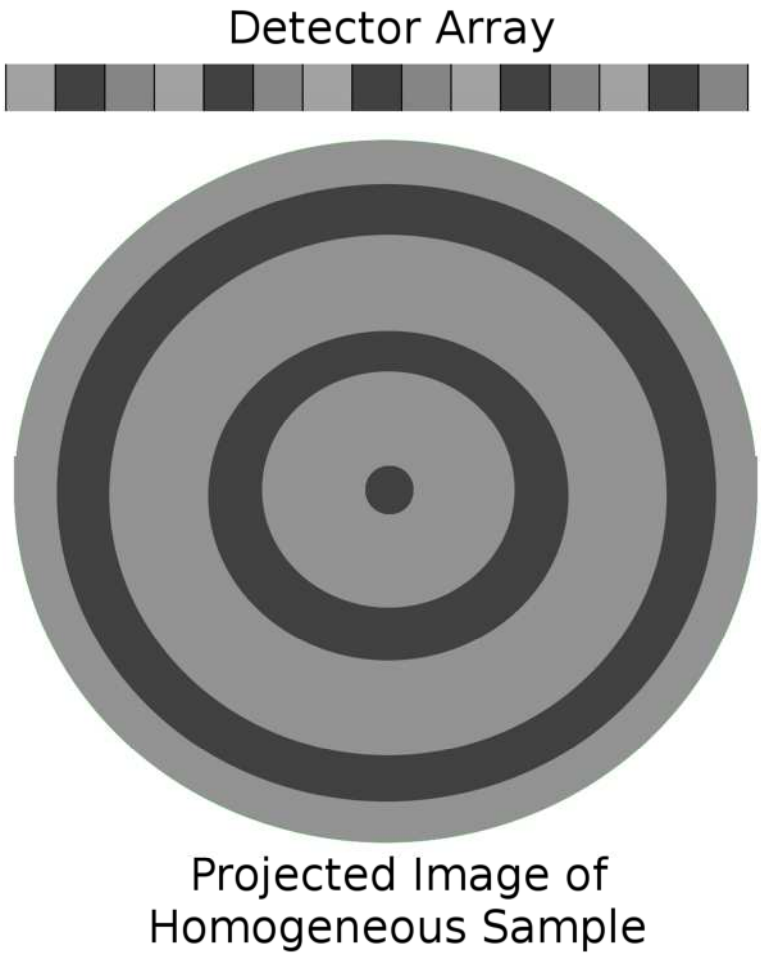

Figure 1-30 Example of the difference in sensitivity of the detectors in a detector array and the resultant ring artefact in the sample.

1.3.6 Summary

X-rays can be used to image within samples, either in 2D or 3D depending. The quality of the images produced is limited by various factors including the X-ray, beam detector, the type of scan and the sample. These limitations need to be taken into account when deciding on the type and settings of scanner used as well as any measurements and quantification which will be performed on the images, especially when imaging similar materials such as investigated in this study.

1.4 Image Segmentation and Validation Methods

Once the Micro CT images of bone and synthetic bone grafts are collected, they need to be processed so that the regions of interest can be identified, in this case the bone and the graft. This is performed by a process called segmentation, because of the large number of images in this study the optimal way to perform the segmentation is by automated computer programming. This not only requires automated image processing methods to be produced which can segment out the three regions (bone graft and background) but also methods to determine the "quality of the segmentation". The hunt for a segmentation method is made more difficult due to the similar properties of the synthetic graft and bone.

1.4.1 Automated Region Segmentation techniques

1.4.1.1 Threshold based Methods

A common method for segmentation is defining the regions by their intensity and applying thresholds, thus referred to as the threshold method. For example labelling every pixel/voxel with an intensity higher than a threshold of 100 as region A. For the situations in this study, at least two threshold regions will be required as there are three regions that need to be identified. Three region segmentation is more complex than two regions of interest, as two regions have four possible sections on a histogram region A, region B, mix of regions A and B and no region. While three regions has eight possible sections on the histogram comprising region A, region B, region C and all their possible combinations and a section of no regions.

The values for these threshold values can be determined by inspecting the samples via a histogram and using that to define the different regions, example images with different pixel intensities distributions and their resultant histograms are shown in Figure 1-31 & Figure 1-32 respectively.

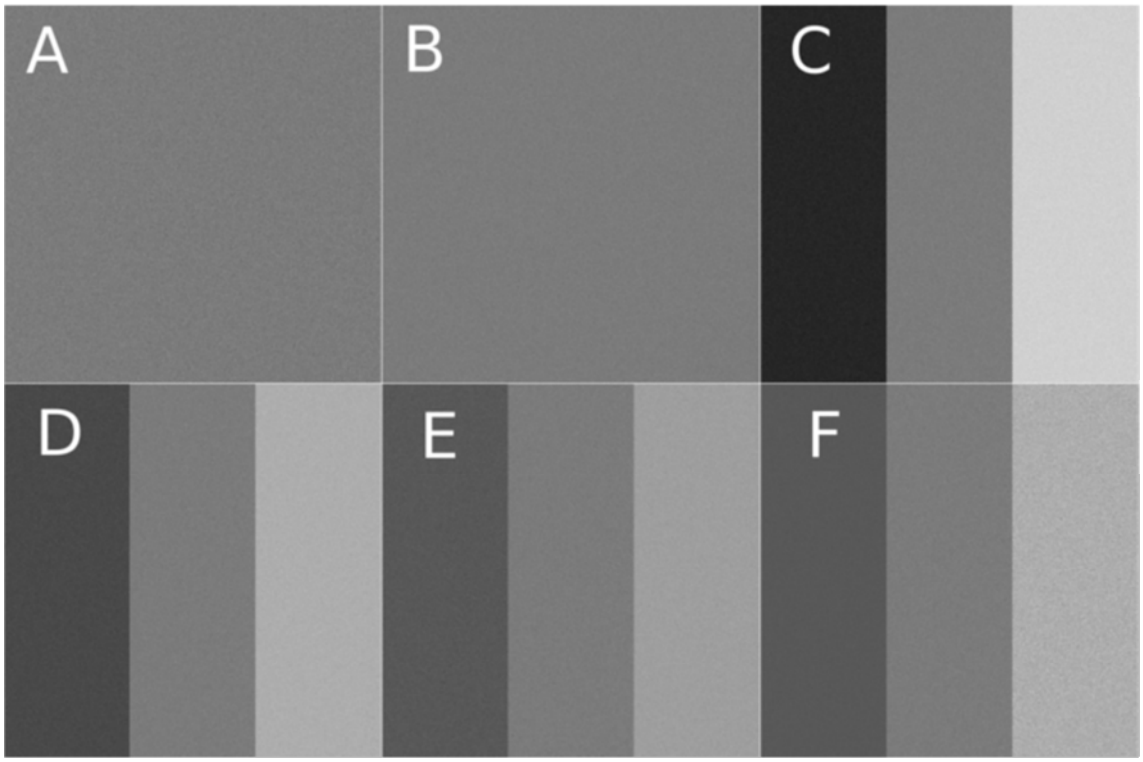

Figure 1-31 Example images A: Single region of distribution between 100-150 intensity, B: Gaussian distribution of mean of intensity 125 and standard deviation of 10 , C: Three Gaussian distribution of means of intensities 40, 125 & 210 and all standard deviations of 10, D: Three Gaussian distribution of means of intensities 75, 125 & 175 and all standard deviations of 10, E: Three Gaussian distribution of means of intensities 90, 125 & 160 and all standard deviations of 10 and F:Three Gaussian distribution of means of intensities 90, 125 & 175 and all standard deviations of 5, 10 & 20.

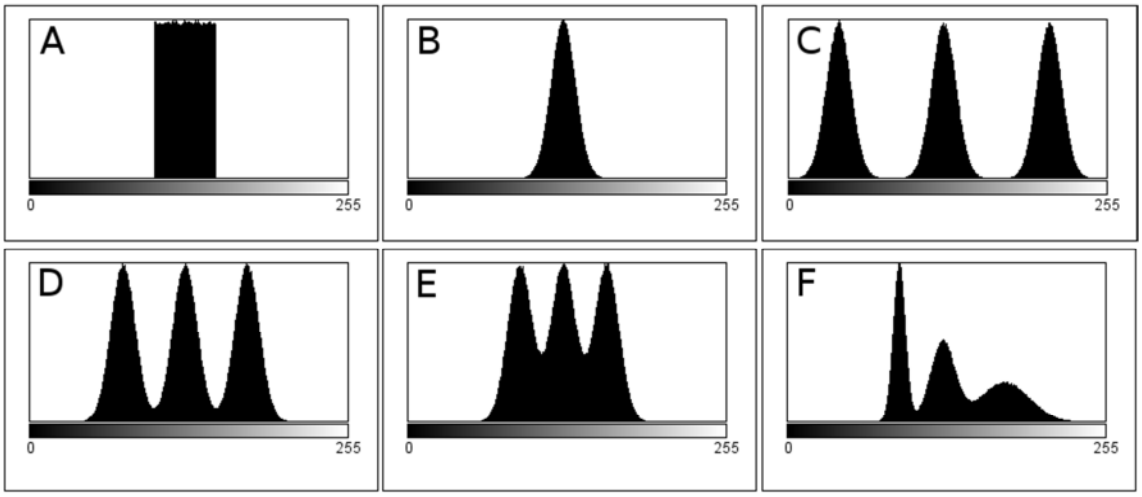

Figure 1-32 Histograms of A:Single region of distribution between 100-150 intensity, B:Gaussian distribution of mean of intensity 125 and standard deviation of 10 , C:Three Gaussian distribution of means of intensities 40, 125 & 210 and all standard deviations of 10, D:Three Gaussian distribution of means of intensities 75, 125 & 175 and all standard deviations of 10, E:Three Gaussian distribution of means of intensities 90, 125 & 160 and all standard deviations of 10 and F:Three Gaussian distribution of means of intensities 90, 125 & 175 and all standard deviations of 5, 10 & 20 respectively all produced in imageJ.

For a single region in a sample it would be expected that there would be a range of intestines within the region, a simple example of this would be a uniform distribution shown in Figure 1-32 A, but because of the properties of materials in real life it will more often than not appear with distribution similar to a Gaussian distribution shown in Figure 1-32 B.

If there are multiple regions in the sample there should be multiple peaks on the resultant histogram shown in Figure 1-32 C, D, E and F. These regions can however overlap due to them exhibiting similar intensities (including ones resulting from the partial filled voxels, Section 1.3.5.2) shown in Figure 1-32D, Figure 1-32 E and Figure 1-32 F. These overlapping regions, means that there is no clear boundary between the regions on the histogram as shown in Figure 1-32 D, Figure 1-32E and Figure 1-32F. In the case of separating out bone and synthetic bone graft various methods have been developed to overcome this problem, one method is to define the threshold points between the regions as the lowest point between the regions as shown in Figure 1-32 A (Varshavskii *et al*., 1983). The regions also can be separated by taking the point between the peaks in the histogram shown in Figure 1-32 B (Udagawa *et al*., 2013). These method however can result in over and under counting of regions as well as misidentification of regions at edges as the position of the threshold can cause significant difference to the segmentation (a difference of 0.5% in the threshold values

resulting in a 5% difference in volume measurement) (Hara, Tanck, Homminga, & Huiskes, 2002). Other similar methods include using a double threshold layer so that there is an undefined region between the regions of interest (Figure 1-32 C) (Buie, Campbell, Klinck, MacNeil, & Boyd, 2007).

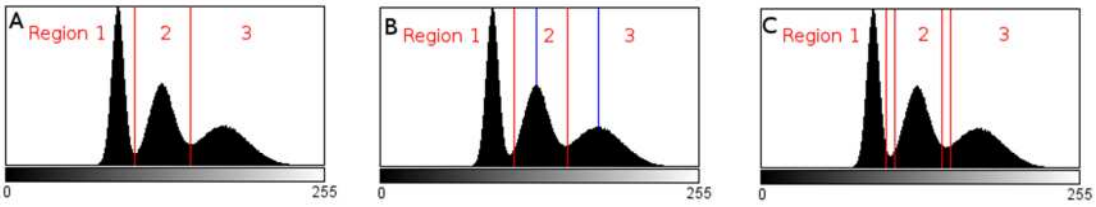

Figure 1-33 Histogram of Three Gaussian distribution of means of intensities 90, 125 & 175 and all standard deviations of 5, 10 & 20 respectively, with thresholds separating their regions defined by A: lower turning points, B: Positions in-between peaks of the histogram & C: Double threshold layers around the lowest turning points in the histogram. All produced in ImageJ.

Another method is to predict the shape of the regions pre-overlap, assuming their distribution shapes (such as a Gaussian distribution) (Hilldore, Wojtowicz, & Johnson, 2007) shown in Figure 1-34. On a two region sample this gives three regions of interest, the two distinct regions and their border, with a 4% error compared to a by hand method (for a sample with two regions) (Hilldore, Morgan, Woodard, & Wagoner Johnson, 2009).

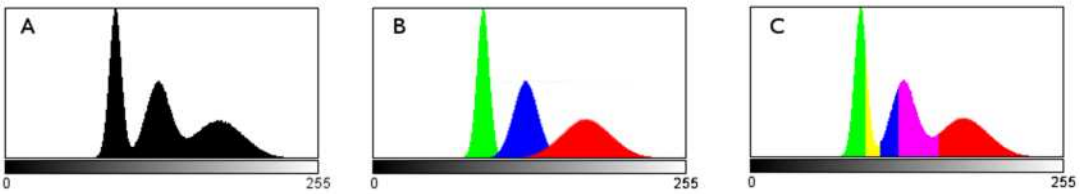

Figure 1-34 Histogram of three Gaussian distribution of means of intensities 90, 125 & 175 and all standard deviations of 5, 10 & 20 respectively, B:Individual overlaid histograms of three Gaussian distribution of means of intensities 90, 125 & 175 and all standard deviations of 5, 10 & 20 respectively.

The regions with no overlap which are represented in Figure 1.33C can be used to segment the non-edges in the image, and these inner regions can then be expanded to define the whole region (Subburaj, Ravi, & Agarwal, 2009).

These methods are limited to what information can be determined from the straight intensities values, which is subject to errors caused by similar densities and the partial filled voxels (Section 1.3.5.2).

Another method for defining the regions is by using an intensity-gradient histogram.

this method allows for a simple way to identify the stable parts of each of the regions in two region system (A. C. Jones *et al.*, 2007), however it still exhibits the problem of overlapping regions.
A method to improve the segmentation is to use not only the intensity of the voxel to define its region, but also other values such as the mean and variance (J. Zhang, Yan, Chui, & Ong, 2010). These other values can be treated the same way as the intensity when determining the threshold values with boundaries for each of the variables.

1.4.1.2 Edge Finding

An alternative to defining entire regions by thresholding methods is to use the properties at the edges of the regions can be used to define the boundaries of the regions. After the boundaries have been defined the regions inside can then be filled, (sometimes requiring the boundary to be expanded first) (Youssef, Maire, & Gaertner, 2005).
Methods which can be used to define the boundary of the regions are edge finding algorithms, such as the Sobel (Parker, 2010) and Canny (Canny, 1986) algorithms.
The Canny algorithm has shown to be an effective tool to assess bone shape (A. Zhang, Gertych, & Liu, 2007) but this is only when using only two regions of different densities (bone and background).
While edge methods do not fully identify the regions, they do identify their outer boundaries so that the shape of the region is preserved. However with three or more regions it becomes complex to separate out the three different edge types.

1.4.1.3 Shape Registration Methods

While the methods mentioned up to now could be used on any intensity images, other methods which have been used to define and segment out the regions of bone and graft, take into account the properties of the bone and graft and their characteristic shapes.
One example of such a method (which showed near 95% accuracy compared to a manual selection), works by using the unique features of the example graft of their known and predicable shape as well as the graft's straight line based shape being aligned with the detector array (S. J. Polak, Candido, Levengood, & Wagoner Johnson, 2012).
However if the segmentation methods works off the characteristic shape of the samples the methods need to be tooled to each sample set and the shape must be objectively known.

1.4.1.4 Summary

There are multiple methods which have been developed to segment out regions from X-ray CT images. These methods have limited success in identifying the edges of regions, which is further complicated when there are more than two regions.
Since the samples in this study have two regions of interest (and a background region) these methods need to be investigated into how successfully they can segment out three regions and if they need to be modified, or new methods developed, this is the focus of section 4.

1.4.2 Validation Methods

When deciding what segmentation method to use or when developing a new method, there needs to be a way to validate its effectiveness for different sample types. Segmentation methods can be validated either analytically by a direct investigation of their underlying methodology or empirically by indirect analysis of images that have been segmented by said method (Y. Zhang, 1996). Empirical methods can be further divided into measures of the properties of the segmentation "goodness" and a comparison to a reference segmentation of the image which is a measurement of the "discrepancy" (Y. Zhang, 1996).

1.4.2.1 Analytical Methods

Analytical validation methods work by investigating the segmentation algorithm directly without using example segmentations (Y. Zhang, 1996).
Analytical methods can provide a numerical value for the possible error in a segmentation method by determining the probability of correct and incorrect segmentation based on the data set (such as identifying edge and non-edge) as shown in Equation 1-29 & Equation 1-30 (Abdou & Pratt, 1979).

Equation 1-29

$$P_c = \int_t^{\infty} p(A|edge)dA$$

Equation 1-30

$$P_F = \int_t^{\infty} p(A|no-edge)dA$$

While analytical methods can provide an idea of which segmentation methods will and will not be appropriate, as well as providing a numerical method of determining the quality of the method, it does not provide an "objective" comparable value for which segmentation method (and its calibration) is the "best" for a region identification.

1.4.2.2 Empirical Goodness Methods

An Empirical goodness validation method determines the quality of the segmentation by inspecting the individual regions without needing a reference image to compare them to (Y. Zhang, 1996).

One such measurement is the grey-level; uniformity measure (GU) which determines the variance of the pixels (f(x,y)) in a region (R_i) computed using the area of the region (A_i). as shown in Equation 1-31 (Levine & Nazif, 1985).

Equation 1-31

$$GU = \sum_i \sum_{(x,y)\in R_i} \left[f(x,y) - \frac{1}{A_i} \sum_{(x,y)\in R_i} f(x,y) \right]^2$$

The uniformity can also be measured by the entropy of the regions (H^2), based off the threshold value (T) and the probability of an occurrence within paired regions ($p_{i,j}$) as shown in Equation 1-32 (Pal & Pal, 1989).

Equation 1-32

$$H^2(T) = -\sum_{i=0}^{T} \sum_{j=0}^{T} p_{ij} ln\, p_{ij}$$

Inter-region contrast can also be measured to determine how difference the regions, the grey-level contrast method works by comparing the average grey scale of the object region (f_0) to the background region (f_b) as shown in Equation 1-33 (Levine & Nazif, 1985).

Equation 1-33

$$GC = \frac{|f_0 - f_b|}{f_0 + f_b}$$

These methods can only be used if the homogeneity of the regions can be used as a measurement of accuracy of segmentation, for example a region which is defined by being comprised of a heterogeneity distribution of intensities would perform badly in these metrics and they would therefore not be a good choice for validation.
The shape of the regions can also be defined and used as a metric of goodness, the shape measurement (SM), defines the shape by the grey-level of the pixels in the region (f(x,y)), their neighbours (N(x,y)), as well as their gradient at a certain threshold value (T) using the unit step function, (and a normalisation factor C) as shown in Equation 1-34 (Sahoo, Soltani, & Wong, 1988).

Equation 1-34

$$SM = \frac{1}{C}\left\{\sum_{(x,y)} Sgn\left[f(x,y) - f_{N(x,y)}\right] g(x,y) Sgn[f(x,y) - T]\right\}$$

The limitation of goodness validation methods is in their inherent need for parameter to measure against, whether it is uniformity or shape, meaning that if the sample lacks either of these or is fact unknown, these methods become impractical/unreliable.

1.4.2.3 Empirical Discrepancy Methods

Empirical discrepancy validation methods work by comparing the segmentations to a reference image and then providing a numerical score of accuracy (Y. Zhang, 1996). These methods require a reference, either an image or a numerical value of a property of the sample which can be compared to the segmentation to determine the accuracy/error of the segmentation. A reference image can be collected by using experts (such as

radiographers when measuring mammography images) (Byrd, Zeng, & Chouikha, 2007) or by non-experts with more images and or more user produced reference segmentations per image (One such database uses three users per image (D. Martin, Fowlkes, Tal, & Malik, 2001)).

With a reference image to compare the segmented regions against, the number of true positive (N_{TP}), true negative (N_{TN}), false positive (N_{FP}) and false negative (N_{FN}) pixels can be determined. From these values, regions properties (RP) can be defined, including the Overlap of the segmented and correct region, the Accuracy of the segmented region, Sensitivity of the segmented region and Specificity of the segmented region as shown in Equation 1-35, Equation 1-36, Equation 1-37 & Equation 1-38 (Byrd *et al*., 2007).

Equation 1-35

$$Overlap = \frac{N_{TP}}{N_{TP} + N_{FP} + N_{FN}}$$

Equation 1-36

$$Accuracy = \frac{N_{TP} + N_{TN}}{N_{TP} + N_{TN} + N_{FP} + N_{FN}}$$

Equation 1-37

$$Sensitivity = \frac{N_{TP}}{N_{TP} + N_{FN}}$$

Equation 1-38

$$Specificity = \frac{N_{TN}}{N_{TN} + N_{FP}}$$

A similar function can be used to determine the multi-class error ($M_{I/II}$)of each segmentation, these measure the error in each segmentations by measuring the number of pixels in each of the reference image regions (j) that are classified as each of the regions in the segmented image (i), (C_{ij}), either taking into account only that reference region (M_I) or the whole set of reference regions (M_{II}) as shown in Equation 1-39 & Equation 1-40 (Yasnoff, Mui, & Bacus, 1977).

Equation 1-39

$$M_I^{(k)} = 100\frac{\left[\left(\sum_{i=1}^{N} C_{ik}\right) - C_{kk}\right]}{\left[\sum_{i=1}^{N} C\_ik\right]}$$

Equation 1-40

$$M_{II}^{(k)} = 100\frac{\left[\left(\sum_{i=1}^{N} C_{ik}\right) - C_{kk}\right]}{\left[\left(\sum_{i=1}^{N}\sum_{j=1}^{N} C_{ij}\right) - \sum_{i=1}^{N} C\_ik\right]}$$

The probability of error (PE) can also be used to define the error in the segmentation if the collective probability of the labelling of the object (O) and background regions (B) are known, as shown in Equation 1-41 (Lee, Yoon Chung, & Park, 1990).

Equation 1-41

$$PE = P(O)P(B|O) + P(B)P(O|B)$$

With the form for multiple regions being shown below as shown in Equation 1-42 (Lim & Lee, 1990).

Equation 1-42

$$PE = \sum_{j=1}^{c}\sum_{\substack{i=1 \\ i\neq j}}^{c} P(R_j)P(R_i|R_j)$$

Methods which takes into account all the regions (A_i) and their possible segmentations (B_i) include the Global Consistency Error (GCE) and Local Consistency Error (LCE) measuring their interactions using set theory, as shown in Equation 1-43, Equation 1-44, Equation 1-45, Equation 1-46 & Equation 1-47 (D. Martin *et al*., 2001).

Equation 1-43

$$GCE(I_g, I_s) = \frac{1}{n} min\left\{\sum_{j=1}^{M}\sum_{i=1}^{N} P_{ji}, \sum_{j=1}^{M}\sum_{i=1}^{N} Q_{ji}\right\}$$

Equation 1-44

$$LCE(I_g, I_s) = \frac{1}{n}\sum_{j=1}^{M}\sum_{i=1}^{N} min(P_{ji}, Q_{ji})$$

Equation 1-45

$$P_{ji}\frac{|A_j \backslash B_i|}{|A_j|}|A_j \cap B_i|$$

Equation 1-46

$$Q_{ji} = \frac{|B_i \backslash A_j|}{|B_i|}|A_j \cap B_i|$$

Equation 1-47

$$n = \sum_{i=1}^{N}\sum_{j=1}^{M}|A_j \cap B_i|$$

In response to the perceived tolerance to over and under segmenting within GCE and LCE methods, the Object-Level Consistency Error (OCE) was developed, it also uses set theory but checks all the possible region segmentations against each other, and used either the Jaccard index, as shown in Equation 1-48 & Equation 1-50 or the Dice's coefficient to measure equivalence, as shown in Equation 1-48, Equation 1-49, Equation 1-50, Equation 1-51,Equation 1-52 & Equation 1-53) (M. Polak, Zhang, & Pi, 2009).

Equation 1-48

$$OCE(I_g, I_s) = min(E_{g,s}, E_{s,g})$$

Equation 1-49

$$OCEd(I_g, I_s) = min(Ed_{g,s}, Ed_{s,g})$$

Equation 1-50

$$E_{g,s}(I_g, I_s) = \sum_{j=1}^{M}\left[1 - \sum_{i=1}^{N}\frac{|A_j \cap B_i|}{|A_j \cup B_i|}W_{ji}\right]W_j$$

Equation 1-51

$$Ed_{g,s}(I_g, I_s) = \sum_{j=1}^{M}\left[1 - \sum_{i=1}^{N}\frac{2|A_j \cap B_i|}{|A_j| + |B_i|}W_{ji}\right]W_j$$

Equation 1-52

$$W_{ji} = \frac{\bar{\delta}(|A_j \cap B_i|)|B_i|}{\sum_{k=1}^{N}\bar{\delta}(|A_j \cap B_k|)|B_k|}$$

Equation 1-53

$$W_j = \frac{|A_j|}{\sum_{l=1}^{M}|A_l|}$$

The methods based on misidentified pixels do provide clear numerical values for properties of regions (either single region such as RP, M_I & M_{II} or all the regions such as LCE, GCE, OCE & OCEd) compared to a reference image, however it does not take into account the relative position of the incorrect pixels.

A method which takes into account the position of the incorrectly labelled pixels is the discrepancy measure (D), which measures the distance of miss-identified pixels (d) to the nearest correctly identified pixel of its region, as shown in Equation 1-54 (Yasnoff *et al*., 1977).

Equation 1-54

$$D = \sum_{i=1}^{N} d^2(i)$$

Another way to validate a segmentation is by the number of objects in the segmented image compared to the reference image. The Object Count Agreement (OCA) compares

the number of objects of one region in the reference image (R_i) with the number of objects of the same region in the segmented image (S_i) based on probability theory (where M is the degrees of freedom N-1, and p is a correlation factor) as shown in Equation 1-55 & Equation 1-56 (Yasnoff & Bacus, 1984).

Equation 1-55

$$F_{oca} = \int_{L}^{\infty} \frac{1}{2^{\frac{M}{2}}\Gamma\frac{M}{2}} z^{\frac{(M-2)}{2}} e^{-\frac{z}{2}} dz$$

Equation 1-56

$$L = \sum_{i=1}^{N} \frac{S_i - R_i}{pR_i}$$

A similar validation method is the Fragmentation method (FRAG), which compares the total number of objects in the reference image (A_N) with the total number of objects in the segmented image (T_N) (with a scaling factor p & q) as shown in Equation 1-57 (Strasters & Gerbrands, 1991).

Equation 1-57

$$FRAG = \frac{1}{1 + p|T_N - A_N|^q}$$

If a reference property is used instead of an image (for example the absolute Bone %) the Ultimate Measurement Accuracy (UMA) can be used to validate the segmentation by computing feature values from the segmented images (S_f) and comparing them to the feature value from the reference image (R_f) either working out the absolute (AUMA) or relative values (RUMA) as shown in Equation 1-58 & Equation 1-59 (Y. J. Zhang & Gerbrands, 1994).

Equation 1-58

$$AUMA_f = |R_f - S_f|$$

Equation 1-59

$$RUMA = 100\frac{|R_f - S_f|}{R_f}$$

The use of UMA of course, also relies on the accuracy of determining these features

from the segmented images.

1.4.2.4 Summary

There are a number of different validation theories and associated methods, which work by comparing different properties of the segmentations and their related reference images. The methods can be compared by identifying their different properties and requirements (Table 1-8).

These requirements and properties of interest include:

- All Regions: Does the method look at all the regions in the segmented image or just one.
- Assumed/Known Properties: Is there an assumption made about the regions properties (such as homogeneity) or is there knowledge about the sample's properties which is required.
- Reference Required: Does the process require a reference image to compare the segmentation to.
- Known Probability: Is the probability of each region appearing at each intensity required.
- Edge/Shape/Object Based: Is the measurement based on either the defined edge, shape or number of objects in a reference opposed to an area/pixel measurement.
- Region Matching: Does the method require the regions in the segmented image to be matched to corresponding region in the reference image.

Table 1-8 Comparison of the validation methods, defining if all the regions are defined, if it requires known properties, if they require a reference image, if the probability is required to be known, if the measurement require an edge/shape or object segmentation and does the segmentation and reference need to be matched.

Method	All Regions	Assumed/Known Properties	Reference Image	Known Probability	Edge/Shape/Object Based	Need Regions Matching
Pc/PF	x	-	-	x	x	-
GU	x	x	-	-	-	-
H^2	x	x	-	-	-	-
GC	x	x	-	-	-	-
SM	x	x	-	-	x	-
MI/MII	-	-	x	-	-	x
RP	-	-	x	-	-	x
PE	-/x	-	-	x	-	-
GCE/LCE	x	-	x	-	-	-
OCE/OCEd	x	-	x	-	-	-
D	x	-	x	-	-	-
Foca	x	-	x	-	-	x
FRAG	x	-	x	-	-	-
AUMA/RUMA	x	x	-	-	-	-

Depending on the properties of the regions in the samples that are to be segmented, as well as their segmentation methods appropriate validation techniques can be chosen from the information in Table 1-8.

1.5 Post Segmentation Quantification

Once the images have been segmented into the different regions, it is then possible to determine and quantify information about the volume area, shape and distribution of the bone within the implants.

1.5.1 Volume and Surface area

Assuming correct segmentation, simple voxel counting has been shown to be a precise method for volume measurement compared against stereographic methods (Kubínová, Janáček, Guilak, & Opatrný, 1999).

Because of this, the most common quantifications of the bone and graft's structure are volume related (Buie *et al*., 2007; Hilldore *et al*., 2009; Jensen, Kragskov, Wenzel, & Sindet-Pedersen, 1998; S. J. Polak *et al*., 2012). While this gives the amounts of each region, it does not provide any information about distribution or structure of the regions.

Another measurement is the surface area of the bone and graft being presented as a distinct value and also as a ratio to the volume of the bone (Cooper, Turinsky, Sensen, & Hallgrimsson, 2007; Ulrich, van Rietbergen, Laib, & Rüegsegger, 1999).

Because of the limitations of edge visualisation (from segmentation and image collection), there had not been much work into the contact surface area between the graft and the bone, which is an interesting value to qualify the position of the bone in respect to the graft.

The relationship between the volume and surface are of the regions has been thought of as a shape factor (Bouxsein *et al*., 2010; Hara *et al*., 2002). This measurement is however flawed as it is dividing a 2 dimensional value by a three dimensional one (This will be explained further in Section 5.1.2).

1.5.2 Shape Measurement

There is limited amount of work done on the 3D shape because the sample data either comes from stereographic 2D data, or from computational segmented data, with limited resolution at the edges of regions

As bone strength is defined by bone mass, geometry and quality as well as possessing a complex hierarchical structure, the geometry of the bone is important to investigate (Section 5) (Compston, 2006).

There has been work on shape measurement of bone via CT with the measurement of

trabecular thickness and number, (Hara *et al*., 2002; Hildebrand & Laib, 1999; Judex, Boyd, Qin, & Miller, 2003; Xiang *et al*., 2007). This does provide a measurement of the shape and quality of the bone, but only at the micro level of bone (Section 1.1.1.4) and as such, is of limited use when investigating bone growth below the micro scale into the pores of a SBG which are on the order of 100's of microns. The Structure Model Index (SMI) provides a measurement of the shape of the trabecular in relationship to its rod and plate like structure (Ding & Hvid, 2000; Hildebrand & Ru, 1997). The SMI measurement is of limited use in this thesis as the samples will be imaged and measured before the bone's structure is fully connected into a trabecular network and the interconnectivity of the bone is of interest not just the relationship between plates and rods. Shape measurements can also be carried out via Euler number and connectivity indexes, which provide a numerical measurement of the connections exhibited between the voxels of a solid. (Toriwaki & Yonekura, 2002). A similar novel method to measure the shape of the bone via the measure of the connectivity of the bone is discussed in Section 5.

1.5.2.1 Pores

Because of the limitation of measuring more than two regions in a CT scan (object and background), a lot of the shape measurement to date with the quality of synthetically bone grafts has been focused on characterising the empty grafts themselves.
The pores have been characterised in various different ways, using multi scale tomography (Tariq, Haswell, Lee, & McComb, 2011), virtual packing of spheres of differing properties (Sweeney & Martin, 2003) and by dilating pores from the pore walls (J. Jones, Poologasundarampillai, Atwood, Bernard, & Lee, 2007). These methods allow for volume measurements of the pores within the grafts. From this, average volumes and distributions of the pore size can be calculated; however these measurements are only as useful as the knowledge of how the bone growth will react to the pores (Section 1.2.4.1.A).

1.5.3 Summary

The quantification of the regions is limited by the segmentation, whether it is the number of regions which are segmented or the quality of the segmentation at the edge regions. For this reason automated quantification of bone and SBG measurements and segmentation methods have been limited to either "simple" volume measurements or

analysis of just the SBG and from that extrapolating the reaction of the bone to the SBG. This means that if triple region automated segmentation can be performed it would be possible to perform more complex bone quantification measurements, which would provide additional direct insights into the bone growth within the SBGs.

2 Materials and Methods

2.1 SBG samples and specimens for CT Analysis

There are two sets of samples which were investigated in this study.
The first set were porous monoliths of 4.5 mm diameter and height of 6.5mm of Hydroxyapatite (HA) and Silicon substituted Hydroxyapatite (SA) , with substituted silicon amounts of 0.2, 0.4 0.8 and 1.5 weight percent respectively. The HA samples had varying porosities, in both the total and strut (micro porosities) porosities. Which when provided the porosities were stated as being 60% total with 20% strut, as well as both 70 and 80% total with both 10 and 20% strut.
The SA samples where provided with porosities stated as being 70% total and 20% for its strut prorosity.
The monoliths were implanted into the subchondral distal femur site of female white New Zealand rabbits, which were left with free mobility. The rabbits were sacrificed at 3, 6, 12 and 24 weeks and the synthetic bone grafts removed (Table 2-1).
The monoliths are similar to the samples that are used commonly in SBG research. This set is referred to as the Orthotopic sample set. There are previous studies on similar samples in similar testing situations which will be compared to the results in this study in Section 6 (Damien, Hing, Saeed, & Revell, 2003; I. Gibson, Hing, & Revell, 2001; Hing, Annaz, *et al*., 2005; Hing, Buckland, & Moseley, 2005; Hing *et al*., 2006; Hing, Saeed, Annaz, Buckland, & Revell, 2004).

Table 2-1 Samples of Hydroxyapatite and silicon substituted Hydroxyapatite of with stated macro and micro porosities for implantation in the orthotopic sites and the time at which the animals were sacrificed.

Material	Total Porosity %	Strut Porosity %	Week 0	Week 3	Week 6	Week 12	Week 24
Hydroxyapatite	60	20	n=1	n=1	n=1	n=1	n=1
Hydroxyapatite	70	10	n=1	n=1	n=1		
Hydroxyapatite	70	20	n=1	n=1	n=1	n=1	n=1
Hydroxyapatite	80	10	n=1	n=1	n=1	n=1	
Hydroxyapatite	80	20	n=1	n=1	n=1	n=1	n=1
0.2 wt% Si substituted Hydroxyapatite	70	20			n=1	n=1	
0.4 wt% Si substituted Hydroxyapatite	70	20		n=1	n=1	n=1	
0.8 wt% Si substituted Hydroxyapatite	70	20		n=1	n=1	n=1	
1.5 wt% Si substituted Hydroxyapatite	70	20		n=1	n=1	n=1	

The second set of samples were porous granules of SA, all which were provided with stated properties being weight percent 0.8 silicon substitution and macro porosities of 80% with varying micro porosities; while the micro porosities, were 20, 30 and 35% as well as a 30% micro porous samples with surgical putty.

The granules were implanted in the form of a Cylindrical clotted granule masses (15mm ø, 6mL vol.) into the ovine muscle pockets formed by blunt manipulation of para-spinal muscles either side of the spinous processes of L2-L3 of sheep, and then removed after sacrifice at 12 weeks (Table 2-2). This set is referred to as the Ectopic sample set. There are previous studies on similar samples in similar, testing situations (though some are in orthotopic testing conditions) which will be compared to the results in this study in Section 6(Campion *et al*., 2011; Chan *et al*., 2012; Coathup *et al*., 2011; Coathup, Cai, Campion, Buckland, & Blunn, 2013).

Table 2-2 Samples of silicon substituted hydroxyapatite of varying micro porosities for implantation in the ectopic sites and the time of each sample tested.

Material	Total Porosity %	Strut Porosity %	Week 12
0.8 wt% Si substituted Hydroxyapatite	80	20	n=3
0.8 wt% Si substituted Hydroxyapatite	80	30	n=3
0.8 wt% Si substituted Hydroxyapatite with surgical putty	80	30	n=5
0.8 wt% Si substituted Hydroxyapatite	80	35	n=4

2.2 CT Scanner

The micro CT scanner used to scan all the samples was the MuCat 2 system at Queen Mary University of London. The MuCat 2 scanner was designed to provide accurate maps of X-ray attenuation in the samples (Davis, Evershed, & Mills, 2012). This means that the densities of each of the voxels can be taken to be accurate, meaning that it is possible to perform complex segmentation methods on the samples, including but not limited to looking at the highest and lowest values in a local area.

The MuCat 2 implements a cone beam as described in Section 1.3.4.4 as well as the related equations to determine the attenuation in the samples (Equation 1-26, Equation 1-27 & Equation 1-28).

Considering errors inherent in X-ray systems the scanner removes any significant beam hardening (Section 1.3.1.1.F), by using multi-material calibration samples (Evershed, Mills, & Davis, 2012). While ring artefacts (Section1.3.5.5) are obviated in the MuCat 2 by use of time delay integration (TDI) (described in Section 1.3.5.5).

While the scanner takes longer to scan than the conventional industrial models, it provides images with very clear intensity differences between the bone and SBG, while still being significantly more practical to that of a synchrotron.

The samples were scanned in three groups, the Orthotopic (lapin model), the Ectopic (Ovine model) and pre-implantation Orthotopic, with the following variables (Table 2-3).

Table 2-3 CT Variables for the different groups of samples.

	Voltage keV	Currant mA	Pixel size microns	Exposure ms
Orthotopic	90	0.25	30	100000
Pre-implantation Orthotopic	90	0.2	15	10000
Ectopic	90	0.5	30	6000

The SNR of all the samples are above the required 5 as defined by the Rose criterion with the pre-implantation orthotopic samples showing the lowest SNR on the order of 10 and the other samples having SNR in the order of 10's.

2.3 Computer Systems

The majority of the image processing, segmentation and quantification was performed on a multi core server. The server ran on four Oct-core 2GHz (Opteron 6128HE) central Processing Units (CPU), and had 64 GB Ram.

For the stabilisation segmentations method (Section 4.1.3) the processing was performed on a Graphics Processing Unit (GPU) because of the large amount of calculations require, and small size of the individual calculations. The GPU used was a Nvidia GTX 670 (1344 915MHz cores, sharing 2GB Ram.)

2.4 Imaging programs

The imaging programs Gimp (The GIMP Development Team, 2013) and Fiji (Schindelin, Cardona, Longair, & Schmid, 2011) were used for simple image manipulation and quantification such as 2D histograms.

For the creation of the advanced image segmentation and quantification method, the programming languages python (Version 2.7.3) (Python Software Foundation, 2013) and OpenCl (Khronos Group, 2013) were used.

Python was used for the majority of the programming with OpenCl only being using with the stability programming on the GPU, where it was run through a python script. The python programing libraries used included the Python Imaging Library (Secret Labs AB, 2009), NumPy (Community Project, 2013) for array manipulation and matplotlib (John, 2013) which was used for creating the graphs. For the statistical analysis SPSS (version 22) (IBM CORP, 2013) was used.

For the parallelisation of the automated image segmentation and data quantification, parallel python was used (Vanovschi, 2013), which allowed for the program to fully utilise all the CPU cores for some processes.

3 Assessment of Validation Methods

Before the current segmentation methods could be investigated and new methods developed, a method of validation had to be decided upon.
This first involved investigating if any of the current validation methods (Section1.4.2) were valid for this study and if they could be combined and or improved on. This also required the creation of reference images for the different segmentation methods to be validated against.

3.1 Validation Methods

From the methods reviewed in Section 1.4.2 a selection of possible validation methods to be used on the segmentation methods for the bone, bone graft and the background could be chosen from.
The criteria for the validation method, is that can validate images with three regions, not require any assumed knowledge of the sample (except for a reference image as some form of reference is required) and not require any region matching (determining which segmented region relates to which reference region, if there is a reference). A validation method which fitted these ideals would be able to provide a single value for the segmentation, while taking into account all the different combinations of segmented and reference regions (To remove the need to rerun the segmentations for each of the region combinations).
The methods which fit these criteria are GCE/LCE, OCE/OCEd and FRAG, which are highlighted as green in the list of methods (Table 3-1). Methods which fit the ideal criteria except that they require region matching and/or only look at single regions can be modified to provide all the required properties, these include the M_I/M_{II}, RP, D and Foca validation methods and are marked with yellow in the table of methods (Table 3-1).
The AMUA and RUMA methods depend on a property from the samples, the logical property in this study is histology as it has already been performed for some of the Orthotropic samples. The limitation of using the histology data is that it requires a full scan of a sample to compare the values and as such is not currently feasible for a method which compares all possible calibrations because of the time required to fully segment a sample (~ 15 minutes per sample per calibration per CPU (3.7 GHz)). However with increasing computing power this would become possible on a normal

desktop PC, but at this point in time it is not so. The AMUA and RUMA methods can however be used to confirm the sensitivity of the chosen validation method which is expanded on in Section 6.

Table 3-1 Comparison of the validation methods, defining if, all the regions are defined, if it requires known properties, if they require a reference image, if the probability is required to be known, if the measurement an edge/shape or object segmentation and does the segmentation and reference need to be matched, coloured to define relevance for validating the segmentation, with red being not relevant and yellow being possible for single regions.

Method	All Regions	Assumed/Known Properties	Reference Image	Known Probability	Edge/Shape/Object Based	Need Regions Matching
Pc/PF	x	-	-	x	x	-
GU/NU	x	x	-	-	-	-
H^2	x	x	-	-	-	-
GC	x	x	-	-	-	-
SM	x	x	-	-	x	-
MI/MII	-	-	x	-	-	x
RP	-	-	x	-	-	x
PE	-/x	-	-	x	-	-
GCE/LCE	x	-	x	-	-	-
OCE/OCEd	x	-	x	-	-	-
D	x	-	x	-	-	-
Foca	x	-	x	-	-	x
FRAG	x	-	x	-	-	-
AUMA/RUMA	x	x	-	-	-	-

3.1.1 Modification and Considerations of Chosen Validation Methods

When considering the seven sets of validation methods the sets of GCE/LCE (Equation 1-43, Equation 1-44, Equation 1-45, Equation 1-46 & Equation 1-47) and OCE/OCEd (Equation 1-48, Equation 1-49, Equation 1-50, Equation 1-51, Equation 1-52 & Equation 1-53) both measure error of the segmentation, where a returned value of one means maximum error and zero means no error. For ease of comparison, the rest of the validations were modified if required, to return a value of zero if no error and show increased error with higher outputs.

The object validation method of FRAG (Equation 1-57) returns a value of one when there is no difference in object number, as such it was modified to return zero with no difference as shown in Equation 3-1 (where T_N is the number of objects in the

segmented image, A_N is the number of objects in the reference image and p and q are scaling factors).

Equation 3-1

$$FRAG = 1 - \frac{1}{1 + p|T_N - A_N|^q}$$

The M_I and M_{II} error measurements (Equation 1-39 & Equation 1-40) return a zero with no error and 100 % if there is maximum error, to return a value of one for maximum error, the equations were modified to remove the multiplication by 100 for ease of comparison with others by making it the same order of magnitude as the other methods as shown in Equation 3-2 and Equation 3-3 (where j denotes the region in the reference image, I denotes the regions in the segmented image and C_{ij} a pixel which is in the reference region of j and segmented region of i).

Equation 3-2

$$M_I^{(k)} = \frac{\left[\left(\sum_{i=1}^{N} C_{ik}\right) - C_{kk}\right]}{\left[\sum_{i=1}^{N} C\_ik\right]}$$

Equation 3-3

$$M_{II}^{(k)} = \frac{\left[\left(\sum_{i=1}^{N} C_{ik}\right) - C_{kk}\right]}{\left[\left(\sum_{i=1}^{N}\sum_{i=1}^{N} C_{ij}\right) - \sum_{i=1}^{N} C\_ik\right]}$$

In the four RP measurements (Equation 1-35, Equation 1-36, Equation 1-37 & Equation 1-38), Accuracy (Equation 1-36) returns a value relating to the whole quality of the segmentation with one being no error and zero being highest possible error as such it was modified to return zero with no error and one with highest error as shown in Equation 3-4 (where N_{TP} is the number of true positive pixels, N_{TN}, is the number of true negative pixels, N_{FP} is the number of false positive pixels and N_{FN} is the number of false negative pixels).

Equation 3-4

$$Accuracy = 1 - \frac{N_{TP} + N_{TN}}{N_{TP} + N_{TN} + N_{FP} + N_{FN}}$$

In the distance validation D (Equation 1-54) zero is returned with no error, while higher values are returned with higher discrepancy of the position of false positive

pixels/voxels. As the highest possible error is dependent on the size of the reference image either the value can either be presented as a measure of total squared distance or as a relative amount of total possible error, because of the high value of potential error, the values will be in simpler form when not divided by total potential error.
Because of the seemingly uniform nature of pixels and voxels the distance are recorded in two forms, the “true” measurement (D(T)) where pixels on the diagonal have their distance taken as the square root of two and the “simplified” measurement (D(S)) when the diagonal distances are taken to be equal to the horizontal and vertical distances. The D validation method also requires a pre-scan to check that there are true positive pixels in each of the region parings as otherwise the error would return as zero as there were no possible measurements. For the situations where an incorrectly identified pixel is segmented in an image and there are no correctly identified pixels of the corresponding region, a distance error of the largest possible distance in the image will be recorded. This allows for rogue pixels to be counted without being ignored or causing such a large error as to invalidate the rest of the segmented image.
The Object count agreement of Foca (Equation 1-55& Equation 1-56) is dependent on the number of degrees of freedom, which in turn is determined by the number of regions of interest, which gives the equation of Foca for three regions as shown in Equation 3.5 (where L is defined by Equation 1-55).

Equation 3-5

$$Foca = \frac{1}{e^{\frac{L}{2}}}$$

In the form of Equation 3-5 Foca returns one for no error and close to zero for highest error, this can be changed in the normalised form of zero being no error with Equation 3-6.

Equation 3-6

$$Foca = 1 - \frac{1}{e^{\frac{L}{2}}}$$

The validation methods that only consider individual regions and require region matching (M_I/M_{II}, RP, Foca and D) were modified to take into account all the possible region matches between the segmented image and the reference image, this modified form will be what is referred to when these methods are mentioned, except where

otherwise stated. The methods which have been modified to take into account all the regions will return a combined error value, such that if the method returns at maximum one for most error in the combined form it will return a three for maximum error.

3.1.2 Validation of Known Segmentations

To test the relevance of these methods for identifying the “best” segmentation method, they were first used to validate the segmentation of example images with known perfect segmentation solutions. As this study looks to segment out two regions of interest from a background, the example images have three regions to make them comparable to the images that will be investigated.

The first example image used to investigate the validation techniques is an eight bit image (256 states Section 1.3.2.1) with three regions each comprised of pixels of randomly determined intensities bounded by upper and lower boundaries such that no intensity of pixel exists in multiple regions. The regions from left to right are bounded by intensity values of (0-50), (100-150) and (200-250) respectively, thus that the left region is only comprised by pixels of intestines between 0 and 50 exclusively, the middle by 100-150 exclusively and the right region by 200-250 exclusively. (Figure 3-1).

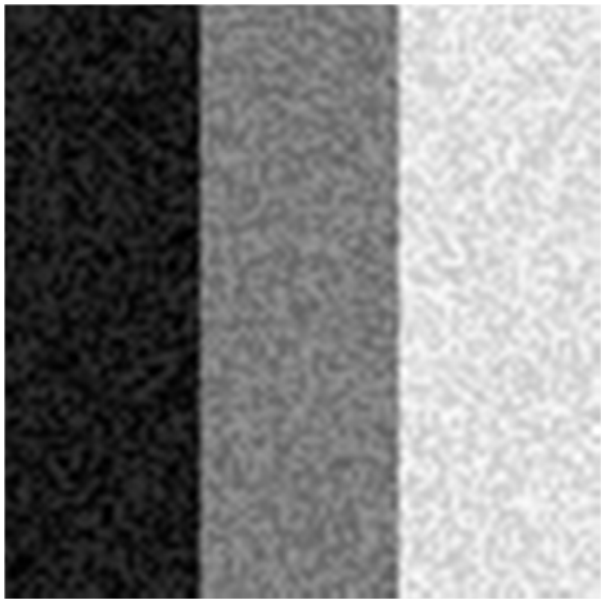

Figure 3-1 Example image comprised of three regions comprised of random intensity pixels between the boundaries of intensities of 0-50, 100-150 and 200-250 from left to right.

Figure 3-1 shows an example image comprised of three regions of bounded intensities

arranged from left to right, if a perfect segmentation of this is created, each of the three equally sized regions from left to right will be clearly defined. Using the colours red, green and blue to define the segmented regions, the three defined regions can be clearly seen, with red showing the highest intensity region, green the lowest intensity region and blue the region with intensity in-between the two other regions (Figure 3-2).

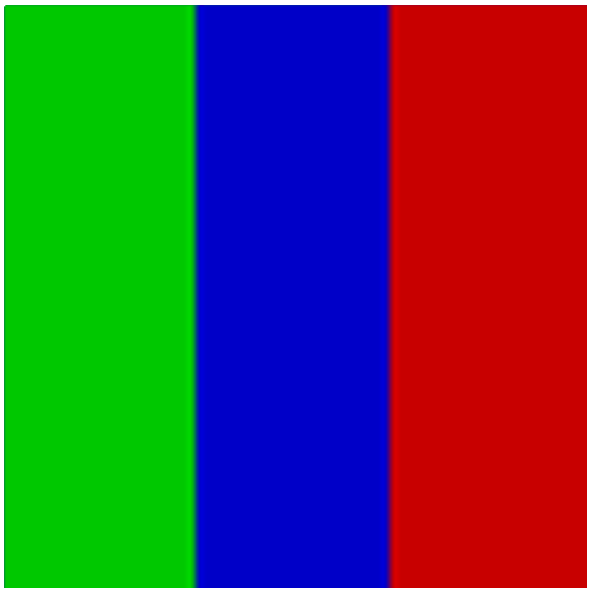

Figure 3-2 The reference image of the three regions in Figure 3-1 defined by the colours red, green and blue.

For the first example image as shown in Figure 3-1 using the boundary threshold segmentation method (Defined in Section 1.4.1.1) boundary values between 50-100 and 150-200 should segment out the three regions perfectly. Taking the two boundaries values at their lowest (49 & 149) (as the boundary is defined as bigger than or equal), the middle of this range (75 & 175) highest (99 & 199), (as the boundary is defined as bigger than or equal) three segmentations with expect zero error can be produced (Figure 3-3 A, Figure 3-3B & Figure 3-3C respectively). It is also important for the validation methods to show an error when the segmentation is not perfect, therefore three expectedly imperfect segmentations are also compared, with boundary intensities of (100 & 200), (25 & 225) and (110 & 140) (Figure 3-3D, Figure 3-3E & Figure 3-3F respectively).

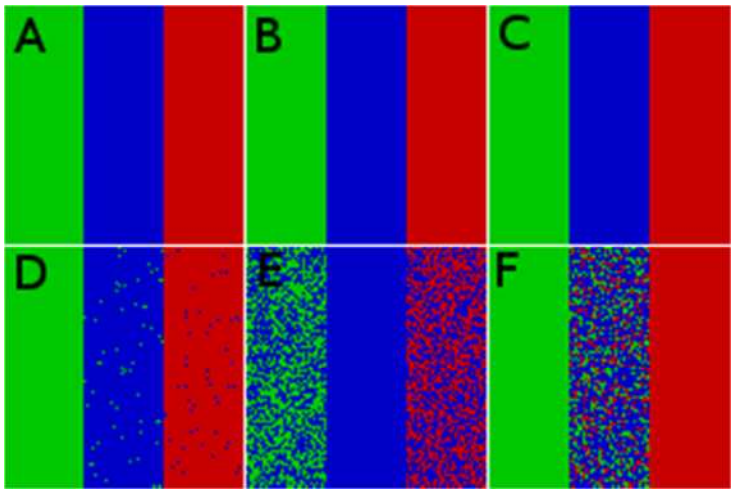

Figure 3-3 Segmentations of Figure 3-1by using the boundary segmentation technique with two boundaries of A:(49 & 149), B:(75 & 175), C:(99 & 199), D:(100 & 200), E(:25 & 225) and F:(110 & 140).

For these six segmentations as shown in Figure 3-3 an error of the complete segmentation (considering all the regions) was calculated using GCE, LCE, OCE, OCEd, FRAG validation methods as well as the modified error measurements MI, MII, Accuracy, D and Foca (Table 3-2).

Table 3-2 The validation error values for the segmentation images in Figure 3-3 compared to the perfect segmentation of Figure 3.1 using GCE, LCE, OCE, OCEd, FRAG,MI, MII, Accuracy, D(S), D(T) and Foca.

	Threshold Values											
	49	149	75	175	99	199	100	200	25	225	110	140
GCE	0.000		0.000		0.000		0.026		0.333		0.188	
LCE	0.000		0.000		0.000		0.019		0.167		0.107	
OCE	0.000		0.000		0.000		0.349		0.634		0.379	
OCEd	0.000		0.000		0.000		0.338		0.511		0.296	
FRAG	0.000		0.000		0.000		0.989		0.984		0.997	
MI	0.000		0.000		0.000		0.040		1.002		0.406	
MII	0.000		0.000		0.000		0.020		0.501		0.203	
Accuracy	0.000		0.000		0.000		0.026		0.668		0.271	
D(S)	0		0		0		35905		865586		346947	
D(T)	0		0		0		35906		865735		346973	
Foca	0.000		0.000		0.000		3.000		3.000		3.000	

Table 3-2 shows that as expected the three threshold boundaries which should give

perfect segmentations showed zero errors in all the methods; while the three non-perfect threshold values returned non-zero. For the non-zero errors the order of the error from lowest to highest is identified by the colours green, yellow and red respectively for each of the validation methods in respect to the three non-perfect segmentations (Table 3-3).

Table 3-3 The validation error values for the incorrect segmentation images Figure 3.3D,3.3E & 3.3F compared to the perfect segmentation of Figure 3.1 using GCE, LCE, OCE, OCEd, FRAG,MI, MII, Accuracy, D(S), D(T) and Foca. error measurements, with error order shown by green, yellow and red from highest to lower.

	Threshold Values					
	100	200	25	225	110	140
GCE	0.026		0.333		0.188	
LCE	0.019		0.167		0.107	
OCE	0.349		0.634		0.379	
OCEd	0.338		0.511		0.296	
FRAG	0.989		0.984		0.997	
MI	0.040		1.002		0.406	
MII	0.020		0.501		0.203	
Accuracy	0.026		0.668		0.271	
D(S)	35905		865586		346947	
D(T)	35906		865735		346973	
Foca	3.000		3.000		3.000	

Out of the eleven total validation methods eight of them (six if only counting one of each of the M and D validation methods) agree that the image with threshold (100 & 200) has the lowest error followed by (110 & 140) and then (25 & 225) (Table 3-3). The relative difference in the error sizes for the different validation methods can be seen by normalising the errors against the lowest error in each of the validation methods (*Table* 3.4).

Table 3-4 The validation error values for the incorrect segmentation images Figure 3.3D,3.3E & 3.3F compared to the perfect segmentation of figure 3.1 using GCE, LCE, OCE, OCEd, FRAG,MI, MII, Accuracy, D(S), D(T) and Foca. error measurements, with error order shown by green, yellow and red, from highest to lower normalised to the lowest error.

	Threshold Values					
	100	200	25	225	110	140
GCE	1.000		12.868		7.257	
LCE	1.000		8.821		5.692	
OCE	1.000		1.816		1.087	
OCEd	1.142		1.726		1.000	
FRAG	1.005		1.000		1.013	
MI	1.000		25.290		10.252	
MII	1.000		25.290		10.252	
Accuracy	1.000		25.290		10.252	
D(S)	1.000		24.108		9.663	
D(T)	1.000		24.111		9.663	
Foca	1.000		1.000		1.000	

From Table 3-4 it can be seen that MI, MII, Accuracy, D(S) and D(T) have similar relationships between the errors in the three segmented samples, with MI, MII and Accuracy showing the same values.

The time it takes for each of the validation methods to process an image is also of importance because of the large number of different variable values which had to be compared in the segmentation techniques (Section 4), because some of the validation methods work off the same data, they are processed in groups, (GCE & LCE, OCE & OCE, FRAG & Foca, MI/MII & Accuracy and D), therefore the times are recorded for the processing groups not the individual methods (On a single 3.7 GHz CPU) (Table 3-5).

Table 3-5 Processing time for GCE & LCE, OCE & OCE, FRAG & Foca, MI/MII & Accuracy and D validation methods

	Threshold Values											
	49	149	75	175	99	199	100	200	25	225	110	140
GCE/LCE Processing Time (s)	0.224		0.159		0.223		0.225		0.154		0.223	
OCE/OCEd Processing Time (s)	0.260		0.173		0.183		0.172		0.239		0.189	
FRAG/Foca Processing Time (s)	2.358		2.660		2.260		2.252		2.434		2.331	
Accuracy/MI/MII Processing Time (s)	0.225		0.160		0.223		0.223		0.125		0.144	
D Processing Time (s)	0.686		0.691		0.776		69.219		196.368		58.778	

Table 3-5 shows that the D validation method has highest processing time than the other methods when an error is recorded, this fits with the method as it has to "find" the closest correctly identified pixel/voxel in the segmentation.

To test the validation values further, explicitly incorrect segmentations were compared again the first test image (Figure 3-4).

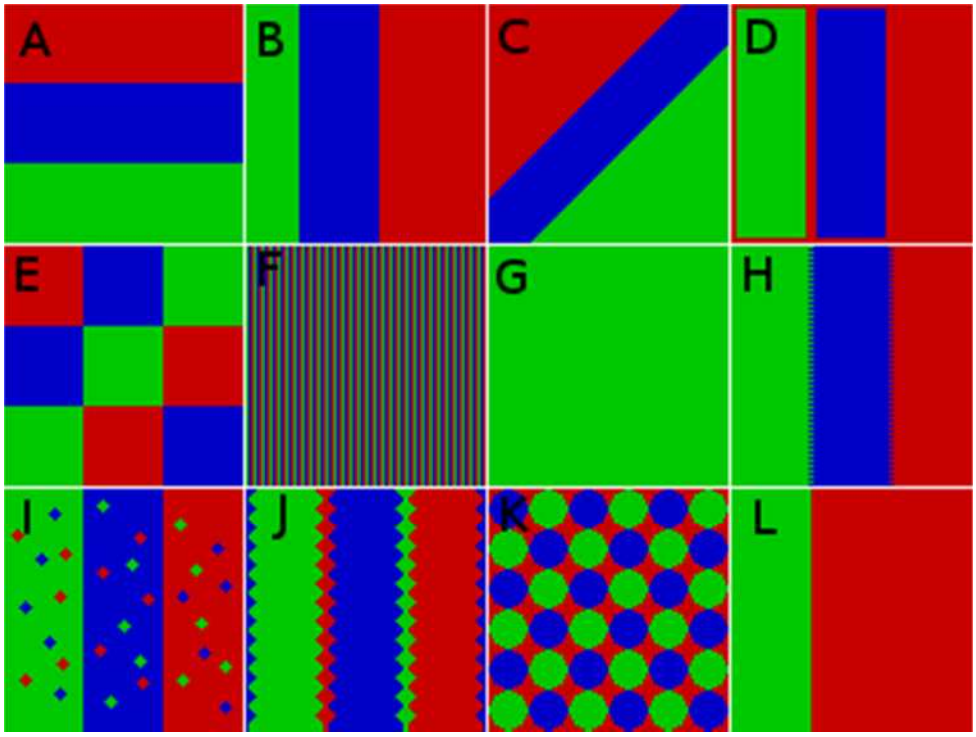

Figure 3-4 Incorrect segmentations of Figure 1-1

The Incorrect segmentations can be defined as follows:

A: Correct segmentation rotated by 90 degrees.

B: Correctly aligned regions with incorrect sizing.

C: Segmentations aligned at a 45 degree rotation.

D: Reduced regions sizes for first two regions with correct alignment and position.

E: Correct area of segmentations but only one third in correct position

F: The three segmented regions distributed homogeneously through the image

G: Whole image segmented as one region

H: Correctly general position and areas of segmentation with half of the pixels at the boundary in the wrong positions.

I: Correctly segmented regions with twelve small regions of "noise" in each of the regions

J: Correctly segmented bulk of regions with incorrect segmentation at boundary regions.

K: The three segmented regions distributed homogeneously through the image as circles.

L: One correctly segmented region with other two regions appearing as one region.

The errors for each of the incorrect segmentations (Figure 3-4) and each of the validation methods were calculated (with zero error being highlighted in red) as shown in Table 3-6.

Table 3-6 The validation error values for the incorrect segmentation images in Figure 3.4 compared to the perfect segmentation of Figure 3.1 using GCE, LCE, OCE, OCEd, FRAG,MI, MII, Accuracy, D(S), D(T) and Foca, error measurements, with zero errors being highlighted in red.

	A	B	C	D	E	F	G	H	I	J	K	L
GCE	0.667	0.296	0.538	0.185	0.667	0.667	0.000	0.044	0.093	0.268	0.663	0.000
LCE	0.667	0.222	0.535	0.095	0.667	0.667	0.000	0.044	0.093	0.268	0.649	0.000
OCE	0.800	0.518	0.780	0.408	0.800	0.800	0.667	0.569	0.689	0.728	0.799	0.333
OCEd	0.667	0.391	0.667	0.425	0.667	0.667	0.500	0.556	0.667	0.667	0.666	0.222
FRAG	0.000	0.000	0.000	0.000	0.667	0.988	0.750	0.000	0.968	0.966	0.988	0.500
MI	2.000	0.667	1.333	0.344	2.000	2.000	2.000	0.067	0.144	0.453	2.000	1.000
MII	1.000	0.333	0.667	0.172	1.000	1.000	1.000	0.033	0.072	0.227	1.000	0.500
Accuracy	1.333	0.444	0.889	0.229	1.333	1.333	1.333	0.044	0.096	0.302	1.333	0.667
D(S)	9991800	138600	1490014	1227416	7255180	5279040	1701900	360	329306	1184742	5009502	850950
D(T)	9991800	138600	1857802	1227472	8399700	5279040	1701900	360	329456	1190568	5246238	850950
Foca	0.000	0.000	0.000	0.000	1.180	3.000	-3.351	0.000	2.998	2.997	3.000	-0.852

Table 3-6 shows that in seven out of the twelve incorrect segmentations two validation methods show a false zero error. In the case of the incorrect segmentations which relate to Figure 3-4 A, Figure 3-4 B, Figure 3-4 C, Figure 3-4 D and Figure 3-4 H this is due to there being the same number of objects in the incorrect segmentations as in the

correct segmentation, causing the miss identified zero error in the validation methods of FRAG and Foca. While in the case of the incorrect segmentations which relate to Figure 3-4 G and Figure 3-4 L this appears to be connected with two or more regions being "perfectly" segmented as a single region, giving a false zero error in the methods of GCE and LCE.

As the methods of GCE, LCE, FRAG and Foca give zero errors when the segmentation is not perfect, they are limited in their use as a method to validate the error of a segmentation method, especially when comparing a large number of segmentations automatically. In regards to the amount of error in each of the other incorrect segmentations, the segmentations of Figure 3-4 B, Figure 3-4 D, Figure 3-4 H, Figure 3-4 I and Figure 3-4 J are expected to have lower error that the other segmentations as they have approximately the same shape, area and position of regions as the correct segmentation (Figure 3-2). Therefore any error values which are lower for the segmentations of any of Figure 3-4 A, Figure 3-4 C, Figure 3-4 E, Figure 3-4 F, Figure 3-4 G, Figure 3-4 K & Figure 3-4 L compared to Figure 3-4 B, Figure 3-4 D, Figure 3-4 H, Figure 3-4 I & Figure 3-4 J would appear to be measuring the error incorrectly and are marked accordingly by a red highlight Table 3.6.

Table 3-7 The validation error values for the incorrect segmentation images in Figure 3.4 compared to the perfect segmentation of Figure 3.1 using GCE, LCE, OCE, OCEd, FRAG,MI, MII, Accuracy, D(S), D(T) and Foca. error measurements, with zero errors and lower than expected errors being highlighted in red and expected lower error segmentations being highlighted in green.

	A	B	C	D	E	F	G	H	I	J	K	L
GCE	0.667	0.296	0.538	0.185	0.667	0.667	0.000	0.044	0.093	0.268	0.663	0.000
LCE	0.667	0.222	0.535	0.095	0.667	0.667	0.000	0.044	0.093	0.268	0.649	0.000
OCE	0.800	0.518	0.780	0.408	0.800	0.800	0.667	0.569	0.689	0.728	0.799	0.333
OCEd	0.667	0.391	0.667	0.425	0.667	0.667	0.500	0.556	0.667	0.667	0.666	0.222
FRAG	0.000	0.000	0.000	0.000	0.667	0.988	0.750	0.000	0.968	0.966	0.988	0.500
MI	2.000	0.667	1.333	0.344	2.000	2.000	2.000	0.067	0.144	0.453	2.000	1.000
MII	1.000	0.333	0.667	0.172	1.000	1.000	1.000	0.033	0.072	0.227	1.000	0.500
Accuracy	1.333	0.444	0.889	0.229	1.333	1.333	1.333	0.044	0.096	0.302	1.333	0.667
D(S)	9991800	138600	1490014	1227416	7255180	5279040	1701900	360	329306	1184742	5009502	850950
D(T)	9991800	138600	1857802	1227472	8399700	5279040	1701900	360	329456	1190568	5246238	850950
Foca	0.000	0.000	0.000	0.000	1.180	3.000	-3.351	0.000	2.998	2.997	3.000	-0.852

The lower than expected errors appears in the segmentations of Figures 3.4E, 3.4G and 3.4L and in the validation methods of OCE, OCEd and Foca (Table 3-7). The unexpectedly low errors in Figure 3-4 G and Figure 3-4 L again can be related to the

“perfect” segmentation of two regions as one, while the low error in Figure 3-4 E can be related to the high sensitivity of the number of objects in the segmentations when the number of objects is low. The lower error in both the D methods can be explained by the fact that only one third of the image is incorrect and due to the position of the region there is a short distance between an incorrectly segmented pixel and a correctly identified pixel.

Because of the false zero errors shown in the segmentation validation methods of GCE, LCE, FRAG and Foca, these were not used to determine the best segmentation method for this thesis (Section 4). As lower than expected error was observed in the OCE and OCEd segmentation validation methods when exposed to two or more regions segmented as one, these methods were also not used to determine the best segmentation methods.

Therefore the methods that were considered for validation of the segmentation methods were MI, MII, Accuracy, D(S) and D(T).

3.1.3 Using Validation to Determine Segmentation Solutions

Because of the high number of possible variable combinations in some of the segmentation methods that were investigated (Section 4), the validation methods for the segmentations methods need to be able to identify the best possible segmentation out of all the possible combinations of variables in a timely fashion.

The distance based validation methods of D(S) and D(T) were deemed unsuitable for determining the best segmentation method because of their high run time when used on a segmentation with non-zero error (Table 3-5). As even assuming only half the segmentations would have significant error and taking the processing time to be a minute testing all the calibrations of a double boundary segmentation method would take over eleven days to process.

For this reason the validation of segmentation method of D(S) and D(T) were not used to determine the best segmentation methods.

If all possible variables are tested for a method where there is a possible perfect segmentation, the perfect solution should be easy to identify by the zero error it returns. Using the example image shown in Figure 3-1 which has a known set of possible solutions for a known segmentation method (threshold method, Section 1.4.1.1), the lowest perfect segmentation solutions as defined by MI, MII and Accuracy can be determined by trying all threshold values and returning the lowest values with an error

of zero (Table 3-8).

Table 3-8 Lowest perfect solution for double histogram segmentation method as determined by validation methods Accuracy, MI and MII.

Method	Threshold 1	Threshold 2
Accuracy	49	149
MI	49	149
MII	49	149

Table 3-8 shows that for the example image shown in Figure 3-1 a possible perfect solution (confirmed by knowing the properties of the regions in the image) can be determined by trying all methods and measuring their error. It is however known that there are a range of perfect solutions, this range of possible perfect solutions are possible to see by plotting the three errors against the two threshold values (where the second threshold value has to be larger than the first) and observing where the errors are zero (Figure 3-5, Figure 3-6 & Figure 3-7).

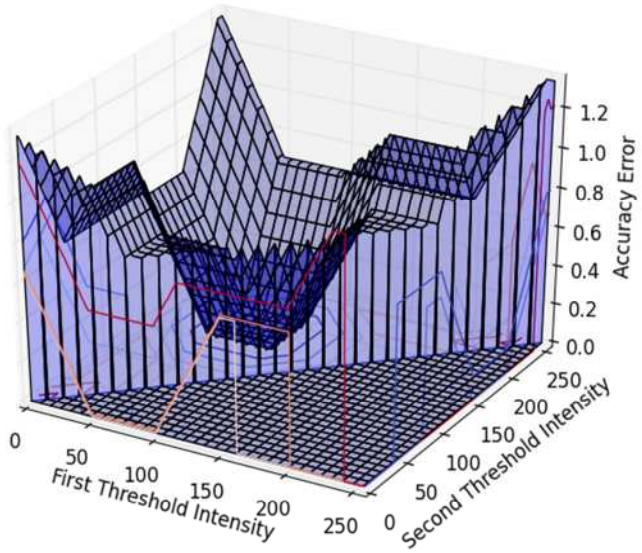

Figure 3-5 Recorded Accuracy errors for segmentation of Figure 1.1 for the threshold values for double threshold segmentation method.

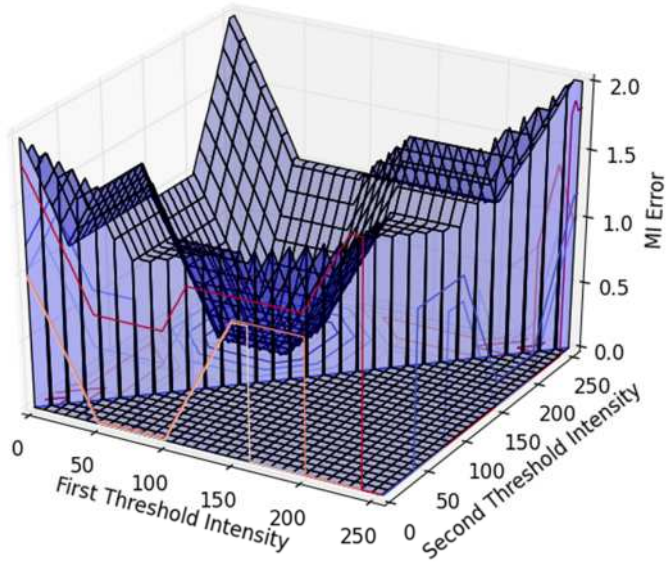

Figure 3-6 Recorded MI errors for segmentation of Figure 1.1 for the threshold values for double threshold

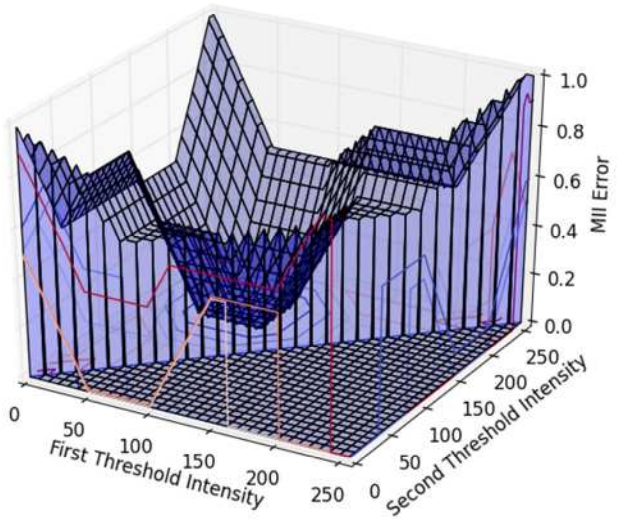

Figure 3-7 Recorded MII errors for segmentation of Figure 1.1 for the threshold values for double threshold segmentation method.

Figure 3-5, Figure 3-6 & Figure 3-7 all show a clear area of threshold values which return zero error in the validation methods of Accuracy, MI and MII.

As the samples that will be segmented cannot be expected to have perfect solutions it is also important to consider how this method will determine the “best” segmentation in an

image that does not have a “perfect” segmentation, which can be achieved by using an example of an image with a heterogeneous region (Figure 3-8). The example image which is used uses both homogenise regions which are defined by intensity boundaries and a heterogeneous region which is created from the same set of pixels that are in the two homogenise regions (Figure 3-8, Figure 3-9 & Figure 3-10).

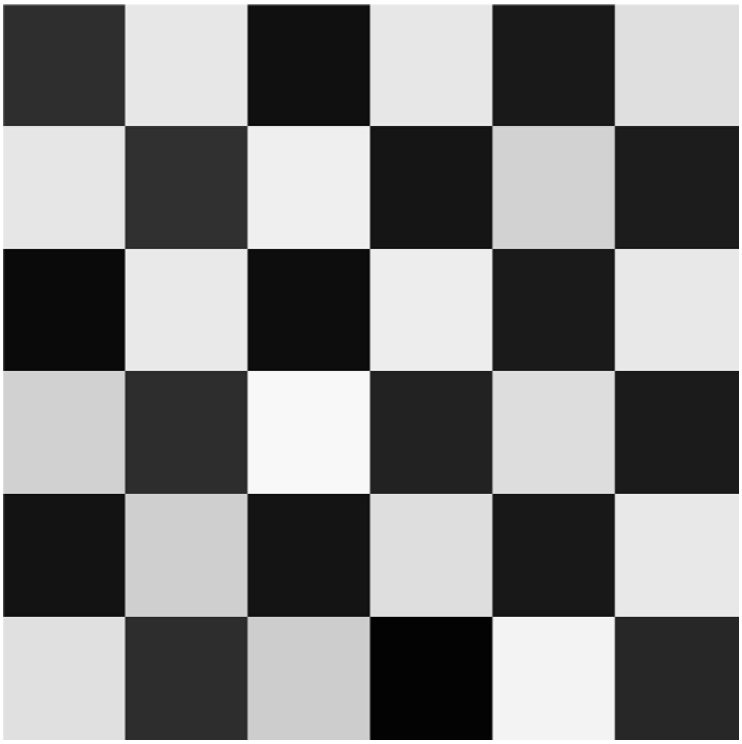

Figure 3-8 A heterogeneous region comprised out of two sets of pixels with random intensities with intensities boundaries by pixels of 0-49 and 200-249 respectively, arranged in a “chessboard pattern” of size of six by six pixels.

Figure 3-9 Example image comprised of three equally sized regions with two comprised of random intensity pixels between the boundaries of intensities of 0-50, and 200-250 as well as a heterogeneous region comprised out of two sets of pixels with random intensities.

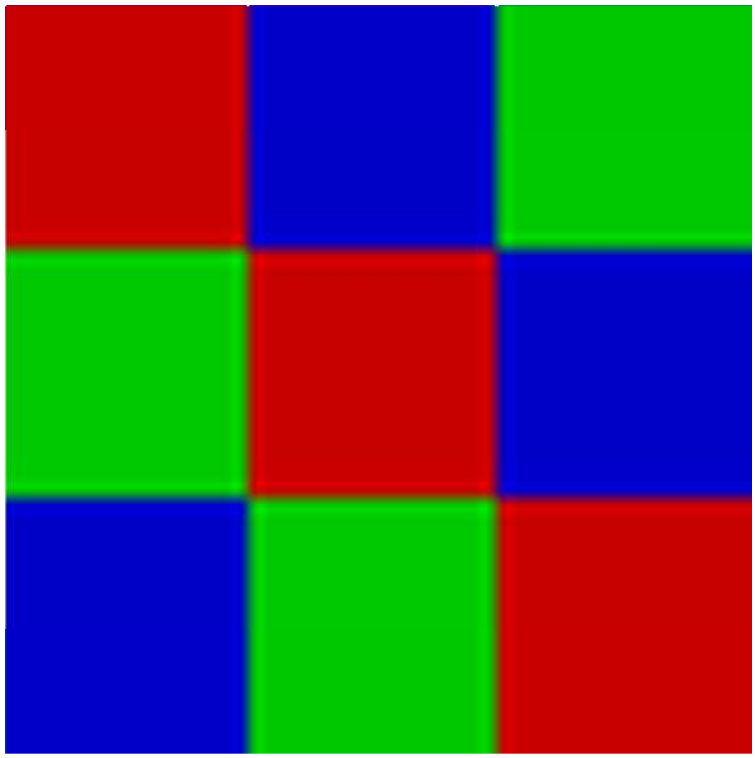

Figure 3-10 Perfect segmentation of the three regions in the example image shown in Figure 3-9.

As there is no expected perfect segmentation for Figure 3-9 when using the double

boundary method (Section 1.4.1.1) (as pixels of the same intensity exist in multiple regions) when attempting all the possible threshold values the lowest error will be recorded as well as the threshold value when it first occurs (Table 3-9).

Table 3-9 Measured lowest perfect solution error for double histogram segmentation method as determined by validation methods Accuracy, MI and MII.

Method	Lowest Error	Threshold 1	Threshold 2
Accuracy	0.667	49	149
MI	1.000	49	149
MII	0.500	49	149

Table 3-9 shows that the lowest errors for each of the validation methods occurs at the same threshold value, the resulting segmentation from this threshold value are shown in Figure 3-11.

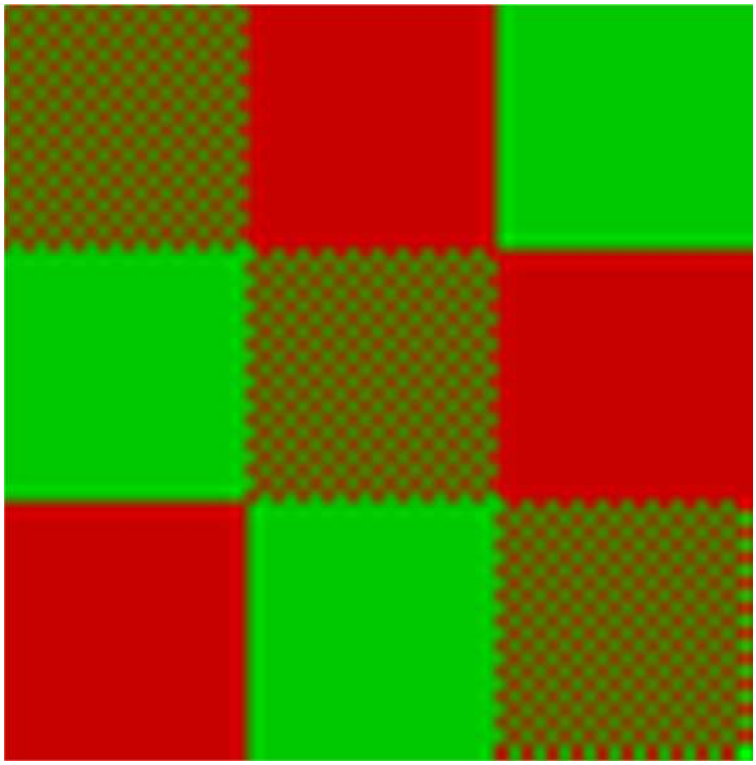

Figure 3-11 Resultant segmentations for the following threshold values in the double threshold method (49& 49).

From observation of the segmented regions (Figure 3-11)there are both red and green regions as well as an apparent third region which appears “yellow” but is actually is comprised of red and green regions arranged in a “chessboard” pattern.

To determine the trends of the error compared to the position of the thresholds the 3D graphs of threshold values to error, for Accuracy, MI and MII validation methods were created using each of the thresholds as an axis (Figure 3-12, Figure 3-13 & Figure 3-14).

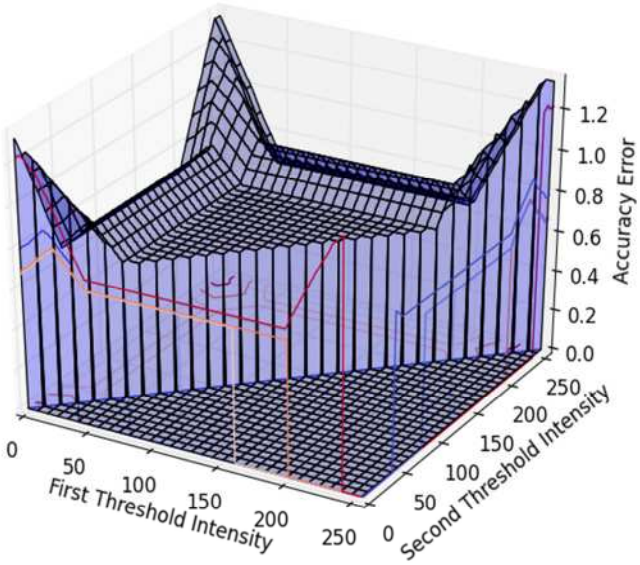

Figure 3-12 Recorded Accuracy errors for segmentation of Figure 3-9 for the threshold values for double threshold segmentation method.

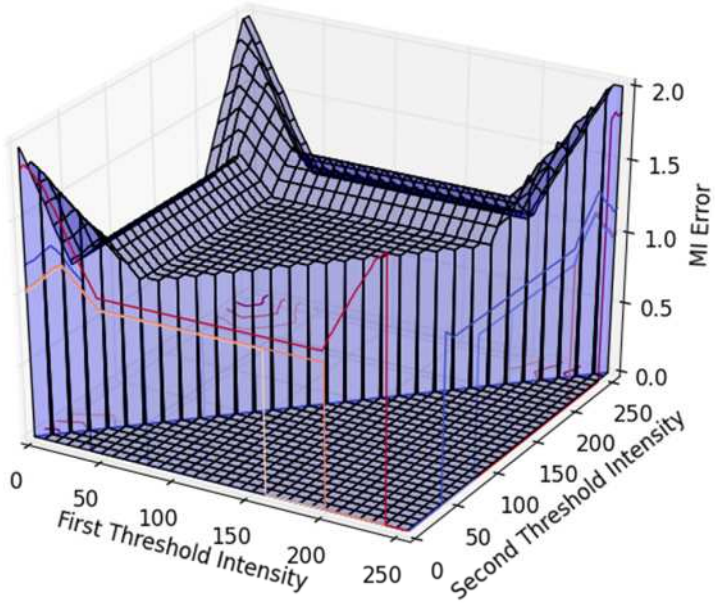

Figure 3-13 Recorded MI errors for segmentation of Figure 3-9 for the threshold values for double threshold segmentation method.

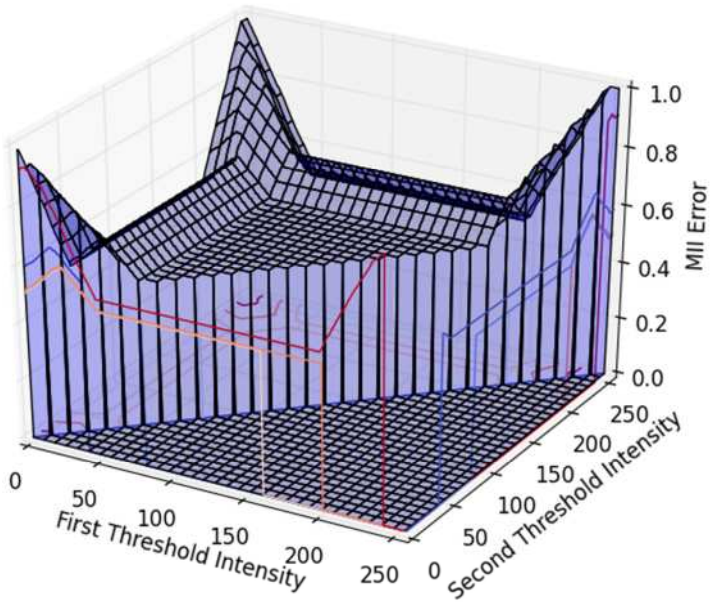

Figure 3-14 Recorded MII errors for segmentation of Figure 3-9 for the threshold values for double threshold segmentation method.

For all the three error validation methods of Accuracy, MI and MII (Figure 3-12, Figure 3-13 and Figure 3-14) there is a plateau region of constant lowest error in the middle of the threshold values.

As the properties of the regions in the example image (Figure 3-9) were known it can be determined that it is not possible to determine a perfect segmentation using a double threshold method. Therefore the best segmentation would be by defining the two homogeneous regions and not heterogamous region, which would result in an error equivalent to a third of the image not being correctly segmented. While the highest errors would result from when the entire image is segmented as a single region.

Upon inspection of the error functions(Figure 3-12, Figure 3-13 & Figure 3-14), it can be clearly seen that there is a constant ratio between the errors determined by the three different methods, this can be seen in the ratio between lowest and highest error, which occur in the same threshold positions (Table 3-10).

Table 3-10 Minimum and maximum errors as determined by the validation methods of Accuracy, MI and MII.

Method	Min Error	Thresholds		Max Error	Thresholds	
Accuracy	0.667	49	149	1.333	249	249
MI	1.000	49	149	2.000	249	249
MII	0.500	49	149	1.000	249	249

Interestingly the projected lines on to the base of the MI error graph (Figure 3-13) does appear to be different to the MII and Accuracy (Figure 3-12 & Figure 3-14) but this is due to the fact that the total error values are higher and the projection takes arbitrary points along a sloped surface to project onto the base. The similarity in the errors can be seen by dividing the MI error values by two to normalise it to the MII error values (Figure 3-15).

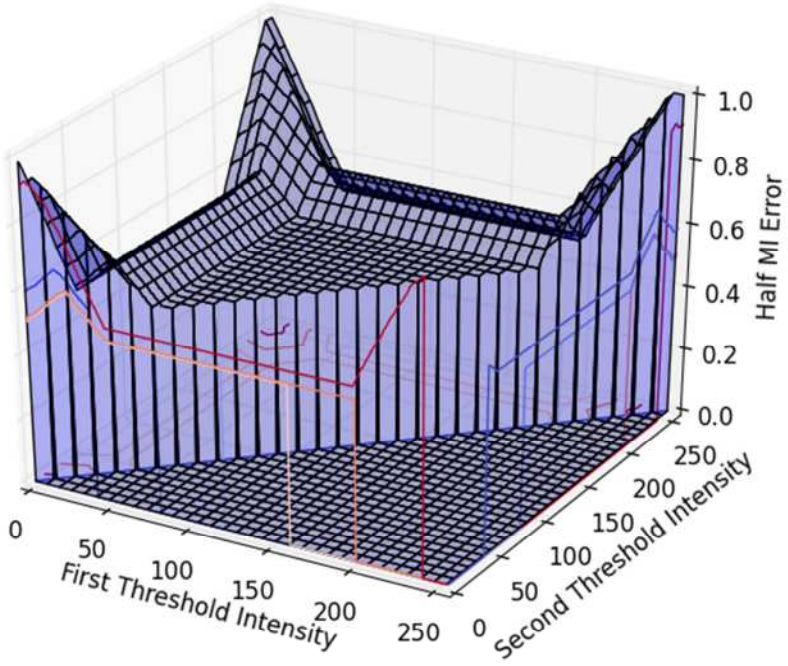

Figure 3-15 Recorded half MI errors for segmentation of Figure 3-9 for the threshold values for double threshold segmentation method.

As the validation methods of MI, MII and Accuracy are equivalent any of them may be used, the validation method of MI will be used in this study for the similar reason that it returns the largest values.

The relationship between the MI validation error value and the perceived error in an image can be approximated by measuring the error on a set of images with known

misidentification compared to a reference image (in this case Figure 3-10) these images are shown in Figure 3-16 with their expected error and measured MI error shown in Table 3-11.

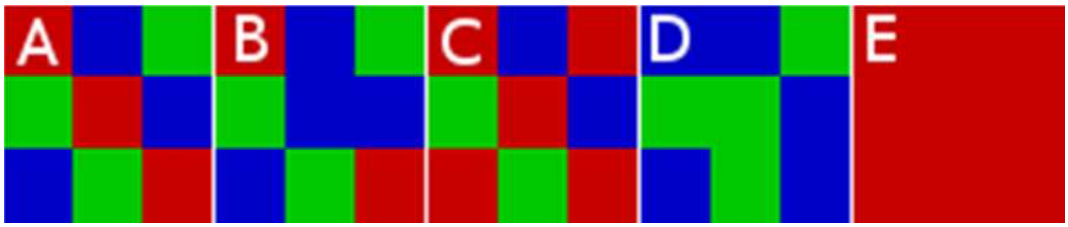

Figure 3-16 Sample Images with expected error compared to image A of A:0%, B:0.11%, C:0.22%, D:0.33%, E: 0.67 %.

Table 3-11 Expected errors and measured MI error for sample images of known error in Figure 3-16

	Sample				
Error	A	B	C	D	E
Expected	0.00	0.11	0.22	0.33	0.67
MI	0	0.33	0.67	1	2

From Figure 3-16 and Table 3-11 it can be seen that the MI error returns an error of three times the expected error value. This clear ratio is also due to the fact that the three regions are of equal size, and the MI value returns a possible maximum error of one for each of the three regions. As the reference images that were used (Section 3.2) each contain three equally sized regions a modified MI validation error method was used which is defined as a third MI and is referred to as Mn, where the Mn error value returns an error value equivalent to the proportion of the image which is miss-identified. The validation method of Mn was used to compare the different segmentation methods (Section 4) and determine the calibration values of the methods when determining the segmentation for the sample sets (Section 6).

3.2 Creation of Objective Reference Images and Segmentation

For the validation method of Mn there is the need for test images and their objectively correct reference segmentations to measure the error of the different segmentation methods against.

The factors in the reference segmentation are the shape and position of the regions and

the distribution of the pixel intensities within the regions.

As the methods are derived to segment out bone and graft from the background and between themselves, there has to be three different regions in the test images. As each of the regions will have different pixel distributions, to insure that each region and the three different boarders between the regions equally contribute to the error of the methods, the areas and contact surfaces between the three regions have to be constant in the images.

As the regions in the CT images are not all defined with clear straight lines this needs to be taken into account when investigating the different segmentation methods. As such, three different shapes of regions will be used in the test images (Figure 3-17):

- Regions boundaries are defined as straight lines aligned with the x and y axis of the image.
- Regions boundaries are defined as diagonal lines in respect to the axis of the image.
- Regions boundaries are defined on lines which are based on sine waves.

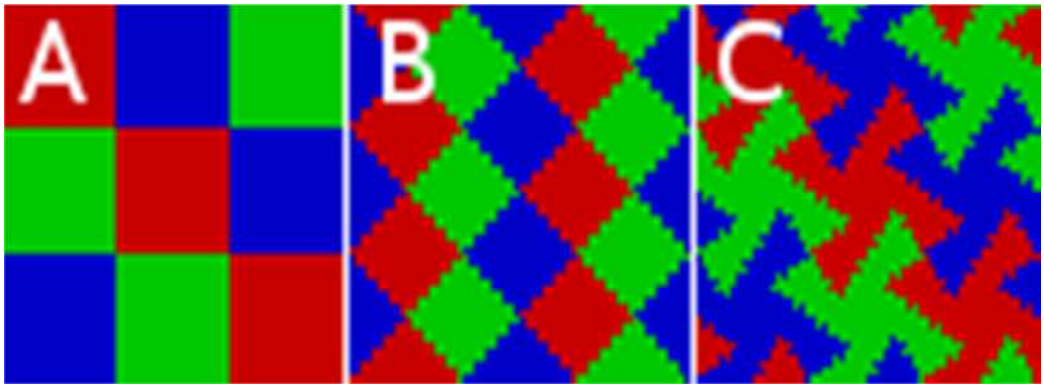

Figure 3-17 Region shapes defined for the objective test images A: Regions defined by parallel lines to the axis of the image, B: lines at diagonals to the axis of the images & C: Lines defined by approximate sin waves.

By testing each of the possible segmentation methods with these three different shapes of regions it is possible to determine if the methods are limited by the shape of the regions they are segmenting. The three shapes are referred to as α: Regions defined by parallel lines to the axis of the image, β: lines at diagonals to the axis of the images & γ: lines defined by approximate sin waves respectively.

For the pixel distribution properties of the three regions, these need to be similar in relative properties to the three regions in the test samples of bone and graft.

To investigative the relative properties of the regions within the samples, the histograms

of regions which contain, just background, bone and background, graft and background and all three regions were analysed (Figure 3-18).

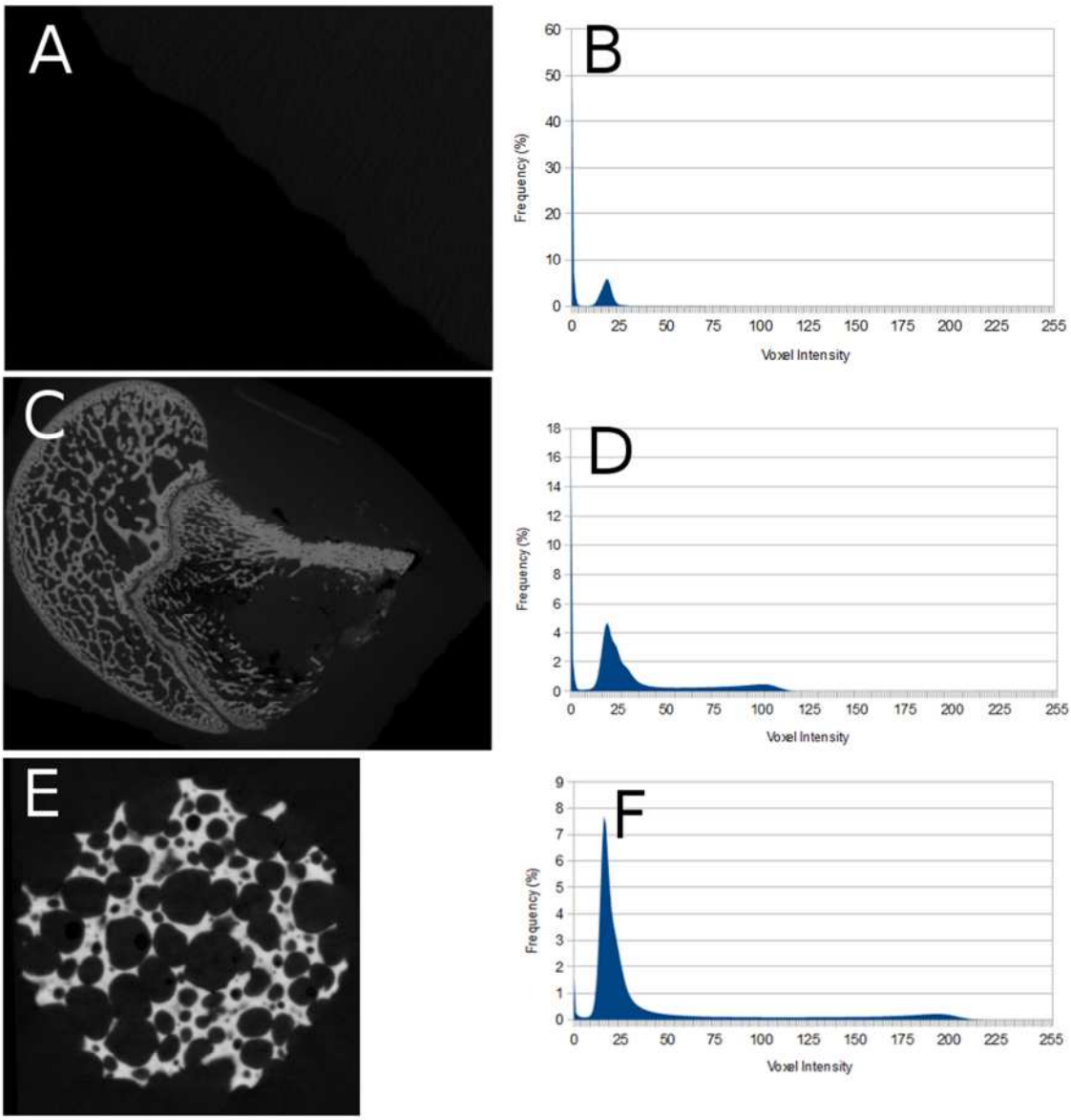

Figure 3-18 Example images from the HA orthotropic sample of 80% total 20% strut porosity at 3 weeks of background, background and bone and implant and graft and background, A, C, E and their histograms (of multiple image stacks)E, D and F respectively.

Assuming that the regions obey Gaussian distributions, the region with the highest intensity in each of the regions of interest can be defined by taking the position of the peak as the mean, with the standard deviation being defined by the values on the higher intensity side of the peak. This gives approximated region properties of background, bone and graft for the different test samples; because the sheep samples are not grown within bone there is not a clear way to define a region of interest they are not used to

define the individual regions. The samples and region of interests used are the five different porosities of HA graft (Section 2), the bone/background was taken from the pre-existing not in contact with the implant bone from the HA samples at three weeks with a region of interest with only background used for the background analysis (Table 3-12).

Table 3-12 Mean and standard deviations of background, Bone and Graft from orthotopic HA samples at 3 weeks (Graft is defined from the pre implantation orthotopic sample) and their average.

Sample		Background		Bone		Graft	
Total	Strut	Mean	SD	Mean	SD	Mean	SD
60	20	19	2.26	102	5.61	184	6.59
70	10	17	1.30	104	5.05	163	9.67
70	20	17	1.63	100	6.54	179	10.12
80	10	18	2.28	98	6.21	164	11.85
80	20	19	2.77	101	6.45	192	9.46
Average		18	2.05	101	5.97	176	9.54

Table 3-12 shows that from the properties of the samples, the three test regions can be defined by the regions by taking the highest mean of each region rounded to the nearest 10 and standard deviation taken as an 1:2:3 ratio based off a background standard deviation of 3 (rounded up to increase the possible overlap between background and bone) (Table 3-13).

Table 3-13 The definition of the three regions by mean and standard deviation of their Gaussian distributions.

Region 0		Region 1		Region 2	
Mean	SD	Mean	SD	Mean	SD
20	3.00	100	6.00	190	9.00

The regions that are just defined by the Gaussian distributions do not take into account either blurring or partial filled voxels (Section 1.3.5.2) which are a cause of error. To model the blurring and partial filled voxels the images will be averaged, using both a radius of two and three pixels, this is because it needs to take into account three dimensional boundaries between the regions and not just pixels which are defined as a

50:50 mix of two regions (Figure 3-19).

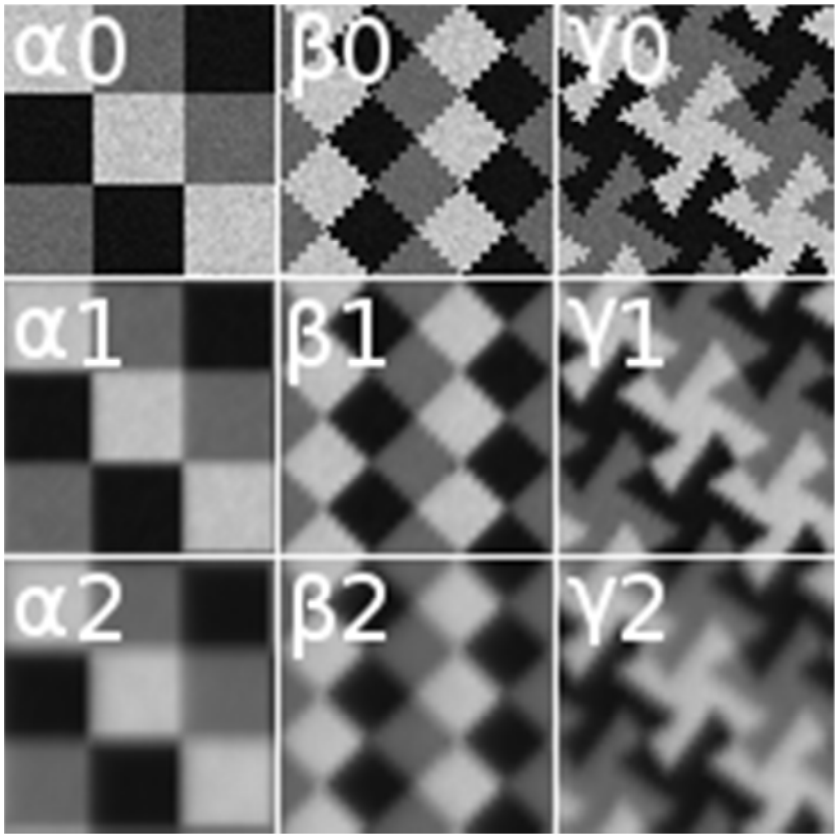

Figure 3-19 The Nine objective test images based of the shapes in Figure 3-17 sets of (A, D & G), (B, E & H & (C, F & I))with the region pixel distributions as defined in Table 3-13, with no averaging, radius of 2 averaging & radius of 3 averaging (A, B & C), (D, E & F) & (G, H & I) respectively.

The different pixel distributions are defined as 0, 1 & 2 for no averaging, averaging of radius 2 and averaging of radius 3 respectively.

3.3 Determining the Error with a Subjective Reference

When determining the best method and calibrations for the sample sets (Section 6.1), the reference images used to determine the lowest Mn error cannot be considered as being objectively correct (Figure 3-19). However as there is histology data for some of the Orthotopic set, the Mn values can be correlated to the histology measurements by the RUMA validation method (Equation 1-59) which is used instead of the AMUA validation method (Equation 1-58) as it returns it's error as a percentage and not as an area measurement.

The correlation with the Mn, RUMA errors was used to determine how the sensitivity the Mn validation was compared to the histology; this is covered in Section 6.1.

3.4 Summary of Validation Methods

Because of current limitations in processing power the modified validation method of Mn was determined to be the best validation method to determine both the best segmentation method for the study based on objective test images, which in turn were based on the samples which were investigated. For the samples which have pre-existing histology data the processor intensive methods of RUMA was used to investigate the sensitivity of the Mn and decide upon the best segmentation calibration, for the determined segmentation method.

4 Development of Segmentation methods for bone and Synthetic bone Graft

To determine which segmentation method is best suited to segment out bone, graft and background (which includes resin), the objective test images and the validation method of Mn (Section 3.4) were used.
As the objective test images have sizes of only 60 by 60 pixels an additional 49 equivalent images were created (defined by the same Gaussian distributions), to provide the data for the histograms mentioned in this section.
The methods covered in this section include some currently used methods, some modifications on current methods and some novel methods designed for this study. The criteria for the methods is to fully segment the images, with every pixel being defined as one of the three regions, based on the properties of the pixels and not on the relative position of the pixels (e.g. not using an edge defining method and then filling in the regions). The test images are only two dimensional, and as such, explanations on how to modify the methods to work in three dimensions will be described when necessary. For this section, both pixels and voxels will be referred to as voxels as they are treated in the same way.

4.1 Methods and Segmentation Techniques

4.1.1 Global Thresholds

The method of using a single set of thresholds and just the intensity of the voxels to define the regions across an entire sample is referred to as using a global threshold. As there are three regions to define, the threshold will have two threshold values relating to the two boundaries. The values for these thresholds can be determined by inspection of the histogram of the sample or by finding the thresholds which result in the lowest error if a reference is available.
As the test images are all eight bit images there are 256 possible threshold values, for each of the thresholds.

4.1.1.1 Histogram Inspection

From the histogram, the locations where the thresholds need to be positioned can be

determined via either the identification of the point of lowest frequency between the peaks of the regions, or by taking the middle point between the peaks, as described in Section 1.4.1.1.

4.1.1.2 Brute Force

Because of the “low” number of possible threshold values (As the second threshold value is less than or equal to the first threshold value, the total number of combinations is: $\sum_{n=1}^{256} n = 32{,}896$) it is possible for each of the combinations to be attempted and the errors recorded. This will be carried out in the same way as stated in Section 1.4.1.1, as the test images were procedurally generated from the reference images, it can be assumed that there is no error in the reference image.

4.1.2 Local Thresholds

The properties of the local voxels surrounding the voxel of interest can be used to define the segmentation regions. To utilise the advantage of the local properties, two local properties will be used in tandem to define the segmented regions.
As the histograms for local thresholds need to consider two local properties, they have to be displayed in three dimensions (tri-histogram) also meaning there is not a simple automated way to define where the threshold values should be positioned (such as defining the peaks in the two dimensional histogram). While the peaks could be defined in the axis of the two variables this would result in six regions, which would require further processing, as such a set of novel ways to define the “threshold” regions on the histograms were developed.

4.1.2.1 Histogram Overlays

The properties of the local area (which is defined as a three by three square of voxels in 2 dimensions and a three by three by three voxel cube in three dimensions) that were considered are (and their reference letters):

- Intensity (A) (Which is simply the intensity of the voxel of interest)
- Mean (B)
- Highest Value (C)
- Lowest Value (D)

- Range between the highest and lowest Value (E)
- Standard deviation (F)

For the tri-histograms, one variable will be assigned to each of the axis e.g. AB would be Intensity on the X-axis and Mean on the Y-axis (Using the objective test image of α-0 as an example shown in Figure 4-1). The histograms are displayed looking down the Z axis with the intensity of the pixels in the histogram at each point being defined by the frequency (number of voxels with corresponding values) value (V) of the histogram at that point and the total number of voxels (T) in the sample as shown in Equation 4-1.

Equation 4-1

$$P_v = 25\, log_{10}\, \mathbb{Z}\left(1 + 256^2 \frac{1000V}{T}\right)$$

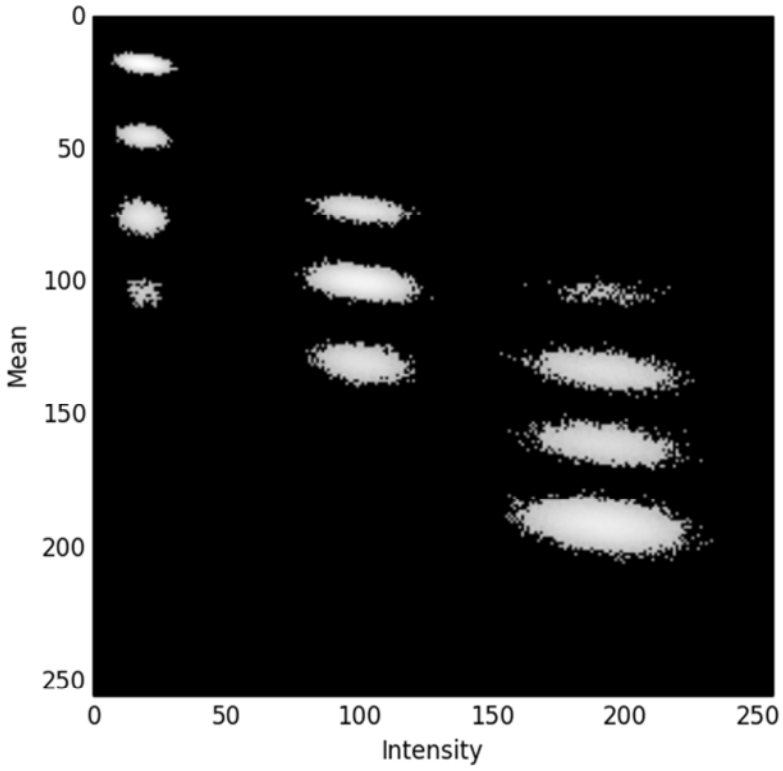

Figure 4-1 The Intensity/mean histogram (AB) for the sample image α-0.

4.1.2.2 Expanded Overlays

From the three dimensional histogram a "map" can be created to assign each of the sets of properties (as defined by the axis of the histogram) to one of the three regions. The maps can be created by identifying regions from the reference images of the objective test images, this is performed by taking the colour of the pixel in the reference image (Figure 3-17) and position of the equivalent pixel from the test image (Figure 3-19).

The example colour map of the test image of α-0 for local properties of AB can be seen in Figure 4-2, while the complete possible set of combinations of the local properties is shown in Figure 4-3.To complete fill the maps, the regions are. The expansion of the regions can occur in one of the axis of the histograms then in axis once it is fully expanded or by expansion in both axes at once.

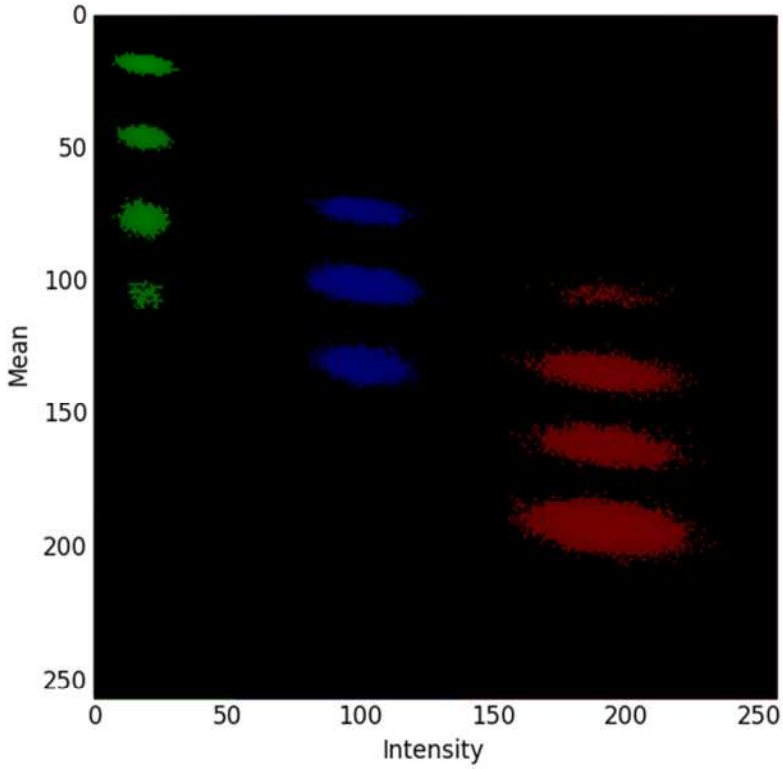

Figure 4-2 The Intensity/mean histogram (AB) map for the sample image α-0 with colours determined from the reference images.

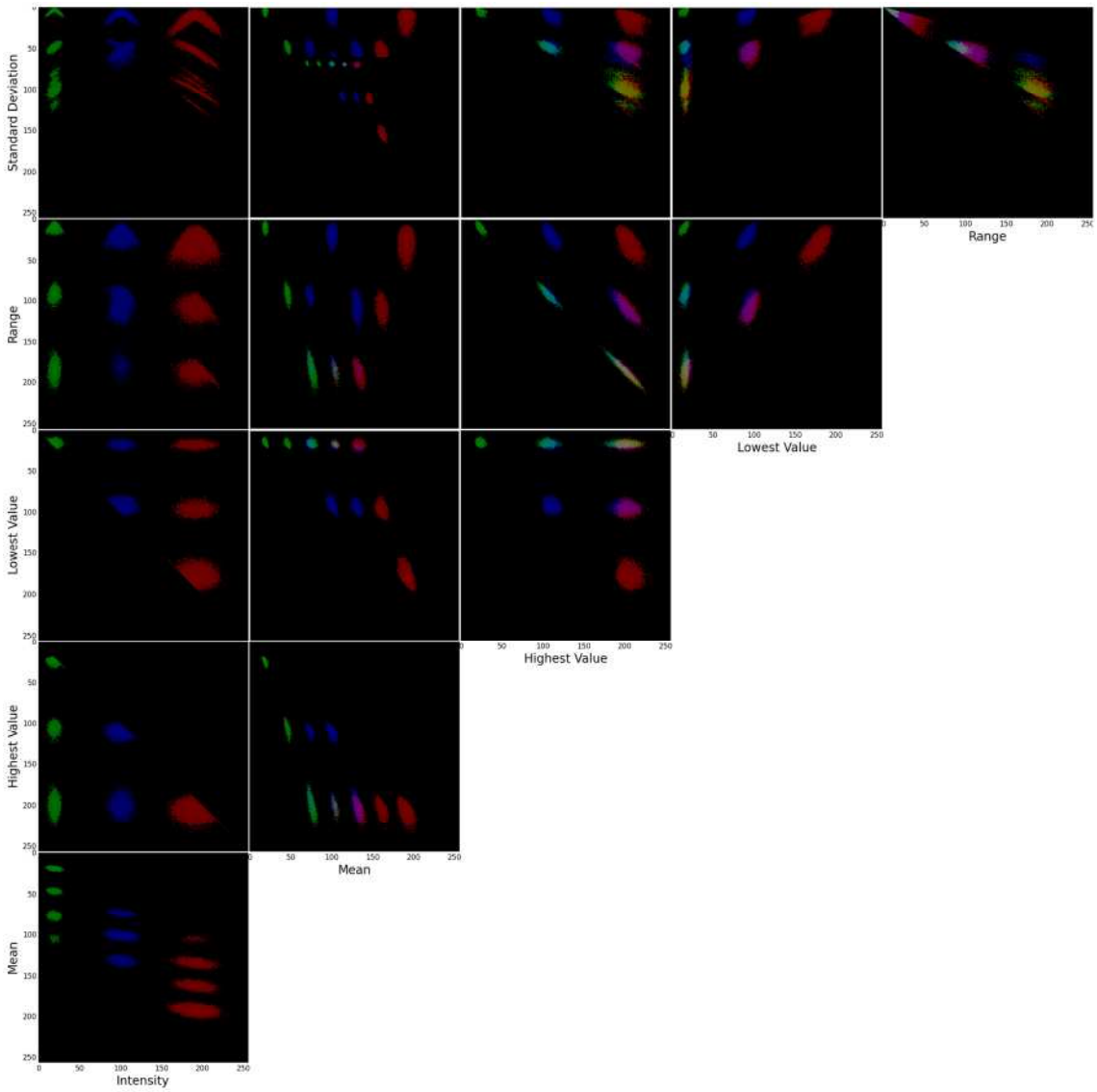

Figure 4-3 The possible histogram maps determined from the possible local variables of Intensity Mean, Highest Value, Lowest Value, Range, Standard Deviation for the sample image α-0 with colours determined from the reference images.

The expansions are formed based on the following rules:

- Only areas on the histogram which are assigned to a single region are expanded.
- When two expanded regions interact with each other they stop expanding.
- The regions will be expanded until the entire map is defined.

The expanded histogram maps which were considered were:

- Expanded regions in the single X axis of the histogram then by the Y axis (Figure 4-4).

- Expanded regions in the single Y axis of the histogram then by the X axis (Figure 4-5).
- Expanded regions in both X and Y together (Figure 4-6).

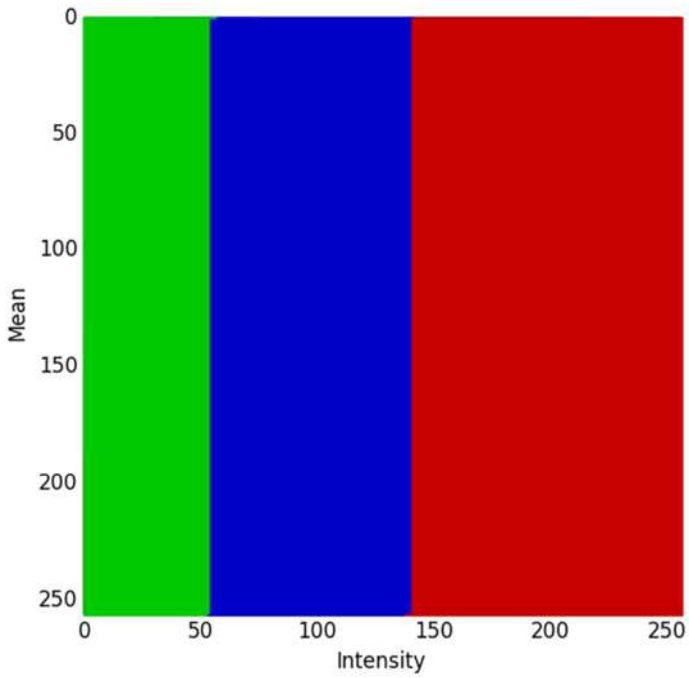

Figure 4-4 The Intensity/mean histogram (AB) map expanded along the X axis for the sample image α-0.

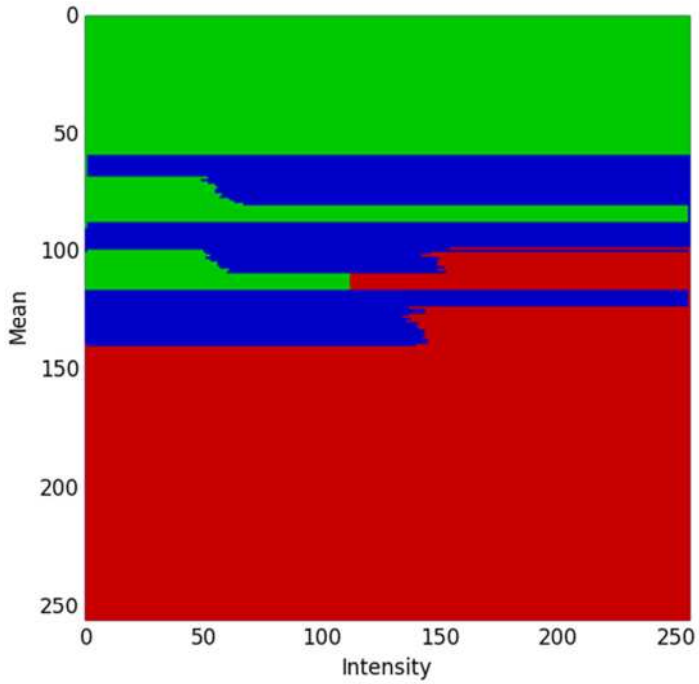

Figure 4-5 The Intensity/mean histogram (AB) map expanded along the Y axis for the sample image α-0.

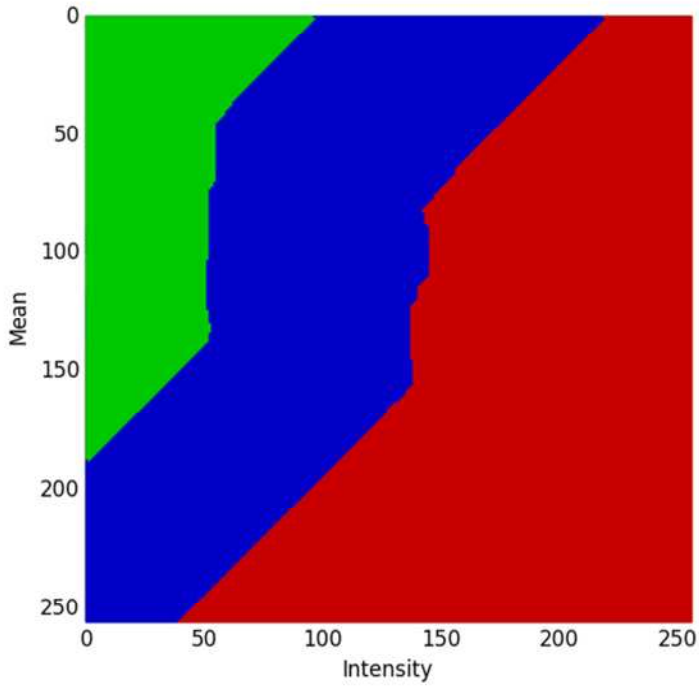

Figure 4-6 The Intensity/mean histogram (AB) map expanded along the both X & Y axis for the sample image α-0.

4.1.2.3 Colour Maps

An equivalent “brute force” method can be applied to the local threshold histogram by

attempted every different possible iteration of an overlay map, which would be three to the power of 256 squared iterations (3^{256^2}), for each map.

As it takes a single processor (of ~3 GHz speed) 0.267 seconds to test a single map the amount of time to try every iteration with the available equipment would be significantly longer than the life expectancy of the author.

As it is not feasible to investigate every interaction of every possible map, a set of overlays were created to mimic the shapes of regions that appear in the histograms. These maps will be referred to as colour maps and they are defined by patterns of changing colours and not by any information from the sample it will be used to segment.

From the histograms it can be seen that the regions are separated by both straight and curved lines. To emulate these different regions and their positions on the colour maps, each of the three colours will go from zero to 255 based off a rule of expansion. At every point on the map the region will be defined by the colour which has the highest intensity that point. The weighting of the intensities can also be modified to shift the position of the region boundaries.

The 16 different patterns that shall be considered in the colour map are listed below (Figure 4-7):

- 0. Horizontal increasing right to left
- 1.Horizontal increasing left to right
- 2.Vertical increasing Bottom to top
- 3.Vertical increasing top to bottom
- 4.Diagonal increasing bottom right to top left
- 5.Diagonal increasing top left to bottom right
- 6.Diagonal increasing top right to bottom left
- 7.Diagonal increasing bottom left to top right
- 8.Circular decrease from left corner
- 9.Circular increase from left corner
- 10.Circular increase from centre
- 11.Circular increase from top centre

- 12.Circular decrease from top centre
- 13.Circular increase from left centre
- 14.Circular decrease from left centre
- 15.Circular decrease from centre

With each colour (Red, Green & Blue) taking a different pattern and no combination of patterns repeating (because the Mn error method does not require region matching repeats) there are 560 possible colour maps.

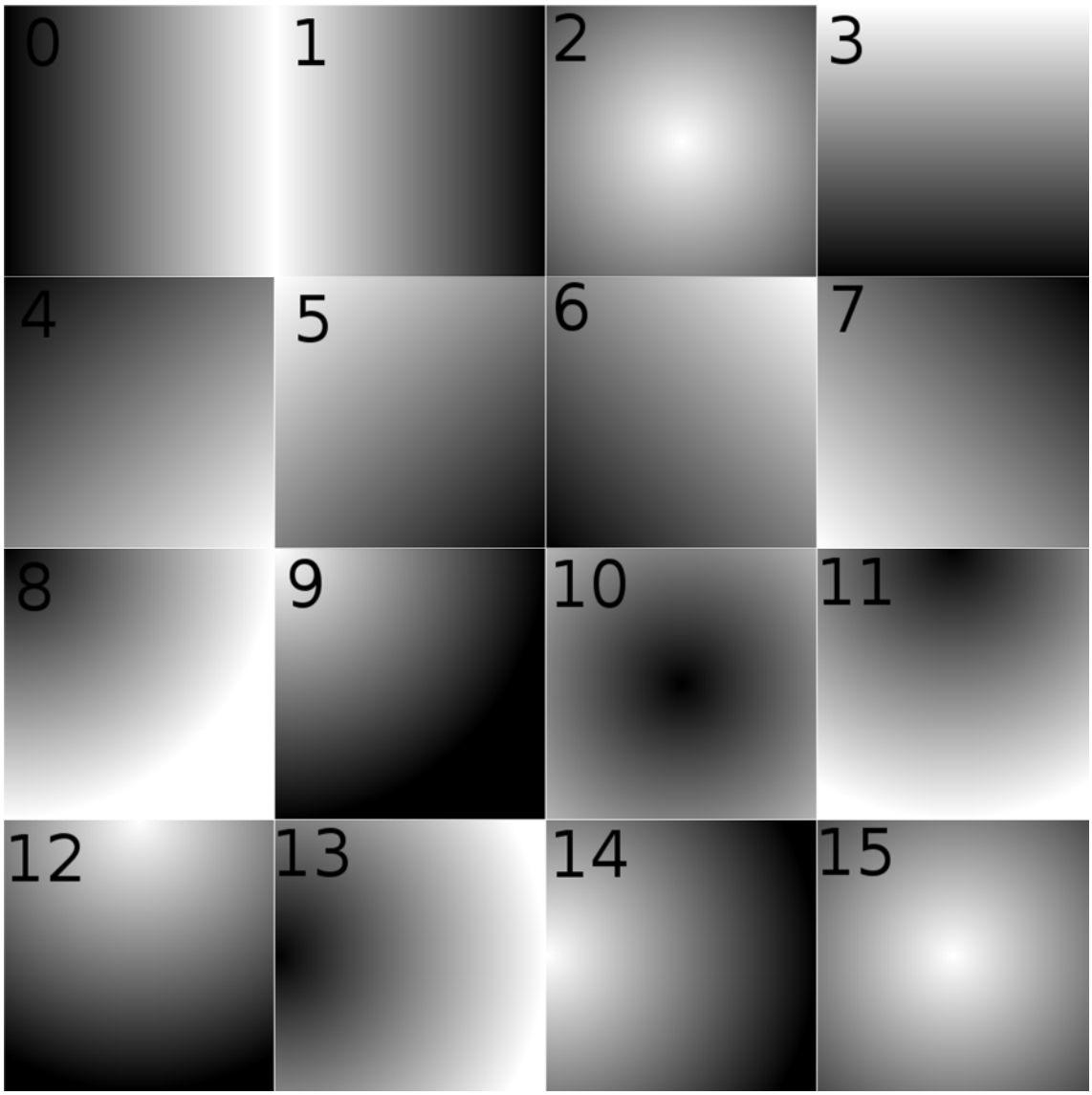

Figure 4-7 Grey scale representations of colour maps defined in Section 4.1.2.3.

Each of the three region can also be weighted, in this case from one to three as shown in Figure 4-8, which increases the number of possible colour maps to 14,000, each of the

maps can be used with each of the local variable pairs, which is ten, twenty if both three and two dimensional scans are considered. This brings the number of iterations to 140,000 for just two dimensional and 280,000 for two and three dimensional scans.

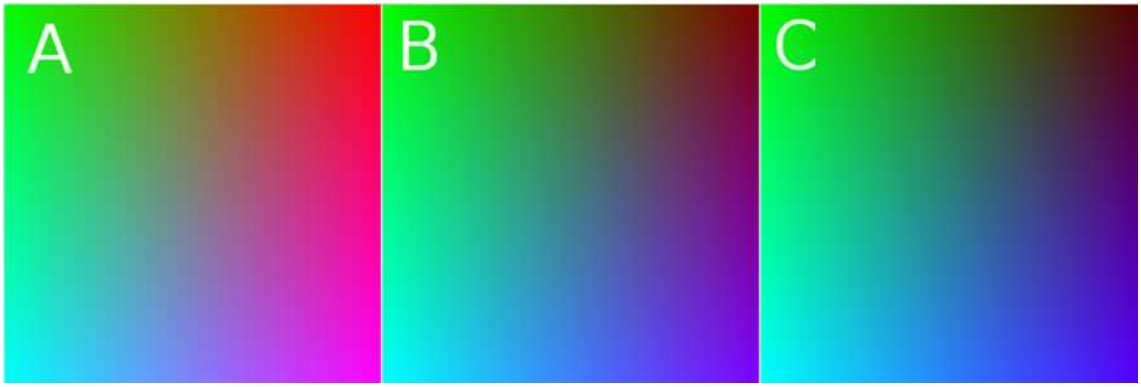

Figure 4-8 Colour maps of 0-1-2 with red weighting of A: 1 (none), B: 2 and C: 3.

More colour maps and weightings can be used with this method, because of the current limitations in hardware, sixteen colour maps and three weights were chosen as they provide a large number of interactions in not an unreasonable amount of processing time (~10 hours on a single CPU, per image, for all two dimensional scans).

4.1.3 Stability Based Segmentation

The change in the local properties in an expanding area can be used to define the region that a voxel inhabits. It is expected that a voxel in a single region will have similar properties to the local area around it until the local area is expanded into another region. This can be measured by tracking the changes in its five local properties as the areas it scans out (square of side 3, square of size 5…) are increased from the voxel of interest, in (Figure 4-9, Figure 4-10 & Figure 4-11).

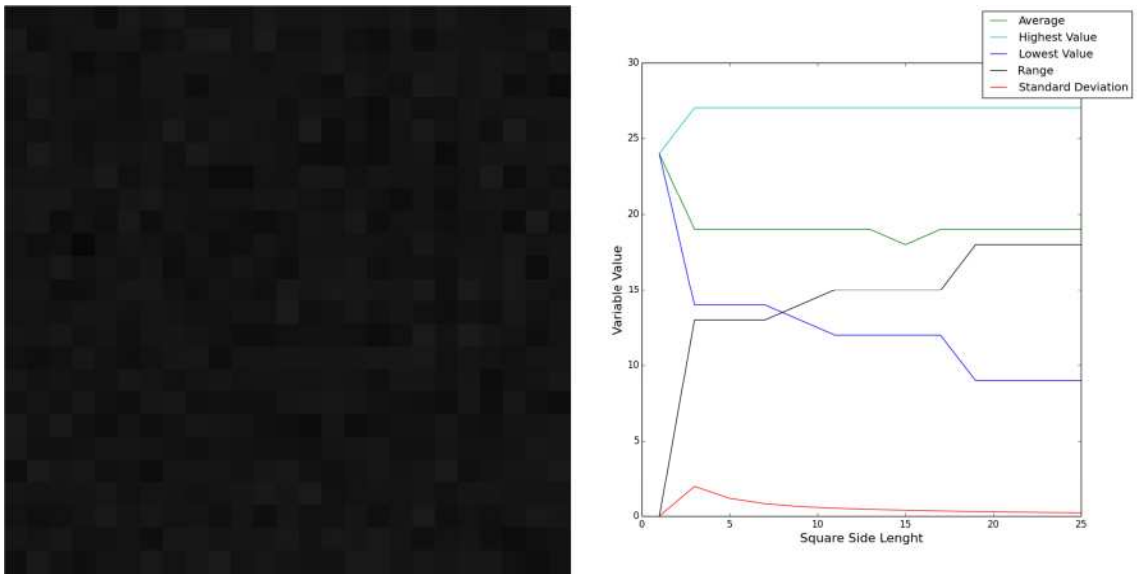

Figure 4-9 Change in local properties of Average, Highest value, Lowest Value, Range and Standard deviation, with increase local area from edge size of 1 to 25 for region 0 as defined in Table 3-13.

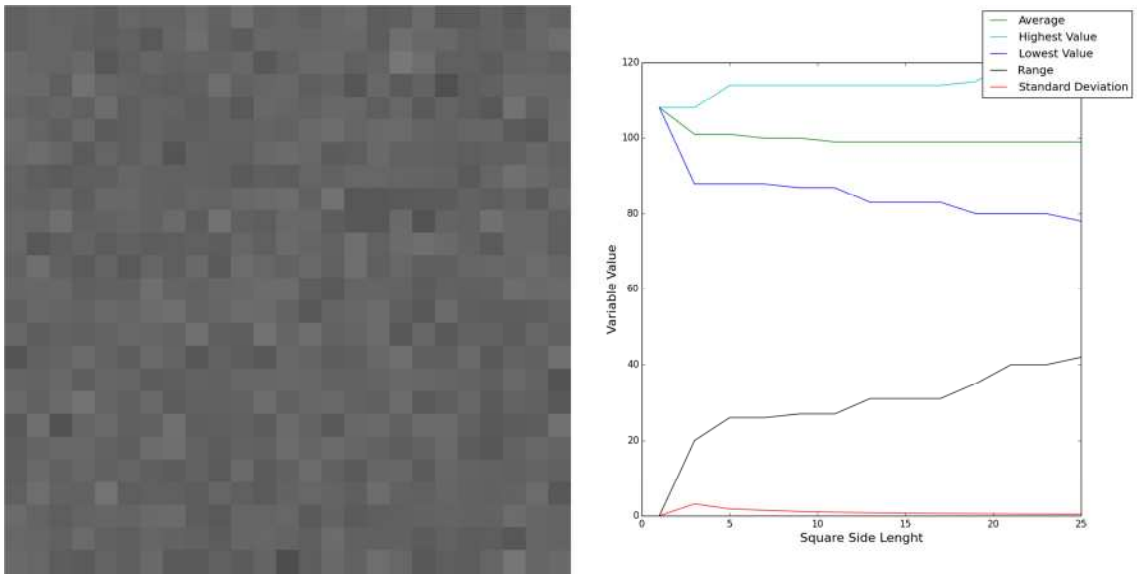

Figure 4-10 Change in local properties of Average, Highest value, Lowest Value, Range and Standard deviation, with increase local area from edge size of 1 to 25 for region 1 as defined in Table 3-13.

.

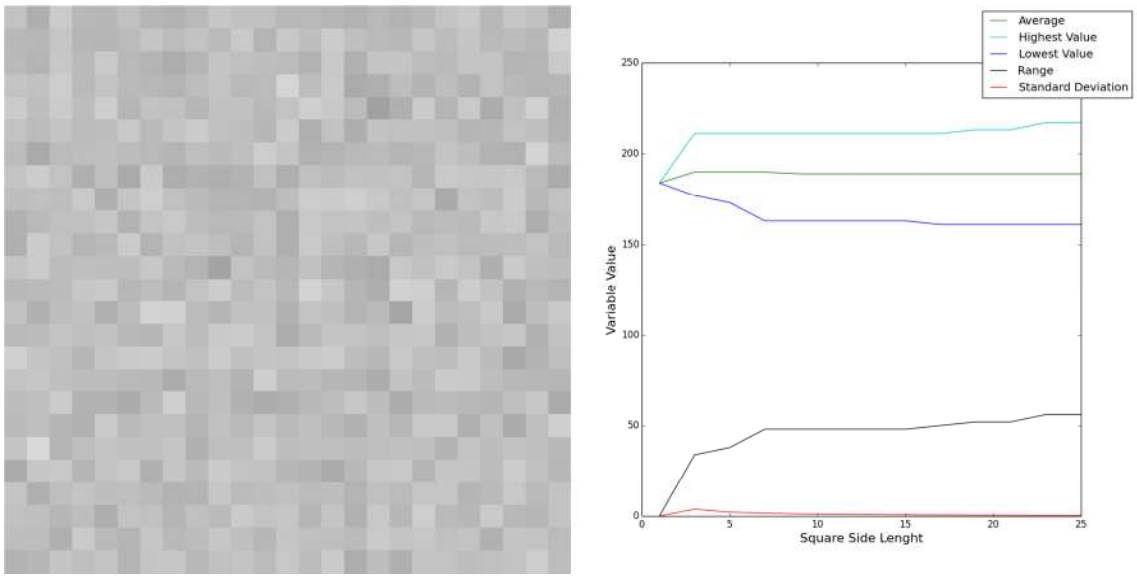

Figure 4-11 Change in local properties of Average, Highest value, Lowest Value, Range and Standard deviation, with increase local area from edge size of 1 to 25 for region 2 as defined in Table 3-13.

Figure 4-9, Figure 4-10 & Figure 4-11 show the change in properties for the three regions (as defined in Table 3-13), in all three regions the average and standard deviation starts to stabilise after the local area is expanded to an area of three and the range and lowest (or highest depending on the intensity of the middle voxel) continues to stabilise as the local area increases, with region 2 stabilising quicker than region 1 which in turn stabilises quicker than region 0.

The average of the regions all converge to the average of the Gaussian distribution which was used to create the regions, (20, 100 and 190 respectively).

If the voxel is at the edge of two regions the change in properties with expanding local region will be different to an expanding area within a single region (Figure 4-12, Figure 4-13, Figure 4-14 & Figure 4-15).

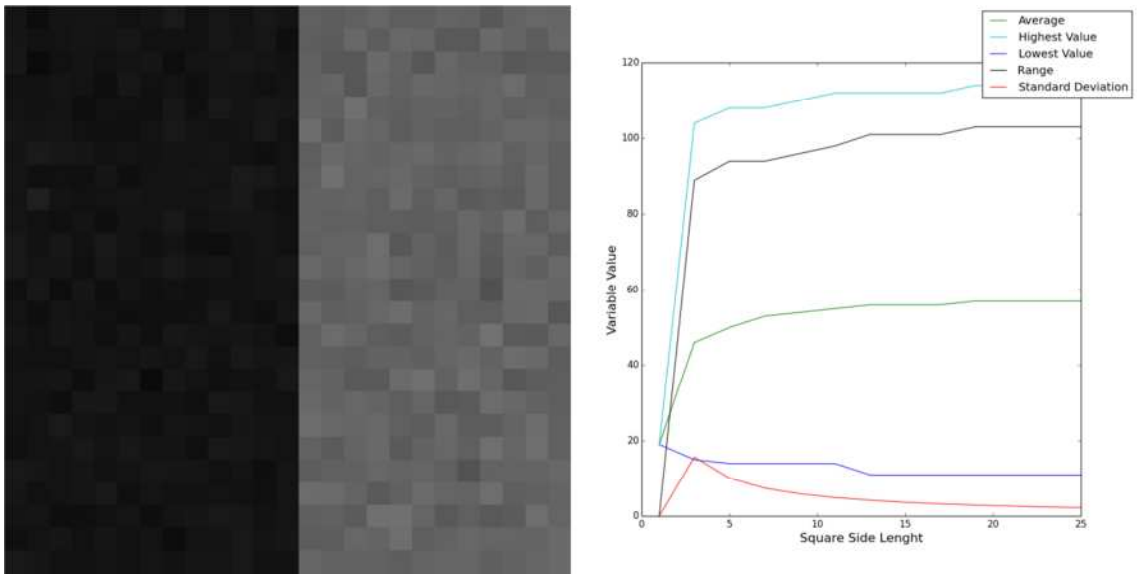

Figure 4-12 Change in local properties of Average, Highest value, Lowest Value, Range and Standard deviation, with increase local area from edge size of 1 to 25 for a voxel at an interface parallel to the Y-axis between region 0 & 1 as defined in Table 3-13, centred on region 0.

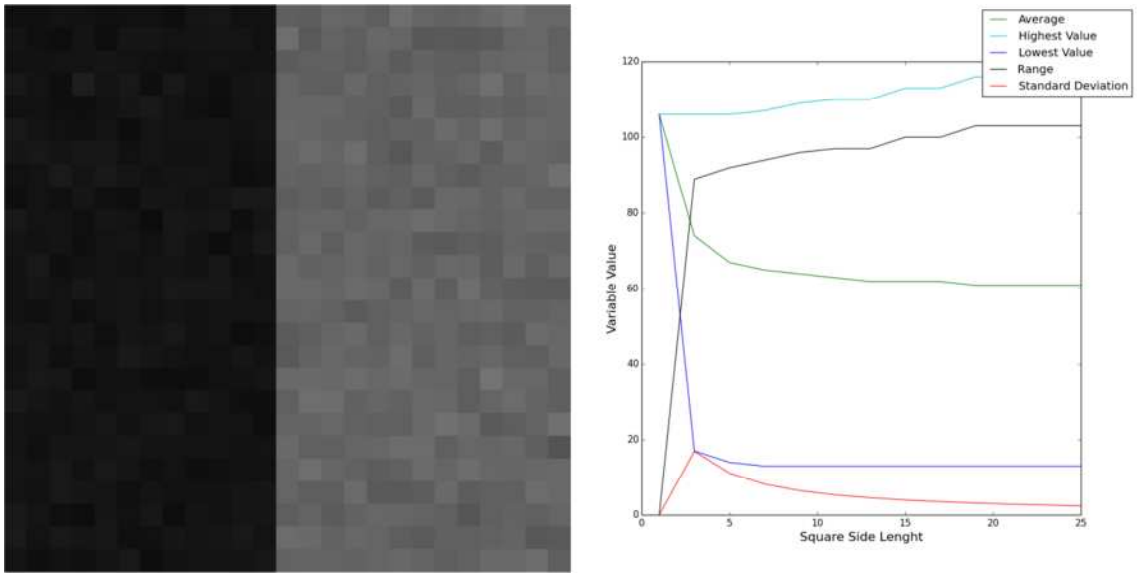

Figure 4-13 Change in local properties of Average, Highest value, Lowest Value, Range and Standard deviation, with increase local area from edge size of 1 to 25 for a voxel at an interface parallel to the Y-axis between region 0 & 1 as defined in Table 3-13, centred on region 1.

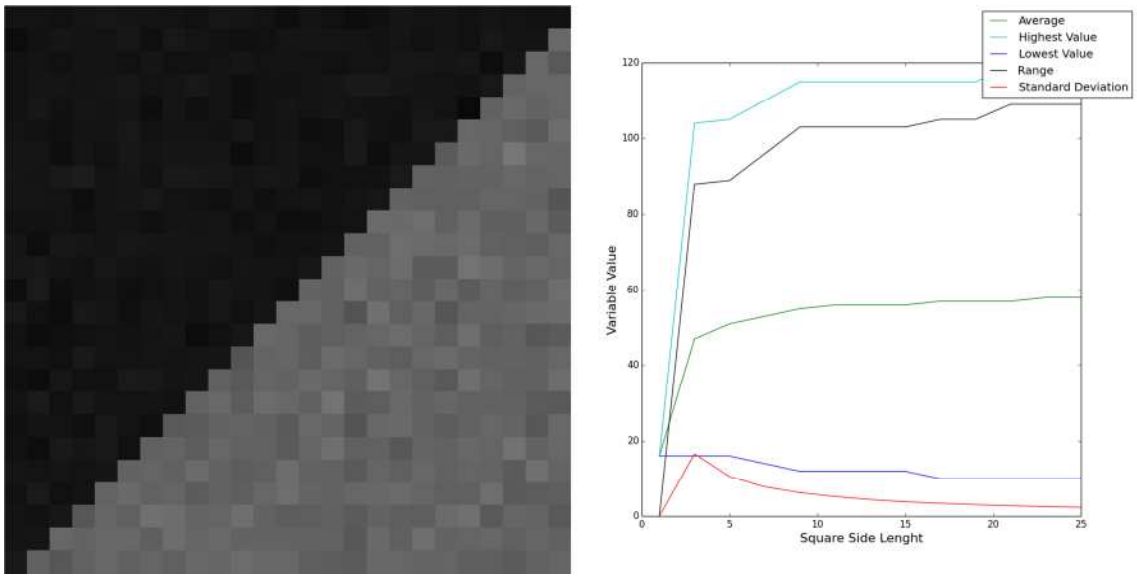

Figure 4-14 Change in local properties of Average, Highest value, Lowest Value, Range and Standard deviation, with increase local area from edge size of 1 to 25 for a voxel at an interface diagonal to the X and Y-axis between region 0 & 1 as defined in Table 3-13, centred on region 0.

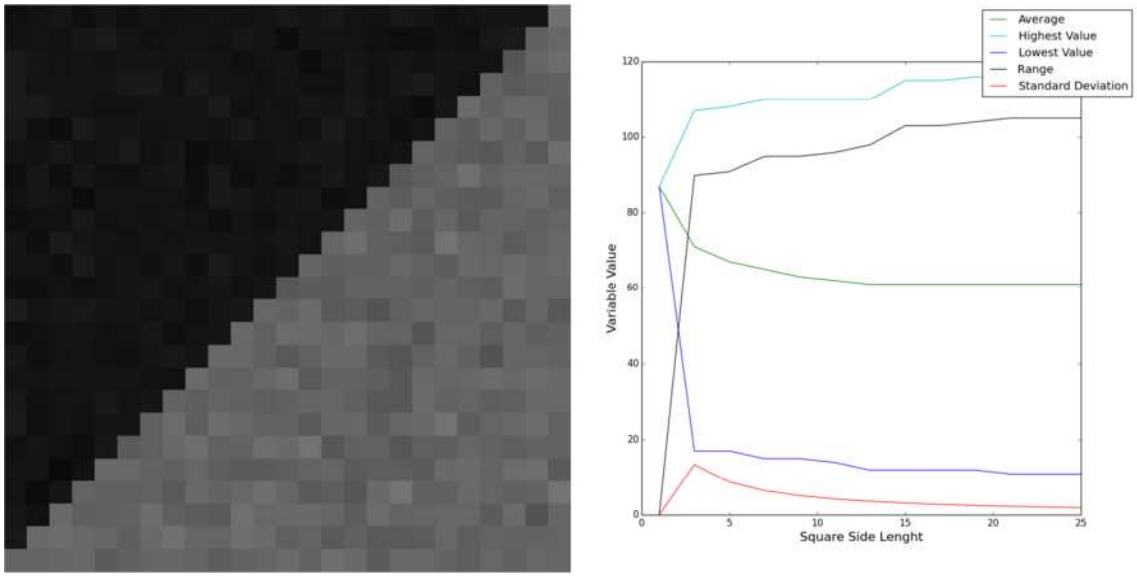

Figure 4-15 Change in local properties of Average, Highest value, Lowest Value, Range and Standard deviation, with increase local area from edge size of 1 to 25 for a voxel at an interface diagonal to the X and Y-axis between region 0& 1 as defined in Table 3-13 centred on region 1.

Figure 4-12, Figure 4-13, Figure 4-14 & Figure 4-15 shows that when the area of increase is centred at the edge of two regions, both the highest and lowest values undergo a change before stabilising with both the range and average stabilising over the expansion of the local area.

If the edge of two regions is an average of two regions the change in properties will not

be the same as when there is a clear edge between the regions (Figure 4-16 & Figure 4-17).

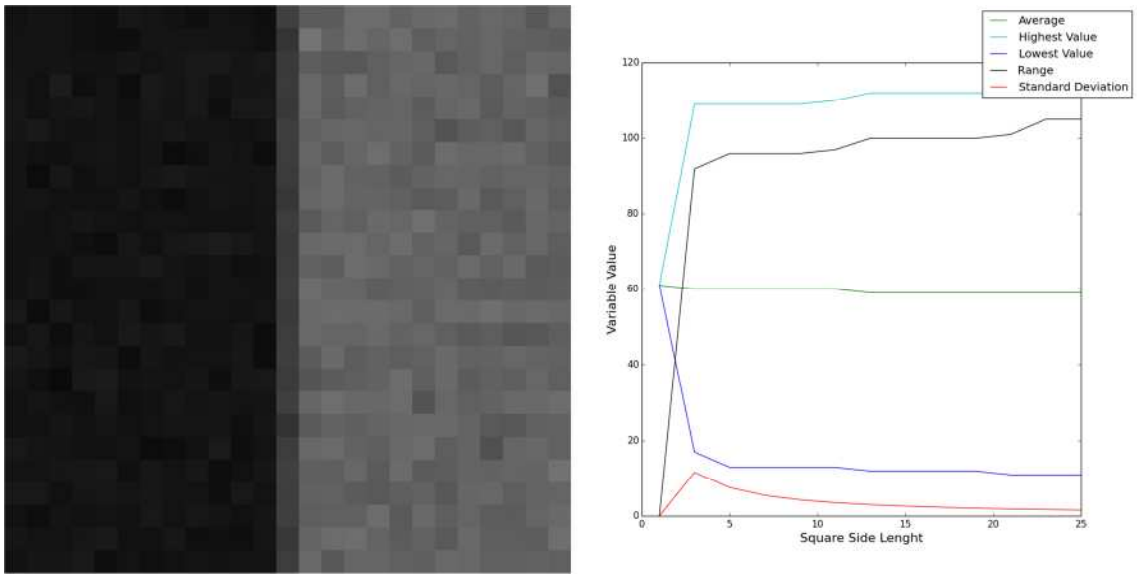

Figure 4-16 Change in local properties of Average, Highest value, Lowest Value, Range and Standard deviation, with increase local area from edge size of 1 to 25 for a voxel at an interface parallel to the Y-axis between region 0 & 1 as defined in Table 3-13, centred on pixel with an average between region 0 and 1.

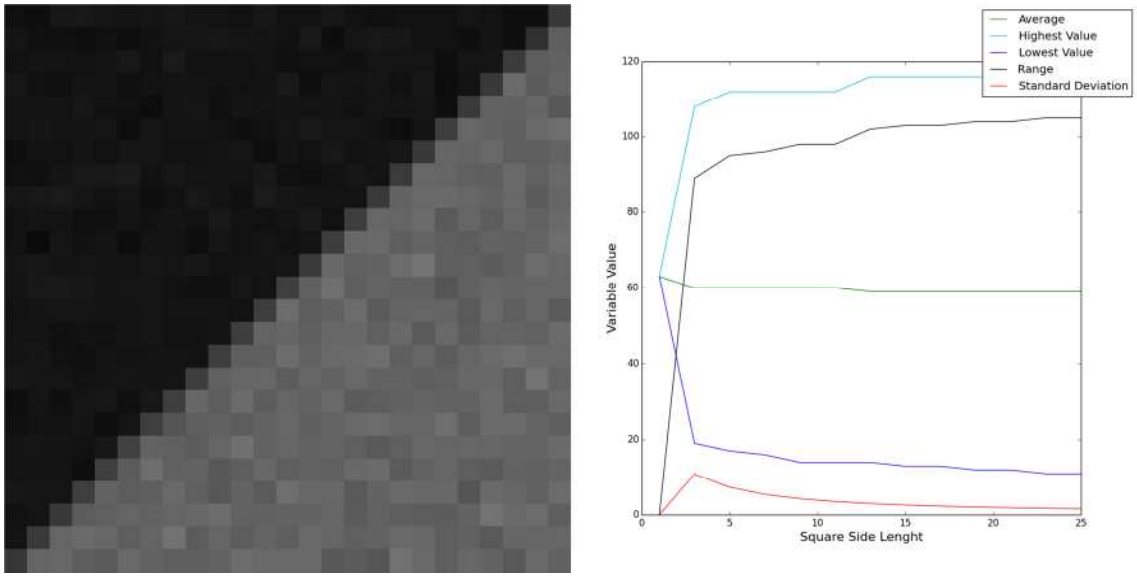

Figure 4-17 Change in local properties of Average, Highest value, Lowest Value, Range and Standard deviation, with increase local area from edge size of 1 to 25 for a voxel at an interface diagonal to the X and Y-axis between region 0 & 1 as defined in Table 3-13, centred on pixel with an average between region 0 and 1.

Figure 4-16 & Figure 4-17 shows that when the voxel in the centre of the local area is on the average boundary between two regions it exhibits the same change in local

properties and stability of said properties as the voxels on edge regions without a sharp change in the average (Figure 4-12, Figure 4-13, Figure 4-14 & Figure 4-15) with the average, lowest value and highest value starting at approximately the average of both the regions.

When the local area expands and interacts with a different region and or the edge region of another region, at different distances from the centre of the local area, the point that the local area expands into the different region can be identified by the change in the properties (Figure 4-18, Figure 4-19, Figure 4-20 & Figure 4-21).

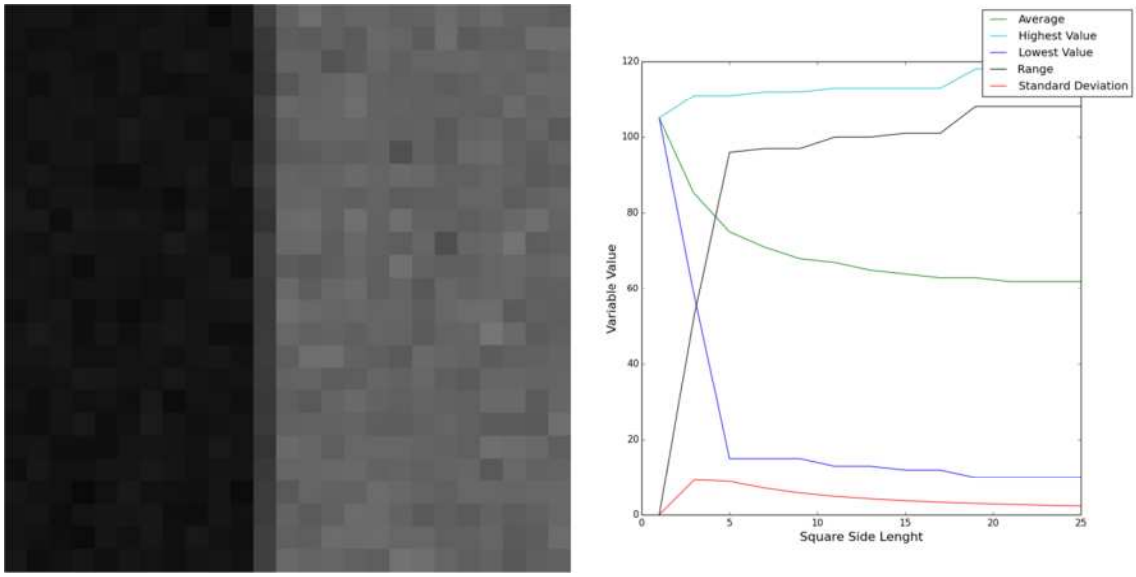

Figure 4-18 Change in local properties of Average, Highest value, Lowest Value, Range and Standard deviation, with increase local area from edge size of 1 to 25 for a voxel at a distance of one pixel from an edge region at an interface of region 0 and 1 parallel to the Y-axis between region 0 & 1 as defined in Table 3-13, centred on pixel in region 1.

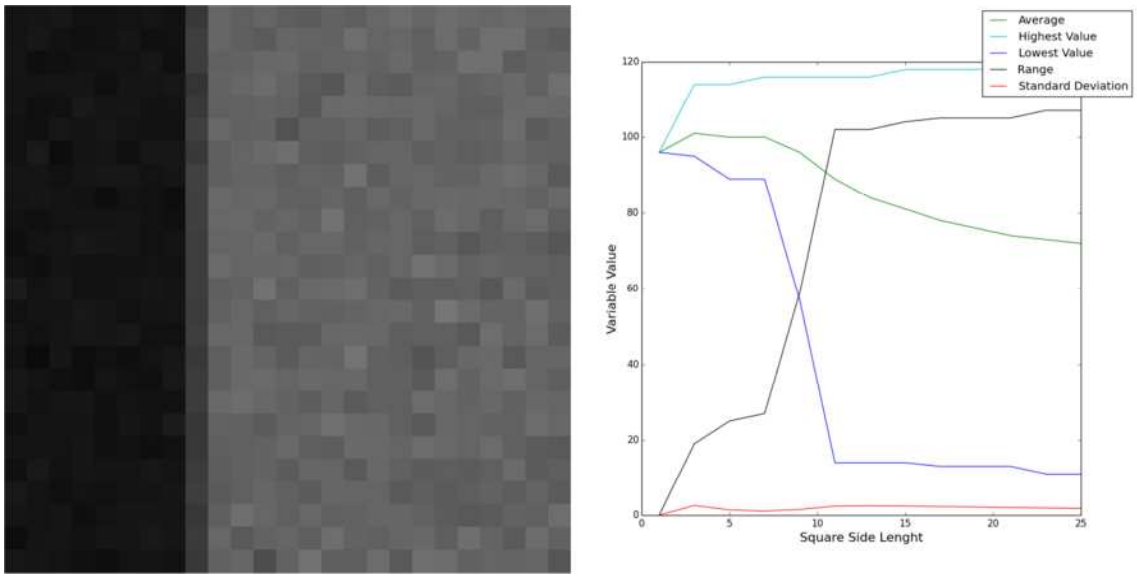

Figure 4-19 Change in local properties of Average, Highest value, Lowest Value, Range and Standard deviation, with increase local area from edge size of 1 to 25 for a voxel at a distance of three pixel from an edge region at an interface of region 0 and 1 parallel to the Y-axis between region 0 & 1 as defined in Table 3-13, centred on pixel in region 1.

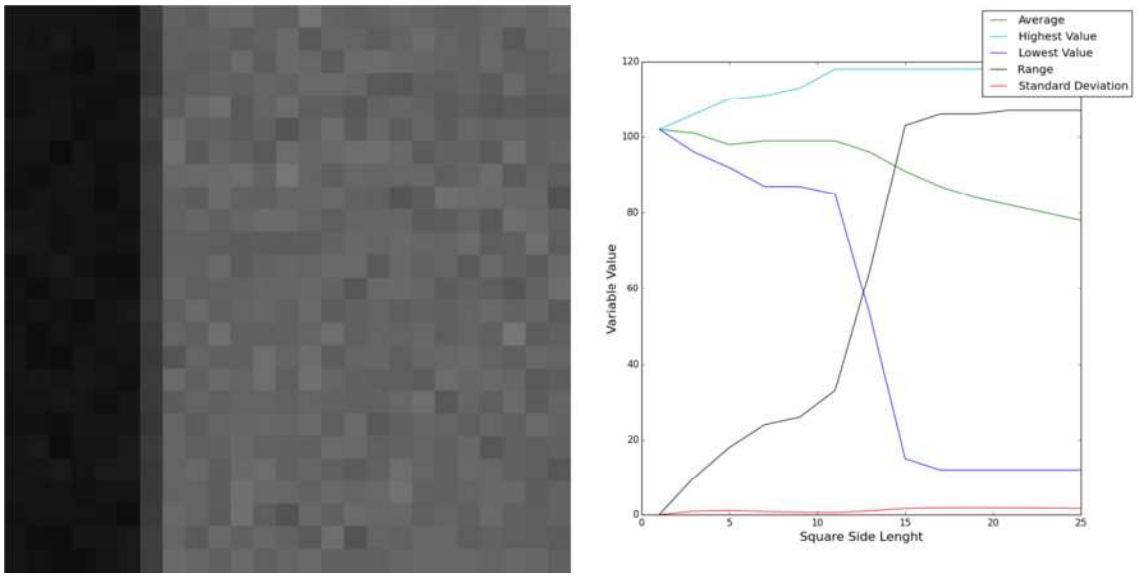

Figure 4-20 Change in local properties of Average, Highest value, Lowest Value, Range and Standard deviation, with increase local area from edge size of 1 to 25 for a voxel at a distance of five pixel from an edge region at an interface of region 0 and 1 parallel to the Y-axis between region 0 & 1 as defined in Table 3-13, centred on pixel in region 1.

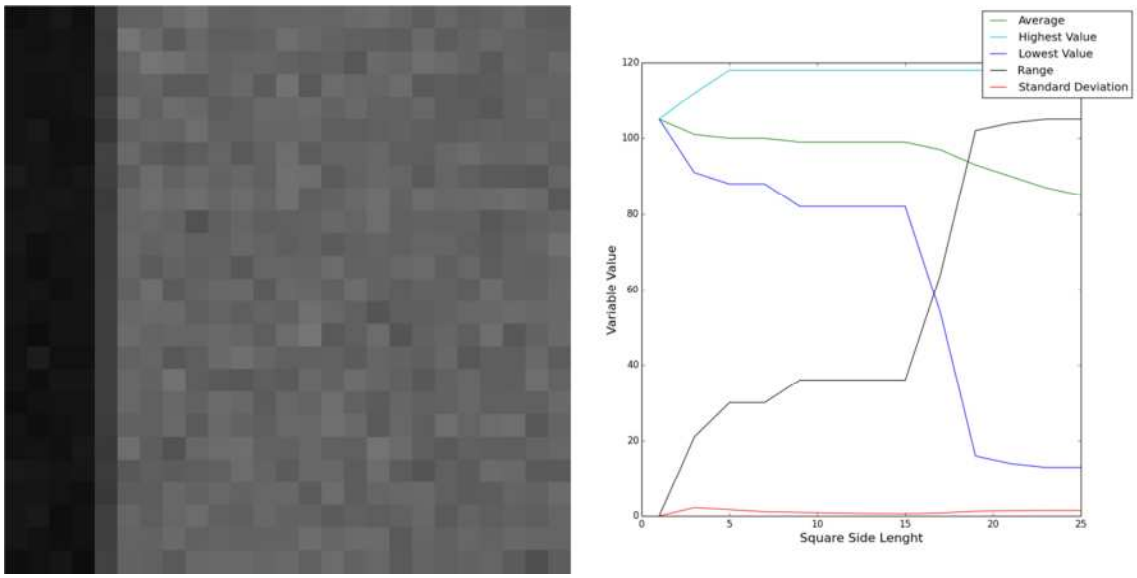

Figure 4-21 Change in local properties of Average, Highest value, Lowest Value, Range and Standard deviation, with increase local area from edge size of 1 to 25 for a voxel at a distance of seven pixel from an edge region at an interface of region 0 and 1 parallel to the Y-axis between region 0 & 1 as defined in Table 3-13, centred on pixel in region 1.

Figure 4-18, Figure 4-19, Figure 4-20 & Figure 4-21 show that as the distance from the voxel in the middle of the local area to the edge of the second region (including an edge region) is increased, the change in region can be seen by a sharp change in the range and lowest value, as well as a slight change in the average. As the change would be seen in the highest value instead of the lowest value, if the voxel in the middle of the local area was in the lower intensity region as shown in Figure 4-22, the range and to some extend the average can be said to denote the interactions between regions.

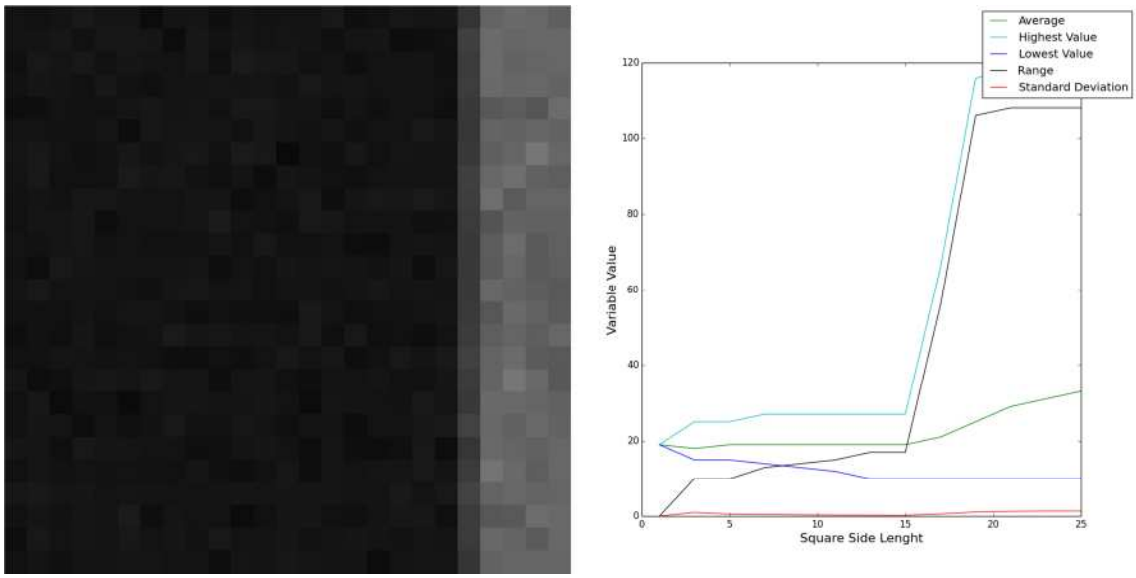

Figure 4-22 Change in local properties of Average, Highest value, Lowest Value, Range and Standard deviation, with increase local area from edge size of 1 to 25 for a voxel at a distance of seven pixel from an edge region at an interface of region 0 and 1 parallel to the Y-axis between region 0 & 1 as defined in Table 3-13, centred on pixel in region 0.

By comparing the range and average at each of the distances between the voxel in the centre of the local area and the edge region, the change in the two properties can be related to the position of the edge (Figure 4-23).

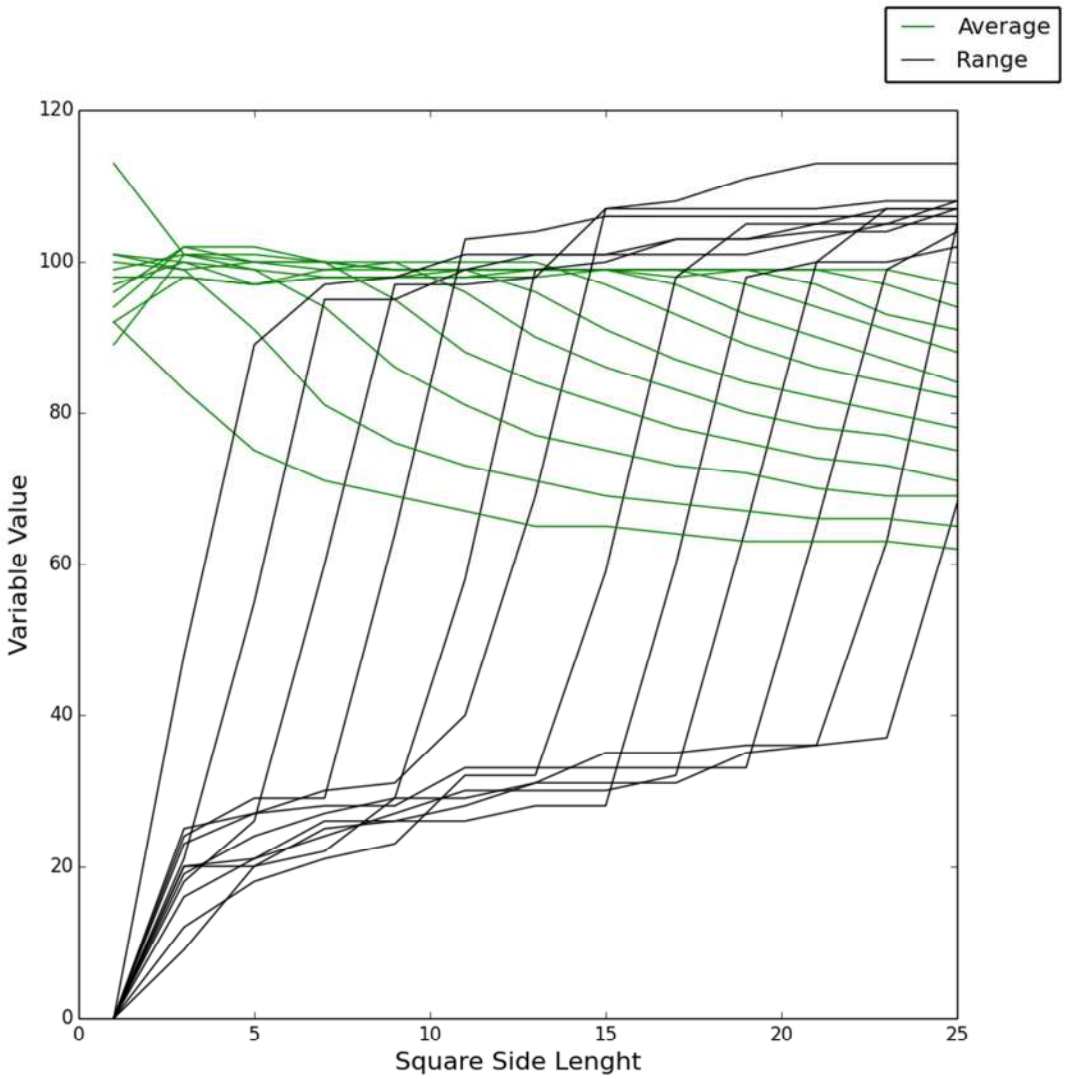

Figure 4-23 Change in local properties of Average and, Range, with increase local area from edge size of 1 to 25 for a voxel at a distances from zero to twelve pixels from an edge region at an interface of region 0 and 1 parallel to the Y-axis between region0 & 1 as defined in Table 3-13, centred on pixel in region 1.

Figure 4-23 shows that the average and range will change with the position of the edge region relative to the voxel in the centre of the local area.

This change in average and range can be confirmed by running ten iterations for each of the distances (Figure 4-24 & Figure 4-25).

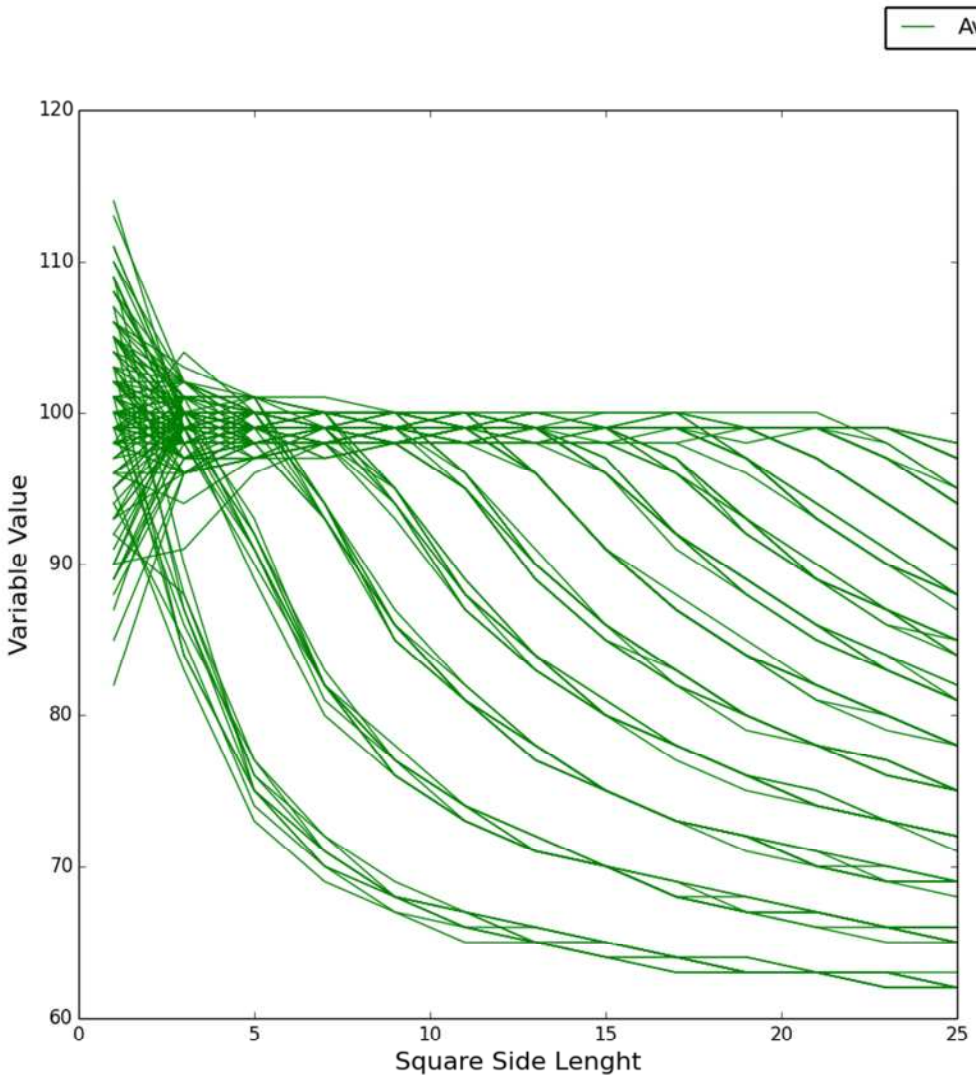

Figure 4-24 Change in local property of Average, with increase local area from edge size of 1 to 25 for a voxel at a distances from zero to twelve pixels from an edge region at an interface of region 0 and 1 parallel to the Y-axis between region 0 & 1 as defined in Table 3-13, centred on pixel in region 1, performed over ten iterations.

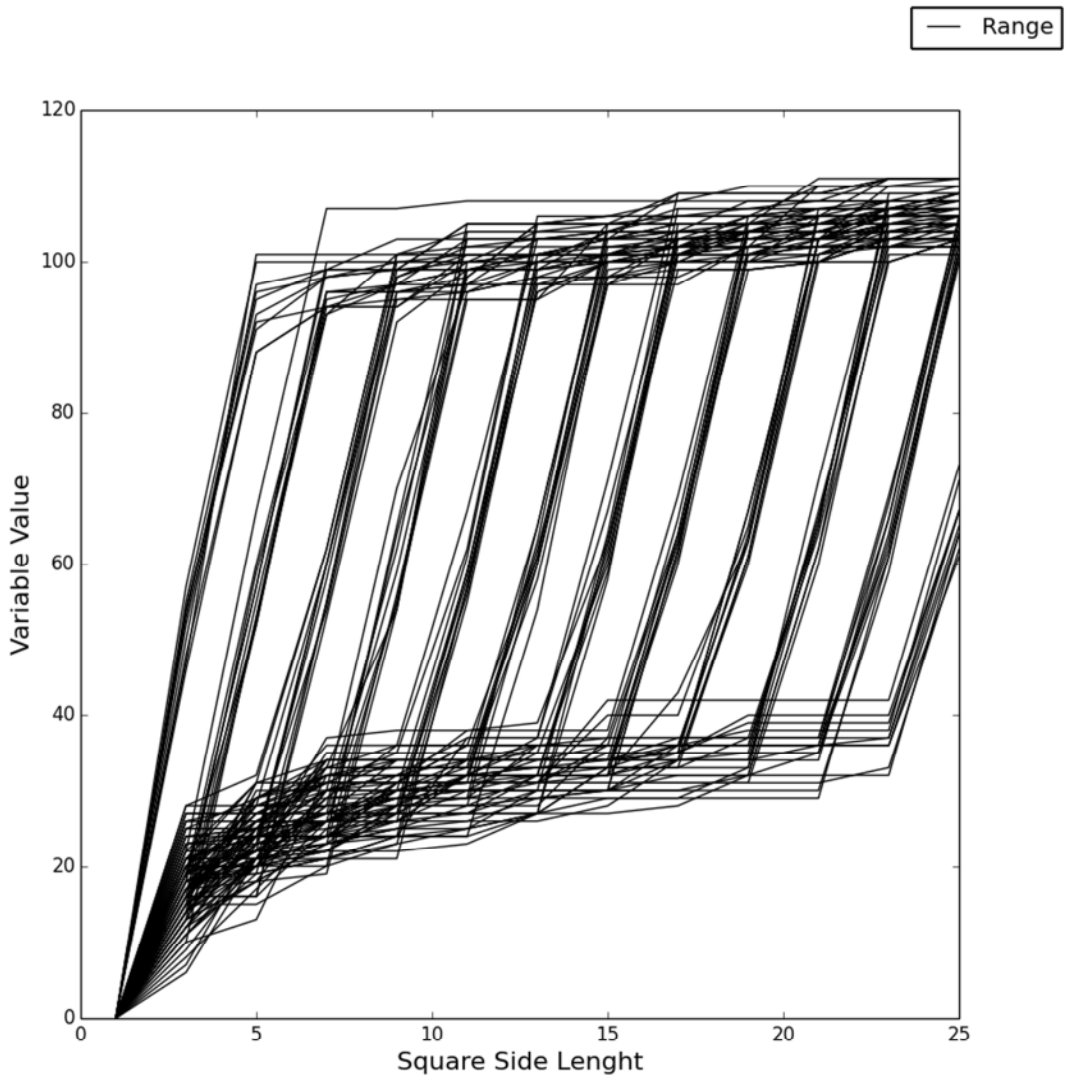

Figure 4-25 Change in local property of Range, with increase local area from edge size of 1 to 25 for a voxel at a distances from zero to twelve pixels from an edge region at an interface of region 0 and 1 parallel to the Y-axis between region 0 & 1 as defined in Table 3-13, centred on pixel in region 1, performed over ten iterations.

Figure 4-24 & Figure 4-25 shows that as the distance between the centre of the local area and the edge can be seen by position of the change in both average and the range, with the range stabilising quicker than the average.

To define the position of the different regions the stability of the local properties with the expanding local area has to be defined, this can be performed by taking the multiplication of the change of range by expansion of local area from three sequential positions to (with each change having one added to it, so that one change of zero does not give an abnormally low value) this value is defined as the stability (Figure 4-26).

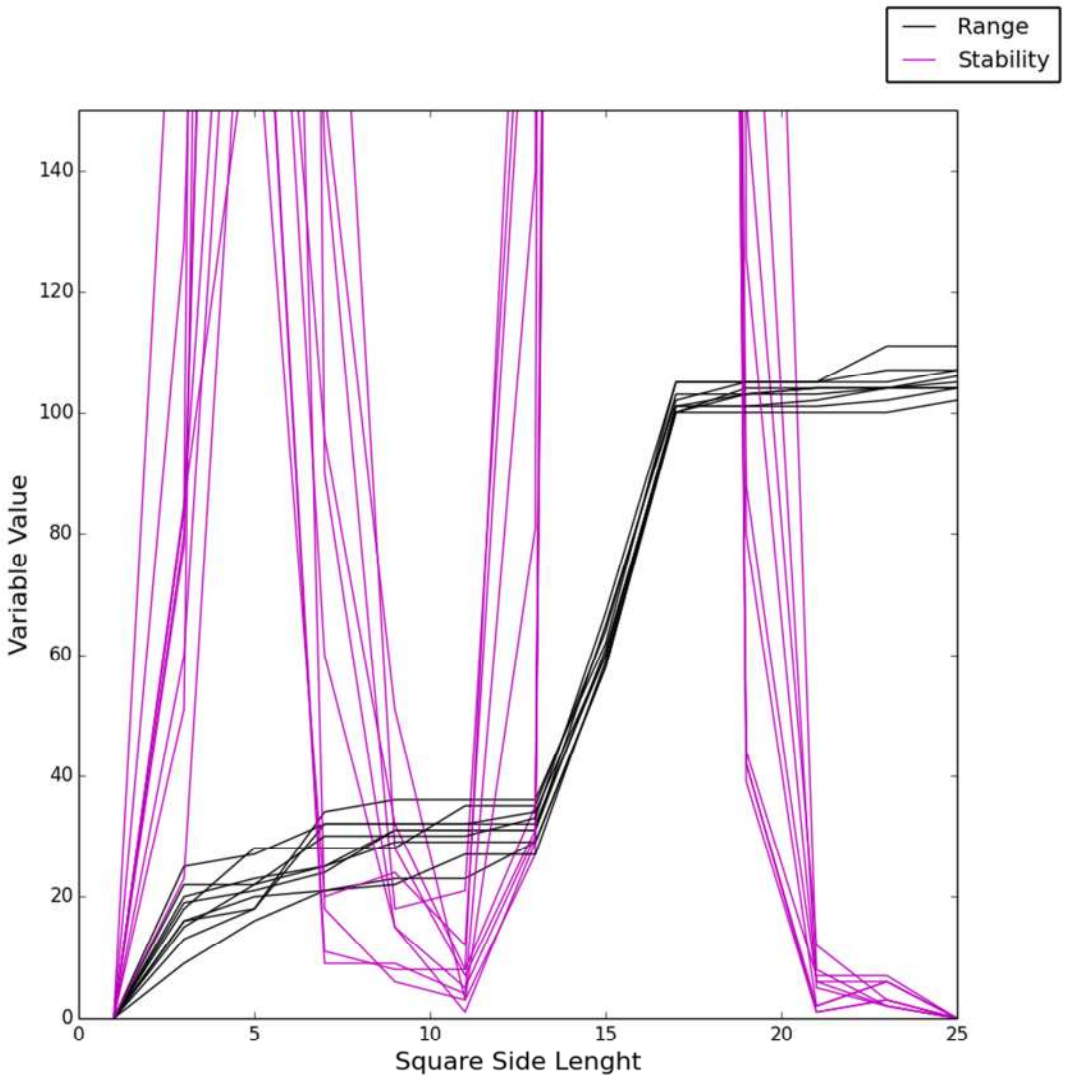

Figure 4-26 Change in local property of Range and stability, with increase local area from edge size of 1 to 25 for a voxel at a distances of seven pixels from an edge region at an interface of region 0 and 1 parallel to the Y-axis between region 0 & 1 as defined in Table 3-13, centred on pixel in region 1, performed over ten iterations.

Figure 4-26 shows that the stability measurement of the range decreases when the range plateaus, where a value of equal than or less than twenty can be taken as a value to define stability. At the first point of stability the average (A_s), highest value (H_s) and lowest (L_s) are collected and used with the value of the voxel in the centre of the local area (O_v) to define the meta-stable values as defined in Equation 4-2 & Equation 4-3.

Equation 4-2

$$M_{s0} = \frac{100(A_s)}{H_s + 1}$$

Equation 4-3

$$M_{s1} = \frac{100(A_s - L_s)}{(H_s - L_s) + 1}$$

The meta-stable values will return the relationship between the average and the highest value in the local area, with M_{s1} taking into account, the lowest value as well.
The meta-stable values are compared to the intensity of the voxel in the centre of the local area to give a comparative value of the original voxel and the region it is in, shown in Equation 4-4 & Equation 4-5.

Equation 4-4

$$V_0 = \frac{100(O_v)}{M_{s0} + 1}$$

Equation 4-5

$$V_1 = \frac{100(O_v)}{M_{s1} + 1}$$

The average at the stable value as well as the V_0 or V_1 values can be used to segment the three regions. Using a threshold value of the stable average to determine that the voxel is in region 0 if it is below and either region 1 or 2 if it is above. With another threshold based on either V_0 or V_1 value to determine if the region is 1 or 2. An example of the stable regions for sample α-0 can be seen in Figure 4-27 & Figure 4-28.

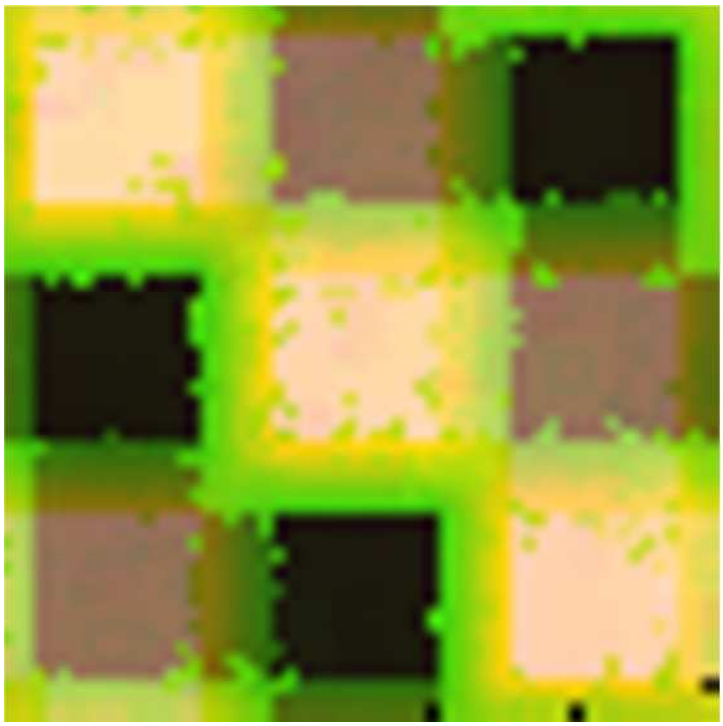

Figure 4-27 The average (Red), highest value (Green) and lowest value (Blue) of the stable regions from image α-0.

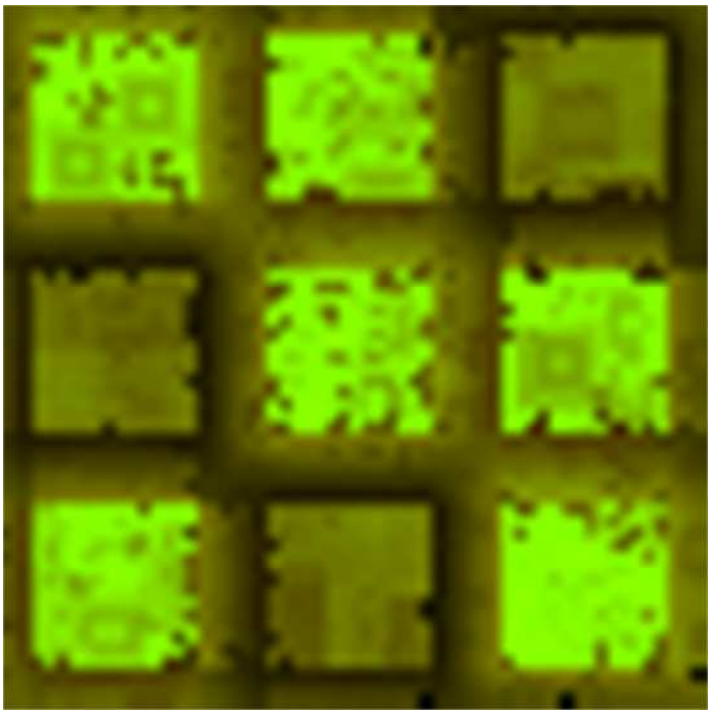

Figure 4-28 The V_0 (Red), and V_1 (Green) of the stable regions from image α-0.

4.2 Segmentation Validation Results

For each of the methods the Mn errors are collected and their related best calibrations if applicable are determined.

4.2.1 Global Thresholds

4.2.1.1 Lower Point

In the lower point segmentation method the turning points of the histograms of the samples are used to determine their thresholds values (Table 4-1).

Table 4-1 The Mn errors and binary threshold values as defined by lowest turning points histogram of the sample images.

Distributions	Shape	Mn Error	Thresholds	
0	α	0.00	54	139
	β	0.00	54	139
	γ	0.00	54	139
1	α	0.05	60	139
	β	0.10	73	159
	γ	0.12	56	130
2	α	0.11	49	130
	β	0.18	58	157
	γ	0.17	75	136

Table 4-1 shows that the error increases with the increased blurring in the distributions as well as the complexity of the shapes of the regions within each of the distributions (though lower error in β-2 than γ-2), the resultant segmentations can be seen in Figure 4-29.

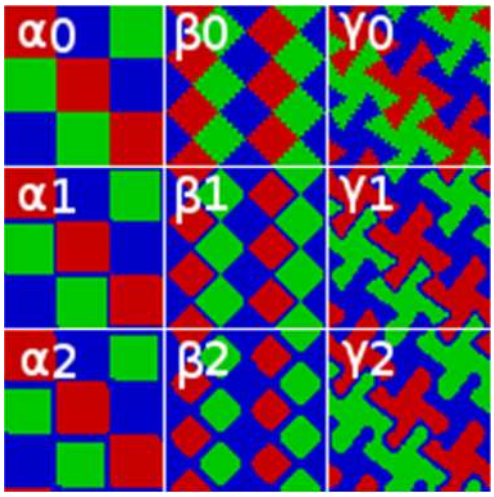

Figure 4-29 The segmentations determined by the lowest turning points in the histogram of the test samples.

4.2.1.2 Peak

In the peak segmentation method the peaks of the histograms of the samples are first determined with the thresholds being defined as between the peaks (Table 4-2).

Table 4-2 The position of the peaks in the histogram of the sample images.

Distributions	Shape	Peaks		
0	α	19	100	191
	β	19	102	191
	γ	18	101	190
1	α	19	100	190
	β	18	99	190
	γ	19	100	188
2	α	18	100	190
	β	19	99	188
	γ	26	109	175

From the peaks shown in Table 4-2 the threshold values can be calculated as being the points between the peaks (Table 4-3).

Table 4-3 The Mn errors and threshold values as defined by peaks of the histogram of the sample images.

Distributions	Shape	Mn Error	Thresholds	
0	α	0.00	60	146
	β	0.00	61	147
	γ	0.00	60	146
1	α	0.05	60	145
	β	0.09	59	145
	γ	0.12	60	144
2	α	0.09	59	145
	β	0.14	59	144
	γ	0.17	68	142

Table 4-3 shows that as in the lower point method the error increases with the increased blurring in the distributions as well as the complexity of the shapes of the regions within each of the distributions, the resultant segmentations can be seen in Figure 4-30.

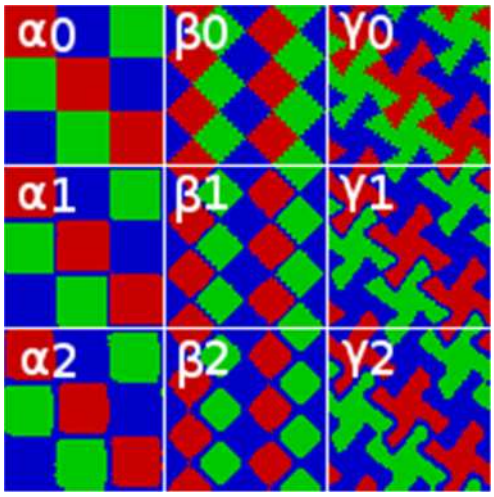

Figure 4-30 The lowest error segmentations determined by the peak points in the histogram of the test samples.

4.2.1.3 Brute Force

The errors for all of the 32,896 iterations of possible threshold values for a double global threshold were collected for the test images as show in Table 4-4.

Table 4-4 The lowest Mn errors as defined by brute force method of testing every possible thresholds and their related thresholds.

Distributions	Shape	Mn Error	Thresholds	
0	α	0.00	29	119
	β	0.00	28	118
	γ	0.00	29	120
1	α	0.05	69	123
	β	0.07	67	132
	γ	0.11	72	134
2	α	0.07	57	138
	β	0.10	73	141
	γ	0.15	67	131

Table 4-4 shows that as in the other global threshold techniques the error increases with the increased blurring in the distributions as well as the complexity of the shapes of the regions within each of the distributions, the resultant segmentations which relate to the lowest error for each test image can be seen in Figure 4-31.

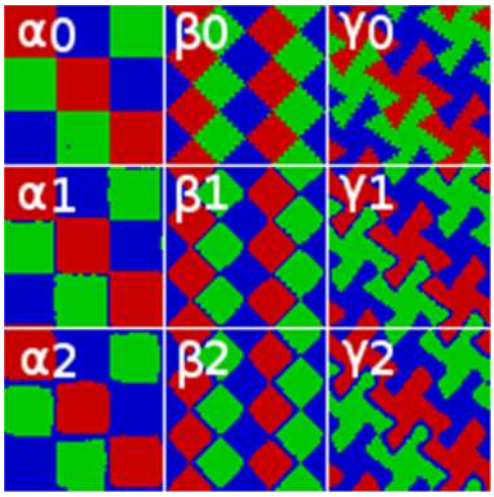

Figure 4-31 The lowest error segmentations determined by the brute force application of the double threshold method for the test samples.

4.2.2 Local Thresholds

4.2.2.1 Expanded Region Maps

For each of the test images, each of the possible ten local variable pairings were collected in the tri-axial histogram and a X-axis expanded region created, from these

region segmentations were created and the errors determined (Table 4-5).

Table 4-5 The Mn errors for the X-axis expanded overlay for the test samples (lowest errors marked in green).

Distributions	Shape	AB	AC	AD	AE	AF	BC	BD	BE	BF	CD	CE	CF	DE	DF	EF
	α	0.0000	0.0000	0.0000	0.0003	0.0000	0.0197	0.0131	0.0031	0.0017	0.0683	0.0711	0.0650	0.0711	0.0850	0.3658
	β	0.0000	0.0000	0.0000	0.0000	0.0000	0.0414	0.0522	0.0147	0.0144	0.1206	0.1295	0.1223	0.1281	0.1464	0.4323
0	γ	0.0000	0.0000	0.0000	0.0000	0.0000	0.1222	0.1147	0.0969	0.0244	0.1806	0.1636	0.1639	0.1636	0.1939	0.4208
	α	0.0042	0.0017	0.0000	0.0006	0.0000	0.0006	0.0000	0.0003	0.0003	0.0000	0.0000	0.0006	0.0000	0.0000	0.5650
	β	0.1072	0.0336	0.0242	0.0125	0.0192	0.0314	0.0233	0.0147	0.0261	0.0164	0.0164	0.0331	0.0164	0.0181	0.5912
1	γ	0.1556	0.0672	0.0525	0.0481	0.0553	0.0708	0.0600	0.0486	0.0614	0.0506	0.0489	0.0619	0.0489	0.0583	0.6203
	α	0.0394	0.0147	0.0100	0.0042	0.0081	0.0122	0.0064	0.0028	0.0067	0.0056	0.0047	0.0072	0.0047	0.0042	0.5708
	β	0.0536	0.0320	0.0314	0.0244	0.0272	0.0395	0.0322	0.0358	0.0395	0.0381	0.0408	0.0500	0.0408	0.0436	0.5496
2	γ	0.1822	0.0981	0.0881	0.0725	0.0753	0.0953	0.0933	0.0781	0.0897	0.0839	0.0869	0.0994	0.0869	0.0972	0.6292

Table 4-5 shows that the errors increase in distributions with increased blurring as well as the complexity of the shapes of the regions within each of the distributions, with multiple X-axis expanded region maps providing “zero” errors for the un-blurred distributions (and one blurred distribution), the resultant lowest error segmentations can be seen in Figure 4-32.

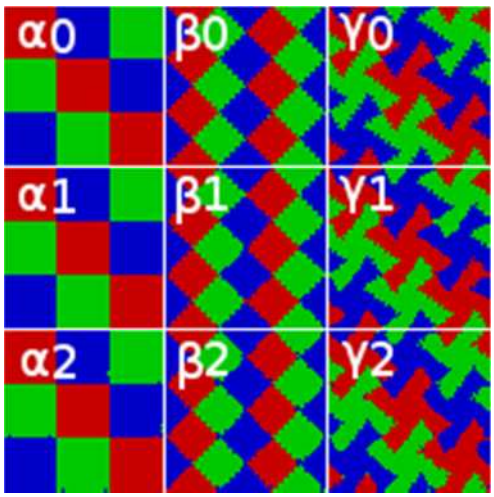

Figure 4-32 The lowest error segmentations determined by X-axis expanded overlays for the test samples.

For each of the test images each of the possible ten local variable pairings and tri-axial histograms were collected and Y-axis expanded region created, from these region segmentations were created and the errors determined (Table 4-6).

Table 4-6 The Mn errors for the Y-axis expanded overlay for the test samples (lowest errors marked in green).

Distributions	Shape	AB	AC	AD	AE	AF	BC	BD	BE	BF	CD	CE	CF	DE	DF	EF
	α	0.0000	0.0000	0.0000	0.0000	0.0000	0.0203	0.0200	0.0039	0.0008	0.0714	0.0708	0.0694	0.0683	0.0892	0.3392
	β	0.0000	0.0000	0.0000	0.0000	0.0000	0.0361	0.0375	0.0136	0.0108	0.1411	0.1375	0.1339	0.1206	0.1461	0.3212
0	γ	0.0000	0.0000	0.0000	0.0000	0.0000	0.1156	0.1122	0.0900	0.0239	0.1803	0.1764	0.1803	0.1806	0.1925	0.3561
	α	0.0039	0.0011	0.0006	0.0003	0.0000	0.0006	0.0000	0.0000	0.0003	0.0003	0.0003	0.0056	0.0000	0.0003	0.5928
	β	0.0706	0.0375	0.0261	0.0153	0.0314	0.0320	0.0278	0.0128	0.0314	0.0161	0.0175	0.0319	0.0164	0.0264	0.6101
1	γ	0.0917	0.0675	0.0514	0.0469	0.0586	0.0689	0.0553	0.0478	0.0594	0.0519	0.0511	0.0767	0.0506	0.0611	0.6281
	α	0.0444	0.0142	0.0156	0.0094	0.0178	0.0108	0.0050	0.0031	0.0158	0.0042	0.0056	0.0139	0.0056	0.0114	0.5797
	β	0.0678	0.0331	0.0356	0.0256	0.0317	0.0336	0.0361	0.0306	0.0400	0.0433	0.0414	0.0717	0.0381	0.0492	0.6084
2	γ	0.1900	0.0900	0.0878	0.0722	0.0792	0.0986	0.0831	0.0719	0.0875	0.0892	0.0897	0.1094	0.0839	0.1044	0.6161

Table 4-6 shows that as in the X-axis expansions, the errors increase in distributions with increased blurring as well as the complexity of the shapes of the regions within each of the distributions, with multiple Y-axis expanded region maps providing “zero” errors for the un-blurred distributions (and multiple “zero” errors for one of the blurred distributions), the resultant lowest error segmentations can be seen in Figure 4-33.

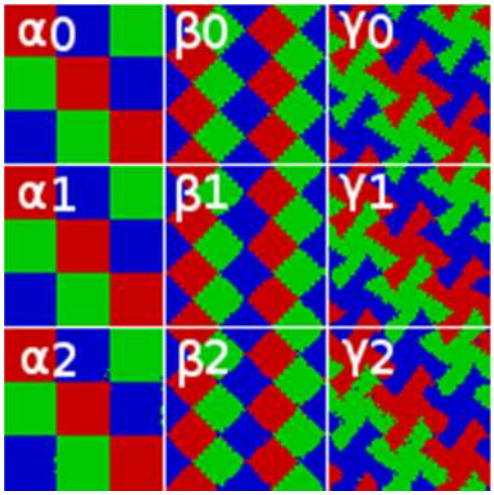

Figure 4-33 The lowest error segmentations determined by Y-axis expanded overlays for the test samples.

For each of the test images the joint XY-axis expanded regions were also created from each of the possible ten local variable pairings and tri-axial histograms and the errors determined (Table 4-7).

Table 4-7 The Mn errors for the XY-axis expanded overlay for the test samples (lowest errors marked in green).

Distributions	Shape	AB	AC	AD	AE	AF	BC	BD	BE	BF	CD	CE	CF	DE	DF	EF
0	α	0.0000	0.0000	0.0000	0.0001	0.0000	0.0066	0.0044	0.0010	0.0006	0.0228	0.0237	0.0217	0.0237	0.0283	0.1219
	β	0.0000	0.0000	0.0000	0.0000	0.0000	0.0138	0.0174	0.0049	0.0048	0.0402	0.0432	0.0408	0.0427	0.0488	0.1441
	γ	0.0000	0.0000	0.0000	0.0000	0.0000	0.0407	0.0382	0.0323	0.0081	0.0602	0.0545	0.0546	0.0545	0.0646	0.1403
1	α	0.0014	0.0006	0.0000	0.0002	0.0000	0.0002	0.0000	0.0001	0.0001	0.0000	0.0000	0.0002	0.0000	0.0000	0.1883
	β	0.0357	0.0112	0.0081	0.0042	0.0064	0.0105	0.0078	0.0049	0.0087	0.0055	0.0055	0.0110	0.0055	0.0060	0.1971
	γ	0.0519	0.0224	0.0175	0.0160	0.0184	0.0236	0.0200	0.0162	0.0205	0.0169	0.0163	0.0206	0.0163	0.0194	0.2068
2	α	0.0131	0.0049	0.0033	0.0014	0.0027	0.0041	0.0021	0.0009	0.0022	0.0019	0.0016	0.0024	0.0016	0.0014	0.1903
	β	0.0179	0.0107	0.0105	0.0081	0.0091	0.0132	0.0107	0.0119	0.0132	0.0127	0.0136	0.0167	0.0136	0.0145	0.1832
	γ	0.0607	0.0327	0.0294	0.0242	0.0251	0.0318	0.0311	0.0260	0.0299	0.0280	0.0290	0.0331	0.0290	0.0324	0.2097

Table 4-7 shows that as in the joint XY-axis expansions as with the X and Y axis expansions, the errors increase in distributions with increased blurring as well as the complexity of the shapes of the regions. There are multiple expanded region maps which provide “zero” errors for the un-blurred distributions and multiple “zero” errors for one of the blurred distributions, the resultant lowest error segmentations can be seen in Figure 4-34.

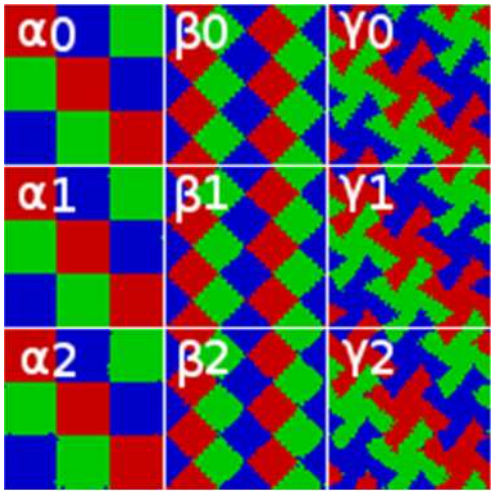

Figure 4-34 The lowest error segmentations determined by XY-axis expanded overlays for the test samples.

4.2.2.2 Colour Maps

By testing every combination of colour map, colour weighting and pairings of local variables the combinations, the lowest errors for the sample images can be determined (Table 4-8).

Table 4-8 Lowest Mn errors as defined by attempting all colour map combinations (Pattern_weighting).

Distributions	Shape	Mn Error	Thresholds			
0	α	0.00	AB	0_1	9_1	12_1
	β	0.00	AB	5_1	10_2	13_1
	γ	0.00	AB	5_1	10_2	13_1
1	α	0.02	AF	4_3	11_3	12_1
	β	0.05	AF	1_1	4_3	12_1
	γ	0.08	AF	4_3	11_3	12_1
2	α	0.04	DE	4_3	11_2	12_1
	β	0.06	AE	0_3	1_2	12_2
	γ	0.12	AE	0_3	1_2	12_2

Table 4-8 shows that lowest errors increase with increased blurring of regions as well as shape complexity, the resultant lowest error segmentations are shown in Figure 4-35.

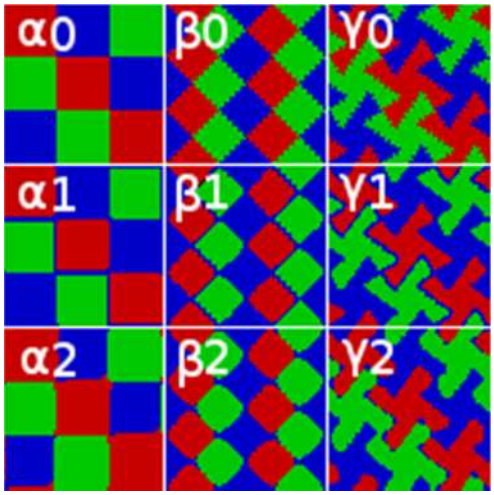

Figure 4-35 The lowest error segmentations as determined by lowest error of colour map combinations of the sample images.

As only one of colour map solutions does not contain the local property of the intensity of the voxel (A) the combinations were attempted only considering maps that contained the local property of the intensity of the voxel (A) (Table 4-9).

Table 4-9 Lowest Mn errors as defined by all colour map combinations, only considering maps that use the local property of the intensity of the voxel (A).

Distributions	Shape	Mn Error	Thresholds			
0	α	0.00	AB	0_1	9_1	12_1
	β	0.00	AB	5_1	10_2	13_1
	γ	0.00	AB	5_1	10_2	13_1
1	α	0.02	AF	4_3	11_3	12_1
	β	0.05	AF	1_1	4_3	12_1
	γ	0.08	AF	4_3	11_3	12_1
2	α	0.06	AE	8_3	12_2	14_3
	β	0.06	AE	0_3	1_2	12_2
	γ	0.12	AE	0_3	1_2	12_2

Table 4-9 shows that by only considering colour maps which contained the local property of the intensity of the voxel (A), the error is only increased for the sample image of α-2, which is not the most complex shape out of all the test images in the distribution. The number of maps that would need to be tested for only considering colour maps which contained the local property of the intensity of the voxel (A) would be half, the resultant lowest error segmentations in this case are shown in Figure 4-36.

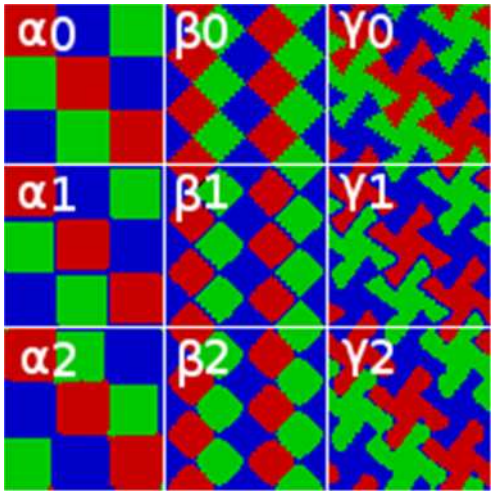

Figure 4-36 The lowest error segmentations determined colour map combinations of the sample images only considering colour maps which contained the local property of the intensity of the voxel (A).

For the segmentations determined by the local property of standard deviation (F) there

is “ghosting” of a region of blue around the other regions, which is not seen in the segmentations using the average (B) or range (E) local properties. For the segmentations with “ghosting” the lowest errors for the colour maps which do not use standard deviation were calculated to determine if the ghosting was related to the local property of standard deviation (Table 4-10).

Table 4-10 Lowest Mn errors as defined by investigation all colour map combinations, only considering maps that use the local property of the intensity of the voxel (A).

Distributions	Shape	Mn Error	Thresholds			
1	α	0.02	AD	0_3	5_2	14_3
	β	0.06	AE	4_2	14_1	15_1
	γ	0.08	AE	4_2	11_2	15_1

Table 4-10 shows that when not considering the standard deviation (F) the error is only increased by 0.01 for the test image of β-1 and by <1 % for α-1 and γ-1, the resultant segmentations are shown in Figure 4-37.

Figure 4-37 The lowest error segmentations determined colour map combinations of the sample images with distribution 1 only considering colour maps which contained the local property of the intensity of the voxel (A) and not the local property of standard deviation (F).

Figure 4-37 shows that the “ghosting” of the blue region is not exhibited in the lowest error segmentations not using the local property of standard deviation, this is implies that the “ghosting” effect is linked to the use of the local property of standard deviation. The effect of the number of possible weighting can be seen by measuring the lowest error for the sample of γ-2 for weighting of only 1, up to 2 and up to 3, as shown in Table 4-11.

Table 4-11 Lowest Mn errors as defined by all colour map combinations, for the γ-2 sample for just the local property pairings with local intensity (A) and the limitations of weighing from 1 to 3.

Weighting	Mn Error	Thresholds			
1	0.15	AD	9_1	13_1	14_1
2	0.14	AE	4_2	11_2	15_1
3	0.12	AE	9_1	13_1	14_1

Interestingly the colour maps with the different weightings are also different, with the error reducing with increasing possible weightings. This implies that if there was more computing power available more weightings could be used, as each weighting drastically increases the number of iterations.

4.2.3 Stability Methods

The segmentation method of stability uses properties determined by the change in the local properties over an increase in local area of interest. The resultant threshold properties which are used are the average of the stable region as well as a resultant stability value of either V_0 (Table 4-12) or V_1 (Table 4-13).

Table 4-12 The lowest Mn errors as defined testing every possible thresholds value of average and V_0 for the stable regions in the test images.

Distributions	Shape	Mn Error	Thresholds	
0	α	0.27	30	95
	β	0.21	29	98
	γ	0.20	30	97
1	α	0.29	70	113
	β	0.23	68	107
	γ	0.24	73	109
2	α	0.30	58	114
	β	0.24	74	114
	γ	0.27	68	116

Table 4-12 shows that the error does only slightly increase with blurring of distributions and not with complexity of shape, the resultant segmentations can be seen in Figure 4-38.

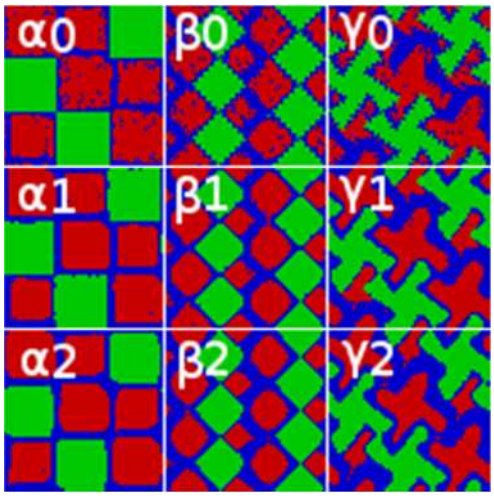

Figure 4-38 The lowest error segmentations as defined testing every possible thresholds value of average and V_0 for the stable regions in the test images.

Figure 4-38 shows that the stability segmentation method based on the value of V_0 identifies both regions 1 & 2 as region 2 with the edges being identified as a separate region.

The stability method can also be used to segment the images using the value V_1 (Table 4-13).

Table 4-13 The lowest Mn errors as defined testing every possible thresholds value of average and V_1 for the stable regions in the test images.

Distributions	Shape	Mn Error	Thresholds	
0	α	0.27	30	84
	β	0.20	29	85
	γ	0.20	30	97
1	α	0.29	70	120
	β	0.23	68	120
	γ	0.24	75	113
2	α	0.32	58	134
	β	0.26	74	136
	γ	0.30	68	131

Table 4-13 shows that there is an increase in error with increase in blurring of regions, with higher error for α shaped images, the related lowest error segmentations are shown in Figure 4-39.

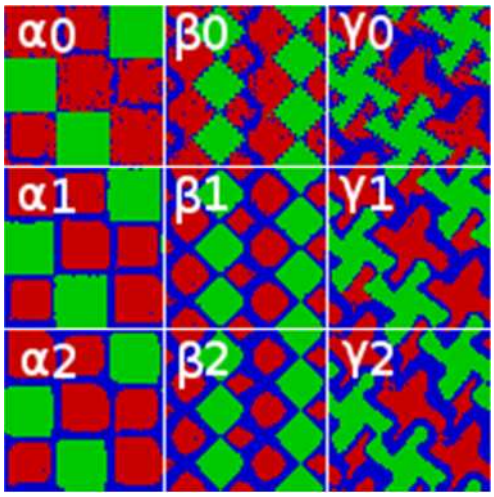

Figure 4-39 The lowest error segmentations as defined testing every possible thresholds value of average and V_1 for the stable regions in the test images.

Figure 4-39 shows that the stability segmentation method using V_1 identifies both regions 1 & 2 as region 2 with the edges being identified as a separate region.

4.2.4 Overview of Segmentation Results

The overview of the highest errors recorded for each of the distributions for each of the methods (as well as only using local property of A to determine the region and colour maps) is shown in Table 4-14.

Table 4-14 The highest "lowest" error out of the three shapes of each distribution for each of the methods.

		Distribution		
Method Family	Method	0	1	2
2D Histogram	Lowest Point	0.00	0.18	0.18
	Peak	0.00	0.18	0.17
	Brute Force	0.00	0.11	0.15
Expanded Regions	Expanded X	0.00	0.05	0.07
	Expanded Y	0.00	0.05	0.07
	Expanded XY	0.00	0.04	0.07
	Expanded X (A)	0.00	0.05	0.07
	Expanded Y (A)	0.00	0.05	0.07
	Expanded XY (A)	0.00	0.04	0.07
Colour Maps	Colour Map	0.00	0.08	0.12
	Colour Map (A)	0.00	0.08	0.12
Stability	Stability (V1)	0.27	0.29	0.30
	Stability (V0)	0.27	0.29	0.32

From Table 4-14 it can be seen that the in order from highest to lowest error for the segmentation methods, are Stability, Histogram Based Methods, Colour maps and then

the expanded region segmentation methods. It should be noted that as the three regions in the test images are of equal area the Mn error value can be taken to be equivalent to the overall percentage error in the image (Section 3.1.3), e.g. the brute force method shows a segmentation error of 15% for distribution 2.

4.3 Discussion and Evaluation of Segmentation Techniques

By comparing the resultant Mn error values from the validation method of Mn, the stability segmentation methods can be seen to have the largest errors and does not have an error which relates to the blurring of the distribution regions. The segmented regions from the stability methods (Figure 4-38 & Figure 4-39) show that the stability method segments out the edges of the regions as separate regions which is what results in the method having the highest segmentation error. As the stability methods both work on determining regions of stability it can be concluded that these edge regions are within themselves a stability region, and as such the stability method, while possible useful for some forms of segmentation will not be appropriate for the image sample sets in this study.

The segmentation methods derived from inspection and thresholds applied to the two dimensional histogram all result in a zero error for distribution 0 which does not have blurring, while presenting higher errors for both the distributions of 1 & 2 which have blurring. The segmentation thresholds determined by either the lowest points or peaks are currently used in the field (Section 1.4.1.1) and as such can be considered as a bench mark that all the other segmentation methods can be measured against. Using this benchmark it shows that the brute force method of attempting every threshold value is better than either of the threshold determining segmentation methods, resulting in lower errors for both of the blurred distributions. The errors for the brute force method can be considered to be the lowest errors for any method based on the two dimension threshold segmentation as it attempts every possible value of the thresholds, though it does not consider any form of post process as the aim is to determine a method which can segment out the regions directly without assumption or post processing. All the methods related to the two dimensional histogram show ghosting of region 1 around region 2 when segmenting the blurred distributions of 1 and 2. The ghosting means that shape and distribution analysis of the segmented regions will not be possible, or at least be severely hampered.

The segmentation methods of expanding the regions in the tri-histogram show lower errors than the bench mark values of the two dimensional histogram methods, in all its forms. Within the different forms of the expanded region segmentation methods both the X and Y expanded axis methods result in approximately the same errors, with the joint XY-axis method resulting in lower error in the distribution with the blurred of radius of 2 (identified as distribution 1). The expanded regions which only consider tri-histogram which contain the original intensity local variable are also shown to have the lowest error in all the expanded regions maps except for shape α in distribution 2.

The Colour Map segmentation method is based on the same tri-histogram methods as the expanded region methods and determines the best calibration overlay by determining the lowest error out of all the possible calibrations. The colour Map segmentation method has a recorded error higher than the expanded region method and lower than both the stability and threshold methods based on the two dimension histology methods. Out of the calibrations determined, only one of them uses a tri-histogram which does not consider the local variable of the original intensity, and when only considering tri histogram which do consider the original intensity there is a only a slight drop of 0.01 making the Colour map method still result in lower error than the two dimensional histogram methods. It is important to note that the method uses weights of the colours in the maps to provide more possible segmentation options, with the error decreasing with more weightings. While the current processing power available limits the weighting that can be tested for calibration, in the future it could be possible to quickly test more, thus potentially reducing the error of the method further.

Both the method of expanded regions and the determination of the Colour maps calibrations are determined by a single or set of reference images, with the difference between them being that the expanded regions are defined directly by the properties of the segmented regions on the reference images while the Colour Maps method calibration is defined by the calibration which returns the lowest error when compared to the reference images. Because of this difference in the way that the two methods work, both were considered as the segmentation method be used in this study, with them being compared to the pre-existing histology data for the orthotopic samples, this is expanded on in Section 6. To reduce the time taken in processing all the possible calibrations, only tri-histograms which consider the local property of the original intensity were used to determine the best calibration, as it halves the processing time

and does not result in an overall increase in error in all the test images.

5 Investigation of Novel Parameters for Quantitative Assessment of Bone Repair and Graft Remodelling

One of the advantages of segmentation is that with all the voxels in a sample labelled, more in-depth analysis of the structure and position of the bone within the synthetic bone graft (SBG) can be performed, than just measuring the volume of each region in each sample.

5.1 Identification and Development of Assessment Parameters

5.1.1 Volume of Interest

Before the samples can be assessed the volume of interest (VOI) in the samples need to be defined. The volume of interest in the samples is the SBG and the bone that is inside the porous SBG. Once the three regions of background, bone and graft have been segmented out, the area inside the graft can be defined by performing a four way scan on the segmented image. The four way scan originates from each of the four edges of each slice of the sample, when the scan interacts with the SBG it returns a “hit” for all of the voxels after the first SBG voxel. When a voxels has four hits from each of the four scans it is defined as being inside the SBG, this is used to define the volume of interest in the sample sets, an example of this is shown in Figure 5-1.

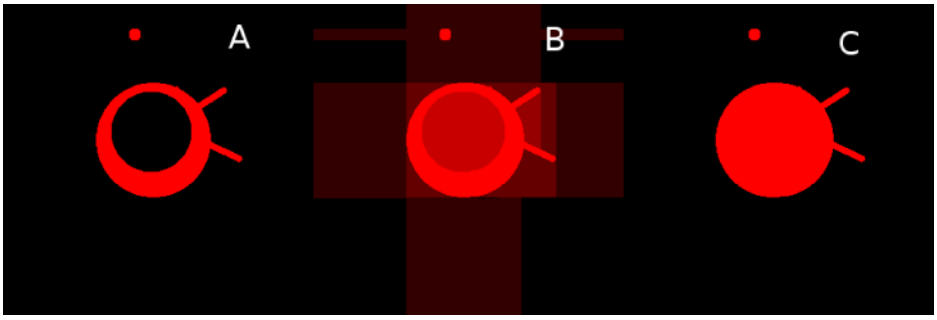

Figure 5-1 Volume of interest definition A: Graft region defined as Red, B:Four way scan of image slice of sample & C:Volume of Interest defined as Red.

5.1.2 Volume and Surface area

Once the volume of interest in the sample has been defined the number voxels of each region inside the VOI can be counted. The volume of each region can be defined by multiplying the number of voxels by the volume of a single voxel. The volume of the bone can be presented in relationship to the graft as either a percentage of the total area

of the VOI or normalised percentage of the possible area it can grow in, inside the VOI as shown in Equation 5-1 & Equation 5-2 respectively.

Equation 5-1

$$Absolute\ Bone\ \% = \frac{Bone\ (mm^3)}{VOI(mm^3)}$$

Equation 5-2

$$Normalised\ Bone\ \% = \frac{Bone(mm^3)}{VOI(mm^3) - SBG(mm^3)}$$

Having identified which region each voxel is in allows for the surface area and surface contact of the different regions to be measured. Because of the shape of the voxels, the surface areas of each of the voxels are distinct, between zero and six sides. Because the position of the six sides do not relate to the actual surrounding area of each of the voxels, the surrounding twenty six voxels are scanned and the surface area normalised to the surface area of a voxel. From the measured surface contact between each of the voxels the surface area of each region can be measured as well as the contact area between each of the different regions.
This allows for the volume and surface areas for each of the regions to be measured as well as the contact area between the regions.

5.1.2.1 Shape Measurements by Cubes

The ratio of surface area to volume has been taken as a measurement of the shape of a region (Section 1.5.2). This measurement however has an inherent flaw as the surface of a region is a two dimensional measurement while the volume is a three dimensional measurement. This means that if a region is increased in size equally in all three dimensions the resultant region will have a different surface to volume ratio than it started with. The result of this division using the example of a cube will be 6 over x (simplification of $6x^2$ over x^3) this can be seen in Figure 5-2.

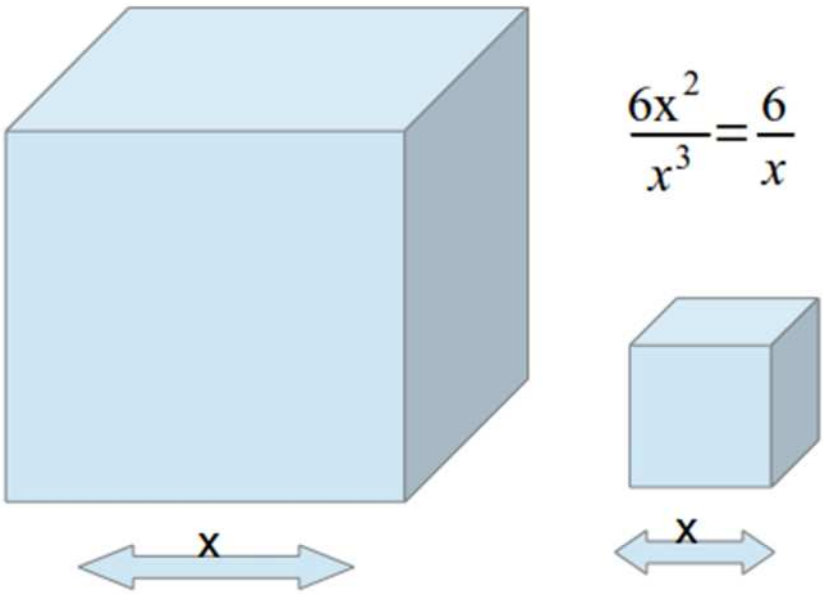

Figure 5-2 The surface to volume ratio of cubes of sides of size x.

This miss-measurement of shape by these ratios can be seen by looking at examples of square-sided rectangles (Table 5-1).

Table 5-1: Change in surface area divided by volume for different sized rectangles.

Square Side	Length	Surface Area (SA)	Volume (V)	SA/V
1	1	6	1	6.00
1	2	10	2	5.00
1	3	14	3	4.67
2	1	16	4	4.00
2	2	24	8	3.00
2	3	32	12	2.67
2	4	40	16	2.50

Table 5-1 shows that the surface area divided by volume does not give a measurement of shape, as the equivalent rectangles give different values as the rectangles of square side 1 and length 1 should have the same value as square side 2 and length of 2. This problem is caused by the dimensional imbalance, however if the surface area was square rooted and the volume cube rooted so that they were both in the form nx the variables of x would be cancelled out, as shown in the example of a cube in Equation 5-3.

Equation 5-3

$$\frac{\sqrt{6x^2}}{\sqrt[3]{x^3}} = \sqrt{6}$$

Equation 5-3 returns a value which is dependent on the shape of the sample and not connected to the "size" of the sample, this can be seen with the example of square-sided rectangles (Table 5-2).

Table 5-2 Change in shape number with differing sized rectangles.

Square Side	Length	Surface Area (SA)	Volume (V)	Rooted SA/V
1	1	6	1	2.45
1	2	10	2	2.51
1	3	14	3	2.59
2	1	16	4	2.52
2	2	24	8	2.45
2	3	32	12	2.47
2	4	40	16	2.51

Table 5-2 shows that the values for the rooted measurements do relate to the "shape" of the rectangles, as equivalent rectangles give the same rooted values. However as this value is not linear it is hard to directly compare two different samples, therefore it should be converted into a linear scale. Linearity can be achieved by working out the number of equally sized cubes of equivalent volume as the region which result in the same surface area as shown in Equation 5-4.

Equation 5-4

$$Cubes = \left(\frac{\sqrt{Surface\ Area}}{\sqrt{6}\sqrt[3]{volume}}\right)$$

When the number of cubes is calculated, twice the number of cubes relates to twice the relative surface area to volume, this can be seen with examples of square-sided rectangles (Table 5-3).

Table 5-3 Change in rooted and Cube values for rectangles of differing sizes.

Square Side	Length	Rooted SA/V	Cube Value
1	1	2.45	1.00
1	2	2.51	1.16
1	3	2.59	1.41
2	1	2.52	1.19
2	2	2.45	1.00
2	3	2.47	1.05
2	4	2.51	1.16

Table 5-3 shows that the cubic shape measurement values relate much closer to the shape of the samples compared to using the rooted values alone (Figure 5-3).

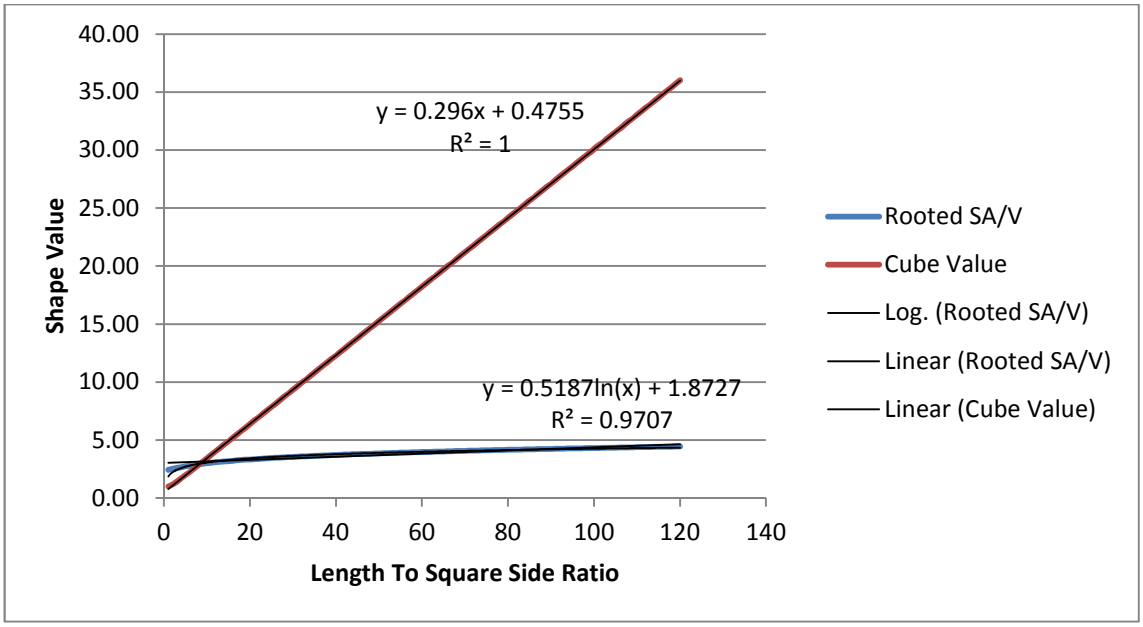

Figure 5-3 The shape values of rooted Surface area to volume ratio (SA/V) and Cube value, in proportion of length to square side ratio.

Figure 5-3 shows that the cube value has a perfect linear relationship with the length to square side ratio of the example rectangles, while the rooted SA/V value relates to a logarithmic relationship, for this reason the cubic shape measurement will be used. The cubic shape measurement value can be presented much like any unit, so that for complex shapes, that would split into thousands of cubes they can have their cubic value presented as Kcubes.

5.1.3 Heat maps

Another way of viewing the bone growth is in the individual 2D distributions. This is

performed by projecting the slices along one of the three axis', with the intensity of each of the regions being presented as the percentage of voxels in the stack which are of that region. This method provides a way of seeing how the bone is distributed within the SBG. The example of a cuboid of SBG with one empty and one bone filled cuboid located inside is shown in Figure 5-4.

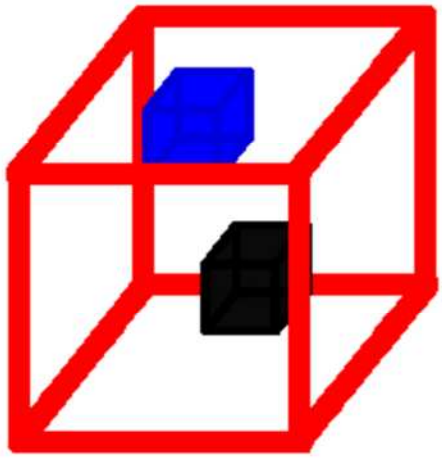

Figure 5-4 Schematic of cuboid of SBG (Red) with smaller cuboids of Bone (Blue) and void (Black) within it.

The example shown in Figure 5-4 when scanned along the three major axis (X,Y,Z) returns the heat maps shown in Figure 5-5.

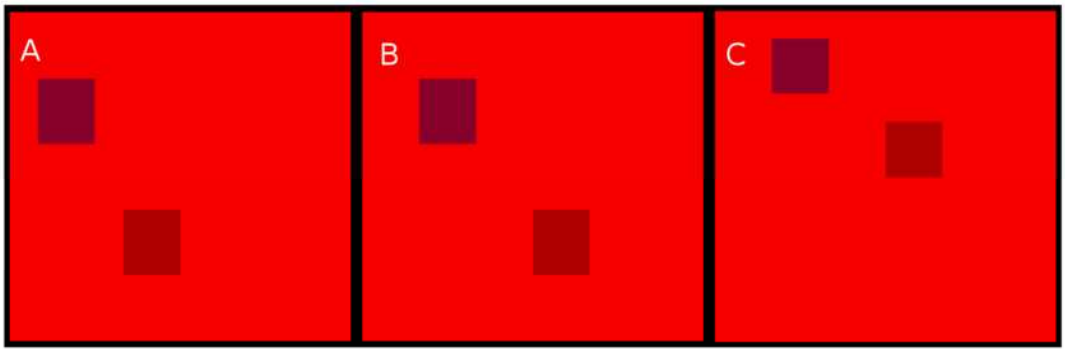

Figure 5-5 Heat maps produced from a cuboid of SBG with a cuboid of bone and a cuboid of empty space with in it, looking along the A: Z-axis, B: X-axis C: Y-axis.

Figure 5-5 shows that looking at the heat maps created from each of the major directions gives an idea of how the bone and empty space in the cube are distributed.

5.1.4 Direction Measurement

Another method for determining the position of the volume of each of the regions is by

relating the distribution to a single dimension, such as distance across the X-axis, or distance from the edge.

5.1.4.1 Axial Direction

If each direction is taken independently it can be used as a one dimensional count of the distribution of the SBG and bone and can be seen in a quantifiable manner. Using any of the major directions (Z, Y, X) as the direction of travel (or even diagonals) would give an idea to how the bone is growing in the different parts of the SBG. For example, whether the bone is growing into the graft from the surrounding bone, or growing out from the centre. Using the earlier example of a cuboid of graft with empty and bone filled cuboids inside (Figure 5-4.), an example of independent directional positioning of regions can be produced as shown in Figure 5-6.

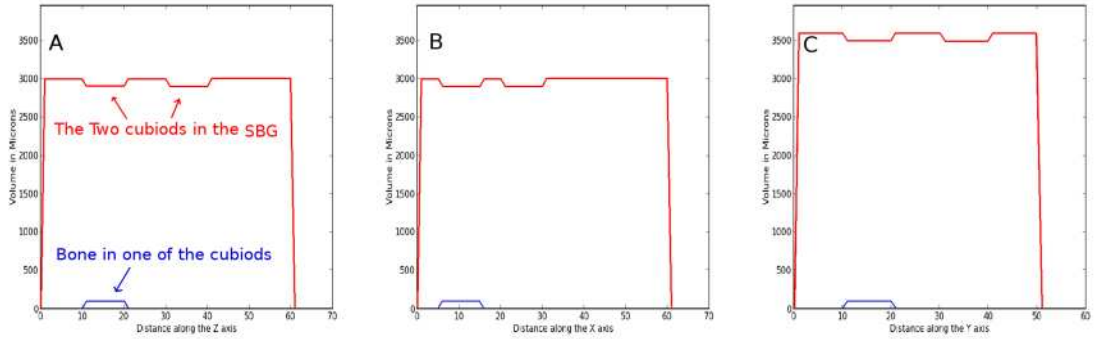

Figure 5-6 Axial direction plots, produced from a cuboid of SBG with a cuboid of bone and a cuboid of empty space with in it, looking along the A: Z-axis, B: X-axis C: Y-axis with red as implant volume and blue as bone volume.

Figure 5-6 shows how the regions inside the cuboid can be easily identified and quantified by using an axial direction measurement, as the positions of the "architecture" of the different regions can be seen in relation to each of the major axis directions.

5.1.4.2 From The Edge

Another way to look at the distribution of the bone growth is to measure the shortest distance from every point in the sample to the edge and then count how much bone and SBG there is at every distance, this can be seen for the example of the SBG cuboid (Figure 5-4) in Figure 5-7.

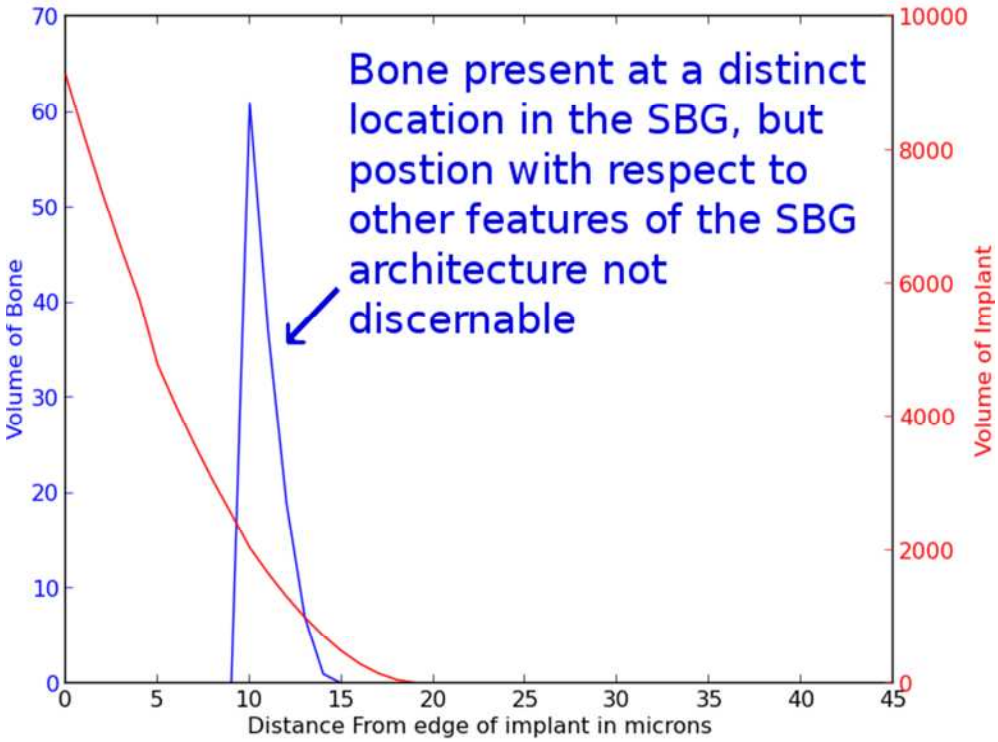

Figure 5-7 Volume to distance from edge for bone and SBG graph produced from a cuboid of SBG with a cuboid of bone and a cuboid of empty space with in it.

Figure 5-7 shows that by viewing the volume by distance from the edge, the overview of the sample can be seen, but relative distributions of the bone within the SBG are lost.

5.1.4.3 Radial and Height Directions

If the samples have or used to have a set shape, the volumes can be presented as a function of that shape. In the case of the orthotopic data, the SBG are cylinders, with the samples placed into drilled holes, so the flat faces of the cylinder (Figure 5-8), are parallel to the surface of the femoral condyle and the centre line of the cylinder passes perpendicularly through the subchondral bone.

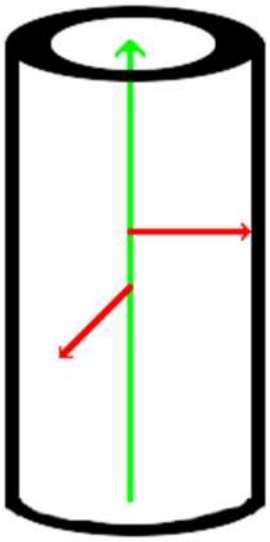

Figure 5-8 Schematic of cylinder showing the Height and radial directions.

This means that the distance from the upper or lower surface, can be calculated by measuring along the central line and the radial distance from the edge can be calculated as the shortest perpendicular distance from the central line.

To identify the central line in the cylinder, first the midpoint of the sample needs to be found. This point can be identified by either taking the average of the volume, or the average of the three major lengths (X,Y,Z) (Figure 5-9).

Once the central point is found the orientation of the cylinder needs to be identified, as the samples are trimmed and embedded, a standardised orientation cannot be assumed. The longest straight line that goes through the midpoint while remaining in the cylinder is not the central line; it is a diagonal across the cylinder. As the shortest distance will be a radius, the central line will therefore be the longest line which is perpendicular to the radius and goes through the centre point (Figure 5-9).

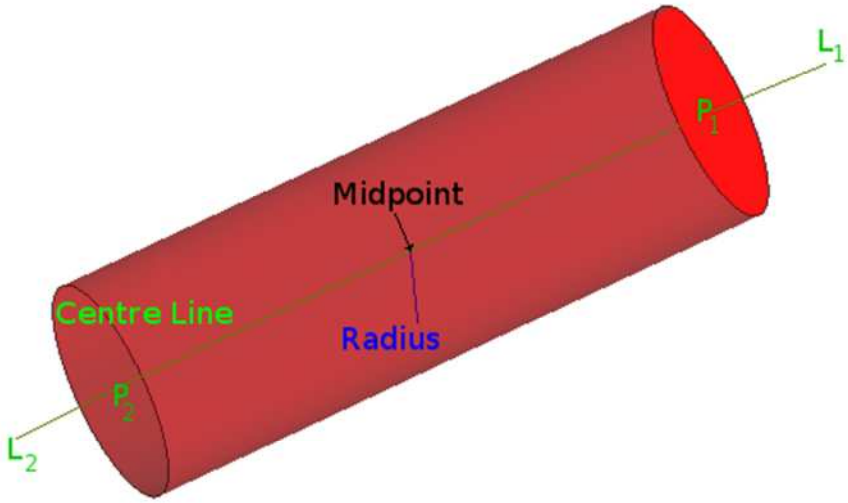

Figure 5-9 Schematic of cylinder showing the Midpoint, Radius, Centre Line and L_1, L_2, P_1 and P_2 positions.

The central line is defined by the positions L_1 and L_2 which lie outside the cylinder, for determining the distribution of the regions within the VOI the two furthest points on the centre line but still within the VOI will be used to define the line and are defined as P_1 and P_2 respectively.

With the central line defined the position of each of the voxels (P_0) inside the cylinder can be measured in both radial direction (D_r) and height (D_H) by using the following equations as shown in Equation 5-5& Equation 5-6.

Equation 5-5

$$D_r = \frac{|P_{1,2} X P_0|}{|P_{1,2}|}$$

Equation 5-6

$$D_H = \left| P_{1,2} \frac{\left| P_{0,1} \cdot P_{1,2} \right|}{\left| P_{1,2}^2 \right|} \right|$$

These distributions can be seen using the example of a cylinder with an outer ring of SBG of radius of 20 and an inner cylinder of bone of radius of 10 with a height of 200 (unit less example) (Figure 5-10).

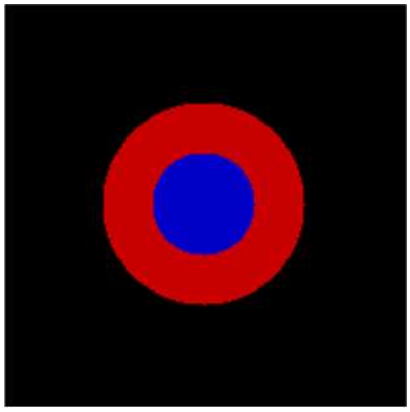

Figure 5-10 Cross section of example cylinder

From this example the distribution of Bone, SBG and VOI can be seen as a function of height (Figure 5-11 A) and as a function of radial distance (Figure 5-11 B).

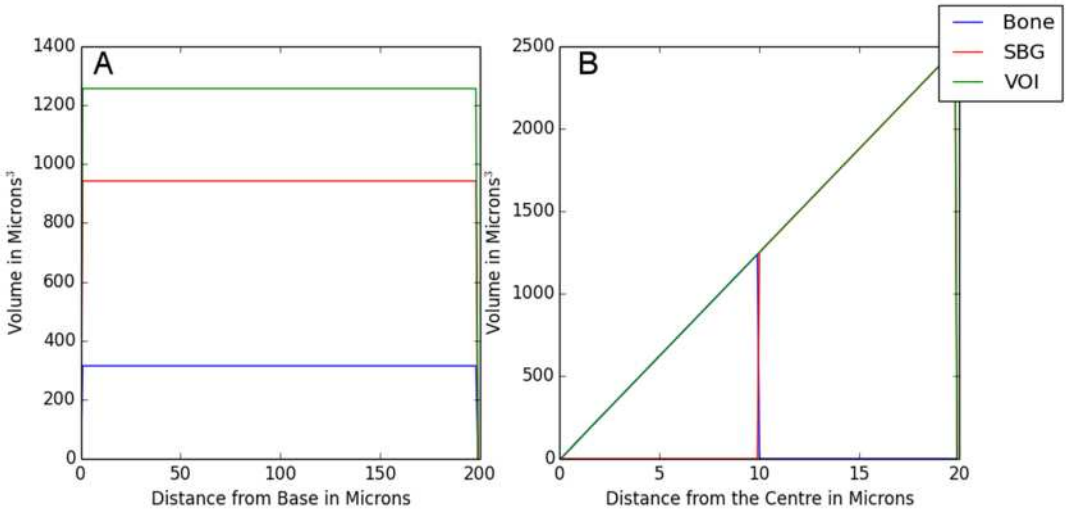

Figure 5-11 Volume of Bone, SBG and total volume of the sample (Figure 5-10) as a function of A: Height and B: radial distance from the centre.

Figure 5-11 shows that as the cylinder is "perfect" with a constant cross section, the amount of bone and SBG remains constant at all heights from the base to the top of the cylinder (Figure 5-11 A). The radial distance shows a triangle shape (Figure 5-11 B),

this is because the area of the circles gets bigger with the function $4\pi hr$ from the inner to outer of the cylinder. The Radial distribution is bisected into the bone and SBG regions which can be identified as where the bone and SBG lines cross (Figure 5-11 B).
As the VOI of interest does not necessarily remain constant in the height distribution and is not constant when viewing the radial distribution, distribution of the regions can also be measured as a percentage of the VOI (Figure 5-12).

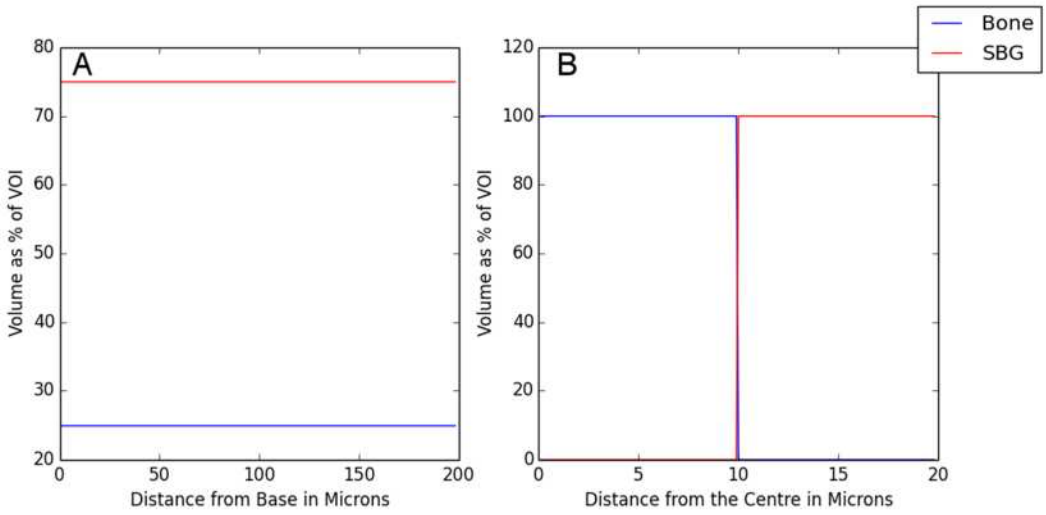

Figure 5-12 Volume of Bone, SBG as % of VOI of the sample (Figure 5-10) as a function of A: Height and B: radial distance from the centre.

Figure 5-12 A and Figure 5-12 B clearly shows the distribution of the Bone and SBG in relation to each other, especially when viewing the change in the radial direction.

Because the SBG and bone data appears as a continuous graph, it is hard to compare two different graphs in a quantifiable way. Therefore the distribution needs to be simplified, this can be accomplished by breaking the data into 5 areas from which the average amount of each region within each area is measured. Both the volume and percentage of VOI measurements can be spilt into five regions (Figure 5-13 & Figure 5-14).

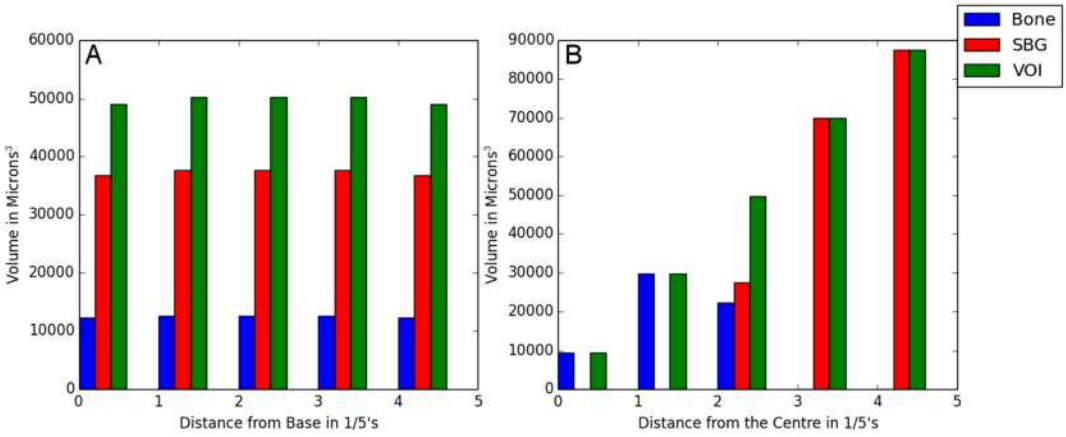

Figure 5-13 Volume of Bone, SBG and total volume of the sample (Figure 5-10) as a function of A: Height and B: radial distance from the centre, separated into fifths.

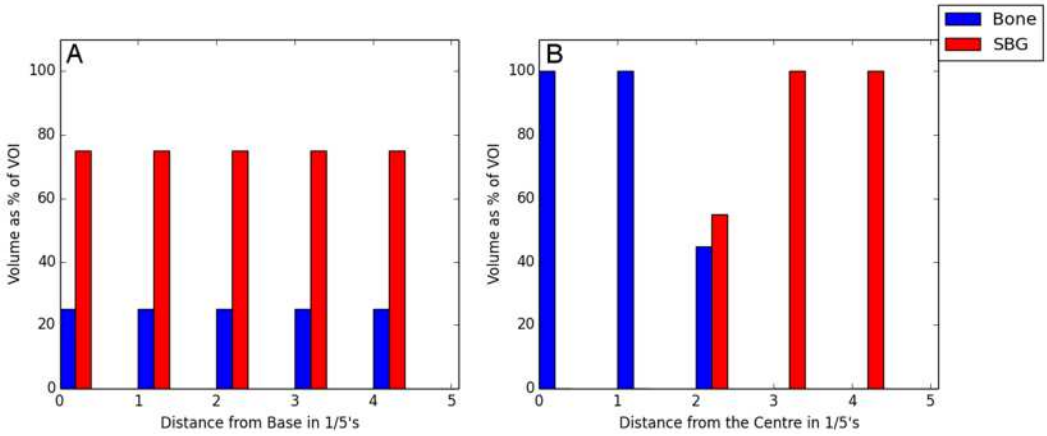

Figure 5-14 Volume of Bone, SBG as % of VOI of the sample (Figure 5-10) as a function of A: Height and B: radial distance from the centre, separated into fifths.

Figure 5-13 & Figure 5-14 shows that the fifth divided distributions show a similar distribution to the full distribution graphs (Figure 5-11 & Figure 5-12). However while these distributions do allow for each fifth to be directly compared, there are still five values and the values at the interfaces of regions do not necessarily represent accurately the interactions between the region distributions.

A measurement which gives the distribution in a single value is the centre of mass of each region, which shows if the region is "weighted" to either the inner or outer of the region, or the top or bottom (Table 5-4).

Table 5-4 Recorded position of the centre of mass for the Height and Radius distributions for the regions of Bone and SBG for both volume and percentage of VOI.

	Volume		% of VOI	
	Bone	SBG	Bone	SBG
Height	100	100	100	100
Radius	7	15.5	5	15

Table 5-4 clearly shows the position of the centre of the regions within the example cylinder, with the percentage of the volume of interest taking into account the inherent change in volume from centre to outside of a cylinder.

5.1.5 Island measurement

As well as measuring the total amounts and distributions of the SBG and bone to assess the sample; the number and size of the discrete pieces or islands that the bone and SBG exist in can be measured.

As the voxels in the samples have already been identified, the islands can be classified by simply determining which voxels connect to each other. This can be performed by checking the connections in each of the three axes in a tri-step method.

A Tri-step island identification method is performed by first taking a voxel of the desired region (in a raster scan across the sample) with the "lowest" most value in the Z axis and giving it the ID value of 1. The three voxels (Figure 5-15) which are one voxel away in the three major axis are viewed; if any of these voxels are also of the desired region and have not got already got an ID region they gain the ID of the starting voxel.

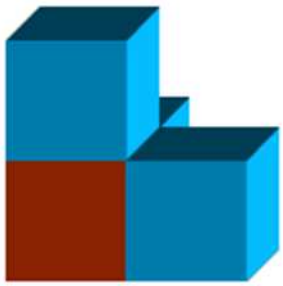

Figure 5-15 The three step cube directions

Once this is done it moves onto the next "raster scan" voxel and the process is started again with this voxel as the new start voxel.

If the a voxel already has an ID, the IDs are marked as being connected:

e.g. ID_2=ID_1 with the lowest ID value being on the right hand side, and if either of them

already have an ID connection these are stacked. For example, if ID_3=ID_2 and ID_2=ID_1, therefore ID_3=ID_1. Once the whole sample has had the tri-step method performed on it, the whole sample is scanned again and the ID equivalent “rules” applied. Now each of the islands has its own unique ID and the number of islands as well as the volume of each island can be measured.

5.1.6 Connectivity Measurement

Since SBGs are usually porous with an open interconnected pore structure, any fully connected bone that grows inside them should ideally form a continuous matrix in order that the healed tissue has mechanical and physiological functionality. To quantify how well the bone has penetrated into the SBG, a measurement of how well the bone is connected is needed.

This is different to measuring the island number and size, as that cannot differentiate between a localised sphere of bone and an open connected network of bone if they are of the same volume.

To measure the connectivity, the regions are split into connections and nodes, which are defined by using a controlled degradation of the sample.

Firstly for each voxel, the shortest straight line distance between two edges of the island which intersects with the voxel is recorded. This value is referred to as the minimum axial value (MAV), which is a one dimensional measurement.

The sample is then degraded by removing the voxels in the order of their assigned MAV value from lowest to highest, and at each step the number of islands of the investigated region in the sample is recorded.

In order to assess the validity of this methods a simple example of two connected spheres, with diameters of D1 and D2 and a connection diameter of C where D1>D2>C1 is used (Figure 5-16).

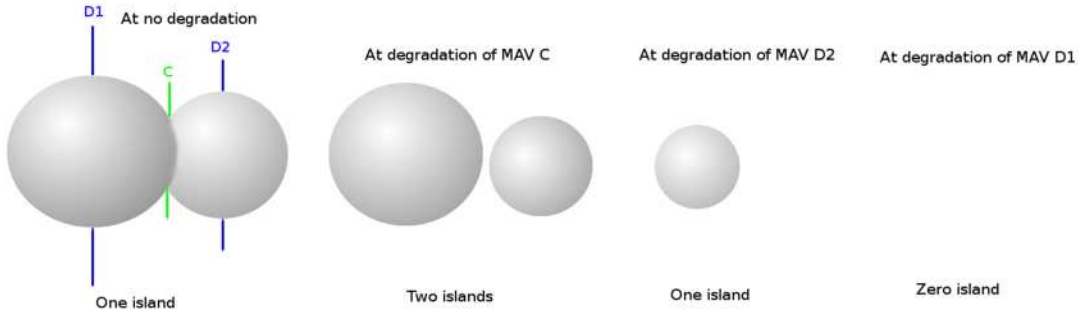

Figure 5-16 Double Sphere based model during controlled MAV based degradation, comprised of two spheres of diameter D1 and D2 respectively and an overlap diameter of C. Shown with the resultant volumes at the degradations.

Using the example in Figure 5-16 it can be seen that during the controlled degradation, when the voxels with MAV equal to the diameter of C are degraded the connection between the two spheres degrades and they separate. Once the degradation reaches the diameter of a sphere, that sphere is fully degraded.

By viewing the number of islands, when a connection breaks the number of islands increases and when a sphere (or node) fully degrades the number decreases (Figure 5-17).

The total volume of the bone can also be measured at each step, and will decrease as more bone is degraded, with the rate of degradation being related to the average size of spheres, with the smaller sphere's volume degrading faster as they have a higher surface area to volume ratio.

Therefore by recording the number of bone islands and volume at different points of the degradation, the size and number of connections and nodes can be determined. As well as a volume degradation measurement which would be expected to relate to surface area.

Using the example of 100 double spheres (Figure 5-16) (with diameters of 25 and 15 and a connection diameter of 10) the resultant MAV degradation pulse can be viewed (Figure 5-17).

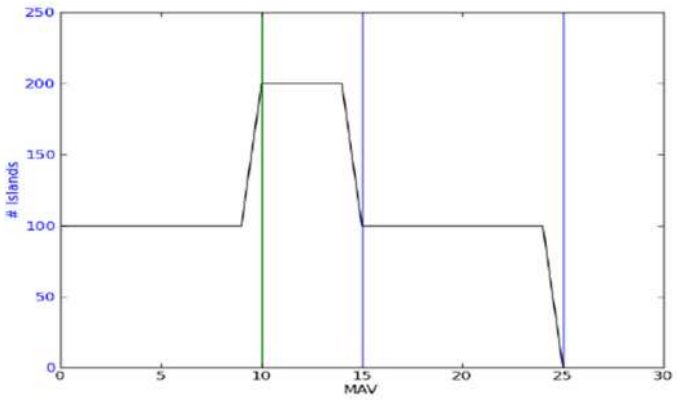

Figure 5-17 Graph of a collection of 100 of the double sphere with the connection size shown by the green line and the sphere's size shown by the blue lines.

Figure 5-17 shows that the pulse has three distinct heights, 100, 200 and 0, the first relates to the original number of sets (100) and the last to the number at the end of the degradation (always zero), while the middle value is double the starting sets (as each double-sphere set splits into two during the degradation).

In more complex situations there will not be the distinct changing points. For this the pulse is used to measure trends in the sample's structure, using such identities as the position of the highest point and the end point. As the breaking and destruction of the islands are counted at the same time, only the combined effect can be seen. This means that if the rate that the spheres are being split apart is the same as rate that other spheres are being destroyed, the pulse's height would remain constant.

For a porous sample the characteristic output pulse will be different. In order to demonstrate/validate how the pulse can be interpreted to deliver quantitative data related to the pore connectivity, a series of model structures were created and analysed using the definitions of a porous structure as shown in Figure 5-18.

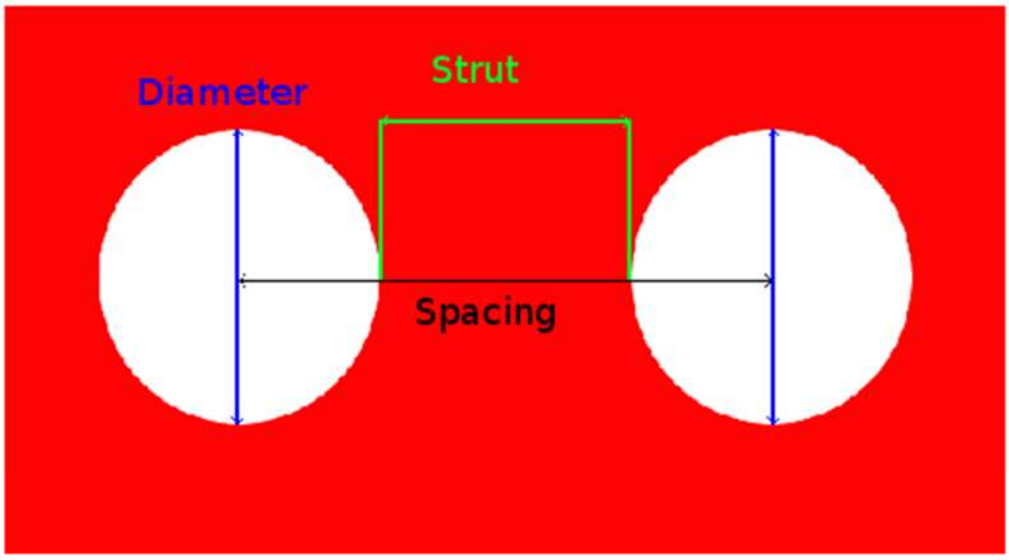

Figure 5-18 Schematic of a model porous structure.

By changing the diameter and strut thickness in the example porous models and recording their MAV pluses the effect of these factors can be measured (*Table 5-5* & *Figure 5-19*).

Table 5-5 Table showing the different test samples, and their differing characteristics.

Colour	Spacing	Strut	Av Diameter
Black	14	4	10
Red	16	6	10
Green	16	4	12
Blue	18	6	12

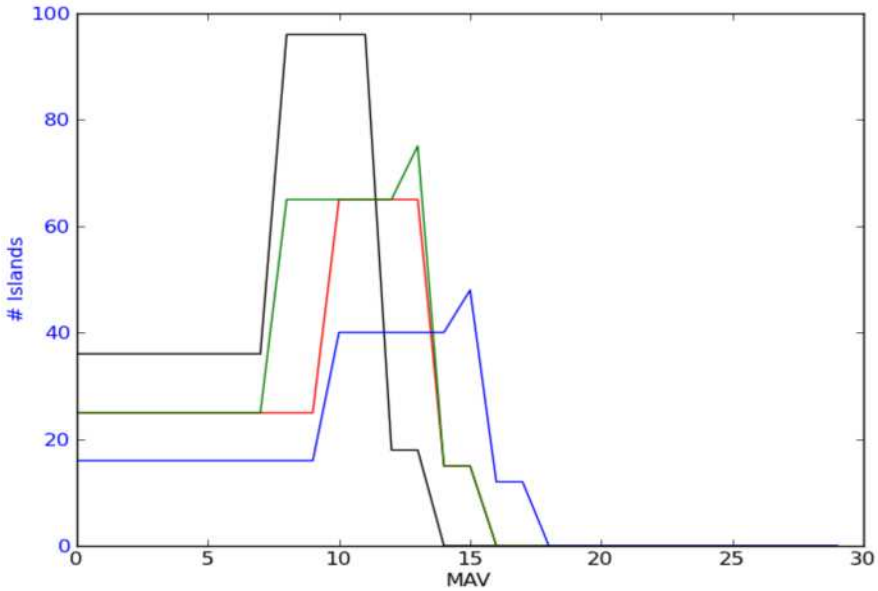

Figure 5-19 Resultant MAV pluses for the test samples as defined in Table 5-5.

Figure 5-19 shows the four shape pulses of the four model examples are all different, as the pulses contain a lot of information, to be useful as an assessment tool, key points on the pulse need to be isolated so they can be directly compared.
To this end four points were selected to give the most comparative information between different samples.

- The number of islands at zero MAV (Start Point) :**Sp**
- Number of islands at the peak number of islands **:P#**
- The MAV at the start of the peak number of islands :**PMAV**
- The MAV endpoint when the islands first hit zeros :**Ep**

These can be then recorded for each of the four examples (Table 5-6).

Table 5-6: Table showing the differing characteristics and four measurement points from the MAV graphs of the different test samples as defined in Table 5-5.

Colour	Spacing	Strut	Av Diameter	Sp	P#	PMAV	Ep
Black	14	4	10	34	91	8	14
Red	16	6	10	24	62	10	16
Green	16	4	12	24	71	8	16
Blue	18	6	12	15	45	10	18

These points relate to the following characteristics in the example models:

- **Sp** relates to how many disconnected islands the sample is comprised of.
- **P#** relates inversely to the spacing, with heavier inverse weighting to the strut thickness.
- **PMAV** directly relates to the size of the struts in the phantoms. This is because they are the controlling factor in the size of the connections in the structure.
- **Ep** varies directly with the spacing, where structures with greater spacing between the pores have higher MAV end point values.

From this information it is now possible to define how these values should be referred to and used to quantify the shape of both the bone and SBG.

- **Sp**, relates to the number of islands the sample is comprised out of and will be referred to as the **Island number.**

- **P#**, relates to the maximum number of nodes when the number of nodes being destroyed outnumbers the number of connections being broken. Where a high value relates to a sample with a large amount of connections and nodes of different sizes, and will be referred to as the **Structural Factor**.
- **PMAV** relates to the change of dominance from connections being broken to nodes being destroyed. This means it gives a measurement of the overall relationship between the connections and nodes in the sample and will be referred to as the **Connectivity Factor.**
- **Ep** directly relates to the largest node within the sample, and as such will be referred to as the **Largest Node**, which can be represented either as a radius, or diameter.
- An additional factor can be created, which is the **Normalised Connectivity Factor,** which is calculated by dividing the connectivity factor by the radius of the largest node. This is presented as a percentage and allows for the connection relationship to be seen independently from the size of the sample.

Both the **Connectivity** and **Structural** factors assume a distinct single peak (or a uniform distribution of peaks) which should be considered when making the analysis.

5.1.6.1 Average connection and node measurements

Another more robust measurement that can be determined from MAV graphs (Figure 5-19) is the average connection size and average node size. An example model to test the measurements of the average of four different connection sizes and five differently sized nodes is shown in Figure 5-20.

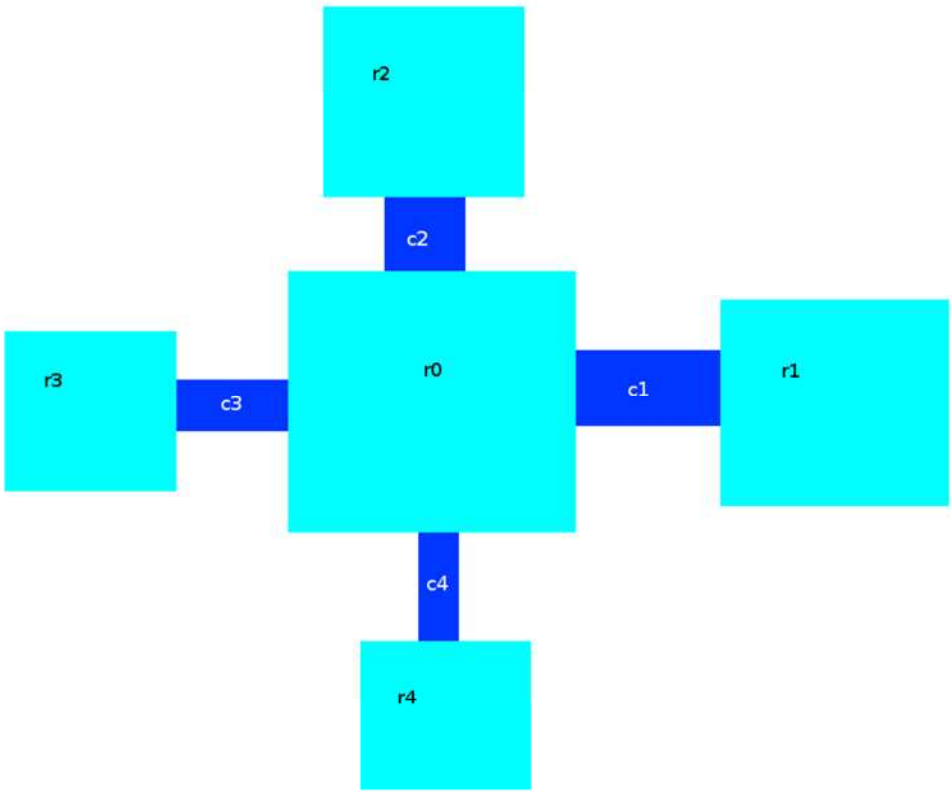

Figure 5-20 Schematic of five nodes with four connections, of diameters ro,r1,r2,r3, r4 and , c1 ,c2 c3 c4 respectively.

As the shape of the pulse is directly related to the connection and island size, the average size of each can be computed from the resultant MAV pluses as seen in Figure 5-21.

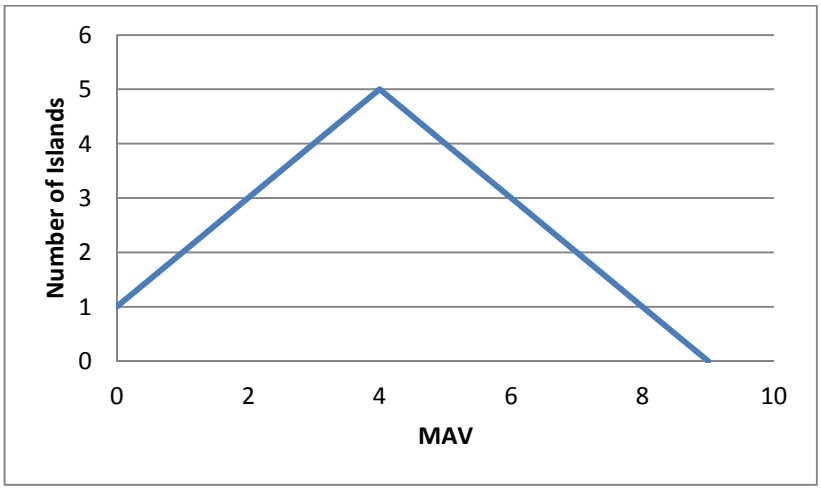

Figure 5-21 Schematic of degradation by MAV against island number graph for a single object with four differing connections and four differing nodes, where the connections and nodes increase in size linearly.

By measuring the gradient at each of the MAV values the size of each connection can be

related, by taking an increase to mean a connection and a decrease in gradient relating to a node as shown in Table 5-7.

Table 5-7 The connection and node diameters for test sample.

	C1	C2	C3	C4	R1	R2	R3	R4	R0
Size	1	2	3	4	5	6	7	8	9

From Figure 5-21 and Table 5-7 the average connection and node size are calculated by taking the mean of connections and nodes respectively, which give 2.5 (average of 1,2,3 & 4) and 7 (average of 5,6,7,8 & 9) respectively.
The peak in the example is at 4 (Figure 5-21), which is the boundary between the connections and nodes, with all nodes being larger and all connections being smaller than or equal.
This allows for the mean connection size and island size to be collected for each scan.

5.1.6.2 Shape comparisons

The MAV pulse can also be used to return a shape measurement, by using the area under the pulse. Using the double sphere example (Figure 5-16), and comparing the change in volume to the change in area under the pulse, key observations can be seen.
Because of the uniform nature of the example, area under the pulse is easily calculated by Equation 5-7.

Equation 5-7

$$A = n(D_1 + D_2 - C)$$

In the example, the area under the pulse can be measured using Equation 5-7, where n is number of sets, the D's and the diameters of the two spheres and C is the diameter of the connection between them, where D_1>D_2>C.
The volume of the double spheres can be calculated by Equation 5-8.

Equation 5-8

$$V = (r_1^3 + r_2^3)\frac{4\pi}{3} - \frac{\pi}{12d}(r_1 + r_2 - d)^2(2d(r_1 + r_2) - 3(r_1 - r_2)^2 + d^2)$$

$$d = r_2 - r_1 - 2(\sqrt{(r_1^2 - r_c^2)})$$

Where:

r_1 :Radius of sphere one

r_2 :Radius of sphere two

r_c :Radius of the connection

Taking the two situations of $D_1=D_2=10$ and $D_1=D_2=20$ with C=5 as the starting situation the change in the area under the pulse can be measured as the ratio between D_1 and D_2 changes (with the connection size remaining constant). By keeping the volume constant for all the different ratios the effect of the different sized nodes can be seen (Figure 5-22).

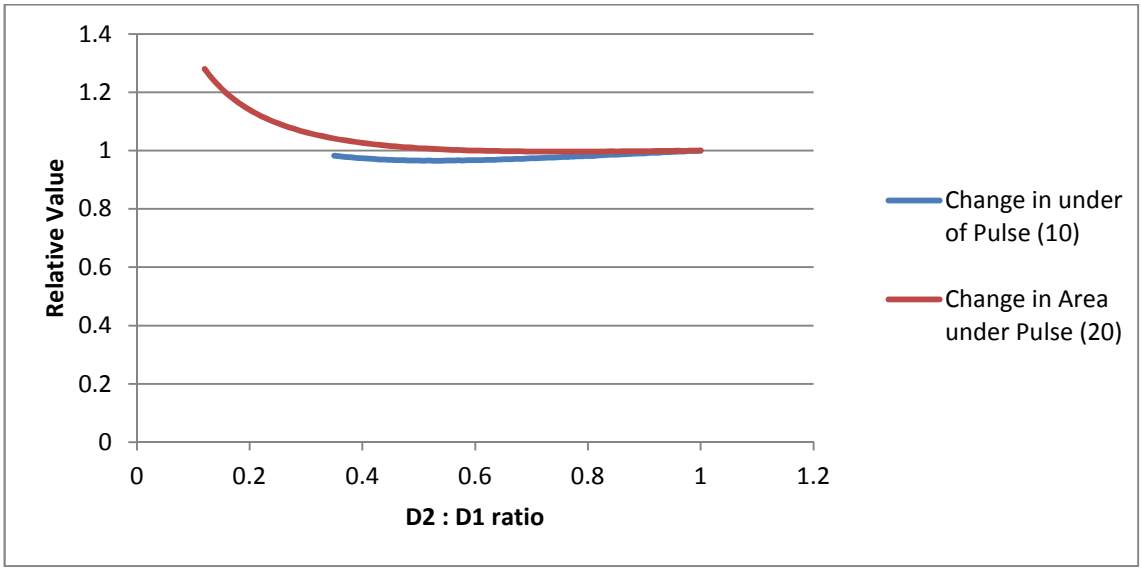

Figure 5-22 Relative change in area of pulse with change in sphere ratios and constant volume, for two scenarios with the largest sphere being 20 and 10 respectively with a connection diameter of 5 in both situations.

Figure 5-22 shows that as the ratio between the spheres decrease (limited by the connection diameter of 5) there is a slight decrease in the area under the pulse (almost undetectable by eye for the 20 diameter samples) followed by a steady increase once the ratio drops below 0.5 (The ratios are limited by the fact that neither sphere can have a diameter less than the connection size). As the volume and the area under the pulse appear to not be directly related, it is of interest to observe how they change in relation to each other when changing the shape and number of the sets of double spheres.

By taking the example of a set of double spheres of diameter 10 and increasing the connection size between them, the change in the area under the pulse and the volume of

the spheres can be seen (Figure 5-23).

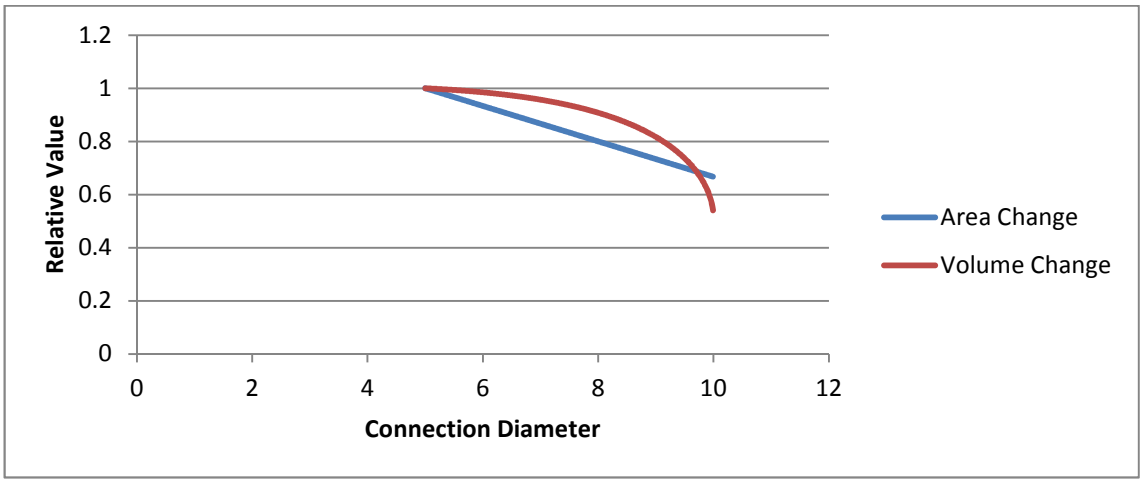

Figure 5-23 Relative change in area under MAV pulse and volume compared to a set of size 10 diameter spheres with change in sphere connection size.

Figure 5-23 shows that as the connection size increases the area under the pulse relates linearly, while the volume decreases in a non-linear manner.

If the pairs of spheres are identical and the number of them is increased the area under the pulse and the volume of the spheres can again be measured (Figure 5-24).

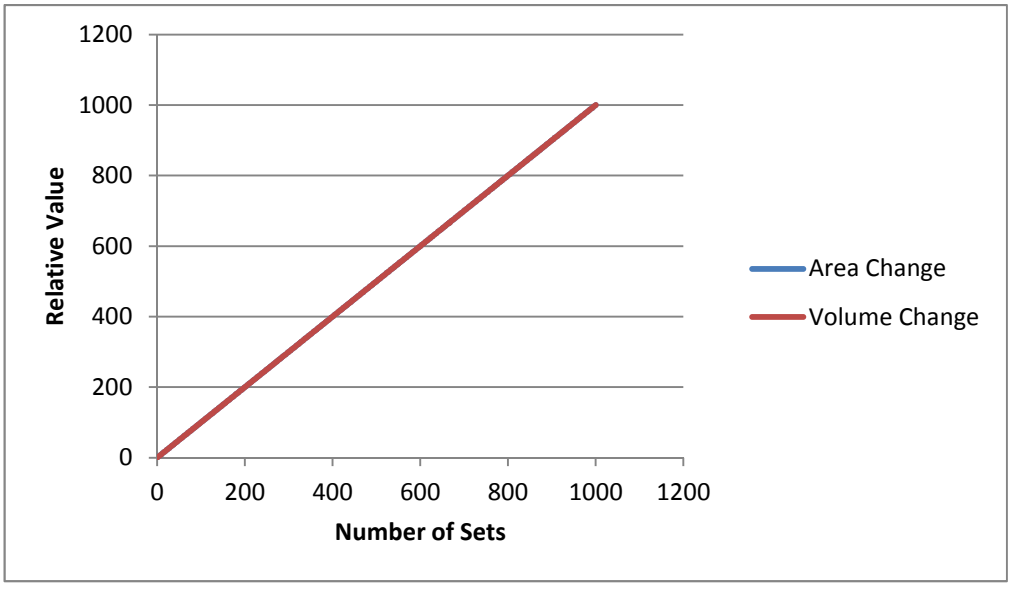

Figure 5-24 Relative change in area under MAV pulse and volume compared to a set of size 10 diameter spheres with change in number of double sphere sets.

Figure 5-24 shows that if each set of double spheres is identical and the number of double spheres increases both the volume and pulse area increase at the same rate.

Finally by taking the simulation of a single set of equal spheres with increasing diameter and tracking the changes in volume and pulse area another relationship can be

seen (Figure 5-25).

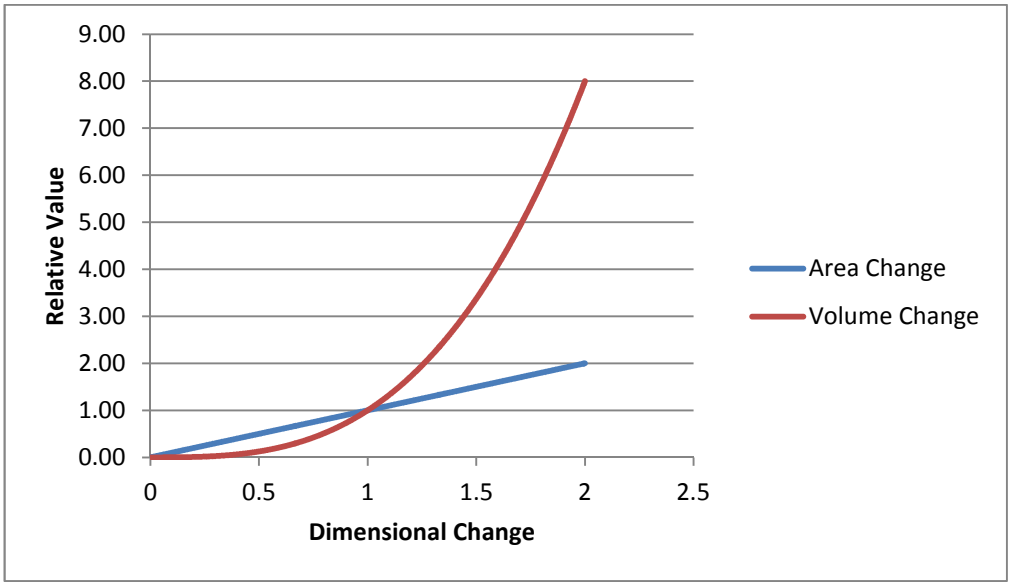

Figure 5-25 Change in area of pulse with change in sphere diameters.

Figure 5-25 shows a rapid increase in the volume (related to r^3) with a linear increase in the area under the pulse.

With these four relationships, some "rules" about the shapes can be constructed. If there are two objects, for example two scaffolds, one larger than the other, there is a simple test to see if the larger sample is a repeat of the smaller one. For this to be true the following equation as shown in Equation 5-9 should be true.

Equation 5-9

$$\frac{P_1}{P_0} \approx \frac{V_1}{V_0}$$

Which can be rearranged to allow for a single value from each sample to be calculated (Equation 5-10).

Equation 5-10

$$\frac{V_0}{P_0} \approx \frac{V_1}{P_1}$$

Therefore by measuring the area under the pulse and comparing the volume it can be concluded to whether the bigger of the two samples is a clear repeat of the other (Figure 5-26).

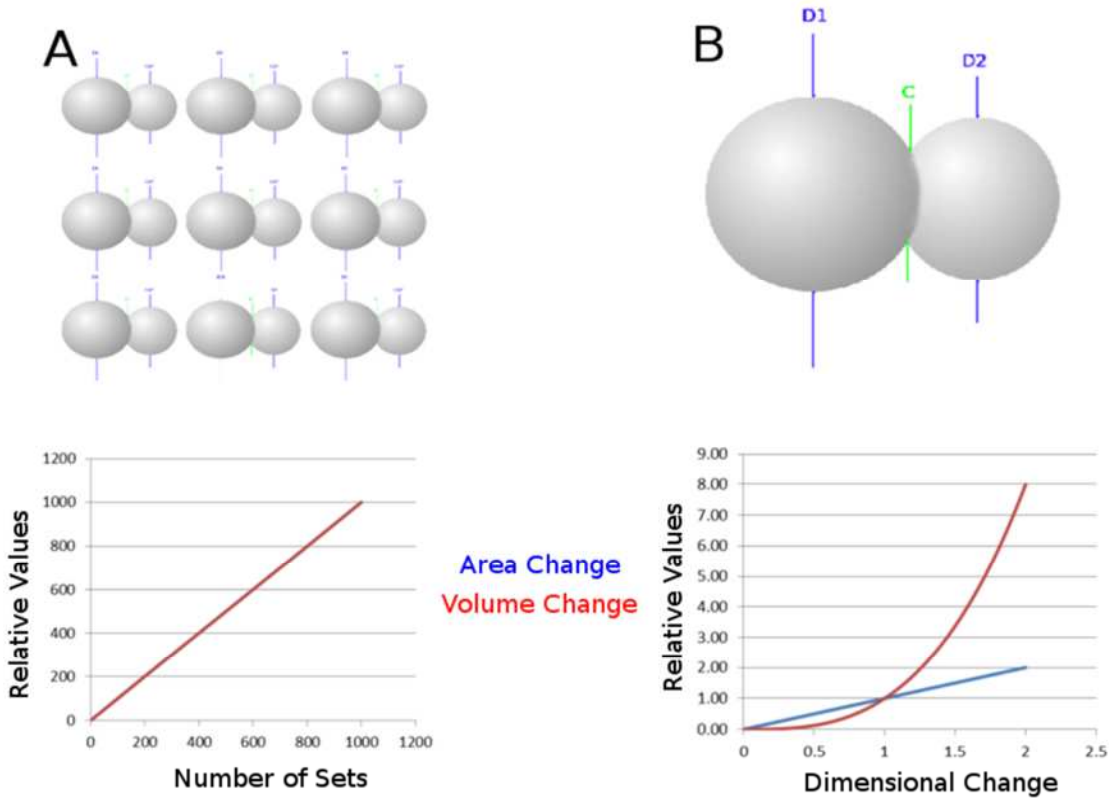

Figure 5-26 Graphs showing the change in volume with change in area under the pulse for A: a repetition and B: an enlargement.

Figure 5-26 shows that a change in shape can be quantified by using the area under the shape pulse combined with the change in volume.

If two samples are compared (given the general notation A and B) the difference in shape can be characterised from the volume (V_n) and area under the MAV pulse (P_n) measurements. From the information from Figure 5-26 the ratios can be defined in terms of enlargement (E) and multiplication (M) (Equation 5-11 & Equation 5-12).

Equation 5-11

$$V_B = MV_A + (EV_A)^3$$

Equation 5-12

$$P_B = MP_A + EP_A$$

However these equations assume that there is a single enlargement or multiplication of the entire sample, which cannot be expected, as such while of interest these equations cannot be expanded upon without further information.

5.1.6.3 Volume change with degradation

Using the same principle of degradation as was used to monitor island number, the change in volume with change in MAV number can be measured to provide a measurement of "roughness" of the samples. As the bone is represented in a distinct Euclidean space, the system is effectively a set of interconnecting spheres made up of cubes. When a "perfect" sphere is made up of cubes (a spheroid), it has two distinct regions an outer region and the inner pure cube. The inner cube (assuming a single cube at the very centre) is equal to half the diameter rounded up.

This means that if the number of cubes removed at a certain MAV value from the sphere is in the outer layer the number degraded is given by Equation 5-13 where V_{mav} is the current MAV value.

Equation 5-13

$$number\ of\ Cubes = 6V_{MAV}^2$$

When the sphere is degrading the inner cube, the number of cubes removed at a certain MAV value is given by Equation 5-14, where D is the diameter of the spheroid.

Equation 5-14

$$number\ of\ Cubes = (D - V_{MAV} + 1)^3 - (D - V_{MAV})^3$$

These equations can predict the degradation of different sized spheres (Figure 5-27).

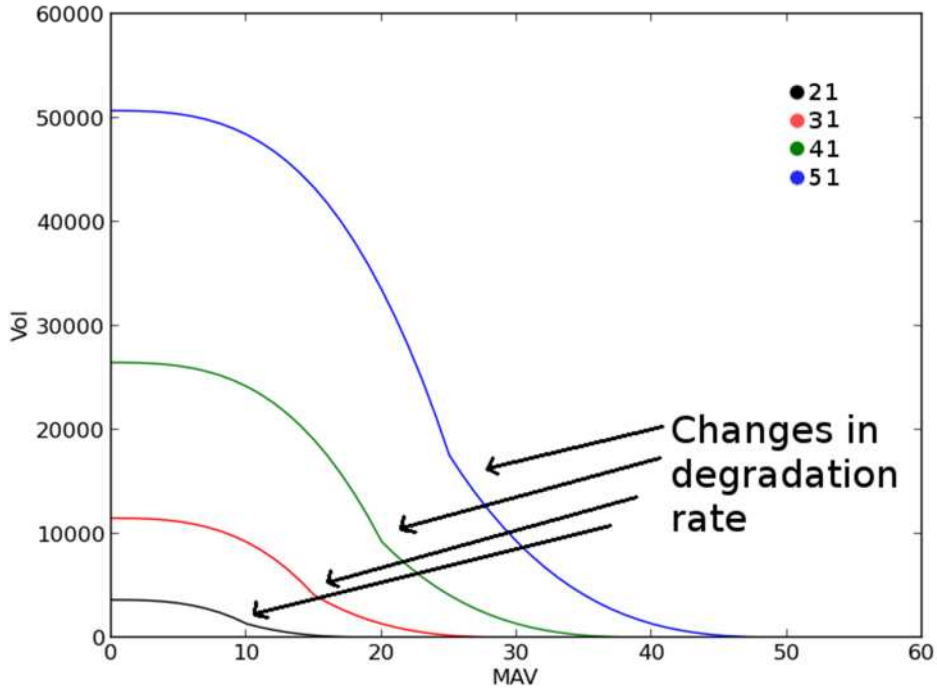

Figure 5-27 Decrease in volume as sphere's are degraded, for spheres of diameter, 21, 31, 41 and 51, with labelled change in degradation rates.

Figure 5-27 shows how the volume degrades from spheres of different sizes, but unless the sample is comprised homogeneously of the same sized spheres that shape of graph will never appear. All the spheres are modelled as having a single voxel in the perfect centre; hence they all have odd numbered diameters. The point at which the degradation switches from the outer to the inner region of the sphere can be easily seen by the change in the curve. Using a mix of differently sized spheres gives a similar but different degradation curve (Figure 5-28).

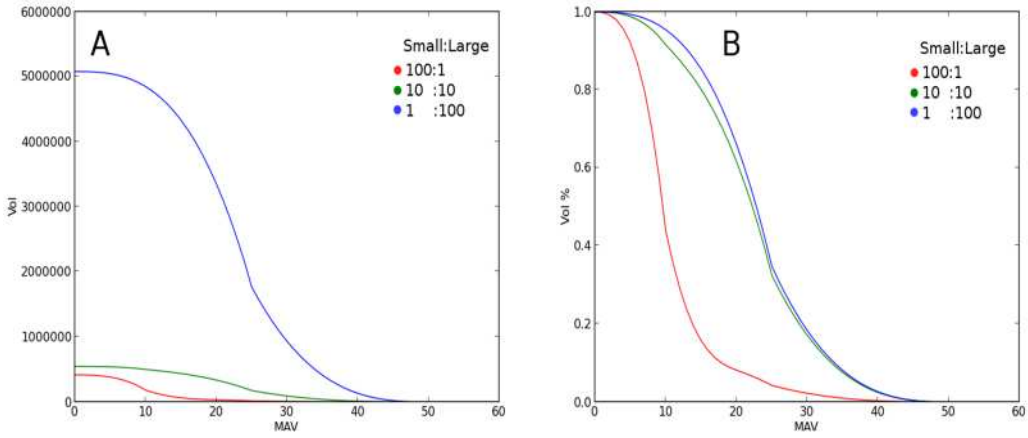

Figure 5-28 Degradation of different sphere mixes comprised of small(21):Large(51) spheres, shown as A:total and B: relative volume loss.

Figure 5-28 A shows that with different mixes of unconnected spheres of different sizes, the rate of change in volume is also changed. The rate of change is not so easy to see because of the difference in the total volumes. However if the volumes are normalised as shown in Figure 5-28B, it is clear to see that smaller spheres degrade faster in approximate proportion to the amount of smaller spheres. This follows on from the fact that the ratio between the outer and inner spheres drops as the spheres get bigger (higher surface to volume ratio), so the change in curve is not only shifted in the positive MAV direction with increasing ratio of large to small spheres but there is also a decrease in rate of volume loss. As the sample sets are comprised of two kinds of spheres the curve change is reduced because of destructive and constructive interference. This distinct shape can be seen across the whole range of small to large sphere ratios (Figure 5-29).

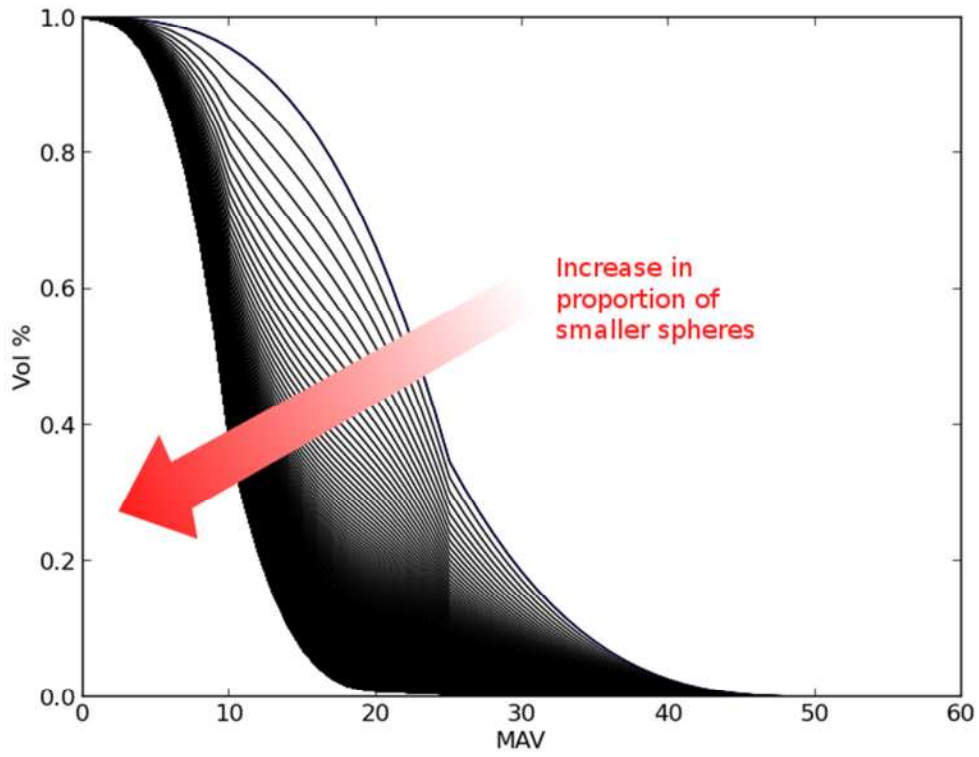

Figure 5-29 Change in loss in volume during degradation in relation to proportion of smaller spheres.

Figure 5-29 shows that the smaller the spheres in the sample the faster the loss of volume. This makes sense as a smaller sphere has a larger surface area to volume ratio so the volume will be lost at a faster rate.

In conclusion this method allows for a continuous surface area analysis (akin to using a controlled acid degradation) but in a non-destructive manner. Which allows for

quantification of another distinct characteristic for the bone and the scaffold, in this case roughness of the samples.

5.1.6.4 MAV Parameters

From this section the distinct parameters obtained from the MAV degradation pulse/graph can be identified and linked to structural qualities of the samples (Table 5-8).

Table 5-8 Overview of MAV parameters, their related structural characteristics and the related variable name.

MAV Parameter	Structural Characteristic	Variable name
Island count at zero MAV	How well connected the sample is	Island Number
Maximum Island value at peak	The largest different in number of connections and nodes	Structural Factor
MAV at peak	The overall change in size between connections and nodes	Connectivity Factor
MAV at End Point	Directly related to the largest node in sample	Largest Node
MAV at peak divided by the MAV at the end point	The overall percentage change between connections and nodes	Normalised Connectivity Factor
MAV pulse area compared with volume	Quantification of enlargement and multiplication between two samples	Shape Factor

5.1.7 Pores and interconnections

Two of the distinct parameters often characterised in the structure of SBGs are the size of pores and the size of their interconnections. To this end a modification to the MAV degradation 3D shape algorithm was made to distinctly measure the pore and interconnect size in a scaffold. When looking at porous samples, knowing the total volume of pores in the sample does not provide enough information about the structure. This is because the pores could be presented in any manner of distributions from completely interconnected to completely isolated. Therefore there needs to be a way to measure and count the individual pores in the sample and their connection to their interconnections.

The methods for performing this works by tracking the connectivity of the empty space in the sample as the sample is virtually expanded, to sequentially fill in the pore space. The simple rules it uses, are: when an island of empty space disappears that is a pore as seen in Figure 5-30 B , when an island of empty space splits it is an interconnect as seen in Figure 5-30 A. This is a similar method to the MAV pulse method, but with the individual islands being isolated and measured, rather than a combined frequency output.

This process provides the full range of pore and interconnection values. This method also identifies the pores by the geometry of their inner surfaces and not the size.

The first thing to consider is the definition of both a pore and an interconnection (Figure 5-30 *A*).

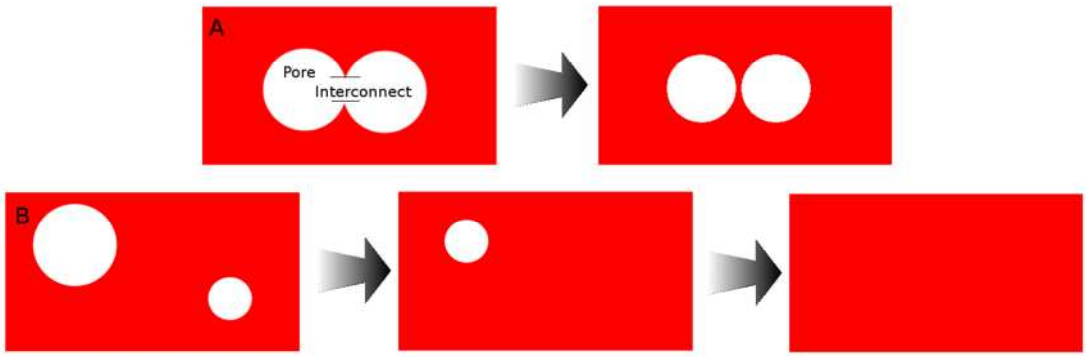

Figure 5-30 Sample scaffold showing an interconnect closing, B: Sample scaffold with pores of diameter 10 and 6 shown at original and, 3 and 5 expansions.

The simplistic diagram in Figure 5-30 A shows the basic split between the pores and the interconnections. The hard part to define is the region between the interconnection and

the pore, the simple solution to this is to extrapolate out the pore shape and define the overlap.

The definitions of the islands is performed using the island measuring tool mentioned earlier (Section 5.1.5). This time measuring the islands of 'space' inside the scaffold (bone & background) these are then ID'd and their positions recorded. Then by following the islands as the scaffold expands, the change in interconnects and pores can be measured.

This simple method therefore provides a full analysis of the scaffolds with the limit of resolution being only the pixel resolution. Limitations to the method are that the results would only be given to the closest average radius as during the expansion process it expands in all directions and the assumption that the pores are all perfect spheres. This also ignores the fact a pore could be comprised of multiple overlapping spheres, to prevent multiple counting of the pore volumes the pores are “re-inflated” and the overlapping volumes identified and cancelled out.

The pore values can be presented as a single quantifiable value by determining the median average pore size for both the total pores in the VOI and for the filled pores. The two values can then be compared by taking the percentage difference between the filled value and the pore distribution value, to determine if there is a preference for pore filling of the smaller or larger pores.

5.1.7.1 Connectivity Index

A connectivity index which relates the number of the interconnections and pores within a SBG can be created by taking the ratio of the number of interconnects to the number of pores as shown in Equation 5-15.

Equation 5-15

$$Connectivity\ Index\ (number) = \frac{\sum Interconnections}{\sum Pores}$$

It can also be calculated by using the diameters (to avoid dimensional miss-match) of the interconnects and pore to make the as shown in Equation 5-16.

Equation 5-16

$$Connectivity\ Index\ (diameter) = \frac{\sum Diameter\ of\ Interconnections}{\sum Diameter\ of\ Pores}$$

The connectivity indexes allow for the relationship between the pores and interconnects in the samples to be viewed in in a single value.

5.2 Summary of Novel Quantification Measurements

5.2.1 Volume and Surface Area Measurements

For measuring the volume and surface areas of the regions the direct measurements (Sections 5.1.2) provide simplest and objective measurements of the segmented regions. These can be presented as the volume of each region, or as an absolute percentage of the VOI or as a normalised value taking into account both the VOI as well as the other regions present within the VOI.

From the surface area measurement the contact areas between the different regions can be calculated, providing a relationship between how the bone and SBG interact with each other within the VOI.

5.2.2 Distribution Measurements

When investigating how the different regions are distributed within the VOI, the heat maps (Section 5.1.3) show how the regions are distributed within the samples in two dimensions. This allows for a" by eye" inspection of how the position of the bone inside the VOI relates to the position of the SBG (and implantation site). The heat maps however are not easily compared as they do not provide quantifiable values.

The axial direction measurements (Section 5.1.4.1) provide a clear measurement of volume of both SBG and Bone within the VOI as a function of distance along the axis. This measurement while being a function of distance does not take into account the orientation of the VOI in relationship to the implant site and while only relating to a single distribution still does not allow for clear quantifiable comparisons between multiple samples.

The measurement of distance from the edge of the VOI (Section 5.1.4.2) removes the need to define the orientation of the VOI, however it does not take into account that the VOI can be of non-uniform shape in all its local axes, as in the cylindrical samples in this study. This means that the direction of growth in relationship to the implant site cannot be discerned. It also does not provide a single easily quantifiable value.

The radial and height measurements of the volume (Section 5.1.4.3) take into account the shape and orientation of the cylindrical VOI's of the samples in this study. While the direct volume measurements do show the distributions of volume along the height and from the centre to the outside of the VOI, they do not take into account the change in

the volume of the VOI from the inner to outer radius. This change in circular cross section can be taken into account by measuring the volume of each region as a percentage of the VOI, which does not negatively affect the interpretation of the distribution along the height of the VOIs.
As the radial and height measurements are both present as a function of distance, they are not easy to quantify the difference between the distributions between multiple samples. By splitting the distributions into five regions the trends can be quantified between two samples by taking each region independently, however this still requires some interpretation. A single value which can be determined for both the height and radial distribution is the centre of mass (which could be also used for the other distributions); this returns a single value for each region relating to the distribution in each of the directions.

5.2.3 Structural Measurements

When determining measurements for the structure or shape of the regions, the measurements can either be for individual parts of the structure or as an overall value relating to the "shape" of the structure.
The island measurement (Section 5.1.5) provides a clear measurement of the number and size of islands that the samples are split into. This allows for quantification of how the regions are structured, e.g., as either a single continuous solid or as multiple disconnected solids.
The structure of the islands can be further quantified by determining the relationship between their nodes and connections, via the MAV method (Section 5.1.6). The average size of each of the nodes and regions can be measured (Section 5.1.6.1) to provide an easily quantifiable measurement of the structure. The measurements of Structural factor, Connectivity factor, Largest Node and the resultant Normalised Connectivity factor can also be measured from the MAV values (Section 5.1.6.4). These measurements give overall values relating to the complexity and connectivity of the regions.

The cubic shape measurement (Section 5.1.2.1) gives a clear representation of the shape in a size independent measurement of surface area to volume. The degradation rate (Section 5.1.6.3) also provides a measurement of shape by the rate at which the regions degrade, however unlike the cubic shape measurement it does not provide a single easily comparable value. The shape comparison formed from the area under the MAV

pulse and the volume of the samples (5.1.6.2) provides another measurement of the shape of the different regions. While this in theory can provide information about whether two samples are enlargements or repeats of each other, this only works if there are only a limited number of repeats or enlargements and not a complex mix of both.

5.2.4 Porosity Measurements

The measurement of the pore distributions and bone filling of pores (Section 5.1.7) provides a method to see if any weighting of the pore filling is towards the larger or smaller pores defined by their curve geometry, not by volume. While the connectivity indexes (5.1.7.1) provide a single easily comparable value (either based off number or area) to see how the connections between the pores with in the samples.

5.2.5 Measurements for Consideration

From these measurements, a shortlist was created of measurements which will be further investigated using the samples in Section 6 (Table 5-9). These measurements were chosen to provide the most information about the regions in the samples, while allowing for easy comparability between samples. From the further investigation and comparison to the original images of the samples, the attributes of the samples will be linked to the different measurements as well as defining the relevance of each measurement (Section 6.3.4).

Table 5-9 Table of measurements of each type which will be investigated.

	Measurements
Volume & Surface Area	Volume Absolute percentage of VOI Normalised Volume Surface Area Contact area
Distribution	Height and Radius in fifths as VOI% Height and Radius centre of mass as VOI%
Structural & Shape	Island number Island Volume Average Node and Connection size Structural factor Connectivity factor Largest Node Normalised Connectivity factor Cubic Shape factor
Porosity	Centre of mass of Pores Centre of mass of filled Pores Filled Pore difference Connectivity Index (number) Connectivity Index (diameter)

6 Application and Validation of Quantification Methods

This chapter details the applications of the techniques introduced in Section 5 to assess their suitability when deployed on real samples, which have been segmented by the methods outlined in Section 4.

6.1 Segmentation Methods and Calibrations

In Section 4 two segmentation techniques were determined to be possible techniques for the type of image data expected in the orthotopic and ectopic sample sets, namely the region expanded and colour map overlay methods. Both these methods require references to calibrate against, these were created from twelve regions of interest (ROI) for each of the orthotopic and ectopic sample sets. The twelve ROI are examples of background, bone, SBG and a mix of all the regions (because of the topography of the samples other regions are seen within the specified ROI) which are then produced for three samples for each set of ROI. The size of the ROI are 50 by 50 pixel squares, which are shown in a larger region of 100 by 100 pixel squares to give context of the individual regions with the ROI being defined by white pixels outside each corner. The author segmented out each of the ROI by hand three times, identifying background as green, bone as blue and SBG as red, these three iterations were then averaged to provide the “by hand” segmentation, which was used as the reference.

6.1.1 Regions of Interest

For the orthotopic samples the three samples which were used for the reference images were HA 80 % total porosity 10 % strut at 3 weeks, SA 0.4 wt% 70 % total porosity 20 % strut at 3 weeks and SA 0.2 wt% 70 % total porosity 20 % strut at 12 weeks referred to as 1, 2 and 3 respectively (Figure 6-1).

For the ectopic samples the three samples which were used for the reference images were SA 0.8 wt% 80 % total porosity 30 % strut at 12 weeks with surgical putty, SA 0.8 wt% 80 % total porosity 20 % strut at 12 weeks and SA 0.8 wt% 80 % total porosity 35 % strut at 12 weeks referred to as 1, 2 and 3 respectively (Figure 6-2).

Each of the different ROI are defined as b: background, B: Bone, S: SBG and M: Mixed regions.

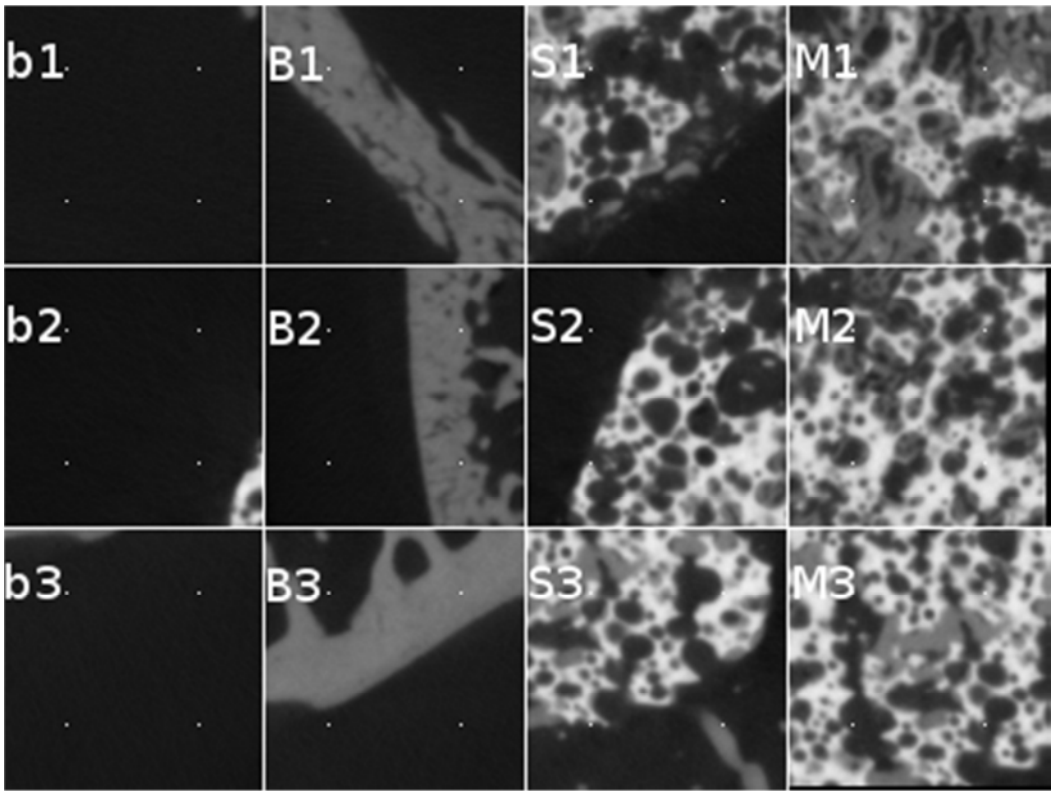

Figure 6-1 ROIs for orthotopic samples for b: background, B: Bone, S: SBG and M: Mixed regions.

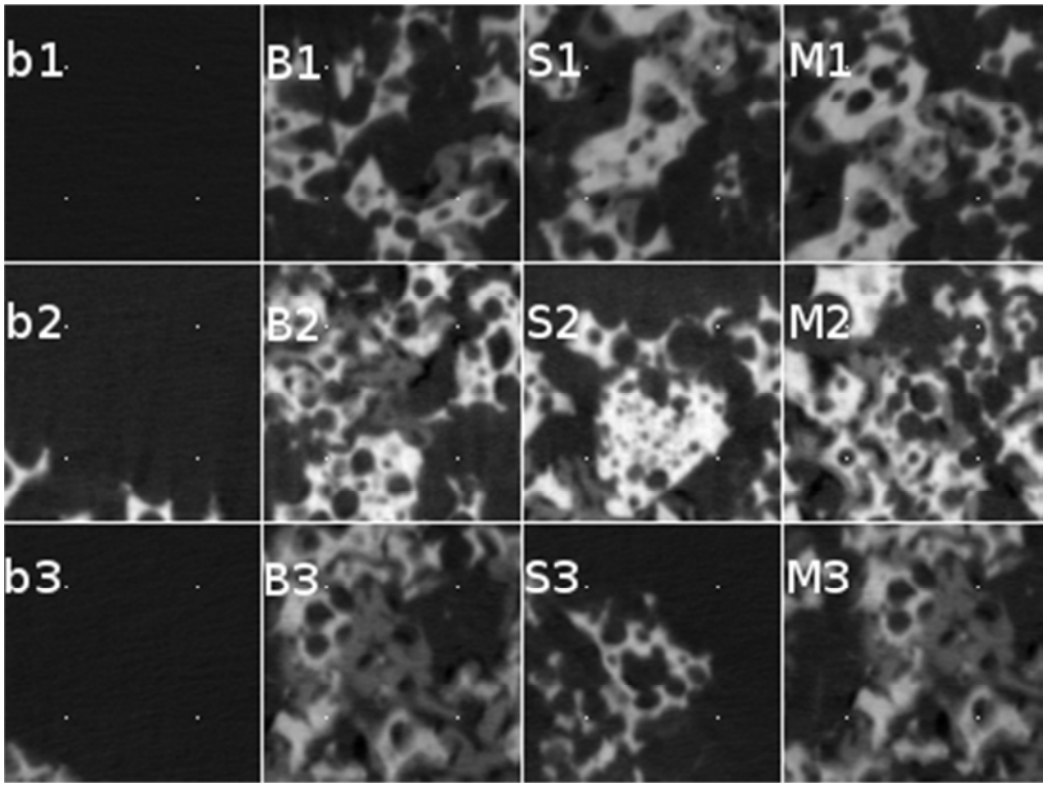

Figure 6-2 ROIs for ectopic samples for b: background, B: Bone, S: SBG and M: Mixed regions.

For the orthotopic ROI's the user defined three iterations are shown as an average of all three iteration in Figure 6-3.

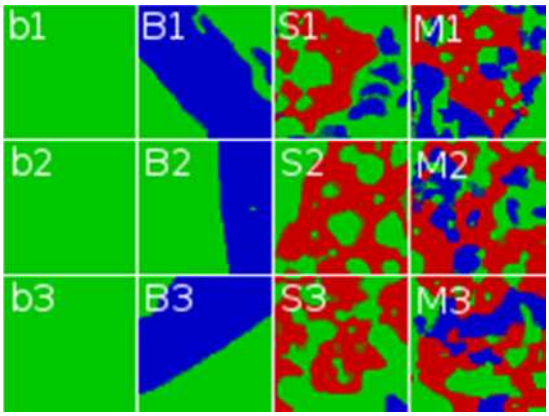

Figure 6-3 User defined segmentations, averages ROIs for orthotopic for b: background, B: Bone, S: SBG and M: Mixed regions.

From the three iterations a set of reference images for the orthotopic sample set can be created by taking the highest intensity region at each of the voxels as shown in Figure 6-4.

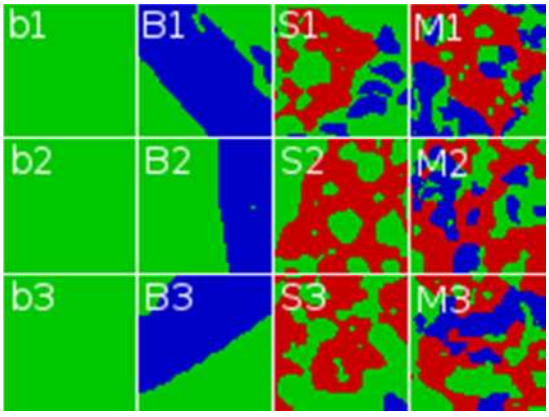

Figure 6-4 User defined segmentations, defined by taking highest intensity regions from averages ROIs for orthotopic for b: background, B: Bone, S: SBG and M: Mixed regions.

For the ectopic ROI's the user defined three iterations are shown as an average of all three iteration in Figure 6-5.

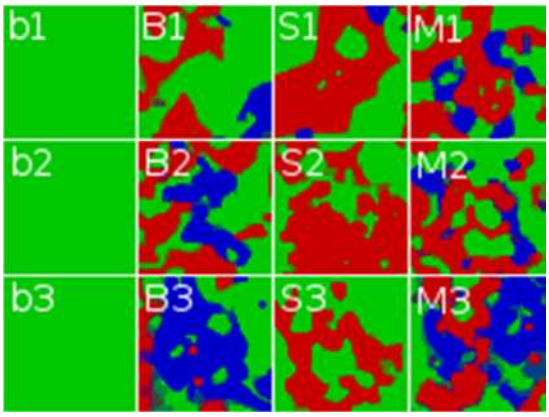

Figure 6-5 User defined segmentation, averages ROIs for ectopic for b: background, B: Bone, S: SBG and M: Mixed regions.

From the three iterations a set of reference images for the ectopic sample set can be created by taking the highest intensity region at each of the voxels as shown in Figure 6-6.

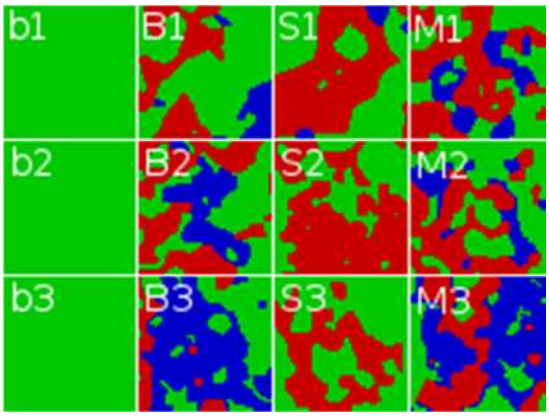

Figure 6-6 User defined segmentations, defined by taking highest intensity regions from averages ROIs for ectopic for b: background, B: Bone, S: SBG and M: Mixed regions.

An additional ROI with a region which could be identified as soft tissue or fibrous tissue or potentially putty, (which will be referred to for simplicity as the "soft region") is used as an additional reference to avoid misidentification of this region, as shown in Figure 6-7.

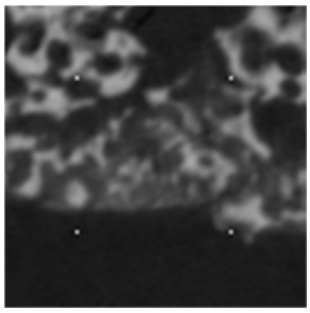

Figure 6-7 ROI of SBG and background from 30% strut and soft region.

The three iteration of the user defined segmentations of the region can be seen in Figure 6-8.

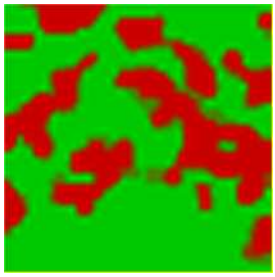

Figure 6-8 User defined segmentation, averages ROI of SBG and background from 30% strut and soft region.

From the three iterations the reference image for the region is defined as shown in Figure 6-9.

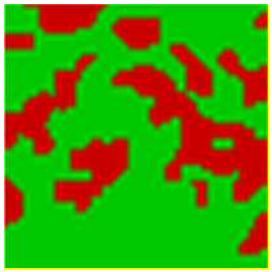

Figure 6-9 User defined segmentations, defined by taking highest intensity regions from averages ROI of SBG and background from 30% strut and soft region.

6.1.2 Histology Comparison

For some of the orthotopic samples there exists previous histology data (kindly provided by Dr K. A Hing) (Table 6-1).

Table 6-1Table of absolute and normalised volume of bone in a selection of orthotopic samples as determined from histology.

Material	Silicon wt%	Total Porosity	Strut Porosity	Time (week)	Absolute Volume	Normalised Volume
HA	0	60	20	3	12	26
HA	0	60	20	6	25	61
HA	0	60	20	12	13	39
HA	0	60	20	24	21	44
HA	0	70	10	6	20	40
HA	0	70	20	3	21	36
HA	0	70	20	6	15	27
HA	0	70	20	12	35	61
HA	0	70	20	24	29	54
HA	0	80	10	3	28	39
HA	0	80	10	6	15	24
HA	0	80	10	12	29	56
HA	0	80	20	6	32	54
HA	0	80	20	12	44	66
HA	0	80	20	24	41	64
SA	0.2	70	20	6	21	36
SA	0.4	70	20	3	27	46
SA	0.4	70	20	6	24	45
SA	0.8	70	20	3	31	44
SA	0.8	70	20	6	34	54
SA	1.5	70	20	3	22	33
SA	1.5	70	20	3	15	28
SA	1.5	70	20	6	26	45
SA	1.5	70	20	12	35	67

The absolute change in bone volume as a percentage of the VOI and the normalised bone growth for both the HA and SA samples which have histology data can be seen in Figure 6-10 and Figure 6-11, showing both the absolute and normalised bone volumes for each sample set.

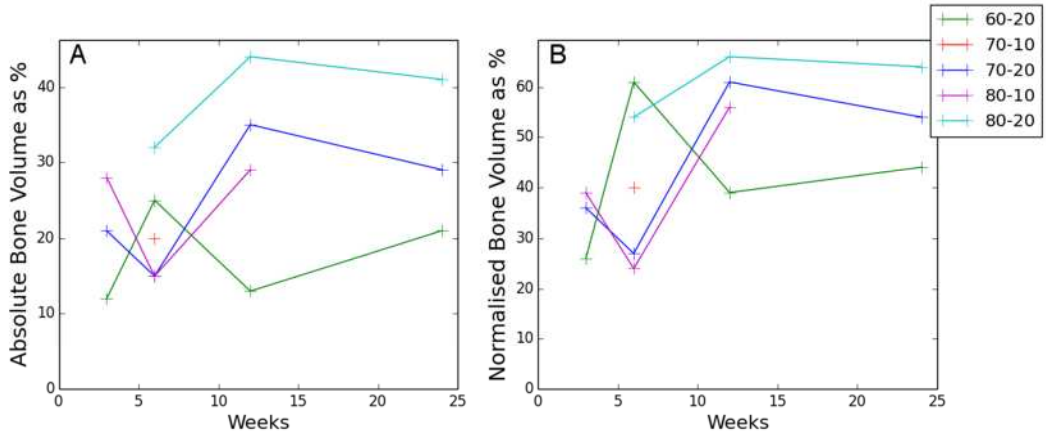

Figure 6-10 A: Absolute bone volume as percentage, B: Normalised Bone volume as percentage, for HA orthotopic samples over time from histology data in Table 6-1.

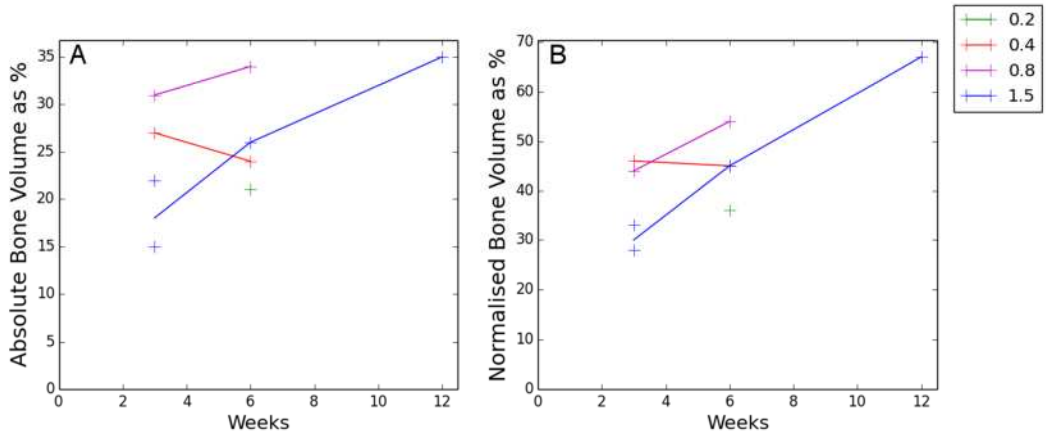

Figure 6-11 A: Absolute bone volume as percentage, B: Normalised Bone volume as percentage, for SA orthotopic samples over time from histology data in Table 6-1.

The normalised volume histology data shown in Table 6-1 was used as a reference value, to compare the quality of the segmentation against as it takes into account all three region types within the VOI and also reduces the effect of differently measured VOIs between the histology and automated segmented images. The comparison between the segmented and histology data was carried out by measuring the normalised bone volume in each of the samples with histology data and then determining the average RUMA error (Equation 1-59) and its standard error for all the tested samples. The expanded region segmentation methods (X & Y expansion) (Section 4.1.2.2) were calibrated for the orthotopic sample set using the ROI and the related reference images (Figure 6-1 & Figure 6-4) as shown in Figure 6-12 and the Mn error for each method collected and the average for all 12 ROI collected is shown in Table 6-2.

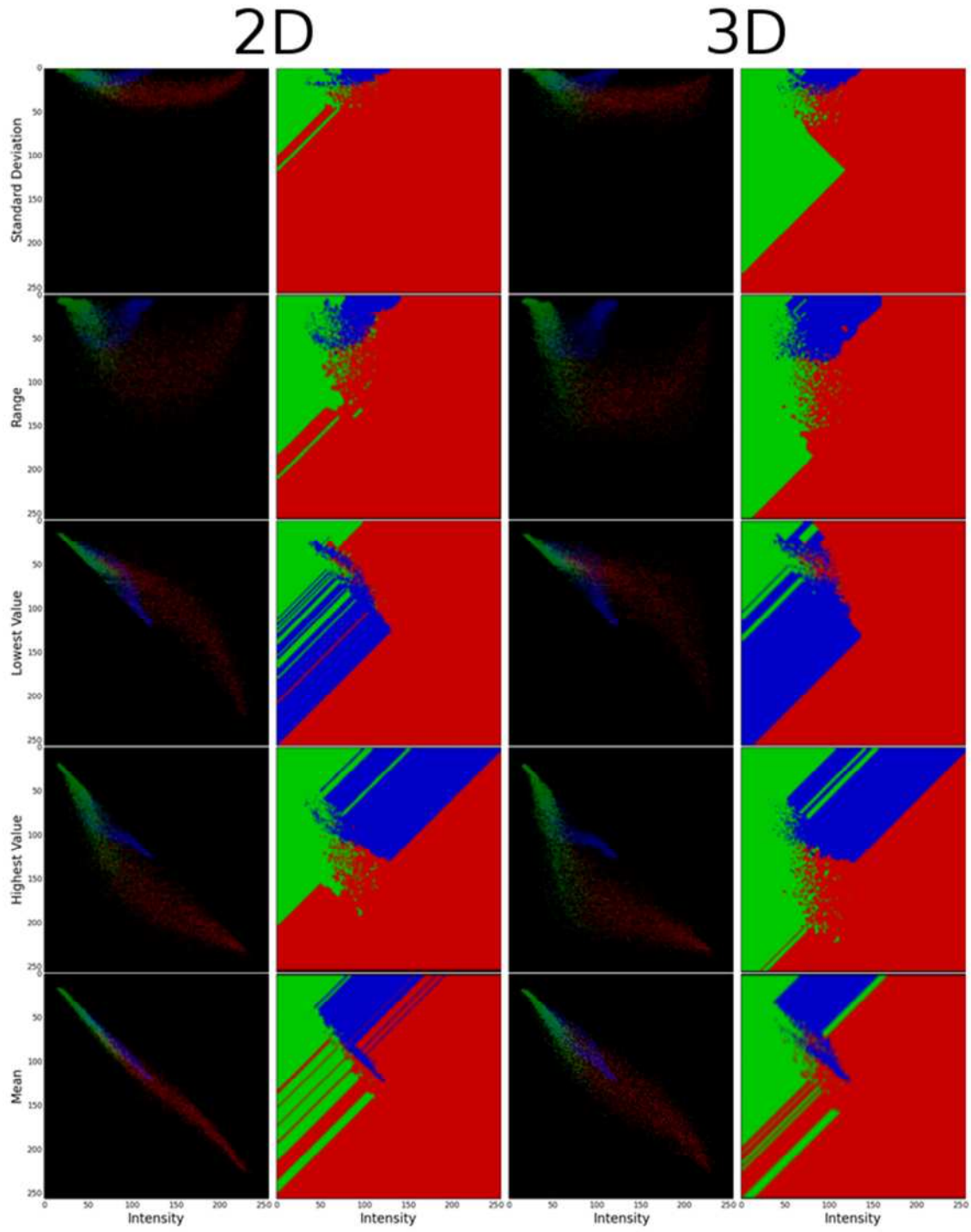

Figure 6-12 The tri-histograms of local properties for two and three dimensional scans and relevant expanded colour maps for the orthotropic samples.

Table 6-2 The Mn error, Mean RUMA % error and the standard error for the RUMA error for the ten different expanded region methods for the orthotopic data set.

Region	Mn Error	Mean RUMA % Error	RUMA Standard Error
AB	0.117	31.47	5.15
AC	0.103	28.68	2.94
AD	0.122	25.85	3.73
AE	0.099	26.86	3.63
AF	0.137	35.85	6.61
AB3D	0.128	26.11	3.68
AC3D	0.096	37.01	4.31
AD3D	0.115	25.81	3.56
AE3D	0.089	23.66	2.82
AF3D	0.153	55.06	8.48

Table 6-2 shows that the expanded map method which results in the lowest error in both Mn and RUMA is the method that uses the AE properties region map. Plotting all the expanded regions methods RUMA errors against their Mn error it can be seen that while there is a relationship between the errors, it is not a clear or concise one, as shown in Figure 6-13.

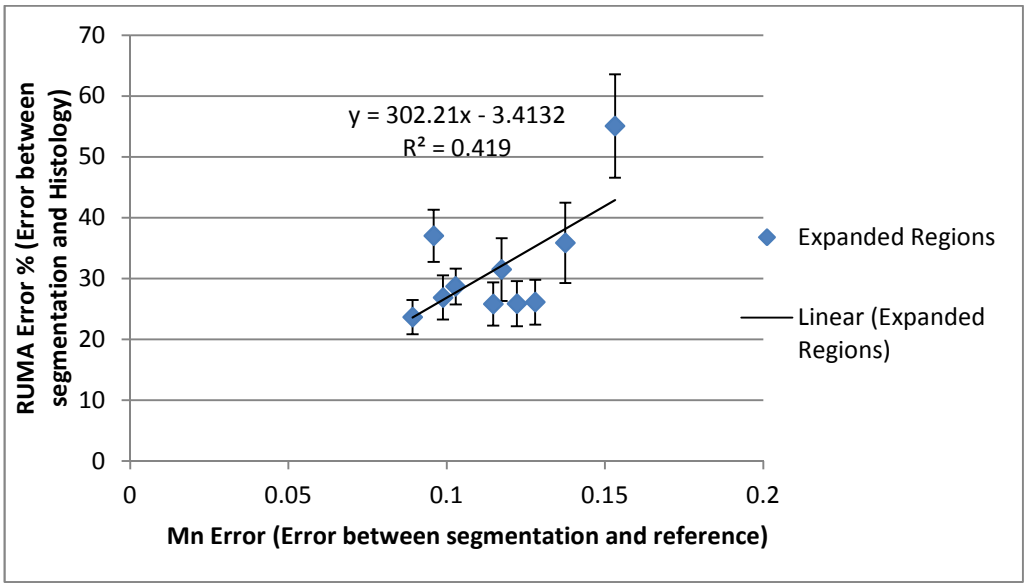

Figure 6-13 RUMA error against Mn error for expanded region segmentation methods.

With the colour map overlay segmentation methods (Section 4.1.2.3) the ten calibration with the lowest Mn error were collected for each of the local variable pairing (the two dimensional and three dimensional methods were considered together) and their RUMA errors collected (Figure 6-14).

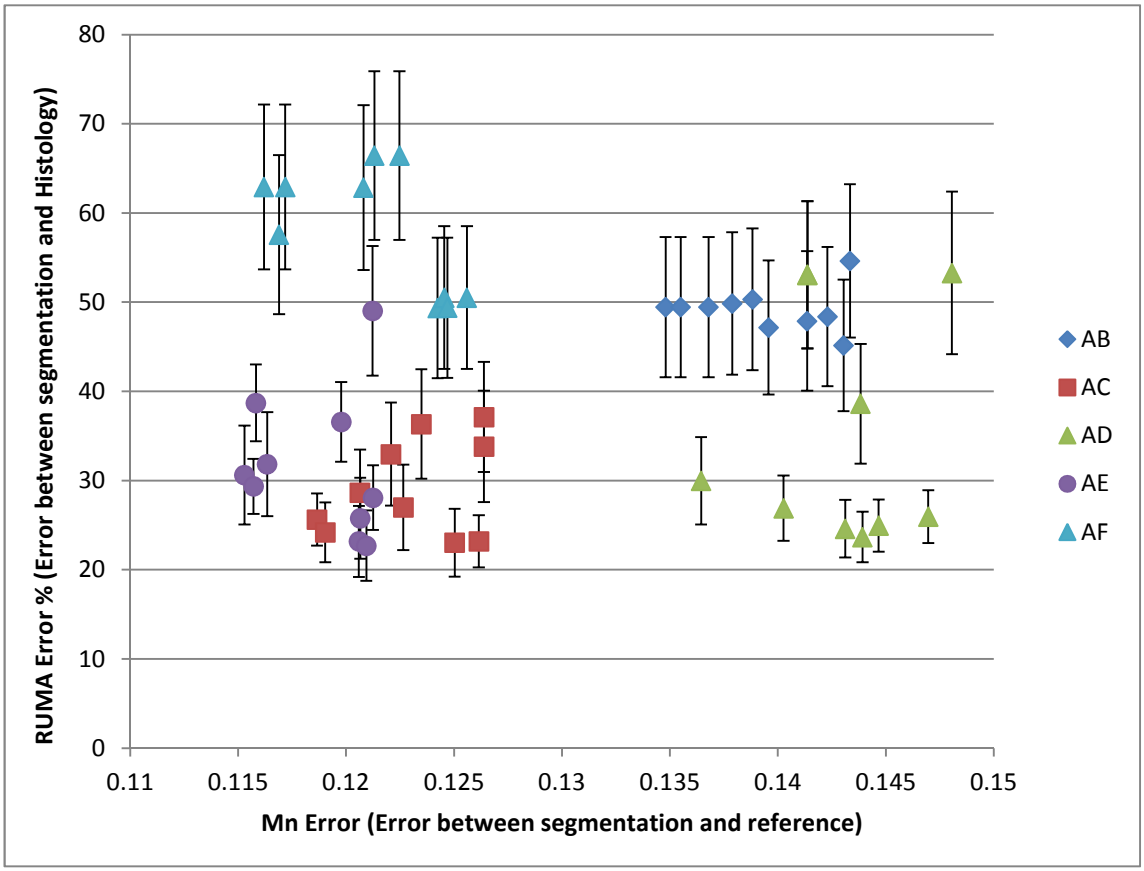

Figure 6-14 RUMA error against Mn error for colour map overlay method segmentation methods.

Figure 6-14 shows that the method of colour map overlay with the region map properties of AC, AD and AE all have calibrations with RUMA errors of below 30%. From these three only the method of AC has RUMA errors of under 40 % for all the ten calibrations and what appears to be a possible linear relationship between Mn and RUMA (Figure 6-15).

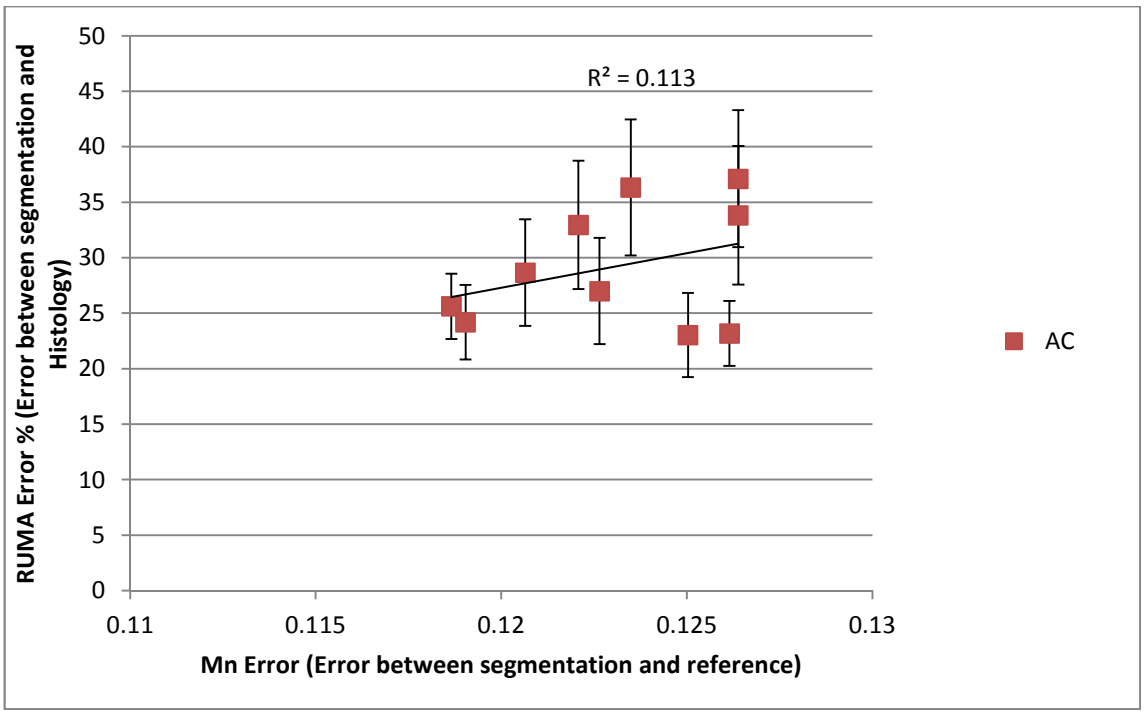

Figure 6-15 RUMA error against Mn error for the colour map overlay segmentation methods using the 10 AC calibrations with the lowest Mn errors.

This relationship between the Mn error and RUMA error for the colour maps of AC can be further seen when the sixty lowest Mn error calibrations of AC were compared to the RUMA errors (Figure 6-16).

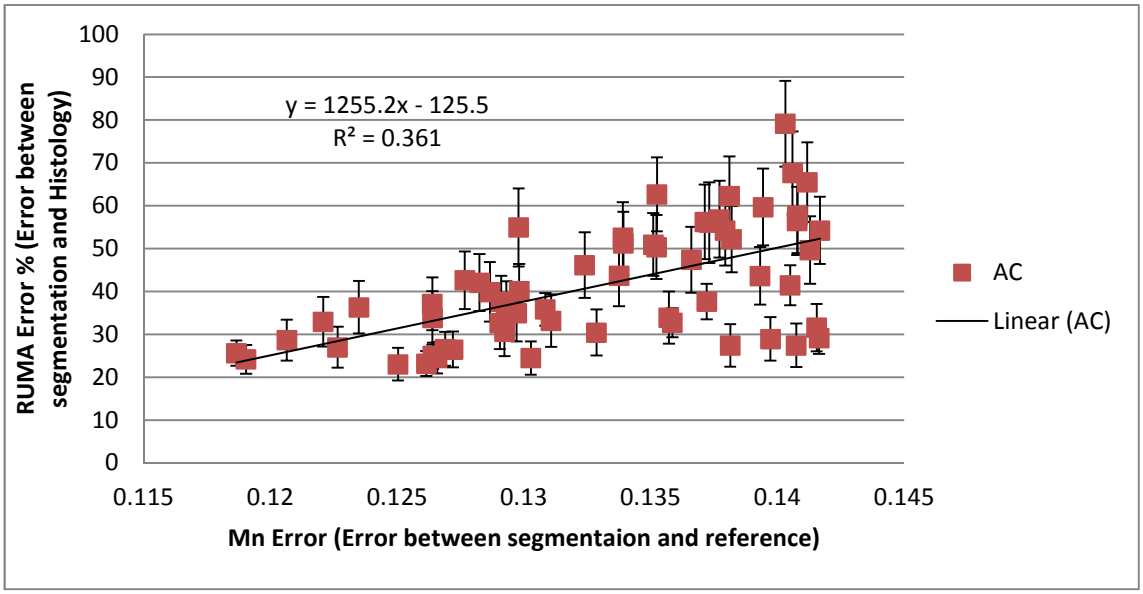

Figure 6-16 RUMA error against Mn error for the colour map overlay segmentation methods using the 60 AC calibrations with the lowest Mn errors.

Figure 6-16 shows that in general as the Mn error decreases for the AC calibrated orthotopic samples the RUMA error decreases and converges. This implies that as the

Mn value decreases the probability of the corresponding RUMA error being lower increases. While the expanded regions methods results in lower error RUMA and Mn error when compared to the Colour map methods there is a distinct difference between the output images when compared to the original CT slice (Figure 6-17) The AE expanded region method and the AC colour map overlay method, as well as the expanded AC region method (For further comparison) were compared for differences in the region shape and distribution, namely the amount of single voxel regions present in the expanded region methods (Figure 6-18, Figure 6-19 & Figure 6-20).

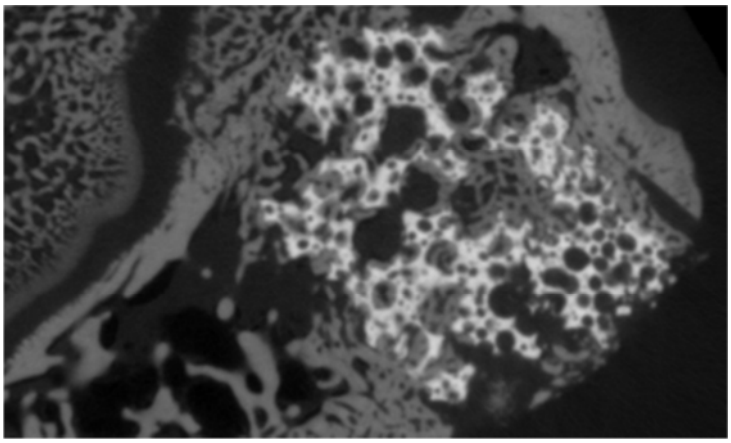

Figure 6-17 Slice of HA orthotopic sample of 80% total porosity and 10% strut porosity at 3 weeks.

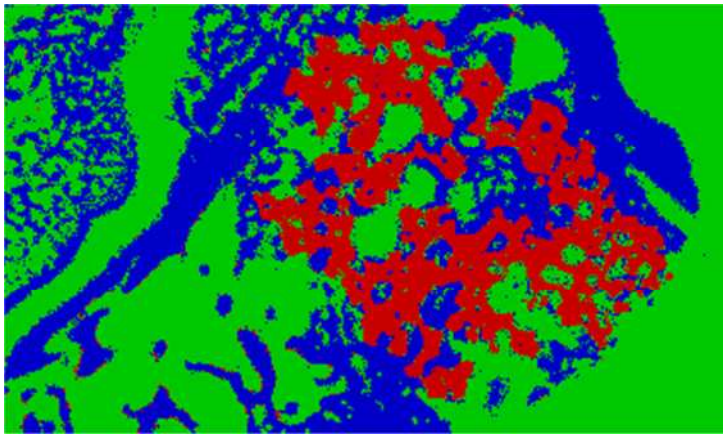

Figure 6-18 Slice of HA orthotopic sample of 80% total porosity and 10% strut porosity at 3 weeks segmented by region expanded method of calibration of AE3D.

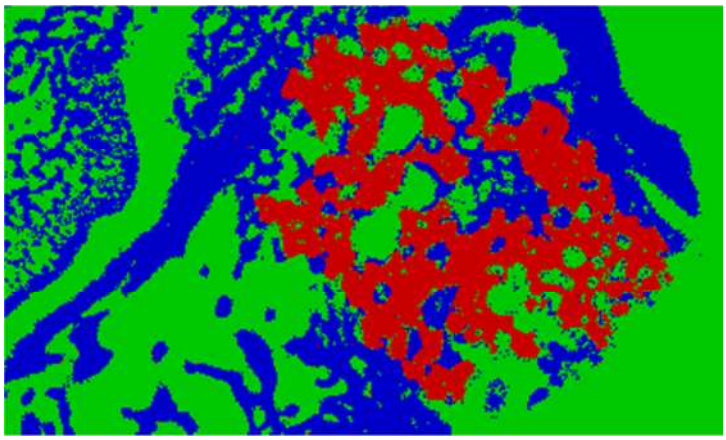

Figure 6-19 Slice of HA orthotopic sample of 80% total porosity and 10% strut porosity at 3 weeks segmented by region expanded method of calibration of AC3D

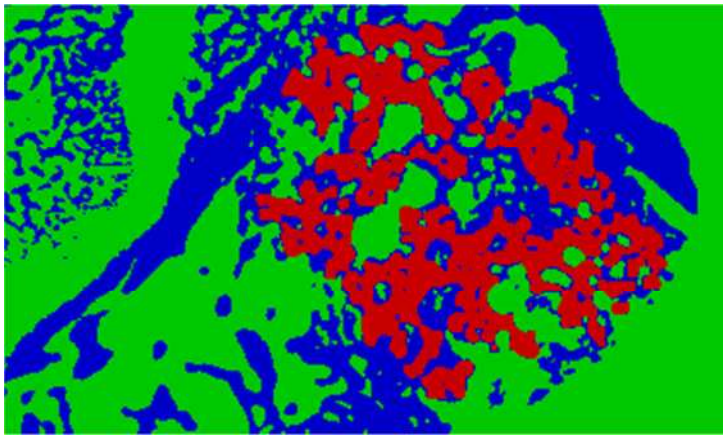

Figure 6-20 Slice of HA orthotopic sample of 80% total porosity and 10% strut porosity at 3 weeks segmented by colour map overlay method of the lowest Mn error calibration of AC.

The segmented slices produced from the expanded regions methods as seen in Figure 6-18 and Figure 6-19 show that the method produces multiple regions of size of only one (or a few) voxel(s). Figure 6-20 shows that the segmentation produced from the colour map overlay methods unlike the expanded region methods produces more continuous regions without the disconnected smaller regions.

These small regions especially the ones of SBG, cause misidentification of the VOIs of the samples as seen in Figure 6-21, Figure 6-22 & Figure 6-23.

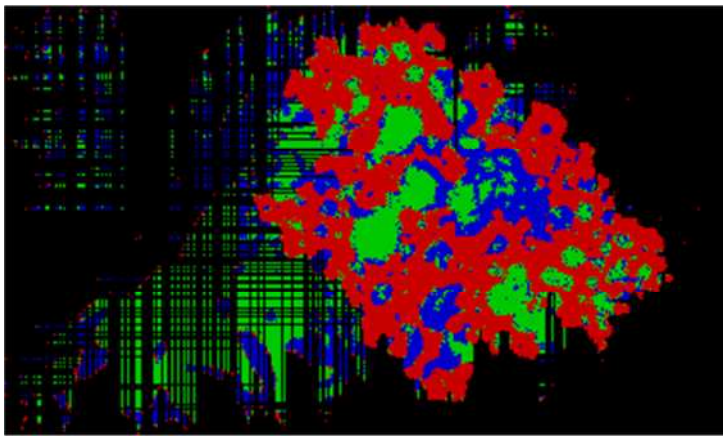

Figure 6-21 VOI of slice of HA orthotopic sample of 80% total porosity and 10% strut porosity at 3 weeks as determined by the region expanded region method of AE3D.

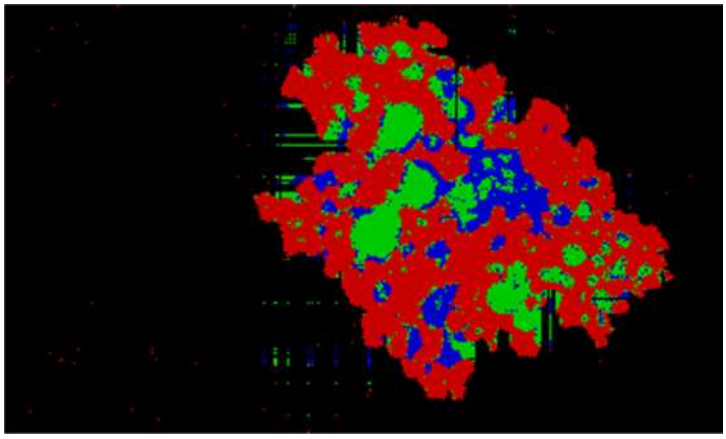

Figure 6-22 VOI of slice of HA orthotopic sample of 80% total porosity and 10% strut porosity at 3 weeks as determined by the region expanded region method of AC3D.

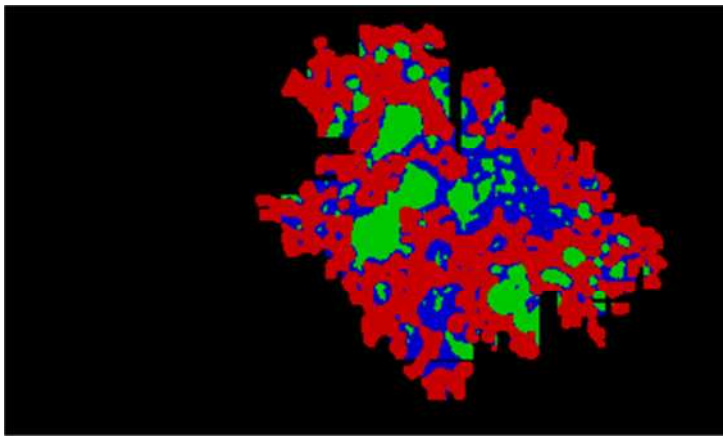

Figure 6-23 VOI of slice of HA orthotopic sample of 80% total porosity and 10% strut porosity at 3 weeks as determined by the region expanded region method of AC-0.

This misidentification of the VOIs when using the expanded regions method means that

the colour map method with the properties of AC was used to segment the samples.

The Ectopic sample set's calibration was also determined by identifying the AC colour map method with the lowest Mn error for all the reference ROIs, in this case also using a thirtieth ROI to take into account the "soft region" in the 30S sample, the calibration values are show in Table 6-3 and Figure 6-24.

Table 6-3 Mn error values and calibration of the colour map overlay methods with lowest Mn errors for orthotopic and ectopic samples.

	Mn	Calibration			
Orthotopic	0.119	AC	7_1	9_2	12_2
Ectopic	0.126	AC	15_2	9_3	12_3

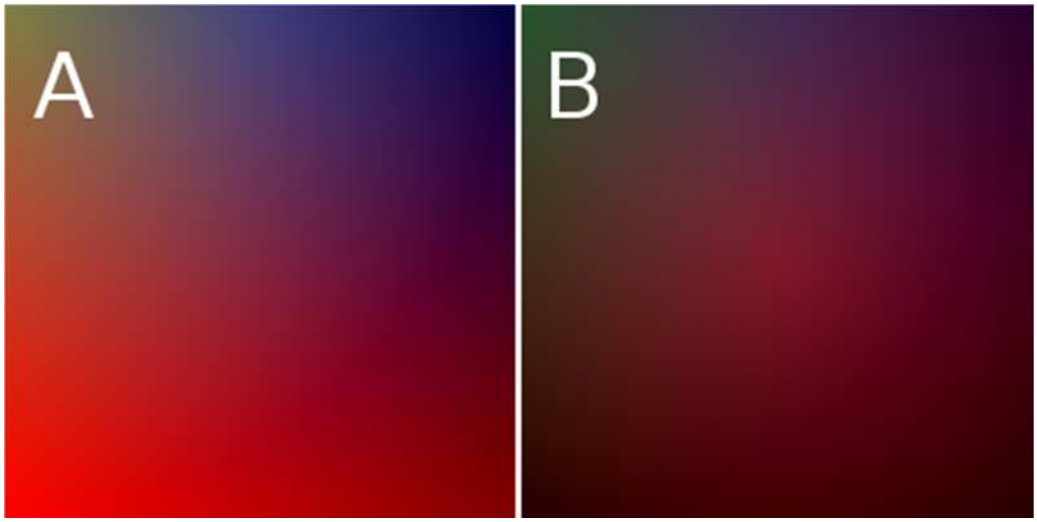

Figure 6-24 Colour map calibrations for A: Orthotopic and B: Ectopic samples.

By comparing the segmented images to the reference images the position of the discrepancies between the segmenting and the reference can be seen. This is shown in segmented images of Figure 6-25 and Figure 6-26, with the highlighted regions showing the segmented regions which are different to the reference image regions.

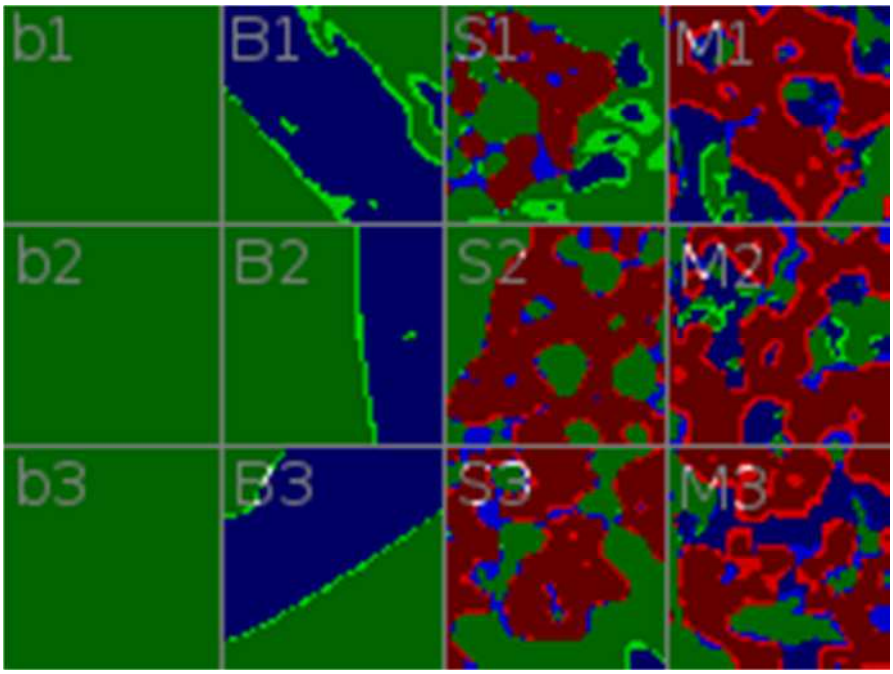

Figure 6-25 Comparison of automatically and User defined segmentations, defined by ROIs for orthotopic for b: background, B: Bone, S: SBG and M: Mixed regions, with differences in segmentations shown by highlighted regions.

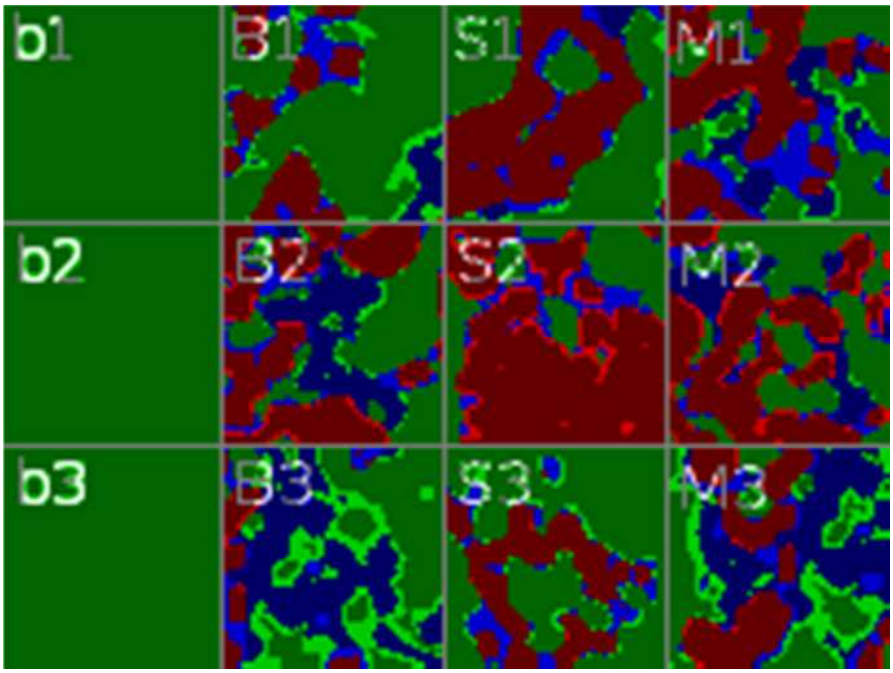

Figure 6-26 Comparison of automatically and User defined segmentations, defined by ROIs for ectopic for b: background, B: Bone, S: SBG and M: Mixed regions, with differences in segmentations shown by highlighted regions.

The comparison between the automatically segmented regions and the regions in the reference images (Figure 6-25 and Figure 6-26) shows that the differences happen most

at the bounders between regions. This can be related to the fact that because some of the voxels are a mix of multiple regions (Section 1.3.5.2) and each voxel in this method of segmentation is only identified as being of one of the three regions and not as a mix of regions, voxels which are a mix will have to be in one region or another, causing either under or over counting. While there is not continuous ghosting of bone around the SBG regions there are regions of bone being identified in the automated segmentation, which are not seen in the reference images. The reason for the appearance of these bone regions could be due to either partial filled voxel effect due the porous nature of the SBG, or due to miss-identification on the reference images. As the difference between the segmentations appear to be at the edges of the regions, the quantifications which are related to the whole shape of the samples should not be compromised, and any discrepancies should be uniform across all the samples, meaning that it should still be possible to perform intra-sample bone penetration quantification.

6.2 Specimens and Data Acquisition

Two different sets of specimens were used to validate the techniques, for full details of all samples and data protocols see Section 2.

6.2.1 X-ray micro tomography

All the samples were scanned as stated in Section 2, with resolution and settings as stated in Table 2-3 for each type of sample. The samples were trimmed to fit into the detector, whilst still retaining the sites of interest.

6.2.2 Scanning electron microscopy

For additional inspect of the ectopic samples scanning electron microscopy was performed (SEM). All the images were collected on a FEI Inspect-F Scanning electron microscope.

The samples were taken from animals models in the form of histology samples and were polished by using increasingly fine grit polishing pads (up to 3 micron grit size), on a motorised polishing wheel to level out the samples. The samples were then gold coated before being imaged.

The SEM was used at 100 and 800 times magnification at 20kV and 10mm working distance in backscatted mode to clearly show the difference between the bone and the

SBG. The reason for using backscatted mode rather than secondary electron mode can be seen in Figure 6-27.

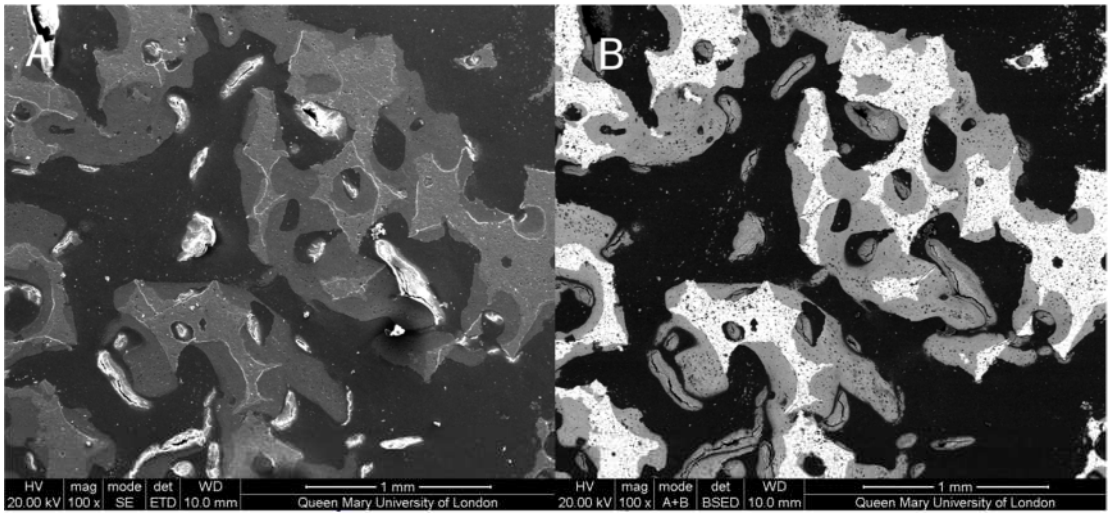

Figure 6-27 A: Secondary electron mode B: Back scatter mode of SEM imaging of 80-30 SA sample in ectopic sites after 12 weeks imaging at 100x and 20kV

Figure 6-27 shows that for the flat SA ectopic samples the back scattering mode shows clearly the SBG and bone and their shapes, with the SBG showing up as white and the bone as grey, while the boundaries are harder to discern in secondary imaging mode.

6.3 Data Analysis

The sample sets were segmented using the colour map overlay segmentation method using the calibration as stated in Section 6.1.

The samples sets will be split into three groups for analysis the HA orthotopic samples, SA orthotopic samples and SA ectopic samples.

The measurements as stated in Table 5-9 were evaluated from the segmented volume of interest (VOI) for each sample set except for the porosity measurements for the ectopic samples which is explained further in the respective section 6.3.3.

The empty orthotopic samples were not used in this section as they were scanned at different resolution to the other orthotopic samples and as such cannot be directly compared. As there is only one repeat of sample types in the orthotopic sample sets namely the SA 1.5 wt% sample, for that sample the line is plotted as the average of the samples at each time point, with the individual sample values being plotted as points. For the distribution measurements the SA 1.5 wt% samples are viewed as two separate samples, so that their trends can be clearly seen.

All the raw data can be found in the Appendix.

6.3.1 Evaluation of HA Orthotopic Samples

6.3.1.1 Volume and Surface Area Measurements

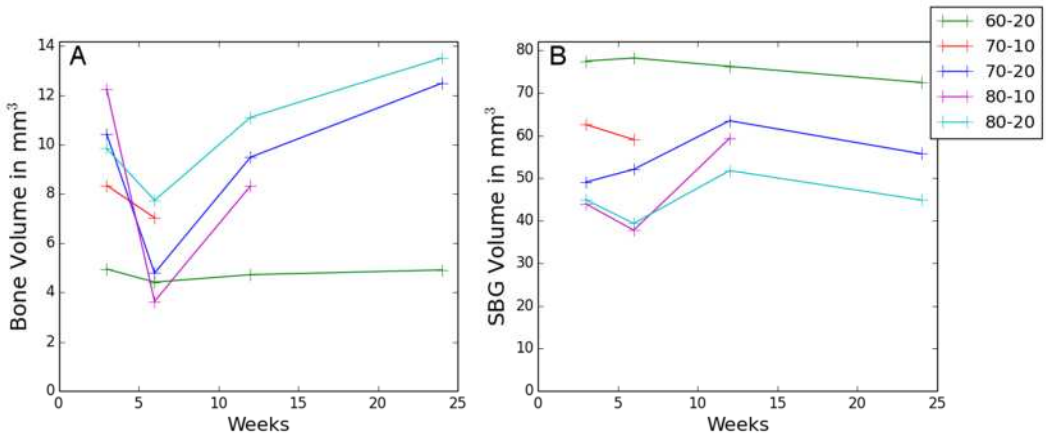

Figure 6-28 A: Bone volume in Microns, B: SBG Volume in microns for HA orthotopic samples over time.

Figure 6-28 A shows that the bone growth in the HA orthotopic samples follow a similar pattern for all the samples apart from the 60-20 (which only shows this pattern slightly), which is a decrease in bone volume from 3 to 6 weeks followed by an increase from 6 to 12 weeks with a slower increase from 12 to 24 weeks (unconfirmed in 70-10 as no data for 12 & 24 weeks). In the order of bone volume produced at 3 weeks the 80-10 has the most bone volume, followed by 70-20, 80-20, 70-10 and 60-20. After 6 weeks (ignoring the 60-20 as it does not present the large drop in bone volume at 6 weeks) the order appears to be 80-20, 70-10 (not enough data point to determine the trend after 6 weeks), 70-20, 80-10.

Figure 6-28 B shows that the 60% porosity samples have the highest volume of SBG followed by 70% and 80%, which is expected, assuming they were all originally the same shape cylindrical implants. Interestingly the amount of SBG does not remain constant over time and more interestingly seems to increase with the 70-20, 80-10 and 80-20 samples. This increase could be due to the edge misidentification in the segmentation methods (Section 6.1).

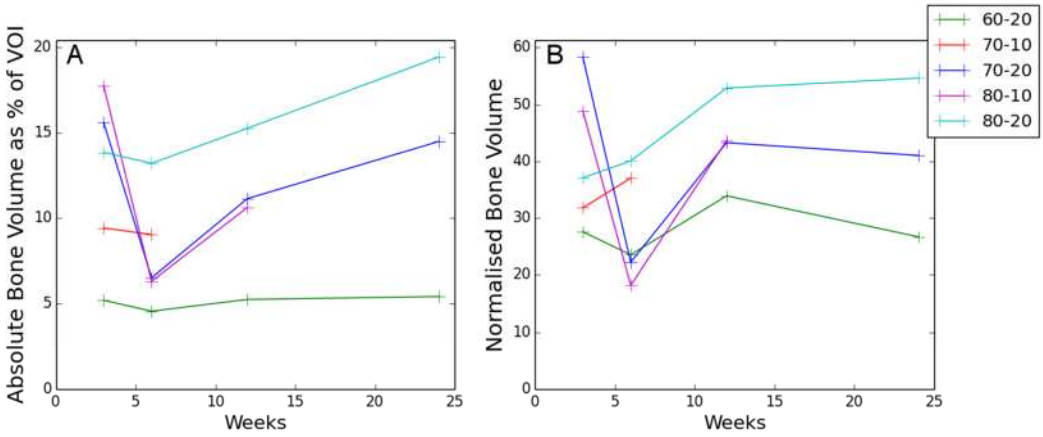

Figure 6-29 A: Absolute Bone volume as % of VOI, B: Normalised Bone volume for HA orthotopic samples over time.

Figure 6-29 A shows the change in bone volume as a percentage of the VOI, this shows that the characteristic shape of the trends which was clear in the volume measurement (Figure 6-28), is again present but with the differences in the severities of change at 6 weeks being clearer, with 70-20 and 80-10 showing a sharp decrease at 6 weeks and 60-20, 70-10 & 80-20, showing a still identifiable but less sharp drop. The order of the amount of bone as a percentage of the VOI at 3weeks is 80-10, 70-20, 80-20, 70-10 and 60-20. From 6 weeks the order changes to: 80-20, 70-10, 70-20, 80-10 and 60.20.

Figure 6-29 B shows the change in normalised bone volume, the trends in this case again show the sharp change at 6 weeks for 70-20 and 80-10, but the samples of 70-10 and 80-20 show an increase at 6 weeks. The order of the amount of bone at 3 weeks from most to least is 70-20, 80-10, 80-20, 70-10 and 60-20, while the order from 6 weeks from most to least is 80-20, 70-10, 70-20, 80-10 with 60-20 being higher than 70-20 and 80-10 at 6 weeks and lower afterwards.

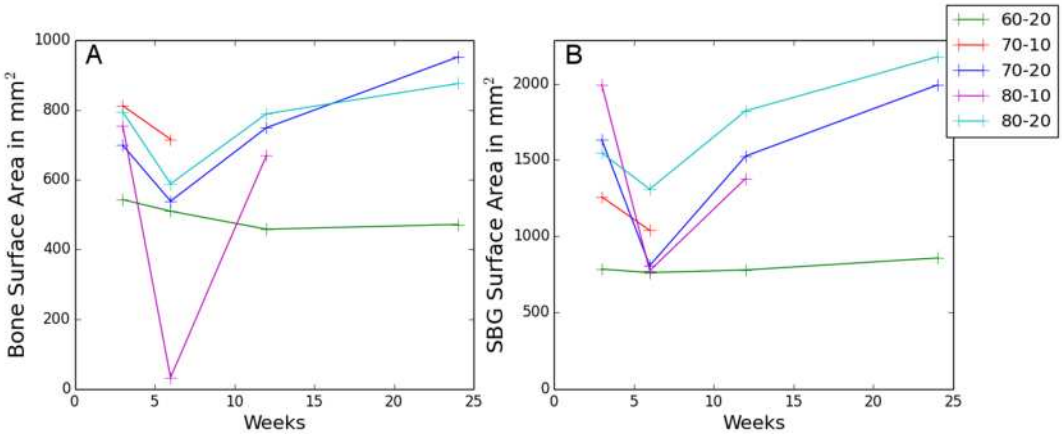

Figure 6-30 A: Bone surface area in microns, B: SBG surface area in microns for HA orthotopic samples over time.

Figure 6-30A shows that there is a change in surface area of the bone at 6 week similar to the change in volume for samples of 70-10, 70-20, 80-10 and 80-20 with the drop of the 80-10 sample being the most severe. At 3 weeks the order of highest to lowest bone surface area is 70-10, 80-20, 80-10, 70-20 and 60-20. While at 6 weeks the order from highest to lowest is 70-10, 80-20, 70-20, 60-20 and 80-10.

Figure 6-30B shows the change in surface area for the SBG show a similar trend as the Bone surface area for the samples, with the drop at 6 weeks. The order of the SBG surface area at 3 weeks from largest to lowest is 80-10, 70-20, 70-10 and 60-20. After 6 weeks the order is 80-20, 70-10, 70-20, 80-10 and 60-20. The similarities between the bone and SBG's surface area will be further discussed in Section 6.3.4.1.

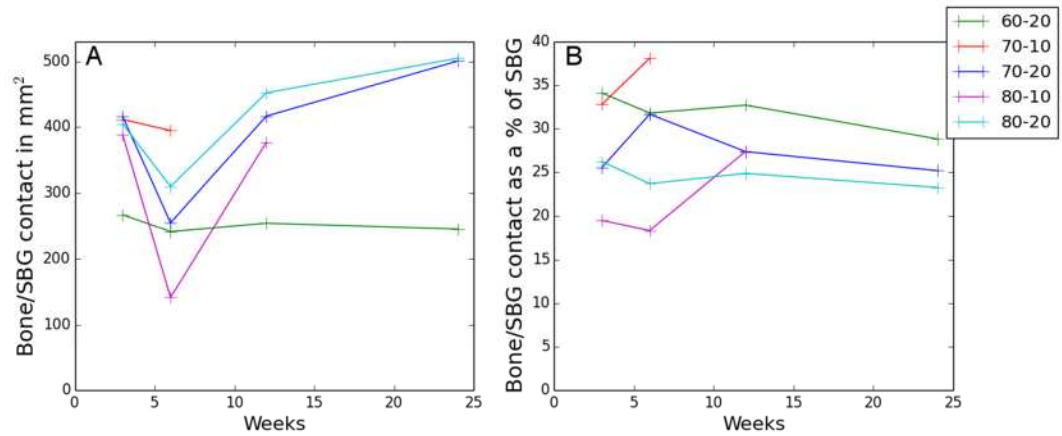

Figure 6-31 A: Bone/SBG contact area in microns, B: Bone/SBG contact area as percentage of SBG surface area microns for HA orthotopic samples over time.

Figure 6-31 A shows the contact area of the Bone and SBG exhibit the sample trend of a drop at 6 weeks as seen in the bone volume change (Figure 6-28) the order of the

contact area from highest to lowest at 3 week is 70-20, 70-10, 80-20, 80-10 and 60-20. The order at 6 weeks is 70-10, 80-20, 70-20, 60-20 and 80-10, and the 80-10 sample increases above the 60-20 sample after 6 weeks.

Figure 6-31 B shows the Bone/SBG contact area as a percentage of the SBG's surface area both the 70-10 and 70-20 samples increased from 3 to 6 weeks, while the 60-20, 80-10 and 80-20 samples all decrease slightly at 6 weeks followed by a slight increase then decrease.

6.3.1.2 Distribution Measurements

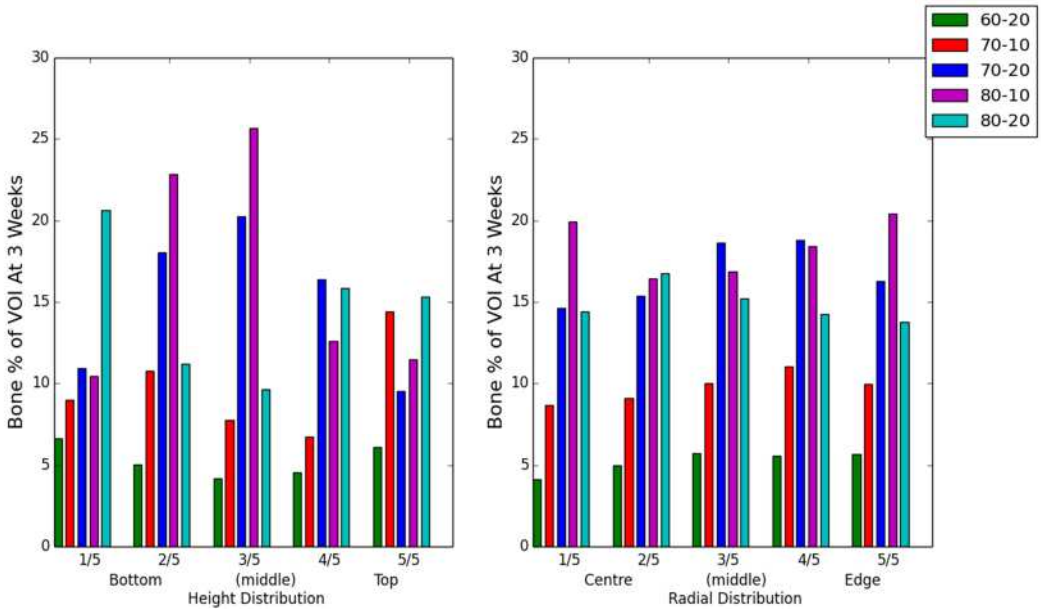

Figure 6-32 A: Height distribution of Bone as a percentage of VOI, B: Radial distribution of Bone as a percentage of VOI for HA orthotopic samples at 3 weeks.

Figure 6-32 A shows the height distribution of the bone as a percentage of the VOI for the HA orthotopic samples at 3 weeks, for the 70-20 and 80-10 samples there is more bone growth in the middle of the height distribution than at either the top or bottom. While for the 60-20, 70-10 and 80-20 there is more growth at the top and bottom of the cylinder.

Figure 6-32 B shows the radial distributing of the bone as a percentage of VOI for the HA samples at 3 weeks, for the 60-20, 70-10 and 70-20 samples there is a slight trend of more bone at the edge of the sample compared to the centre, with the 70-20 showing more bone at the 4/5 position. While the 80-10 sample has as much bone growth in the centre as at the edge with an increase of the other regions from centre to edge and the 80-20 sample peaks at the 2/5 position from the centre.

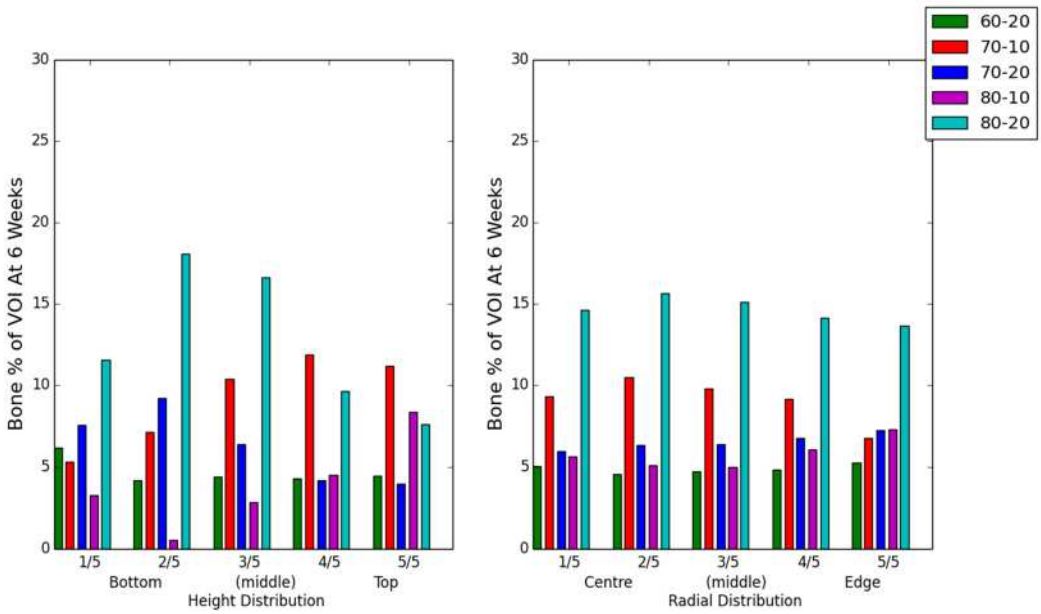

Figure 6-33 A: Height distribution of Bone as a percentage of VOI, B: Radial distribution of Bone as a percentage of VOI for HA orthotopic samples at 6 weeks.

Figure 6-33 A shows the height distribution of the bone as a percentage of the VOI for the HA orthotopic samples at 6 weeks, the 60-20 and 70-20 samples both show more bone at the bottom, with the 70-10 and 80-10 showing more bone at the top than at the bottom, and the 80-20 sample shows more bone in the bottom-middle.

Figure 6-33 B shows the radial distribution of the bone as a percentage of the VOI for the HA orthotopic samples at 6 weeks, both the 70-20 and 80-10 show a slight increase in bone from the centre to the edge. The 70-10 and 80-20 both show more bone at 2/5 from the centre with the lowest about of bone being at the edge, the 60-20 has slightly more bone at the centre and edge than in the middle regions.

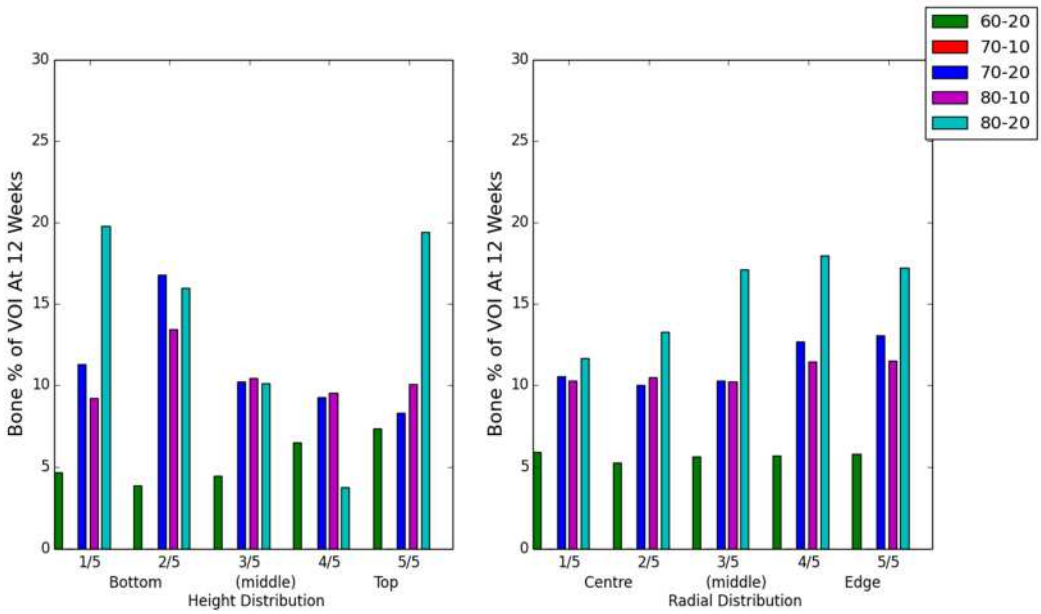

Figure 6-34 A: Height distribution of Bone as a percentage of VOI, B: Radial distribution of Bone as a percentage of VOI for HA orthotopic samples at 12 weeks.

Figure 6-34 A shows the height distribution of the bone as a percentage of the VOI for the HA orthotopic samples at 12 weeks, both the 70-20 and 80-10 samples show more bone at the 2/5 position from the centre, with the 60-20 sample showing a slight trend of more bone at the top and the 80-20 samples having more bone at the top and bottom compared to the middle.

Figure 6-34 B shows the radial distribution of the bone as a percentage of the VOI for the HA orthotopic samples at 12 weeks, the 70-20, 80-10 and 80-20 samples show more bone at the edge than in the centre of the samples, while the 60-20 shows only a slight increase in bone in the centre over the rest of the sample.

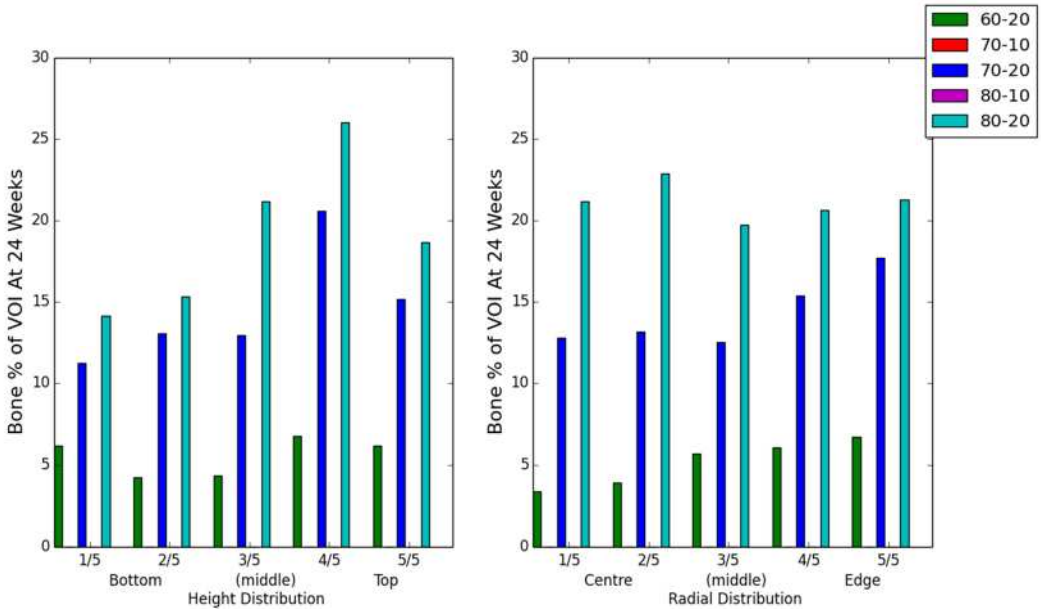

Figure 6-35 A: Height distribution of Bone as a percentage of VOI, B: Radial distribution of Bone as a percentage of VOI for HA orthotopic samples at 24 weeks.

Figure 6-35 A shows the height distribution of the bone as a percentage of the VOI for the HA orthotopic samples at 24 weeks, both the 70-20 and 80-20 samples show a higher amount of bone at the top compared to the bottom, while the 60-20 has more bone at the top and bottom compared to the middle.

Figure 6-35 B shows the height distribution of the bone as a percentage of the VOI for the HA orthotopic samples at 24 weeks, both the 60-20 and 70-20 show a trend for more bone at the edge than in the centre of the samples while the 80-20 shows more bone in the centre than at the edge.

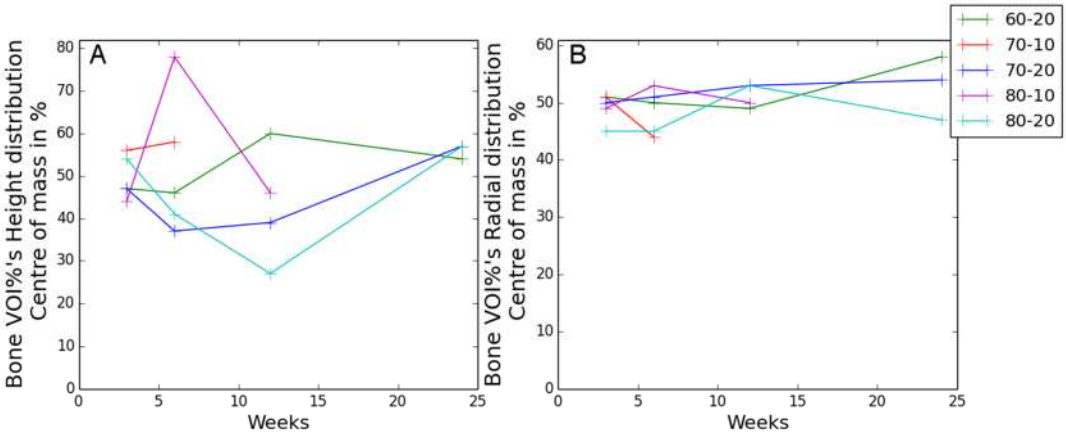

Figure 6-36 A: Height distribution of Bone as a percentage of VOI's centre of mass, B: Radial distribution of Bone as a percentage of VOI s centre of mass for HA orthotopic samples over time.

Figure 6-36 A shows the centre of mass of the height distribution of the bone from 3 to 6 weeks shows that the 70-10 and 80-10 samples have their centre of masses shifted towards the top of the samples while the 60-20, 70-20 and 80-20 all have theirs shifted towards the bottom of the sample. After 6 weeks the distributions all move towards the 50 percent.

Figure 6-36 B shows that for all the samples at all time points the centre of mass for the radial direction do not shift by more than 10% from the middle. With the 60-20 sample seeming to shift towards the edge at 24 weeks and the 80-20 seeming to shift towards the centre at 24 weeks.

6.3.1.3 Structural and Shape Measurements

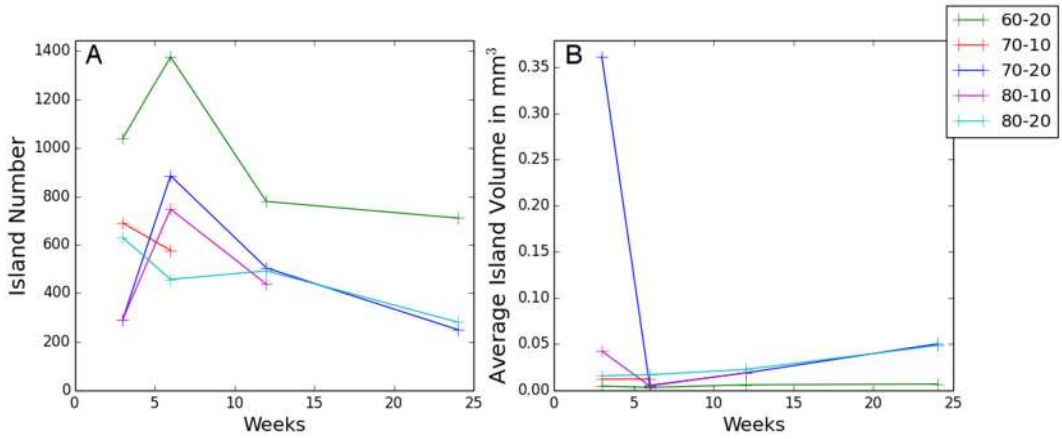

Figure 6-37 A: Island number of Bone, B: Average island volume in microns for HA orthotopic samples over time.

Figure 6-37 A shows that the island number increase from 3 to 6 weeks for the samples of 60-20, 70-20 and 80-10, while decreasing for the samples of 70-10 and 80-20. From 6 to 12 weeks, 60-20, 70-20 and 80-10 decrease, while the 80-20 sample increases. From 12 to 24 weeks 60-20, 70-20 and 80-20 all decrease.

Figure 6-37 B shows that the average island volume from 3 to 6 weeks has a sharp decrease for samples of 80-10 and especially 70-20-10 while remaining relatively constant for the samples of 60-20, 70-10 and shows a slight increase for 80-20.

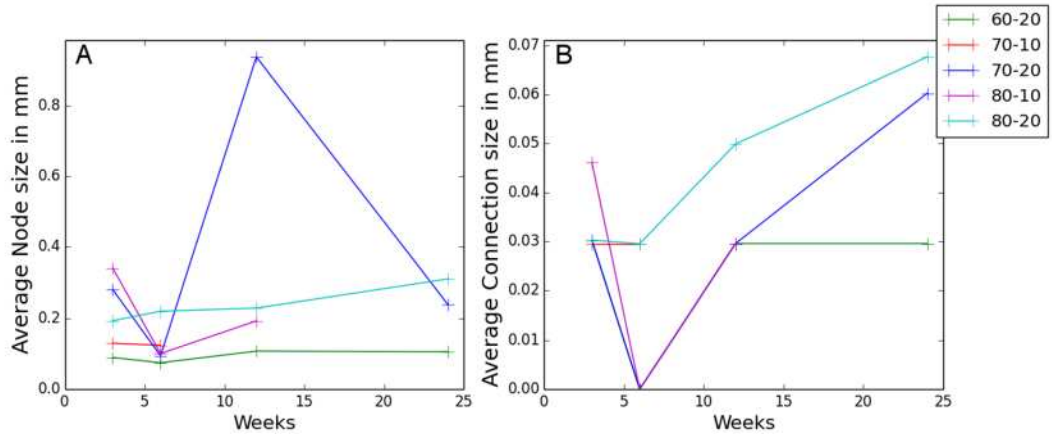

Figure 6-38 A: Average Node size of Bone in mm, B: Average Connection size of Bone in mm for HA orthotopic samples over time.

Figure 6-38 A shows that from 3 to 6 weeks the average node size of the samples of 60-20, 70-10, 70-20 and 80-10 show a decrease in size (with 60-20 and 70-10 showing a smaller decrease than the other two), while 80-20 shows a slight increase. After 6 weeks the 70-20 shows a sharp increase in node size followed by a drop, while the 60-20, 80-10 and 80-20 samples show a general increase.

Figure 6-38 B shows that from 3-6 weeks the average connection size drops to zero for the samples of 60-20, 70-20 and 80-10, while the samples of 70-10 and 80-20 show either a slight decrease or no change in connectivity. After 6 weeks the samples of 70-20 and 80-20 increase while the 60-20 sample remains constant.

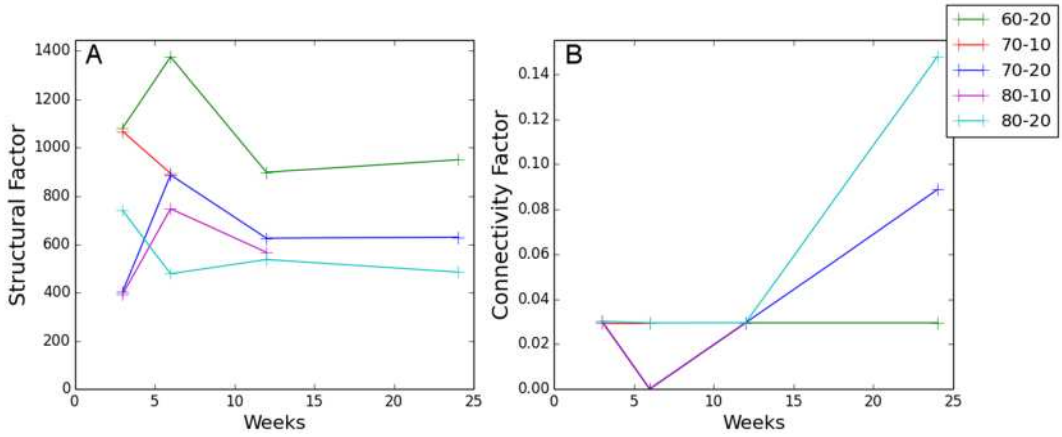

Figure 6-39 Structural Factor for Bone, B: connectivity Factor in mm for HA orthotopic samples over time.

Figure 6-39 A shows that structural factor from 3 to 6 weeks increases sharply for 60-20, 70-20 and 80-10, while decreasing for the samples of 70-10 and 80-20. After 6

weeks the samples with the sharp increase show a decrease while the sample with the decrease shows an increase.

Figure 6-39 B shows that from 3 to 6 weeks the samples of 60-20, 70-20 and 80-10 go to having a connectivity factor of zero while the samples of 70-10 and 80-20 retain a constant connectivity factor. At 12 weeks all the data shows the same connectivity factor as at 3 weeks with 70-20 and 80-20 increasing from 12 to 24 weeks and 60-20 remaining constant.

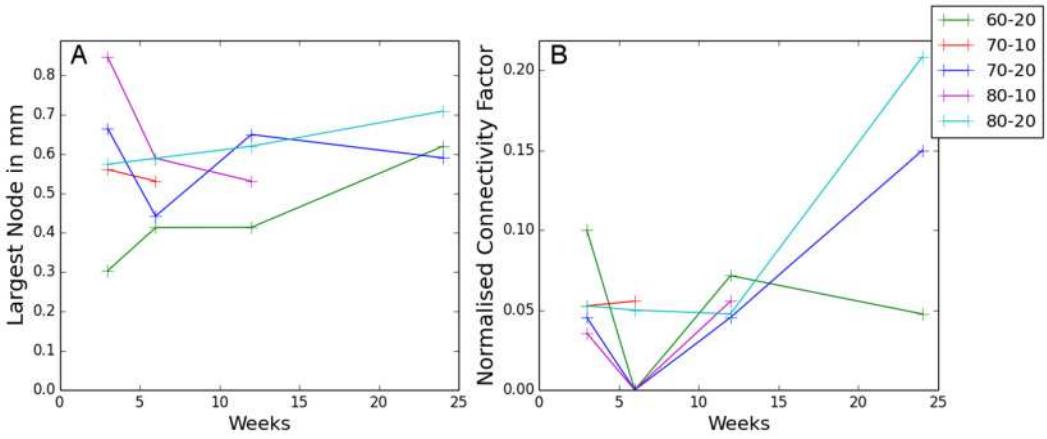

Figure 6-40 A: Largest Node size for Bone in mm, B: Normalised connectivity Factor in for HA orthotopic samples over time.

Figure 6-40 A shows that the largest node in the samples of 60-20 and 80-20 increases from 3 to 24 weeks with the 80-20 showing a smoother increase than the 60-20. The samples of 70-10, 70-20 and 80-10 all show a decrease in largest node size from 3 to 6 weeks with 70-20 then showing an increase to 12 weeks followed by a decrease to 24 weeks.

Figure 6-40 B shows that from 3 to 6 weeks the samples of 60-20, 70-20 and 80-10 normalised connectivity factors go to zero while the 80-20's factor has a slight decrease and the 70-10's factor has a slight increase. After 6 weeks the samples which had a normalised connectivity factor of zero all increase with only the 60-20 showing a decrease after 12 weeks.

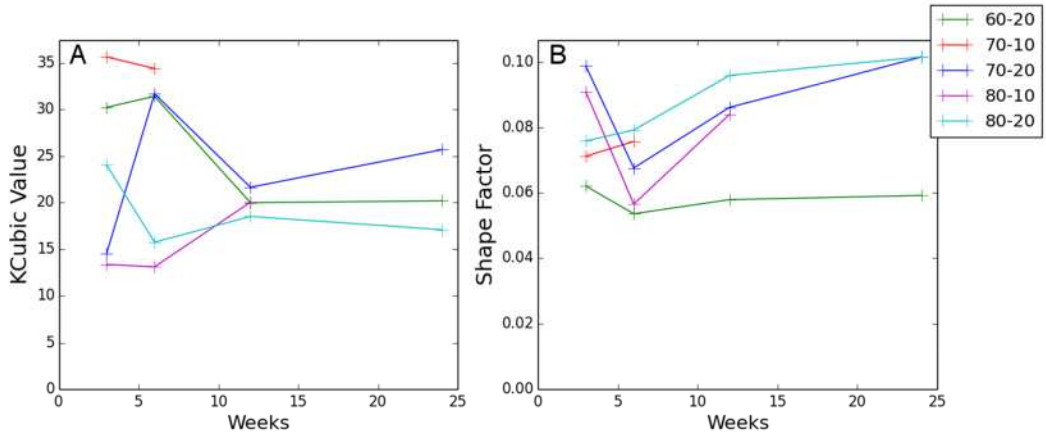

Figure 6-41 A: KCubic value for Bone, B: MAV derived Shape factor for HA orthotopic samples over time.

Figure 6-41 A shows that from 3 to 6 weeks the Kcubic values for the 70-20 sample there is a sharp increase, while the 60-20 shows a slight increase. Both the 70-10 and 80-10 samples show slight decreases in their Kcubic values from 3 to 6 weeks while the 80-20 shows a sharp decrease. All the samples go to values of around 20 at 12 weeks with the 70-20 increasing, the 80-20 decreasing and the 60-20 staying relatively constant.

Figure 6-41 B shows that from 3 to 6 weeks both 70-20 and 80-10 show a sharp drop in shape factor while the 60-20 shows a smaller decrease while both 70-10 and 80-20 show slight increases. After 6 weeks all the samples either show an increase or in the case of 60-20 remain approximately constant.

6.3.1.4 Porosity Measurements

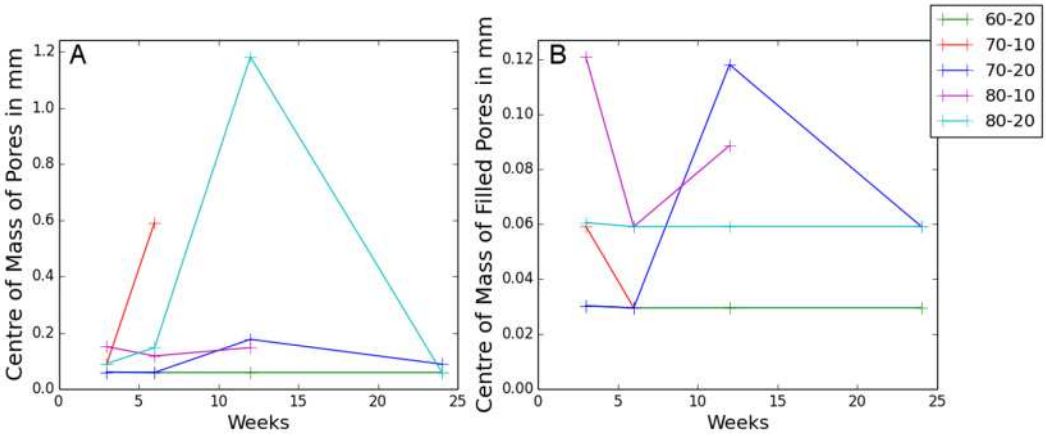

Figure 6-42 A: Centre of mass of pores, B: centre of mass of filled pores for HA orthotopic samples over time.

Figure 6-42 A shows that from 3 to 6 weeks there is an increase in the geometric centre of mass of the pores for the samples of 70-10 and 80-20, with 80-10 showing a decrease and 60-20 and 70-20 remaining constant. From 6 to 12 weeks 80-10 shows a slight increase, while 70-20 shows a larger increase and 80-20 shows the largest increase, with 60-20 remaining constant. At 24 weeks the 80-20's value drops to the sample as the 60-20 and the 70-20 decreases slightly and the 60-20 remains the same.

Figure 6-42 B shows that both the centre of mass for the filled from 3 to 6 weeks decreases for 70-10 and 80-10, while remaining approximately constant for 60-20, 70-20 and 80-20. From 6 to 24 weeks both 60-20 and 80-20 remains approximately constant, while the 70-20 shows a sharp increase to 12 weeks then a decrease at 24 weeks to the same value as the 80-20 sample.

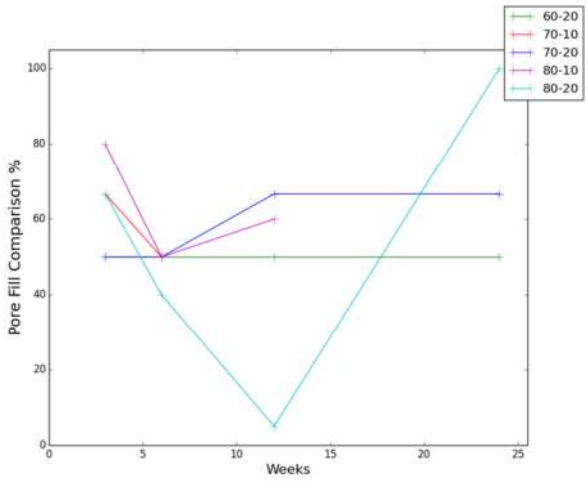

Figure 6-43 Pore fill comparison in percentage for HA orthotopic samples over time.

Figure 6-43 shows that from 3 to 6 weeks the samples of 70-10, 80-10 and 80-20 all decrease in pore fill comparisons while 60-20 and 70-20 remaining approximately constant. From 6 weeks the 70-20 and 80-10 samples show an increase, while the 60-20 sample stays with an approximately constant value and the 80-20 sample decreases to 12 weeks before increasing to the highest value at 24 weeks.

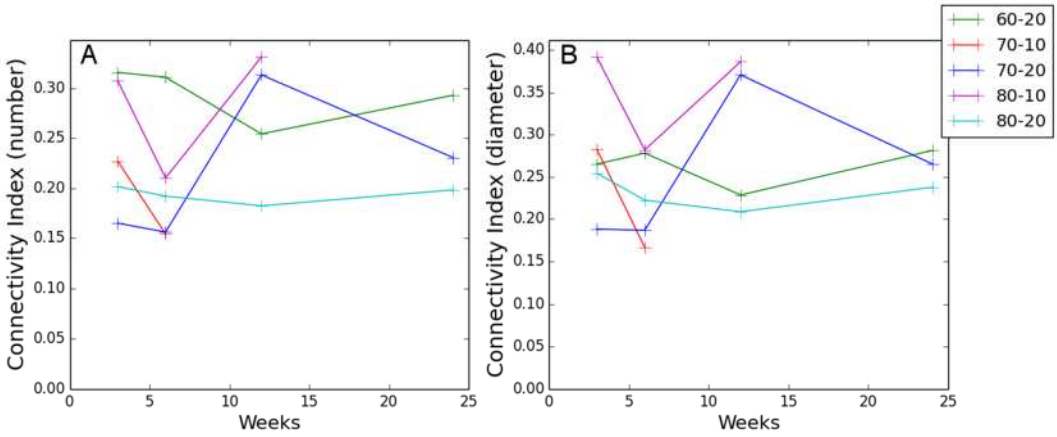

Figure 6-44 A: Connectivity Index (number), B: Connectivity Index (diameter), for HA orthotopic samples over time.

Figure 6-44 A shows that from 3 to 6 weeks all the connectivity index values decrease, with 70-20 and 80-10 increasing from 6 to 12 weeks and 60-20 and 80-20 decreasing. From 12 to 24 weeks the 70-20 decreases, while the 60-20 and 80-20 both increases slightly.

Figure 6-44 B shows that the diameter based connectivity index has a similar trend as the number based connectivity index, but has a higher values for 80-20, and a lower value for the 60-20.

6.3.2 Evaluation of SA Orthotopic Samples

6.3.2.1 Volume and Surface Area Measurements

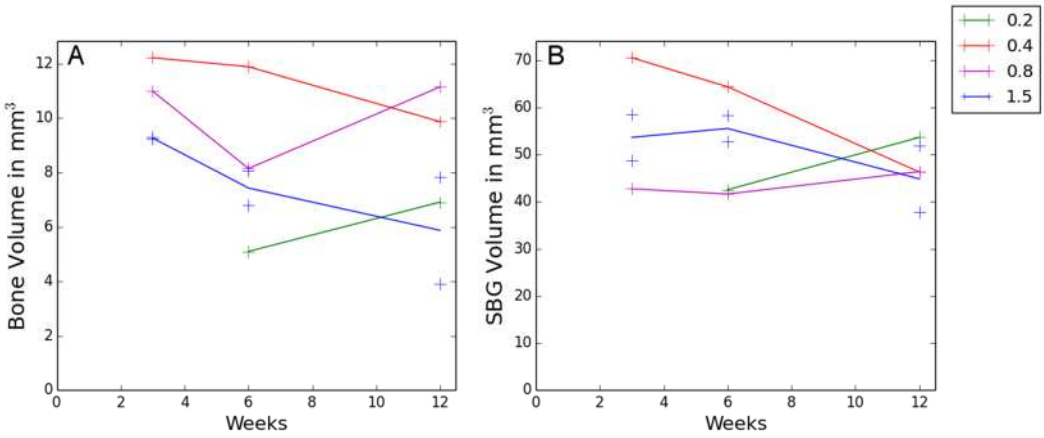

Figure 6-45 A: Bone volume in Microns, B: SBG Volume in microns for SA orthotopic samples over time.

Figure 6-45 A shows that, there does not appear to be and general trend with the change in bone volume with the samples and only the 0.8 sample has a similar trend to the HA

orthotopic samples, with a drop at 6 weeks followed by an increase. At 3 and 6 weeks the order of bone volume from most to least is 0.4, 0.8, 1.5 and 0.2. After 6 weeks the order is 0.8, 0.4, 0.2 and 1.5.

Figure 6-45 B shows the change in volume of the SBG for the SA orthotopic samples, while it could be conceivable that the volume of the SBG would decrease with time, however the 0.2 sample show an increase in volume, this could be related to the error in the segmentation method (Section 6.1) and is discussed further in section 6.3.4.1.

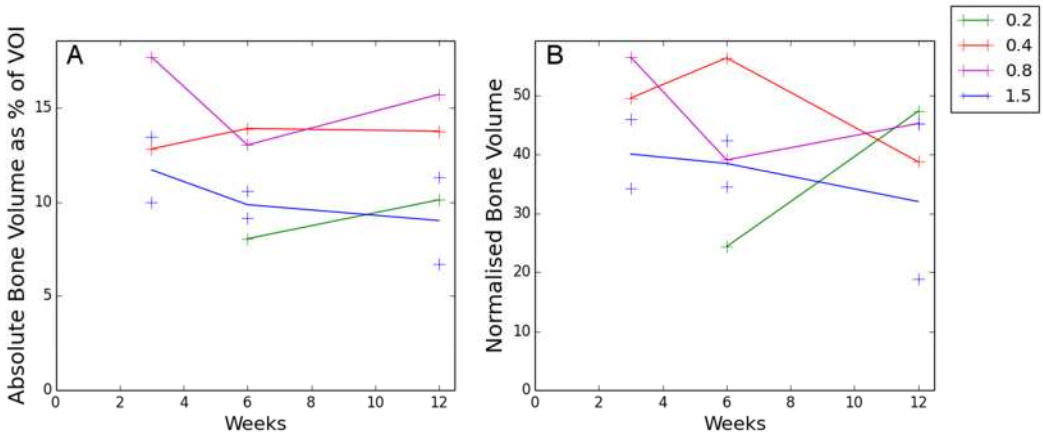

Figure 6-46 A: Absolute Bone volume as % of VOI, B: Normalised Bone volume for SA orthotopic samples over time.

Figure 6-46 A shows that both 0.8 and the 1.5 samples have a decrease in bone volume as a percentage of the VOI from 3 to 6 weeks (could also be true for the 0.2 sample but it does not have data for the 3 weeks sample), while the 0.4 sample shows an increase. From 6 to 12 weeks the samples of 0.2, 0.8 and 1.5 increases while the 0.4 sample decreases.

Figure 6-46 B shows that from 3 to 6 weeks the 0.4 sample has an increase in normalised bone volume, while the 0.8 and the 1.5 samples show a decrease. From 6 to 12 weeks 0.2, 0.8 samples increase while the 0.4 and the 1.5 decrease.

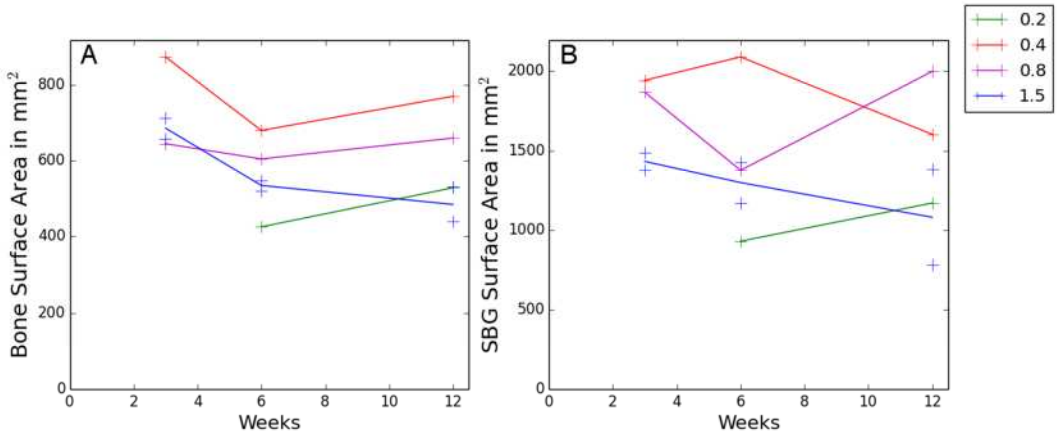

Figure 6-47 A: Bone surface area in microns, B: SBG surface area in microns for SA orthotopic samples over time.

Figure 6-47 A shows that for all the samples from 3 to 6 weeks there is a decrease in bone surface area, with 0.2, 0.4 and 0.8 all samples showing an increase after the 6 weeks and the 1.5 sample showing a decrease.

Figure 6-47 B shows that the 0.4 sample has an increase of SBG surface area from 3 to 6 weeks while the rest show a decrease. From 6 to 12 weeks the samples of 0.2 and 0.8 show an increase while the 0.4 and 1.5 samples show a decrease.

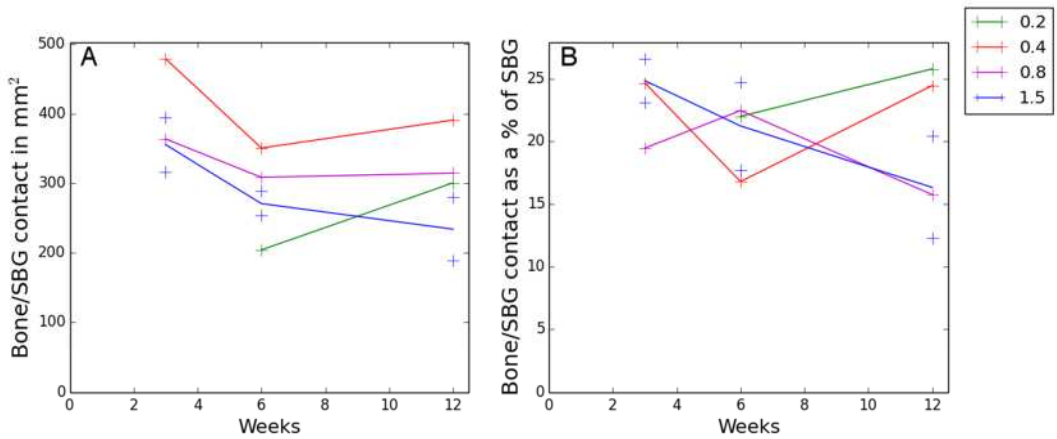

Figure 6-48 A: Bone/SBG contact area in microns, B: Bone/SBG contact area as percentage of SBG surface area microns for SA orthotopic samples over time.

Figure 6-48 A shows that from 3 to 6 weeks all the samples have a decrease in bone to SBG contact surface area, with 0.2, 0.4 samples increasing from 6 to 12 weeks. While the 1.5 sample shows a decrease from 6 to 12 weeks and the 0.8 sample stays approximately constant.

Figure 6-48 B shows that from 3 to 6 weeks the 0.4 and the 1.5 samples decrease, while

the 0.8 sample increases. From 6 to 12 weeks the 0.8 and the 1.5 samples decrease while the 0.2 and 0.4 samples increase.

6.3.2.2 Distribution Measurements

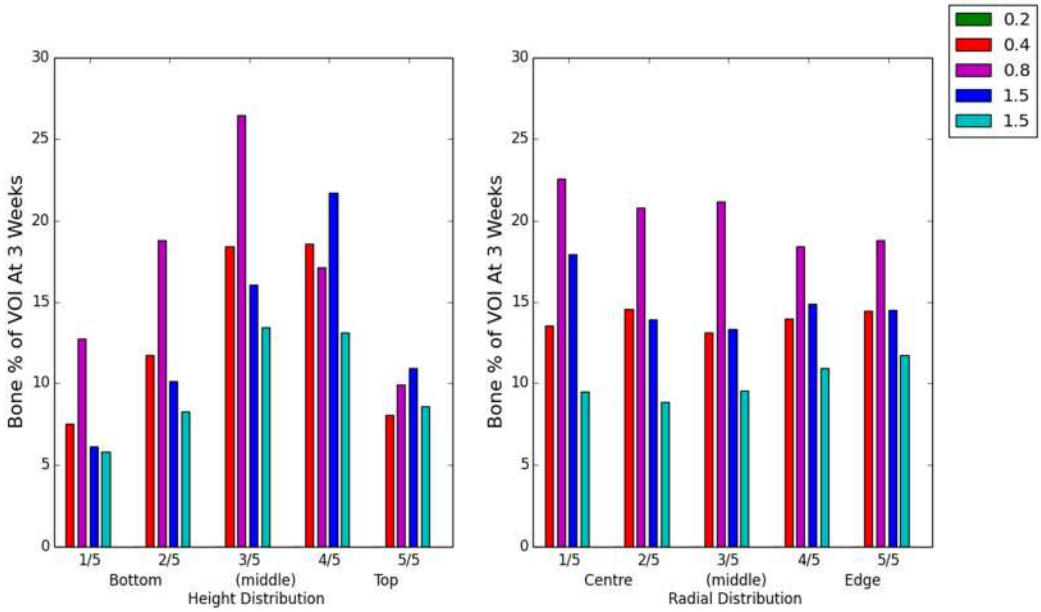

Figure 6-49 A: Height distribution of Bone as a percentage of VOI, B: Radial distribution of Bone as a percentage of VOI for SA orthotopic samples at 3 weeks.

Figure 6-49 A shows that at 3 weeks all the samples show higher amount of bone in the centre of the samples that at either the top or the bottom.

Figure 6-49 B shows that at 3 weeks the 0.8 and one of the 1.5 samples show higher bone amounts at the centre of the samples while the 0.4 shows only slightly higher amounts of bone at the centre than at the edge with less bone in the middle, while the other 1.5 sample shows more bone at the edge than in the centre.

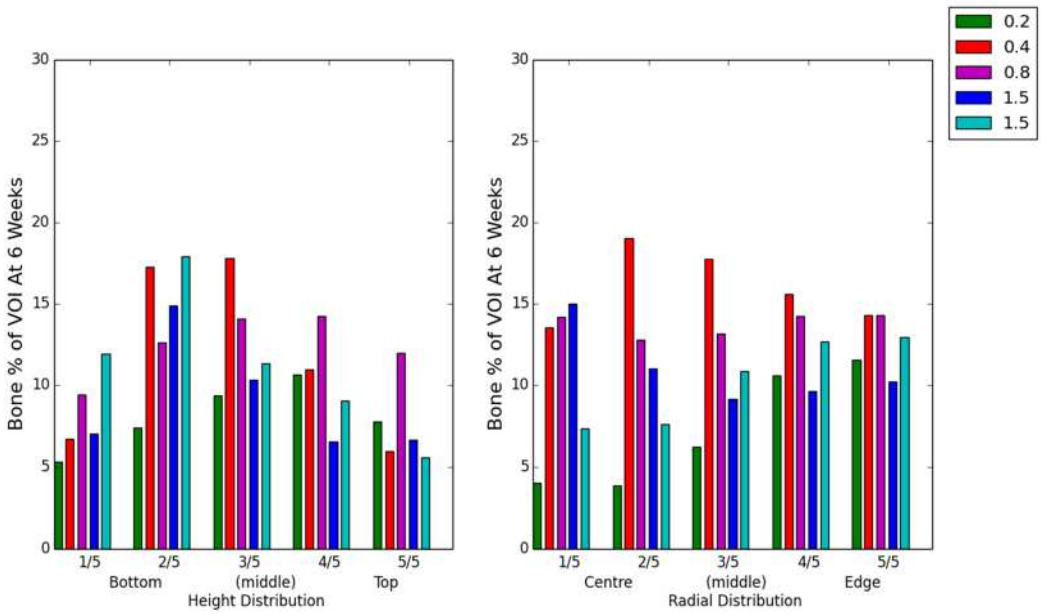

Figure 6-50 A: Height distribution of Bone as a percentage of VOI, B: Radial distribution of Bone as a percentage of VOI for SA orthotopic samples at 6 weeks.

Figure 6-50 A shows that at 6 weeks for all the samples there is more bone in the middle of the samples than at either the top or bottom of the samples.

Figure 6-50 B shows that at 6 weeks the 0.2 and one of the 1.5 samples have less bone in the centre than at the edge while the other 1.5 sample has more bone at the centre than at the edge. With the 0.4 and 0.8 samples having similar bone amounts at the centre and edge and the 0.4 sample having more bone in the middle.

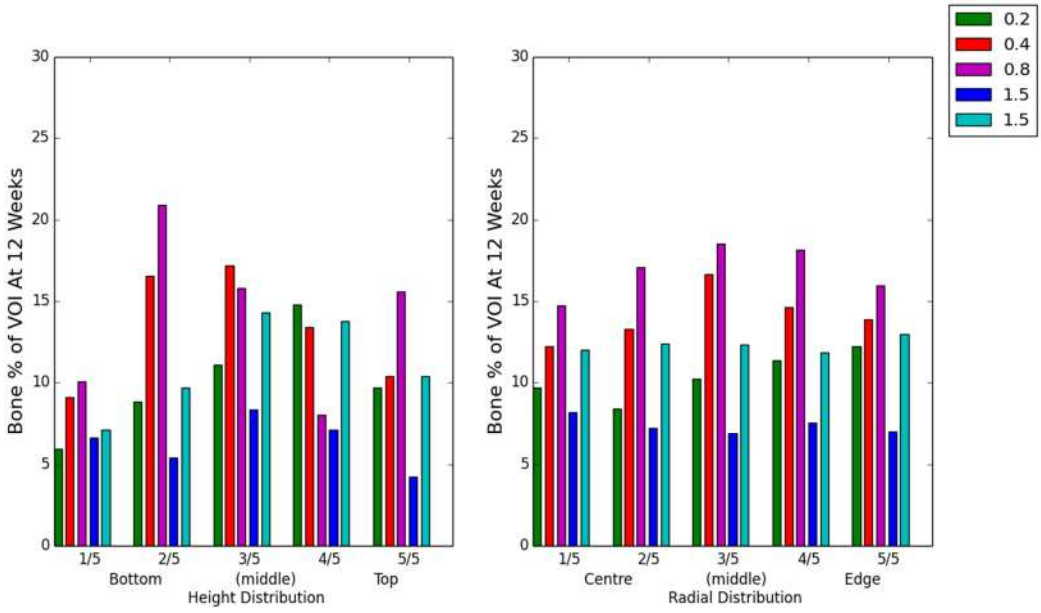

Figure 6-51 A: Height distribution of Bone as a percentage of VOI, B: Radial distribution of Bone as a percentage of VOI for SA orthotopic samples at 12 weeks.

Figure 6-51 A shows that at 12 weeks the 0.2 sample and one of the 1.5 samples show a general trend of more bone at the top than at the bottom with the most bone in the 4/5 region just before the top. The 0.4 and 0.8 sample both show highest amount of bone at the middle bottom region of 2/5 with the 0.8 showing more bone at the top than at the bottom. The other 1.5 sample has more bone in the middle than the top with the bottom having slightly less bone than the middle.

Figure 6-51 B shows that at 12 weeks the 0.2 sample has slightly more bone towards the edge of the sample than in the centre, while the samples of 0.4 and 0.8 have more bone in the middle than either at the centre or at the edge. One of the 1.5 samples shows slightly higher amount of bone at the centre than at the edge, while the other 1.5 sample has slightly higher bone amount at the edge, with both showing relatively evenly distributed growth across the radial direction.

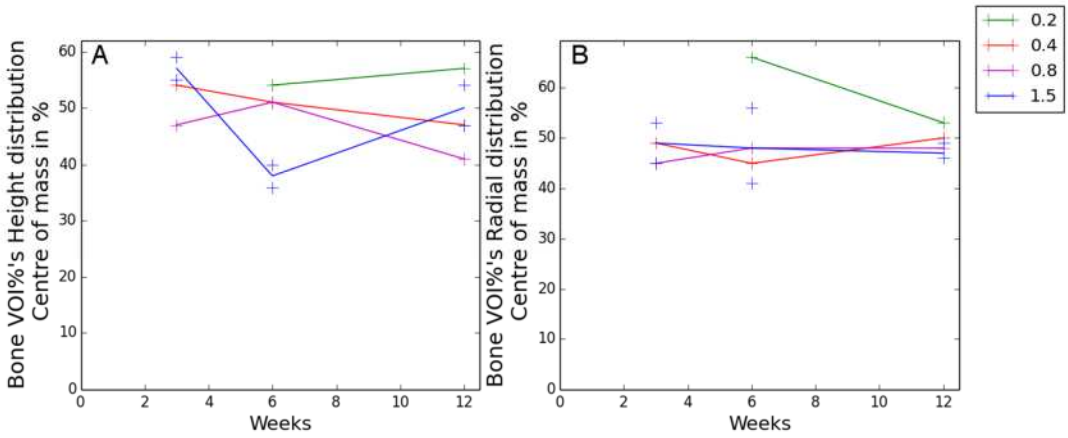

Figure 6-52 A: Height distribution of Bone as a percentage of VOI's centre of mass, B: Radial distribution of Bone as a percentage of VOI s centre of mass for SA orthotopic samples over time.

Figure 6-52 A shows that the centre of mass for the height distribution from 3 to 6 weeks decrease for 1.5 samples and has a slight decrease for the 0.4 sample and an increase for the 0.8 sample. From 6 to 12 weeks the 0.2 and the 1.5 samples increase, while the 0.4 and 0.8 samples both decrease.

Figure 6-52 B shows that the centre of mass of the radial distribution for all the samples except for the 0.2 sample are between 40 % and 60 % with all both them going towards 50 % at 12 weeks.

6.3.2.3 Structural and Shape Measurements

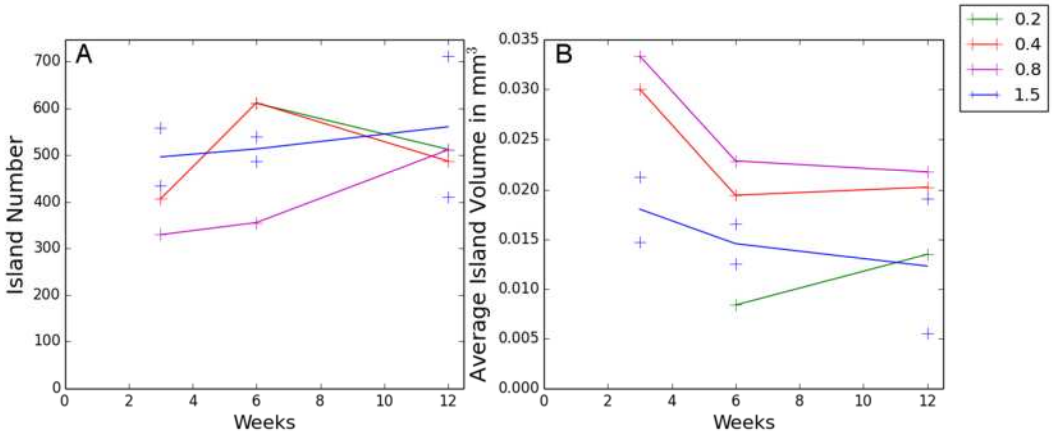

Figure 6-53 A: Island number of Bone, B: Average island volume in microns for SA orthotopic samples over time.

Figure 6-53 A shows that the island number from 3 to 6 weeks increases for all the samples and decreases for 0.2 and 0.4 samples from 6 to 12 weeks while the 0.8 and the 1.5 samples both show an increase.

Figure 6-53 B shows that the average island volume from 3 to 6 weeks decreases for the 0.4, 0.8 and the 1.5 samples. The 0.2 sample increases to 12 weeks, while both the 0.8 and the 1.5 samples decrease to 12 weeks with the 0.4 sample showing a slight increase from 6 to 12 weeks.

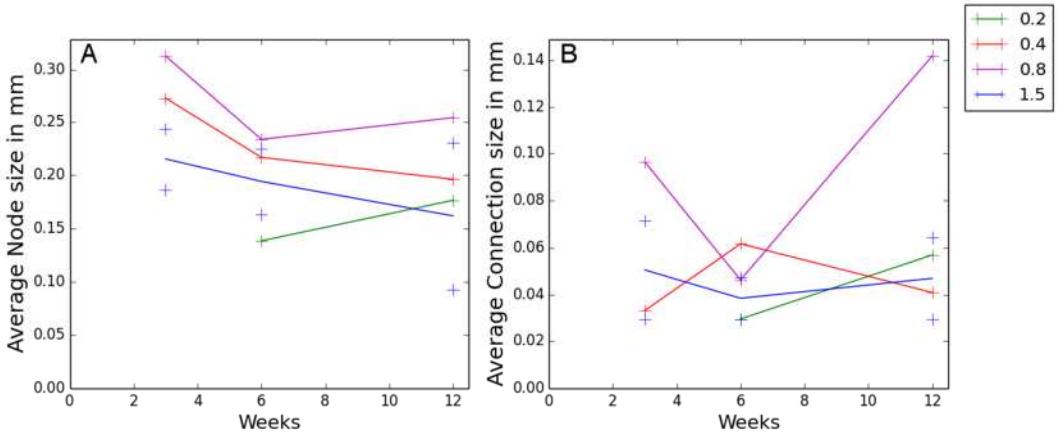

Figure 6-54 A: Average Node size of Bone in mm, B: Average Connection size of Bone in mm for SA orthotopic samples over time.

Figure 6-54 A shows that for the samples of 0.4, 0.8 and the 1.5 samples there is a decrease in node size from 3 to 6 weeks. The 0.2 and 0.8 samples increase from 6 to 12 weeks while the 0.4 and 1.5 samples show a decrease.

Figure 6-54 B shows that both the 0.8 and the 1.5 samples show a drop in average

connection size from 3 to 6 weeks with the 0.8 and 1.5 samples showing an increase from 6 to 12 weeks. The 0.4 sample shows an increase in connection size from 3 to 6 weeks follows by a decrease to 12 weeks. With the 0.2 sample showing an increase from 6 to 12 weeks.

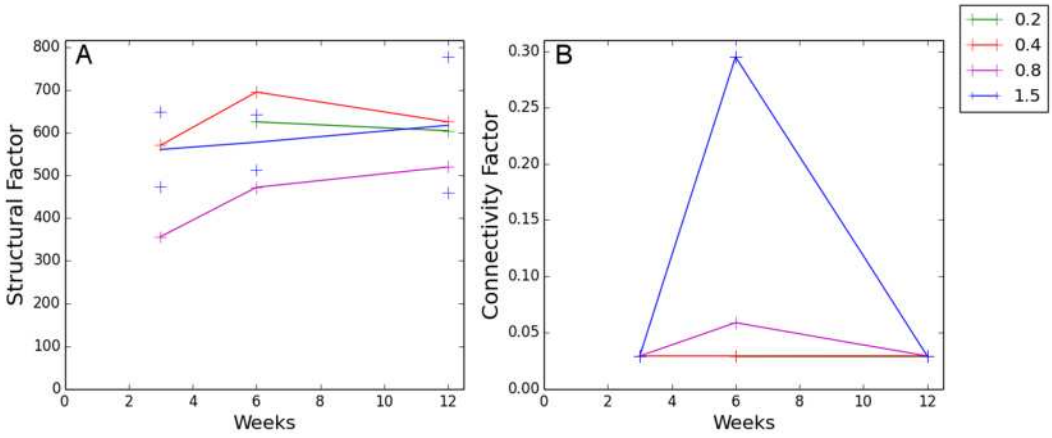

Figure 6-55 A: Structural Factor for Bone, B: connectivity Factor in mm for SA orthotopic samples over time.

Figure 6-55 A shows that from 3 to 6 weeks the 0.4, 0.8 and the 1.5 samples increase. From 6 to 12 weeks 0.2 and 0.4 decrease, while the 0.8 and 1.5 sample both increase to 12 weeks.

Figure 6-55 B shows that both the 0.8 and the 1.5 samples have an increase in connectivity factor to 6 weeks before returning to the same value as at 3 weeks at 12 for all the samples. While the other samples remain at an approximately constant connectivity factor.

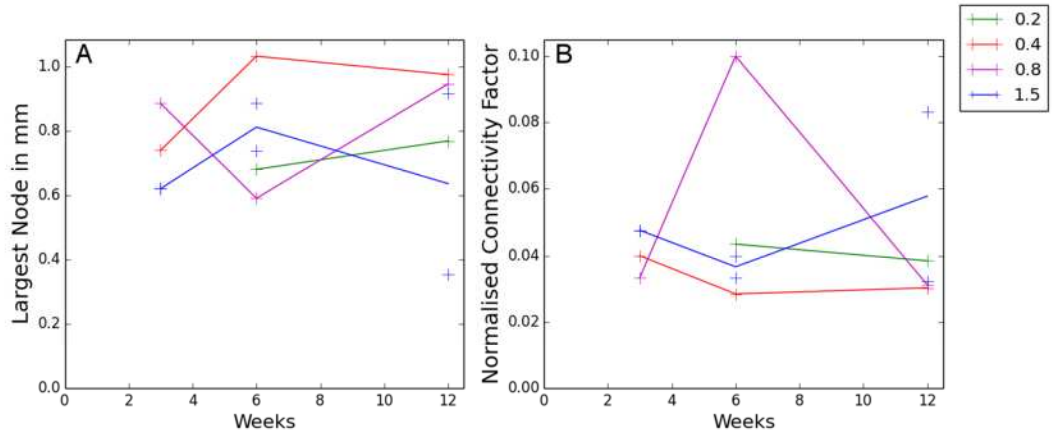

Figure 6-56 A: Largest Node size for Bone in mm, B: Normalised connectivity Factor in for SA orthotopic samples over time.

Figure 6-56 A shows that from 3 to 6 weeks the largest node increases for 0.4 and the 1.5 samples while the 0.8 sample decreases. From 6 to 12 weeks the samples of 0.2 and

0.8 samples increase and the 0.4 and the 1.5 samples decrease to 12 weeks.
Figure 6-56 B shows that from 3 to 6 weeks the 0.8 sample has an increase in normalised connectivity factor, while the other samples decrease. From 6 to 12 weeks the 0.8 has a sharp decrease, while the 1.5 samples increases sharply, with the 0.4 sample shows a slight increase and the 0.2 shows a decrease.

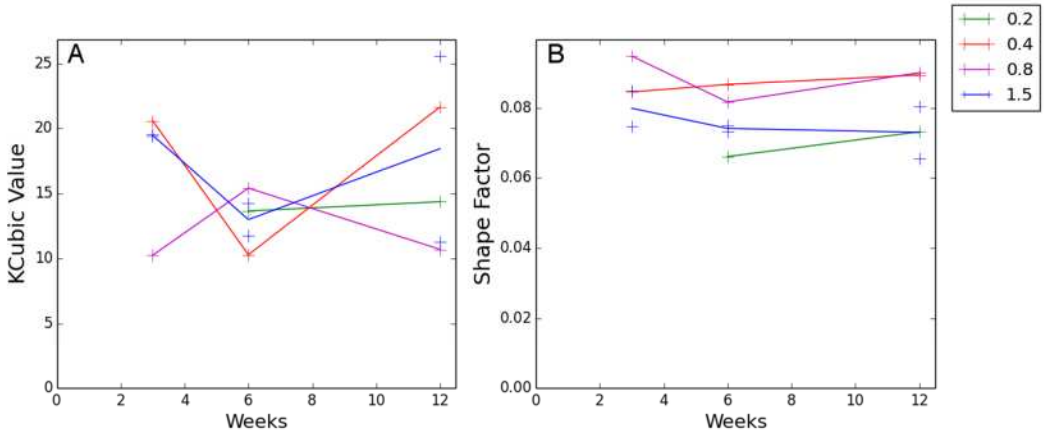

Figure 6-57 A: KCubic value for Bone, B: MAV derived Shape factor for SA orthotopic samples over time.

Figure 6-57 A shows that from 3 to 6 weeks the KCubic value drops sharply for all the sample bar the 0.8 samples, while from 6 to 12 week the 0.8 sample decreases and the other samples increase with the 0.2 only increasing slightly.
Figure 6-57 B shows that the 0.4 sample increases in shape factor from 3 to 12 weeks, while the 0.2 sample increases from 6 to 12 weeks. From 6 to 12 weeks both the 0.8 and the 1.5 samples decrease to 6 weeks with the 0.8 sample increasing to 12 weeks and the o 1.5 samples decreasing to 12 weeks.

6.3.2.4 Porosity Measurements

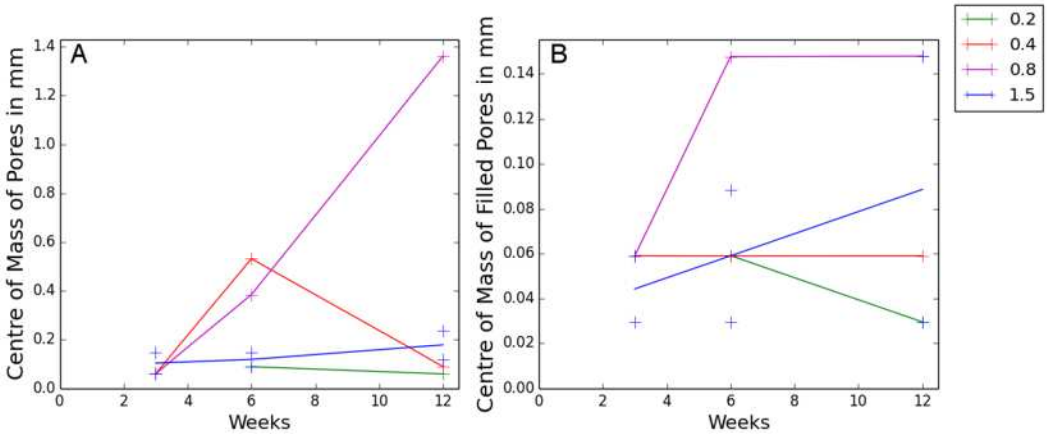

Figure 6-58 A: Centre of mass of pores, B: centre of mass of filled pores for SA orthotopic samples over time.

Figure 6-58 A shows that from 3 to 6 weeks the centre of mass of the pores increases for the 0.4 and 0.8 samples, while the 1.5 samples have a slight increase. From 6 to 12 weeks the 0.4 sample decreases sharply while the 0.2 has a slight decrease and the 0.8 increases sharply with slight increases in the 1.5 samples.

Figure 6-58 B shows that the 0.4 sample shows an approximately constant centre of mass for the filled pores from 3 to 12 weeks while the 1.5 samples show a constant increase. The 0.8 sample shows an increase to 6 weeks and then remaining approximately constant from 6 to 12 weeks while the 0.2 sample decreases from 6 to 12 weeks.

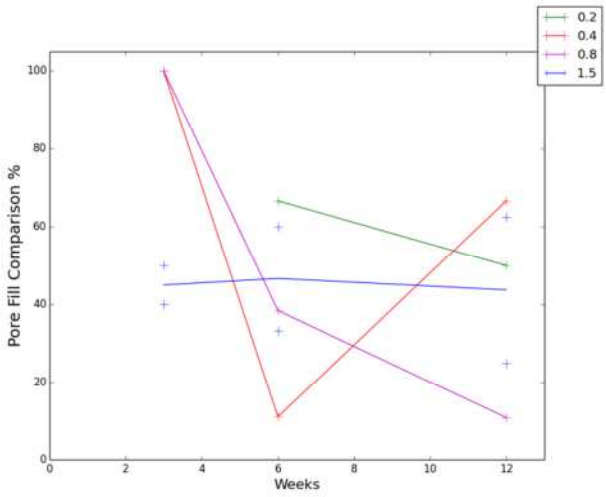

Figure 6-59 Pore fill comparison in percentage for SA orthotopic samples over time.

Figure 6-59 shows that the pore filled comparison shows that from 3 to 6 weeks the 0.4

and 0.8 samples decrease, while the 1.5 samples increases. From 6 to 12 weeks the 0.2, 0.8 and while the other 1.5 samples show a slight decrease and the 0.4 samples shows a large increase.

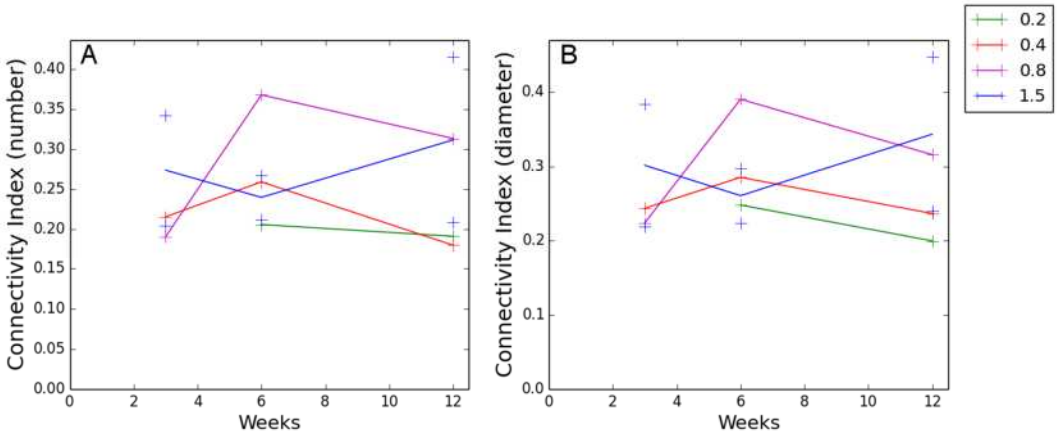

Figure 6-60 A: Connectivity Index (number), B: Connectivity Index (diameter), for HA orthotopic samples over time.

Figure 6-60 A shows that the connectivity index from 3 to 6 weeks increases for both 0.4 and 0.8 samples while the 1.5 samples decrease. From 6 to 12 weeks the 0.2, 0.4 and 0.8 samples decrease while the 1.5 samples increases.

Figure 6-60 B shows that the diameter based connectivity index has the same trends as the number based connectivity index but with the 0.8 sample showing a higher index at 12 weeks than the 1.5 samples.

6.3.3 Evaluation of SA Ectopic Samples

The ectopic samples were segmented using the colour map overlay segmentation method using the calibration as stated in Section 6.1.

Three different groups of ectopic samples were analysed (Section 2), with the 80-20 SA samples not being considered in the quantification because the sample exhibits micro particulates SA (Section 6.3.3.1) which is picked up as bone in the segmentation because of the limitations of the CT scanner resolution (Section 2). All the ectopic samples will be referred to by their strut porosity (e.g. 30%), with the exception of the 80-30 sample with surgical putty which will be referred to as 30s

From the segmented regions, the following measurements as stated in Table 5-9 were performed except for the porosity measurements, which were not used on the ectopic sample sets as they are comprised of particles and as such the spaces between the

particles are identified the same as the porosity.
All the raw data can be found in the Appendix.

6.3.3.1 SEM

Looking at each of the samples and showing a representable sample from each of the different ectopic samples (20, 30, 30s and 35 strut %) the difference between the SBGs and bone growth can be seen by inspection via SEM(Figure 6-61, Figure 6-62, Figure 6-63 & Figure 6-64*).*

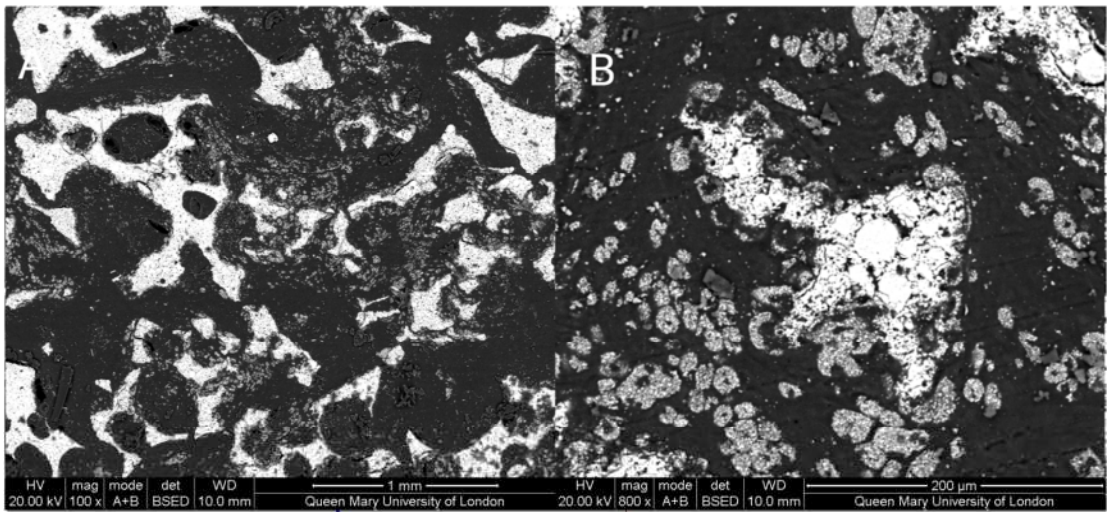

Figure 6-61A: 100x B: 800x magnification of SEM imaging of the 80-20 SA sample in ectopic sites after 12 weeks imaging in backscattering mode and 20kV.

Figure 6-61 shows that the 80-20 SA sample has no significant bone growth and is in fact filled with SA particles which have been broken down, which leads to the miss-identification of those regions as bone.

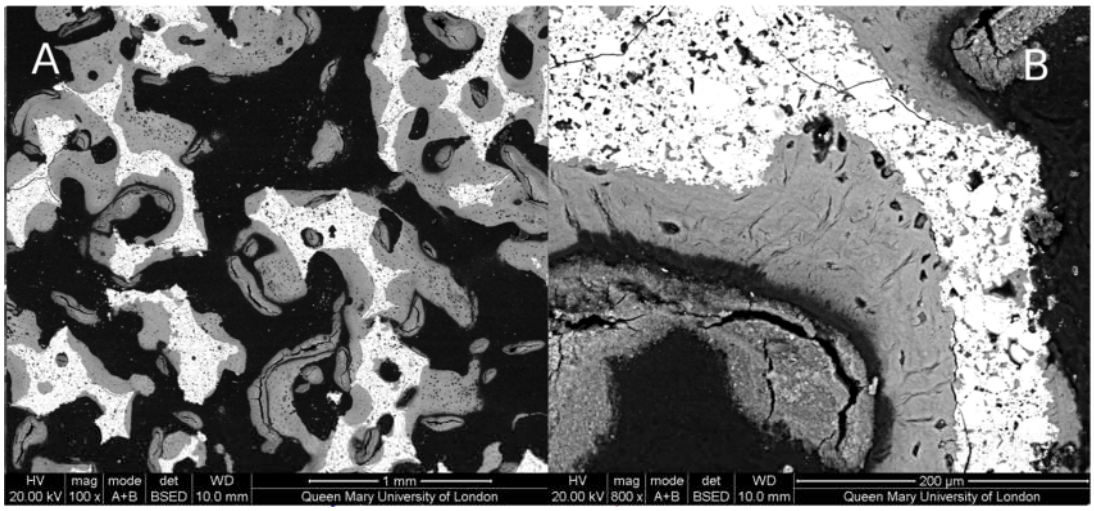

Figure 6-62 A:100x B: 800x magnification of SEM imaging of the 80-30 SA sample in ectopic sites after 12 weeks imaging in backscattering mode and 20kV.

Figure 6-62 shows the clear bone growth in the 80-30 ectopic sample, with the bone growing not only on the surface of the SBG, but having some free flowing bone growth between them.

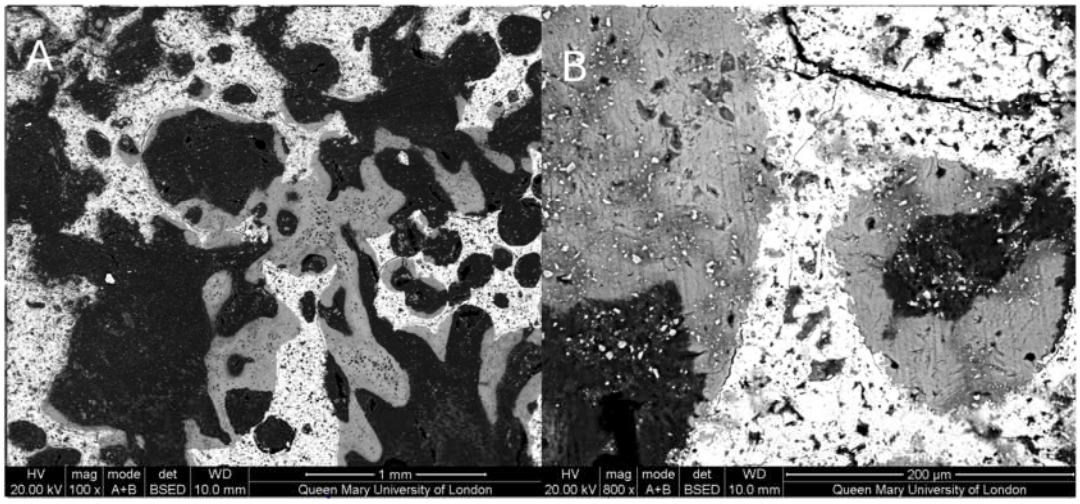

Figure 6-63 A: 100x B: 800x magnification of SEM imaging of the 80-30s SA sample in ectopic sites after 12 weeks imaging in backscattering mode and 20kV.

Figure 6-63 shows that the 80-30s has some contact between the SBG and the bone with some of the bone being formed in free flowing patterns between the SBG particles.

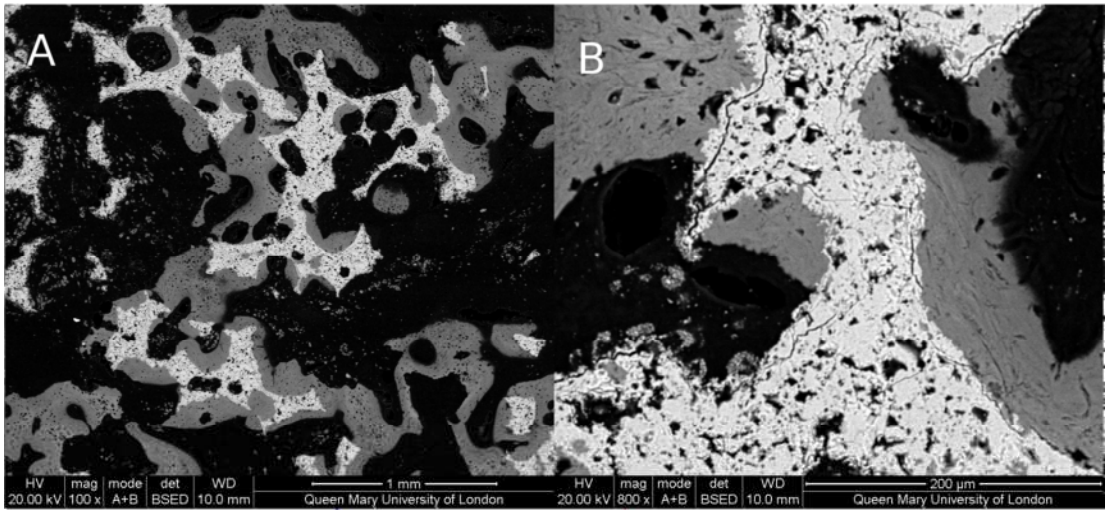

Figure 6-64 A: 100x B: 800x magnification of SEM imaging of the 80-35SA sample in ectopic sites after 12 weeks imaging in backscattering mode and 20kV.

Figure 6-64 shows that the 80-35SA SBG, has both high SBG bone coverage and significant free forming bone between the particles.

The samples types of 30s, 30 and 35, were compared using the measurements defined in Table 5-9 (except for the porosity measurements), as there are multiple samples of each type statistical analysis was performed on the samples. This analysis was be carried out between the 30s and 30 samples and 30 and 35 respectively to determine if the addition of the surgical putty or increase in strut porosity makes a significant difference to the bone grown within the SBGs. The analysis was not carried out between the 35 and 30s samples as there is both a change with the addition of surgical putty and the change in structure porosity meaning that it would not be possible to determine which factor (or combination of both) resulted in the recorded changes. The samples were compared using the Mann-Whitney U test as analysis of similar sample sets have shown the variables related to the bone growth to be nonparametric via the Kolmogorov-Smornov test (Coathup *et al*., 2011, 2013). The analysis was performed with the use of SPSS software (version 22). The required number of samples to detect a difference between the means of 20% is 6 per samples type assuming a statistical power of 0.8 and standard deviation to mean ratio of the samples of 0.1 (Machin, Campbell, Tan, & Tan, 2009). As there are less than six samples for any of the group tested (with the closest being five samples) any differences of below 20% will not possible to significantly determine, where p values of < 0.05 where considered to be significant.

For this reason it was not expected that statistical significant could be determined from

these however, the statistical probability and significance that is shown can still be commented on and some comparison between the sample types determined.

6.3.3.2 Volume and Surface Area Measurements

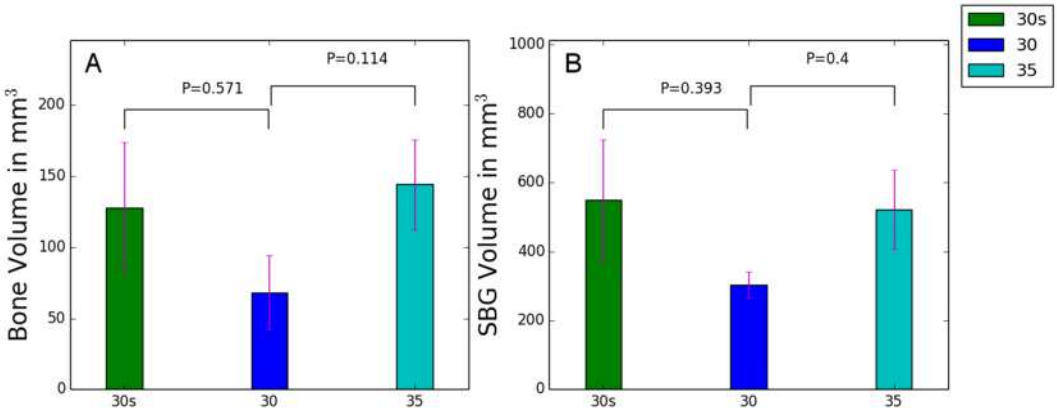

Figure 6-65 A: Bone volume in Microns, B: SBG Volume in microns for SA ectopic samples at 12 weeks, with standard error and P-value.

Figure 6-65 A shows that the 30 samples have less bone than bone the 30s and 35 samples, with no significance difference being seen between any of the sample sets. Figure 6-65 B shows that the volume of the SBG for the 30 samples are lower than both the 30s and 35 samples with no significance difference being seen between any of the sample sets.

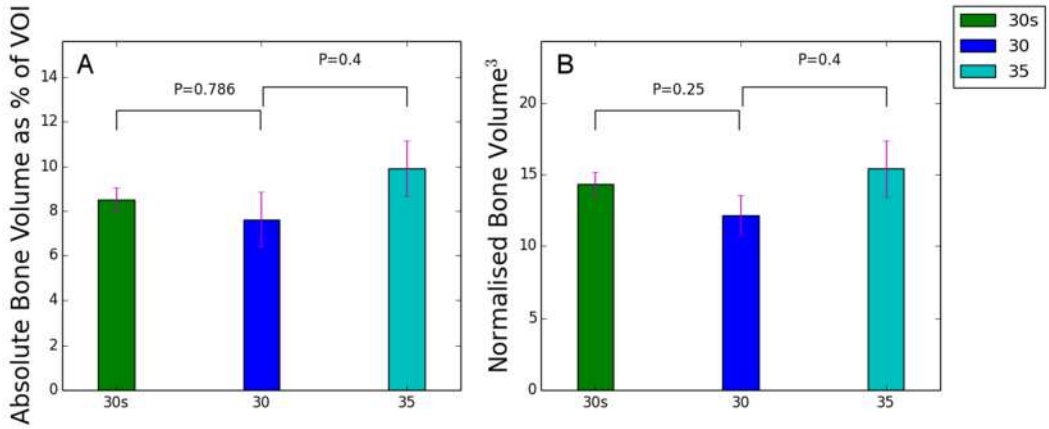

Figure 6-66 A: Absolute Bone volume as % of VOI, B: Normalised Bone volume for SA ectopic samples at 12 weeks, with standard error and P-value.

Figure 6-66 A shows that the 30 samples have the lowest bone growth as percentage of their VOI, with 35 having more bone growth than the 30s, no significance difference being seen between any of the sample sets.

Figure 6-66 B shows the same trend as the volume as percentage of VOI no significance

difference being seen between any of the sample sets.

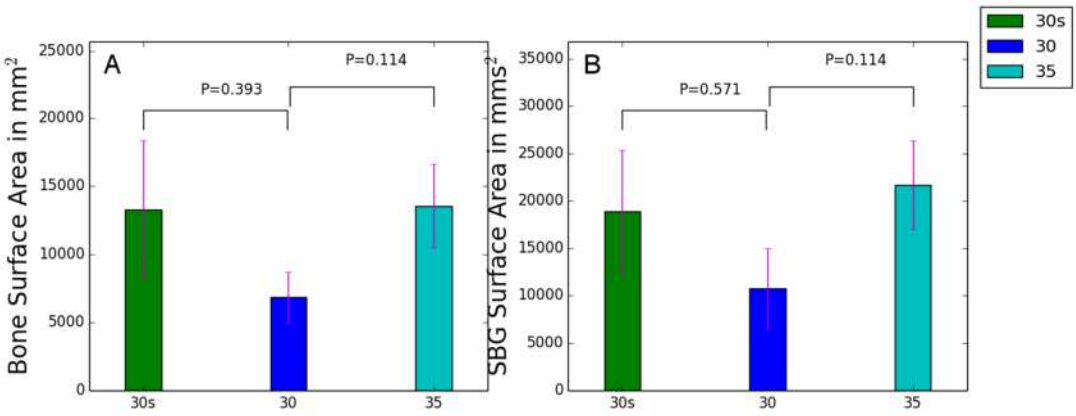

Figure 6-67 A: Bone surface area in microns, B: SBG surface area in microns for SA ectopic samples at 12 weeks, with standard error and P-value.

Figure 6-67 A shows that the bone surface area is lower for the 30 samples than both the 30s and 35 samples with no significance difference being seen between any of the sample sets.

Figure 6-67 B shows that the SBG surface area is lower for the 30 samples than either the 30s or 35 samples, with no significance difference being seen between any of the sample sets.

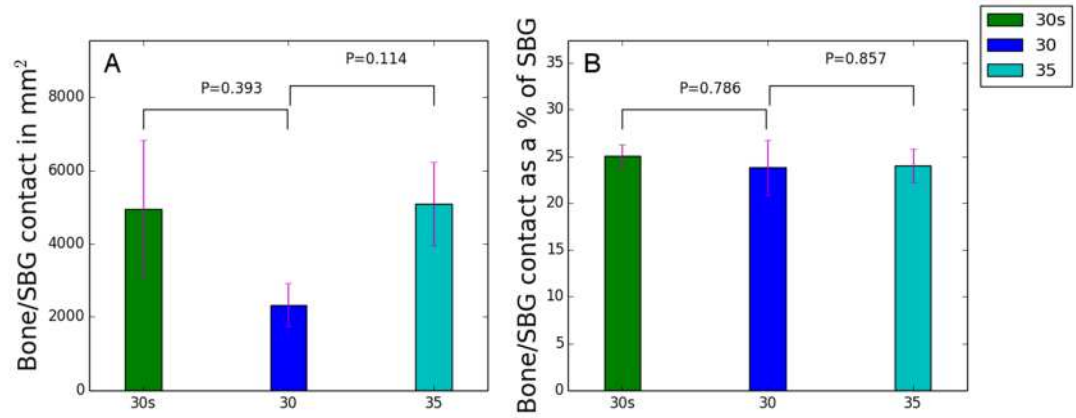

Figure 6-68 A: Bone/SBG contact area in microns, B: Bone/SBG contact area as percentage of SBG surface area microns for SA ectopic samples at 12 weeks, with standard error and P-value.

Figure 6-68 A shows that the bone to SBG contact area is lower in the 30 than both the 30s and 35 samples with no significance difference being seen between any of the sample sets.

Figure 6-68 B shows that the 30s samples show slightly higher bone to SBG contact area as a percentage of the SBG's area, with no significance difference being seen between any of the sample sets.

6.3.3.3 Distribution Measurements

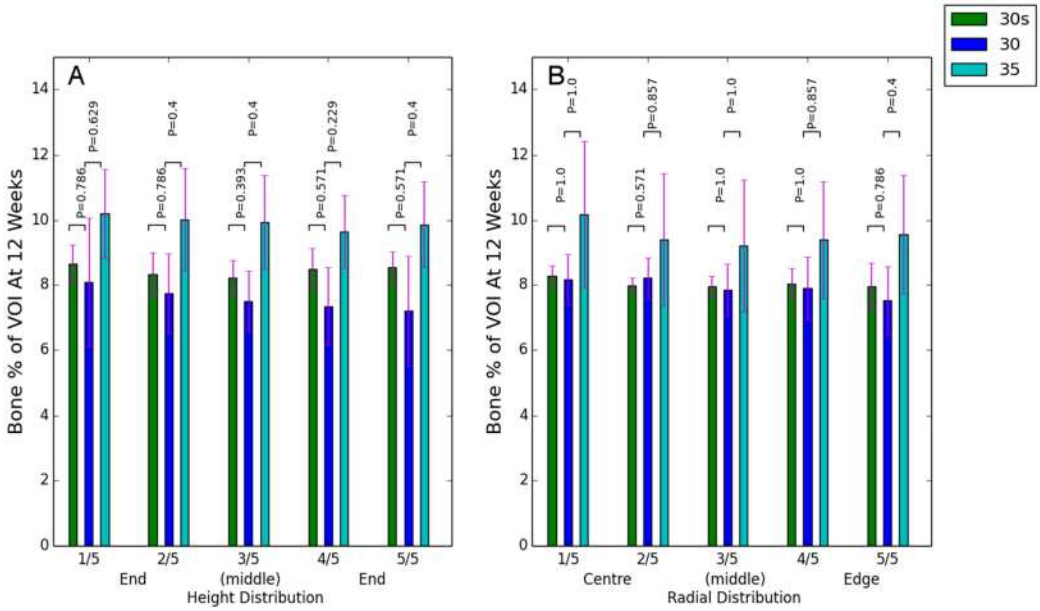

Figure 6-69 A: Height distribution of Bone as a percentage of VOI, B: Radial distribution of Bone as a percentage of VOI for SA ectopic samples at 12 week, with standard error and P-value.

Figure 6-49 A shows that all three samples have similar equally distributed bone along the height distribution with no significance difference being seen between any of the sample sets. However as the samples are not implanted in relation to any pervious existing bone the distributions could be reversed.

Figure 6-49 B shows that all the samples show a slight increase of bone at the centre compared to the outer, with no significance difference being seen between any of the sample sets.

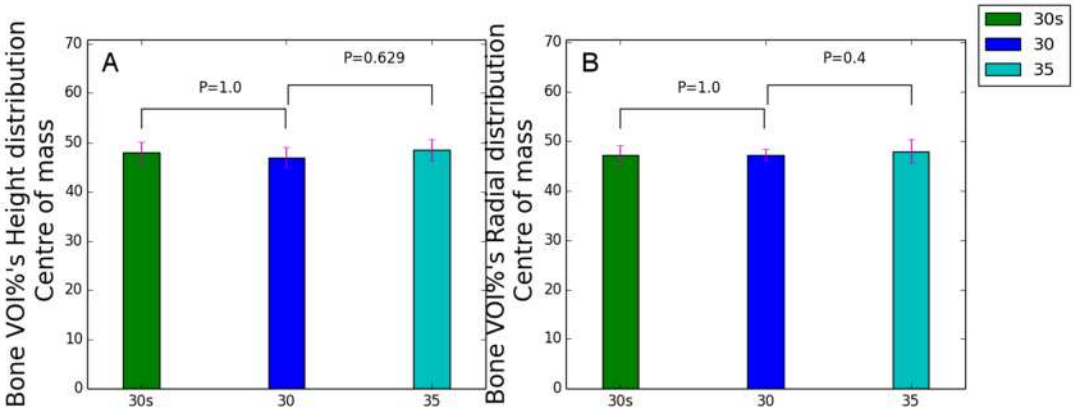

Figure 6-70 A: Height distribution of Bone as a percentage of VOI's centre of mass, B: Radial distribution of Bone as a percentage of VOI s centre of mass for SA ectopic samples at 12 weeks, with standard error and P-value.

Figure 6-70 A shows that for the centre of mass along the height distribution all three sample types' show values of just below 50% with no significance difference being seen between any of the sample sets.

Figure 6-70 B shows that the centre of mass for the radial distributions for the samples as in the height distributions shows that all the samples have values of just below 50 % with no significance difference being seen between any of the sample sets.

6.3.3.4 Structural and Shape Measurements

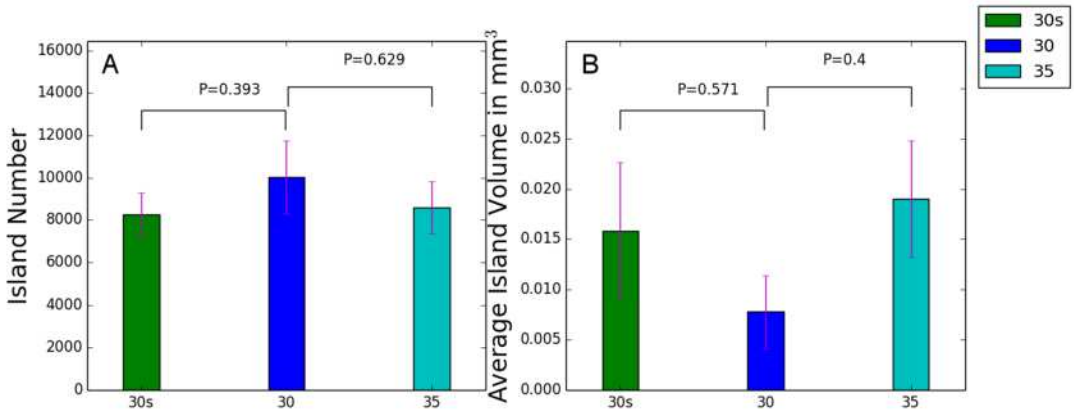

Figure 6-71 A: Island number of Bone, B: Average island volume in microns for SA ectopic samples at 12 weeks, with standard error and P-value.

Figure 6-71 A shows that the 30 sample has a larger number of bone islands than either the 30s or 35 samples, with no significance difference being seen between any of the sample sets.

Figure 6-71 B shows that the 30 samples have smaller average island volume than either the 30s or 35 samples, with no significance difference being seen between any of the sample sets.

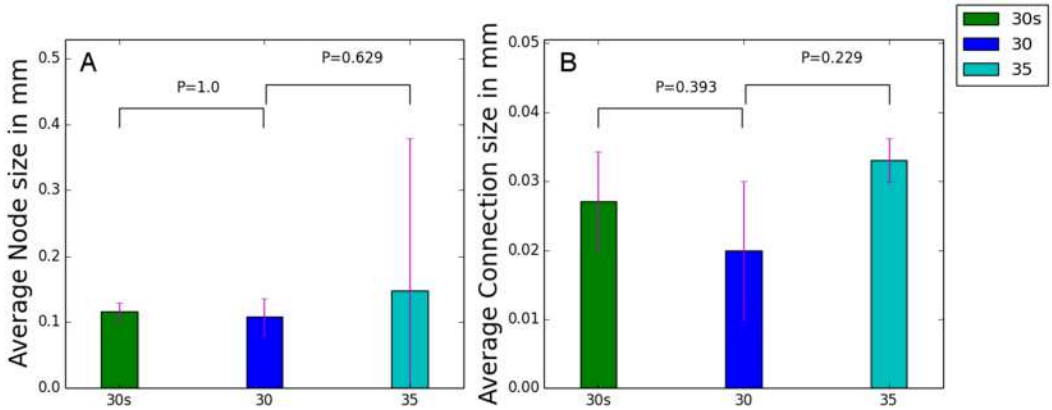

Figure 6-72 A: Average Node size of Bone in mm, B: Average Connection size of Bone in mm for SA ectopic samples at 12 weeks, with standard error and P-value.

Figure 6-72 A shows that 30 samples have a slightly lower average node size than the 30s samples which the 35 samples showing a larger difference with no significance difference being seen between any of the sample sets.

Figure 6-72 B shows that the average connection size of the 30 samples is lower than the 35 and 30s samples with no significance difference being seen between any of the sample sets.

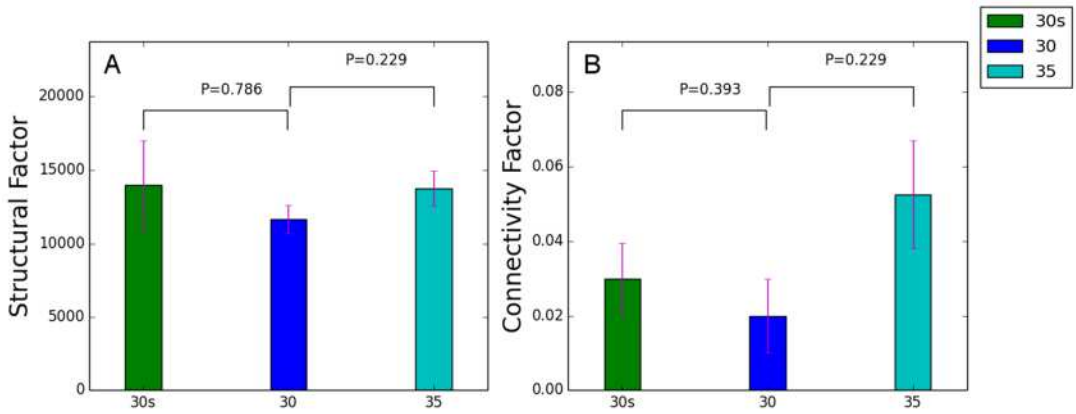

Figure 6-73 A: Structural Factor for Bone, B: connectivity Factor in mm for SA ectopic samples at 12 weeks, with standard error and P-value.

Figure 6-73 A shows that the 30 samples have a lower structural factor than either the 30s or 35 samples with, 30s having a larger structural factor than the 35 samples, with no significance difference being seen between any of the sample sets.

Figure 6-73 B shows that the 30 samples have a lower connectivity factor than either the 30s or 35 samples with the 35 samples showing the highest connectivity factor with no significance difference being seen between any of the sample sets.

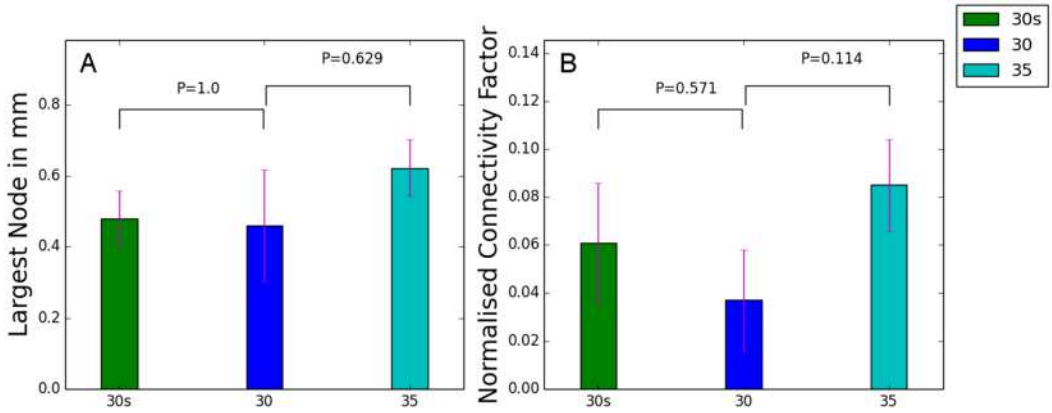

Figure 6-74 A: Largest Node size for Bone in mm, B: Normalised connectivity Factor in for SA ectopic samples at 12 weeks, with standard error and P-value.

Figure 6-74 A shows that the 30 samples have the smallest “largest node”, while the 35

samples are larger than the 30, with no significance difference being seen between any of the sample sets.

Figure 6-74 B shows that the 30 samples have lower normalised connectivity factors than either the 30s or 35 samples, with the 35 having the highest value with no significance difference being seen between any of the sample sets.

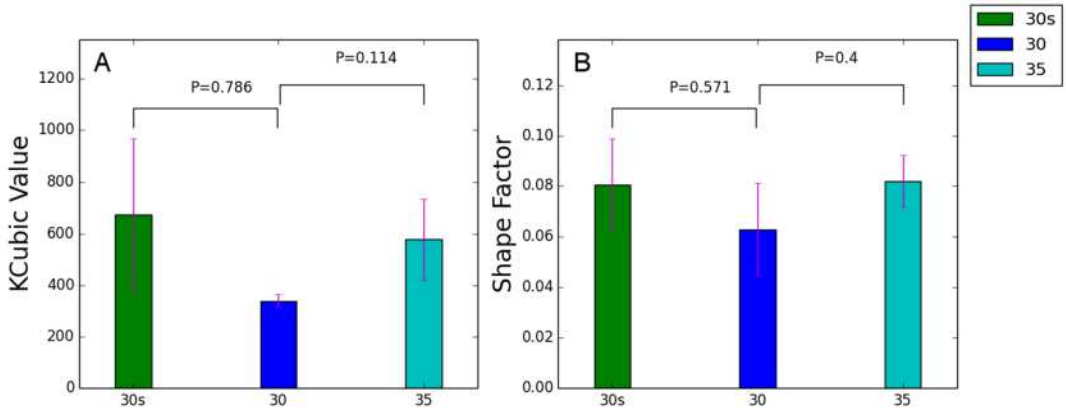

Figure 6-75 A: KCubic value for Bone, B: MAV derived Shape factor for SA ectopic samples at 12 weeks, with standard error and P-value.

Figure 6-75 A shows that the Kcubic value of the 30 samples are lower than both the 30s and 35 samples, with the 30s having more islands than the 35 samples with no significance difference being seen between any of the sample sets.

Figure 6-75 B shows that the shape factor is the lowest for the 30 sample with both the 30s and 35 samples showing similar values, with no significance difference being seen between any of the sample sets.

6.3.4 Parameter Validation

By investigating the different measurements, each measurement can be connected to different parameters of bone quantification as well as a determent of the relevance of each measurement defined, the parameters considered are:

- Volumetric measurement of the bone
- Distribution of bone
- Structure of bone within the VOI
- Structure within the bone islands
- Relationship between the Bone and the SBG

- Properties of the SBG

6.3.4.1 Volume and Surface Area Measurements

There are eight volume and surface area measurements; the aim of these measurements is to represent how much bone is present within the VOI with and without context of the SBG and the contact between the regions. The obvious measurements to use for the amount of bone growth are the volume of bone and either the absolute bone volume as percentage of VOI or normalised bone percentage. The volume of the SBG which is required for the calculation of the normalised volume measurements should only decrease with time, but is seen to increase in some of the orthotopic samples with time. The reason for the increase could be related to the error in the segmentation with an over counting of the SBG at the bone and SBG interface (Figure 6-25 and Figure 6-26). This can be seen by comparing the volume of the SBG to the contact area between the bone and SBG for the HA orthotopic samples as shown in Figure 6-28 B and Figure 6-31 A. For the reason that the SBG measurements appear to be effected by the bone in the samples, the measurements of bone volume and bone volume as an absolute percentage of VOI will be used as a measurement of bone growth as it does not take into account the SBG (even though the segmentation is calibrated to normalised bone volume to reduced miss-segmentation in both the bone and the SBG). The measurement of bone to SBG contact can still be used as a measurement, as even with over and or under counting of regions the interface between the region's general trend will still provide a measurement relating to the contact area.

A validation of the general volume measurement of bone growth can be seen in the samples of 70-20 and 80-10 from 3 to 6 weeks, where they are measured as having a large drop in volume which is confirmed by inspection of the mid slices as shown in Figure 6-76.

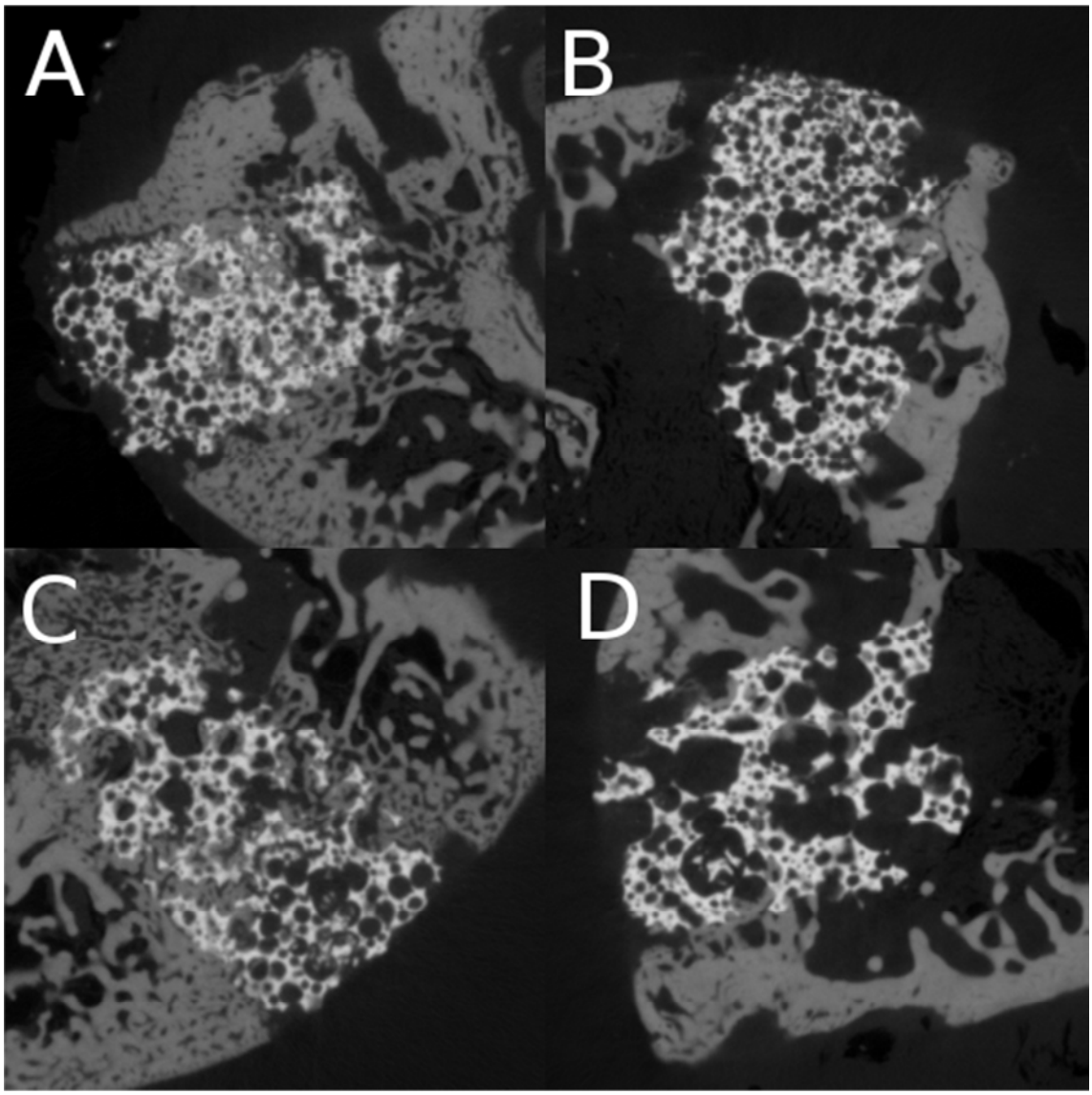

Figure 6-76 Slices of through the middle of the HA orthotopic samples of A :70-20 at 3 weeks, B: 70-20 at 6 weeks, C: 80-10 at 3 weeks D: 80-10 at 6 weeks.

6.3.4.2 Distribution Measurements

There are two types of measurements for the two types of distribution directions, namely the fifths distribution measurements and the weighted distribution measurements and the height and radial distributions.

The weighted distributions provide a single value for each of the distribution directions, however as can be seen by comparing the height distribution of the HA orthotopic samples of 60-20 and 70-20 at 3 weeks (Figure 6-32 A and Figure 6-36A) it cannot discern between equal distributions of bone across the whole distribution direction and more bone in the centre of the distribution directions.

For this reason the fifths distribution method while more complex to compare between

samples can be seen to provide more useful information about the distributions of the bone within the samples. When comparing samples, the radial distribution provides more useful information than the height distribution, as there is not already bone inside the sample, while with the height distribution is affected by the non-uniform distribution of bone in contact with the samples along their height distribution. How the fifths distribution measurements relate to the actual samples can be seen by comparing a 0.2 sample at 3 weeks and a 0.8 sample at 6 weeks (Figure 6-77).

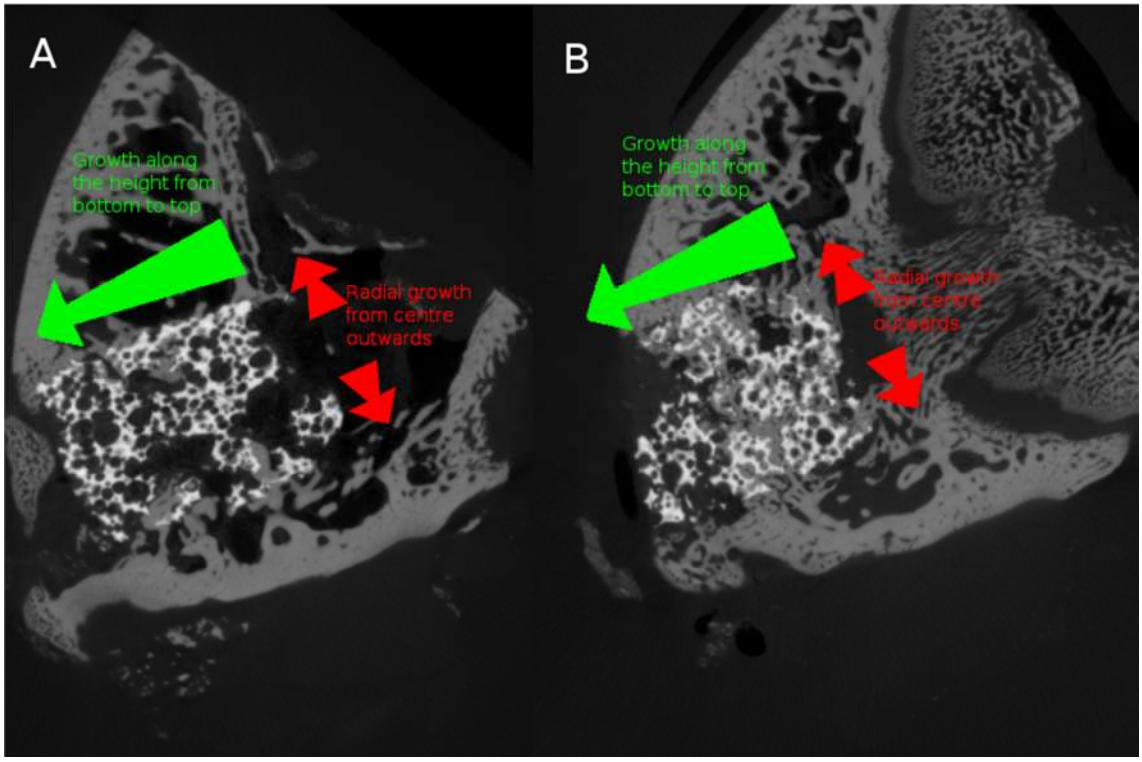

Figure 6-77 Slices of SA orthotopic samples with bone growing within of A: 0.2wt% silicon substituted SA at 6 weeks B:0.8wt% silicon substituted SA at 3 weeks, both with notations of distribution directions.

Figure 6-77 shows that the 0.2 sample shows more bone at the middle of the height distribution than the top or bottom and at the edge of the radial compared to the centre. It also shows that the 0.8 samples more bone in the middle of the height distribution, than the bottom which has more bone than the middle, the radial distribution of the bone shows even distribution with larger bone mass in the centre than at the edge. These observations fit with the distribution measurements (Figure 6-49 and Figure 6-50).

6.3.4.3 Structural and shape Measurements

There are ten structure and shape measurements; these measurements attempt to

quantify how the bone within the samples are structured, with the structural measurements measuring individual characteristics of the bone's structure while the shape measurements give a single measurement for the whole structure.

The structural measurements can be sub defined into two scales, the island data which provides information on how the bone is distributed within the VOI, while the other structural factors look at the structure of the islands, which can be considered to be unrelated to the VOI.

The measurements on the island scale are the island number and average island volume, with the average volume is created from the island number and the total bone volume of the samples; both measurements provide a valuable insight into how the structure of the bone changes over time and between SBG types.

For the factors which measure the structure of the islands, these are based around either the nodes or connections within the islands. There are three measurements based on the connections (average connection size, connection factor and normalised connection factor) which all show the clear change in the HA orthotopic samples over time (Figure 6-38 B, Figure 6-39 B and Figure 6-40 B). The measurement of average connection size, is the only of the three measurements which can be easier compared to the volume measurements as it has a dimension directly related to it, while the two factor measurements relate to the trend of connection to nodes.

For the node measurements the average and largest node measurements can be seen to relate with in general the largest node increase in size with an increase in average node size, this can be seen in Figure 6-78.

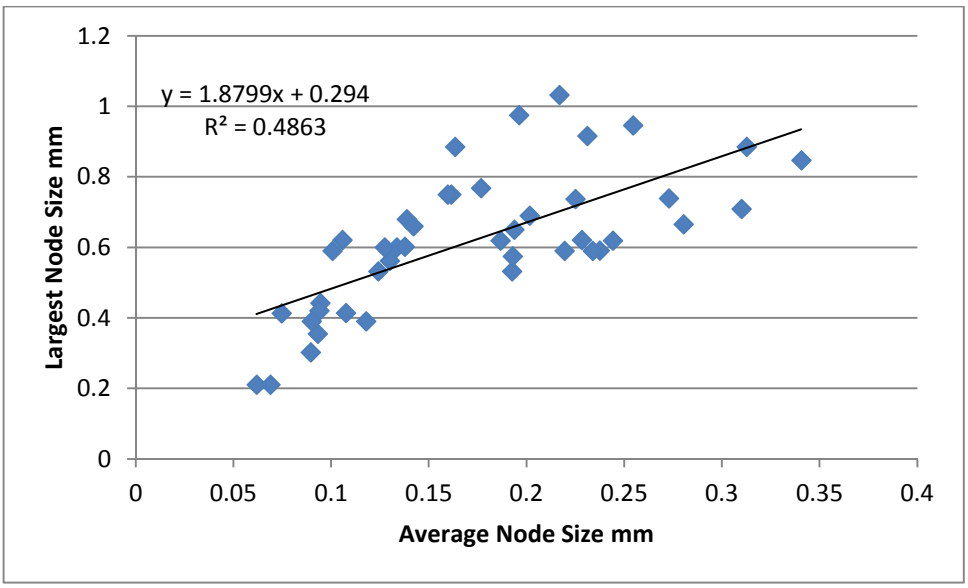

Figure 6-78 Graph of Largest Node in mm against average node size in mm for all orthotopic and ectopic samples.

The relationship between the average and largest node size, means that the average node size can be taken on its own and still represents in general the nodes in the samples with the largest node size providing a value to check the distribution of node sizes.

The structural factor relates to the highest number of islands measured during the MAV degradation, in the samples it can be seen that in general the structural factor's trend is similar to the island number trend, which fits as the higher the number of the islands the higher the number of possible islands during the MAV degradation. For this reason the structural factor can be used in conjunction with the island number to determine information about the structure of the bone, however this information is better represented in the average connection and node sizes as they do not require two measurements to be compared.

The Kcubic and shape factor shape measurements provide an overview of the entire shape, while the KCubic measurements can be easily compare, with a higher value showing a more "complex" shape, the shape factor can only show if two samples are repeating patterns of each other by presenting the same values. Both these measurements have limitations, the Kcubic value because of the uncertainty of the surface area measurements, and the shape factor because of the strong effect of the volume measurement on its value.

The ability of these measurements to define the structure and shape measurements can be seen when comparing the 0.8 samples at 3 and 6 weeks (Figure 6-79).

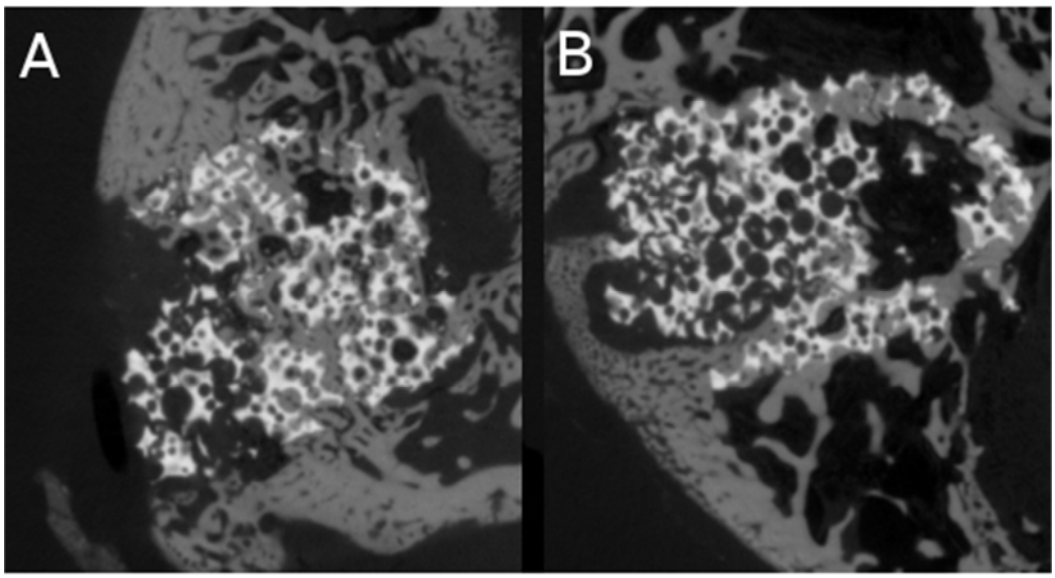

Figure 6-79 Slices taken through the middle of 0.8wt% silicon substituted SA orthotopic sample at A 3 B 6 weeks.

Figure 6-79 shows that at 6 weeks the bone in the 0.8 sample has an more open structure than at 3 weeks with a higher surface area to volume. This fits with the increase in the Kcubic measurement from 3 to 6 weeks, while the difference in the shape factor agrees that the bone shape at 3 weeks in not a “repeat” of the shape at 6 weeks (Figure 6-57).

6.3.4.4 Porosity Measurements

There are five porosity measurements, three relating to the pore geometry and the preference of the pore filling and two measurements related to the relationship between the pores and interconnections.

The measurement which provides the most information about the bone growth within the SBG is the Pore fill comparison, while the measurement which provides the most information about the bone growth is the centre of mass for the filled pores. This is because the filled pore centre of mass is not affected by the degradation of the SBG and can be easily compared between samples of different porosity. The connectivity index values and the centre of mass of the pores provide information about the SBG on its own. The two connective index values both show the similar trends within the samples types over time (Figure 6-44 and Figure 6-60) with the diameter value providing information about the relationship between the size of the pores and interconnection which is considered to be the important ratio (Section 1.2.4.1), therefore the diameter based index is considered to provided more information that the number based index.

The ability of these measurements to define the relationship between the pores and bone growth can be seen when viewing the 70-20 sample from 6 to 12 to 24 weeks (Figure 6-80).

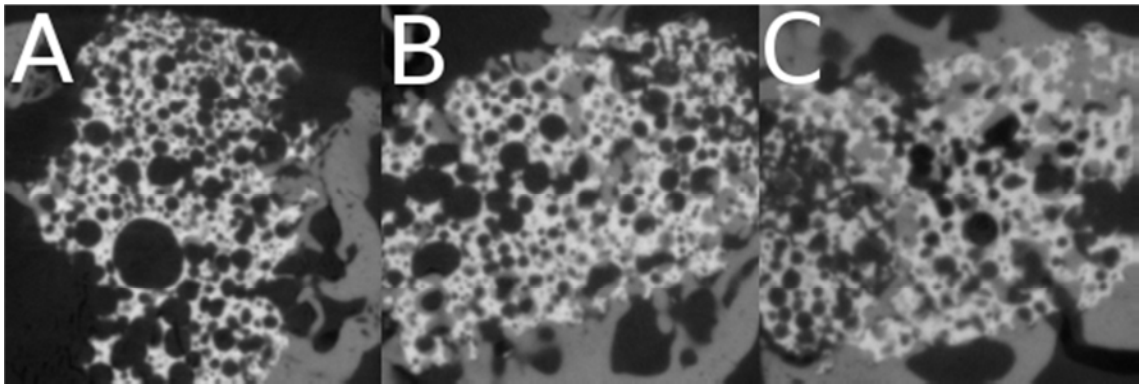

Figure 6-80 Slices of through the middle of the HA orthotopic samples of 70-20 at A: 6 weeks, B: 12 at weeks and C: 24 at weeks.

Figure 6-80 shows that over time the bone goes from only filling the smaller pores to filling the larger pores preferentially to filling both smaller and larger. This fits with the centre mass of filled pores measurements (Figure 6-42), this apparent preference could be caused as a side effect of larger masses of bone growing over time.

6.3.4.5 Parameter Summary

For each parameter in the sample that wants to be investigated the measurements are defined as either primary or secondary, depending on how useful they are at defining their related parameter as shown in Table 6-1.

Table 6-4 The different parameters and their connected measurements which are defined as either primary or secondary.

Parameter	Primary Measurement	Secondary Measurement
Volumetric Growth of Bone	• Absolute Bone as % of VOI	• Normalised Bone volume • Bone Volume
Bone Distribution	• Fifth Distribution	• Weighted distributions
Structure of Bone within the VOI	• Islands number • Island volume • Pore Filled centre	• Bone Surface Area • Shape Factor • Bone surface area • Kcubic
Structure of Bone within the islands	• Average node size • Average connection size	• Largest node size • Connectivity factor • Structural factor • Normalised connectivity factor
Relationship between the Bone and SBG	• Pore fill comparison • Bone/SBG contact area	• Bone/SBG contact area as % of SBG
Properties of the SBG	• Index (diameter) • Pore centre of mass	• SBG Volume • SBG Surface Area • Index (number)

By separating out the measurements as primary and secondary measurements for each parameter, the measurements which measure the bone ingrowth into the SBG can be quantified. This gives seven primary measurements for defining the bone within the VOI and four to define the properties of the SBG and the relationship between the SBG and the bone.

6.3.5 Sample Evaluation and Discussion

With the measurements connected to the different parameters, it is now possible to perform in-depth comparisons between the different samples. Because of this limited number of samples in this study no decisive statements can be made about the SBG's bone forming ability, but an idea of the trends and different bone growth in the different SBGs can be conjectured.

6.3.5.1 Orthotopic Samples

6.3.5.1.A HA samples

The volumetric measurement of the HA orthotopic samples as a percentage of the VOI

(Figure 6-29) shows that there is a trend of a drop in volume from 3 to 6 weeks, showing a large drop of about 10% for 70-20 and 80-10 samples. The 70-10 and 80-20 samples also show a decrease at 6 weeks but on a smaller scale, with the 60-20 also showing a slight drop. In order of the amount of bone it appears that the trend of the bone growth along the entire study goes from highest to lowest growth as 80-20, 70-10, 70-20, 80-10 and 60-20, with the 70-20 and 80-10 being very similar in absolute bone volume as percentage of the VOI.

The histology data (Figure 6-10) shows same trends in both the normalised and absolute bone percentage of VOI except for the 60-20 samples.

From previous work on the effect of porosity in HA scaffolds (of the same porosity as in this study) on the rate of bone apposition the, rates at 3 weeks were recorded as higher with both higher total and strut porosity (Hing, Buckland, *et al*., 2005). While the 60-20 does agree with this trend, the other samples do not, however the 70% and 80% samples show closer values with overlapping error values for the totals, as there are only one of each sample it can be conceivable that these samples are at opposite ends of the bone formation amounts for each sample type. In an study with porous HA (80%) it shows woven bone formation at one week with osteocytes and the bone in lamellar structure at three weeks, which implies that remodelling is not only possible in the bone in the SBG, but is observed happening (Damien *et al*., 2003).

In another study of 70-10, 70-20, 80-10 and 80-20 HA samples in the same conditions the 80-20 and 70-20 are both shown in general to have higher bone formation than the 70-10 and 80-10 samples (with 70-10 showing higher bone formation than the 80-10) (Hing, Annaz, *et al*., 2005). The study by Hing *et al* does not show the bone values at 6 weeks, so the remodelling which is implied by the results in this study cannot be directly collaborated, however the histology of the samples at 12 weeks showed evidence of remodelling via osteoblast presence or “scalloped” morphology (Figure 6-81).

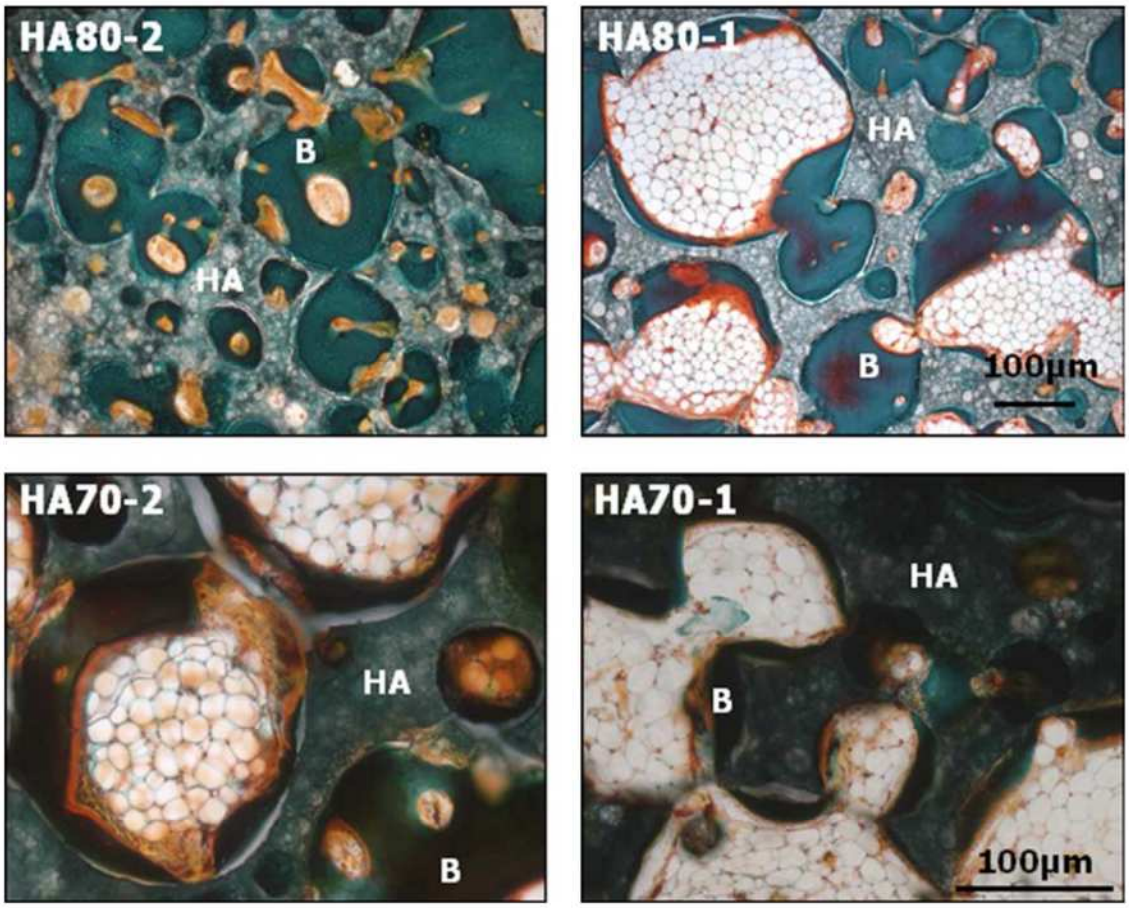

Figure 6-81 Variation in the morphology of bone found within the central porosity of 70 and 80% total-porosity paired high and low microporosity BGS scaffolds after 12 weeks in vivo. (HA = BGS strut, B = bone ingrowth. All Goldners Trichrome) from (Hing, Annaz, *et al*., 2005).

The radial distributions of the bone shows that at 3 weeks (Figure 6-32) that there is a trend for more bone growth at the edges of the samples of 60-20, 70-10 and to a lesser extent the 70-20. While the 80-10 shows higher growth in both the centre and at the edge and while the 80-20 sample shows more growth in the centre. This implies a different growth pattern of bone for the different SBGs, with the 80 percentage porous samples having a shift of bone growth towards the centre either due to an increase in osteoconductive properties or due to osteoinductive growth from the centre of the samples. This trend continuing with the 60-20, 70-20 and 80-20 samples at 24 weeks (Figure 6-35) (no data for the 70-10 and 80-10 at 24 weeks). The radial distribution trend of the 60-20 samples compared to the 80-10 and 80-20 samples would appear to agree with a study performed by Hing *et al* where even though the 60% porous HA samples have significantly lower absolute volume amounts at 5 and 13 weeks, than the Interfacial Shear Stress values (from a push-out test from the host bone) are much closer and are not significantly different (Hing, Best, *et al*., 2004). This difference in volume

and push-out shear would be explained by the preferential radial bone growth at the edge of the SBG.

The change in number of islands over time (Figure 6-37) again splits the HA samples into two sets at the 6 week point with the 70-20, 80-10 and 60-20 (with the different pairing to volume change) showing an increase in the number of bone islands while the 70-10 and 80-20 samples have a drop in the number of islands. After 6 weeks only the 80-20 samples show an increase in island number to 12 weeks with all the other samples showing a clear drop in island number to 12 weeks and then all samples including the 80-20 showing a drop from 12 to 24 weeks. This change in island number for the majority of the samples fits with the idea of a remodelling phase, with the reduction of the number of islands afterwards showing that the bone is growing together forming a more connected structure. The average volume of the islands shows that there is a largest change in size of the bone within the 70-20 sample followed by the 80-10 sample, with the 80-20 having a constant increase from 3 weeks, and the 60-20 and 70-20 remains constant (with the 60-20 showing an increases but it is slight as it has the lowest volume). Both these measurements imply that the 70-20 and 80-10 samples and to an extent the 60-20 samples have a different growth pattern or time scale to the 70-10 and 80-20 samples.

The centre of mass of filled pores (Figure 6-42) shows that there is a decrease in size of filled pores for the samples of 70-10 and 80-10 while the 70-20 shows an increase after 6 weeks and both the 60-20 and 80-20 sample values remain constant. This centre of mass implies that there might be an effect caused by the strut porosity on how the bone relates to the pores, however as seen by observation (Figure 6-80) the pore fill shift might be a side effect of the change in bone volume over time.
The average node and connection size (Figure 6-38) show that for both the samples of 70-20 and 80-10 there is a large drop in both node and connection size at 6 weeks and again at 12 weeks for the 70-20, with the other samples showing a general increase in both node and connection size. With the average node size of the 80-20 sample increasing from 12 to 24 weeks, the 70-20 having a sharp decrease from 12 to 24 weeks and the 60-20 sample remaining relatively constant from 12 to 24 weeks. The average connection size for the 80-20 and 70-20 both show a clear increase from 12 to 24 weeks with the 60-20 samples' connectivity remaining relatively constant. This change in

connectivity and node size fits with the volume change with the idea of the two forms of remodelling at 6 weeks for the samples. The larger nodes and connections seen in the 80-20 samples fits with the observations of Hing *et al* (Hing, Annaz, *et al*., 2005) where thick pore coverage of bone is observed in the 80-20 samples at 12 weeks (Figure 6-81). This thickness difference between the 80-10 and 80-20 (with the 80-20 being thicker) is also seen in another study (which only looks at 80-10 and 80-20), when comparing the samples at three weeks in a similar set up study (Hing, Saeed, Annaz, Buckland, & Revell, 2004).

The relationship between the bone and the SBG can be seen by viewing their contact area (Figure 6-31); this shows, as in the volume change, as drop for all the samples (including 60-20) at 6 weeks followed by a general increase. With the 80-20 showing higher contact area than the 70-20 at all bar 3 weeks and both samples always showing higher contact area than the 60-20 sample, the 80-10 is lower than both the 70-20 and 80-20. But the 80-10 sample does drop below the contact area of the 60-20 at 6 weeks, while the 70-10 is only lower than the 70-20 at 3 weeks. The study of 80-10 and 80-20 samples at three weeks shows the same trend of higher bone formation on the scaffolds of 80-20 than the 80-10 (Hing, Saeed, Annaz, Buckland, & Revell, 2004).

From the pore fill comparison (Figure 6-43) the samples 70-10, 80-10 and 80-20 show a drop from 3 to 6 weeks with there being an increase of the 70-20 and 80-10 after 6 weeks, while the 80-20 takes till 12 weeks to increase and the 60-20 samples remains constant. The connection between the bone and SBG implies that all the contact area and the bone volume are related, but not directly with the order of volume (either total, absolute as percentage of VOI or normalised). This difference between the volume (measured in mm^3) and surface area (in mm^2) suggests that at 3 weeks the 80-10 and to a lesser extend the 70-20 samples are formed more in islands with lower contact area, than the 60-20 and 80-20 while the 70-10 shows islands with a higher ratio of contact area. The mean centre of pore measurement could be connected to the change in total volume, with all the pores filling at a similar rate, but smaller pores being filler quicker than the larger pores as they have lower total volume.

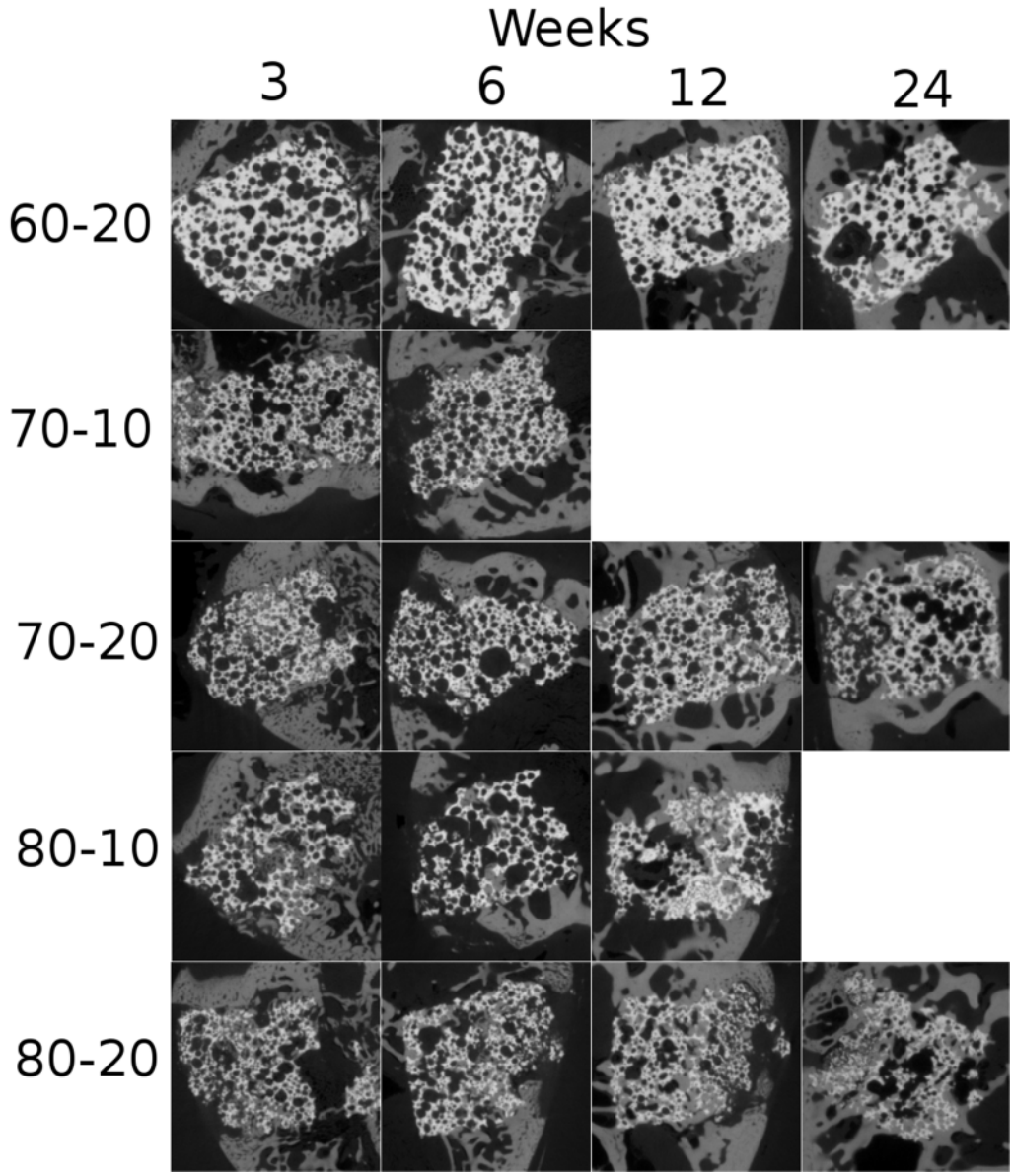

Figure 6-82 CT midway slices of all HA orthotopic samples at all time points for the possible samples.

Connecting these measurements with the knowledge of how bone remodels this implies that the samples undergo remodelling of bone at 6 weeks. This would fit with the mechanostat theory with a large amount of bone growth up to three weeks due to the large amount of strain in the SBG, which then dies back at 6 weeks as the strain on the bone is reduced due to the now newly formed bone structure.

Interestingly the samples appear to remodelling in two distinct manners with the 60-20, 70-20 and 80-10 samples going from a connected network of bone to a large number of disconnected nodes, while the 70-10 and 80-20 samples keep the same internal connection size and in fact end up with less bone islands than at 3 weeks. The average node sizes for both the 70-20 and 80-10 samples are larger at 3 weeks than any of the

other samples, thus giving a lower node to connection ratio. This implies that the 60-20, 70-20 and 80-10 samples are remodelled in a more chaotic manner compared to the 70-10 and 80-20 samples where the bone retains an open connected structure while remodelling the difference between the 80-10 and 80-20 samples during remodelling can be clearly seen in Figure 6-82. Linking this to the mechanostat theory of remodelling (Figure 1-18) this implies that the bone undergoes disuse between 3 and 6 weeks causing the die back, which is caused by a decrease in strain on the samples. This could be because the samples all undergo Pathological Overload causing a fast formation of woven bone which when matured into lamella bone, which reduces the overall strain exhibited on the samples. The samples could also have under gone callus formation from facture healing which when it mineralised would also cause the reduction in strain. In the cases of the 60-20, 70-20 and 80-10 samples this large drop in bone volume and connectivity could be caused by over compensation of the decrease in strain in the bone by the osteoclasts resorbing bone mass (in the Disuse stage of the mechanostat) .

A cause of this difference could be that both the 70-10 and 80-20 samples form bone with a higher contact ratio than the other samples which could potentially reduce the strain on the bone this trend can be observed between the 70-10 and 70-20, and the 80-20 and 80-10 samples at 3 weeks in Figure 6-82 with a shift from more localised mass of bone to more spread out bone between the pairs of total porosity. However it should be noted that as the earliest time point is 3 weeks it is not possible to determine if there is in fact different severities of remodelling or just that they happen at different rates with the 70-10 and 80-20 either being faster or slower than the other samples.

For the 60-20, 70-20 and 80-20 samples which have data at 24 weeks, the 80-20 has the most bone followed by 70-20 and then 60-20 in total and as percentage of VOI, not only this but both the 70-20 and 80-20 have less than half the number of bone islands that are seen in the 60-20 sample showing that the bone is better connected. From the average node and connection size it is also confirmed that the connections in both the 80-20 and 70-20 samples have a generally bigger structure than the 60-20, with 80-20’s being slightly bigger than the 70-20’s. The radial distributions of these samples shows that the 80-20 has the most uniform bone distribution, with both the 60-20 and 70-20 showing more bone at the edges implying more growth from the outside showing osteoconductive properties of the HA SBGs and the potential of osteoinductive properties with the 80-20 samples. The information about the samples at 24 weeks

appears to fit with Figure 6-82, with the 80-20 sample showing thicker bone masses growing across the SBG. If the 70-20 and 80-20 samples do in fact both have higher contact area with the SBG compared to the bone volume, it implies that by changing both the total and strut porosity similar bone reactions to the SBG can be produced.
As there is only one sample (or no sample) for each sample type at each time point a comparison between these samples cannot be taken to be significant or conclusive. However from these measurements it can be said for the samples tested that the 80-20 samples not only have the highest volume of bone at 24 weeks they also have a better connected bone matrix in both number of islands and size of connections from 6 weeks onwards. The HA samples also have a distribution which implies osteoconductive or in the case of the 80-20 samples osteoinductive properties, depending upon whether the bone is being draw further into the SBG or that there is bone formation from inside the SBG as well as from the outside. This implies that with both increased total and strut porosity in a HA SBG better bone properties are achieved.

6.3.5.1.B SA samples

The volumetric measurement of the SA orthotopic samples (Figure 6-46) shows that there is no general trend in the SA samples, with the 0.8 sample showing a similar trend as the HA orthotopic sample. At 12 weeks the 0.8 shows the most bone volume, followed by 0.4, then the 0.2and 1.5 samples.
However unlike the HA samples trends cannot be matched to the trends in the histology measurements (Figure 6-11) this could be in part due to the lack of majority of the 12 week histology data. While the general relative positions of the 1.5 samples compared to the 0.4 and 0.8 samples (and the single 0.2 measurement) is similar to the measurements acquired, this could be due to how the VOI is determined as the SA samples appear to break up over time (Figure 6-85) unlike the HA samples (Figure 6-82) and fits with an increase in the centre of mass of the pores for both 0.4 and 0.8 samples from 3 to 6 weeks (Figure 6-58). The breaking up of the 0.8 samples at 12 weeks can be clearly seen in Figure 6-83.

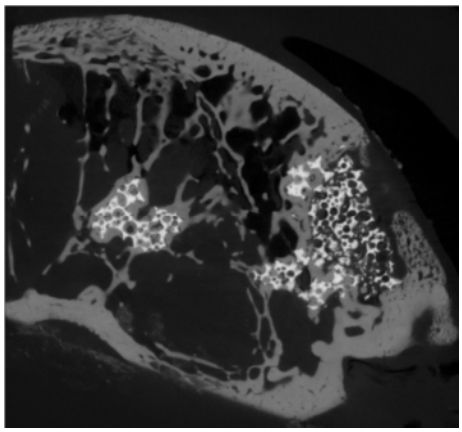

Figure 6-83 CT slice of 0.8 SA sample at 12 weeks.

In the study in which these samples were taken from the trend of the 0.8 sample having the highest amount of bone agrees including the drop at 3 to 6 weeks which is theorised to be due to the remodelling in a study with similar samples (Hing *et al*., 2006). However the study by Hing *et al* does not agree directly with the other samples, however they all present overlapping error values, and with only limited numbers of samples it cannot be concluded either way if the data in this study does statically disagree. The study also identified osteoclastic activity in the 0.8 samples which would fit with the remodelling which is suggested by this study. To continue with the discussion about remodelling the study as states that it appears that all the sample types were in differing stages of remodelling as shown by the presence of active “plump” osteoblast and “scalloped” topography. This fits with the identification that unlike the HA samples in this study the SA samples do not all show a characteristic drop in bone volume from 3 to 6 weeks (Hing *et al*., 2006) (Figure 6-84).

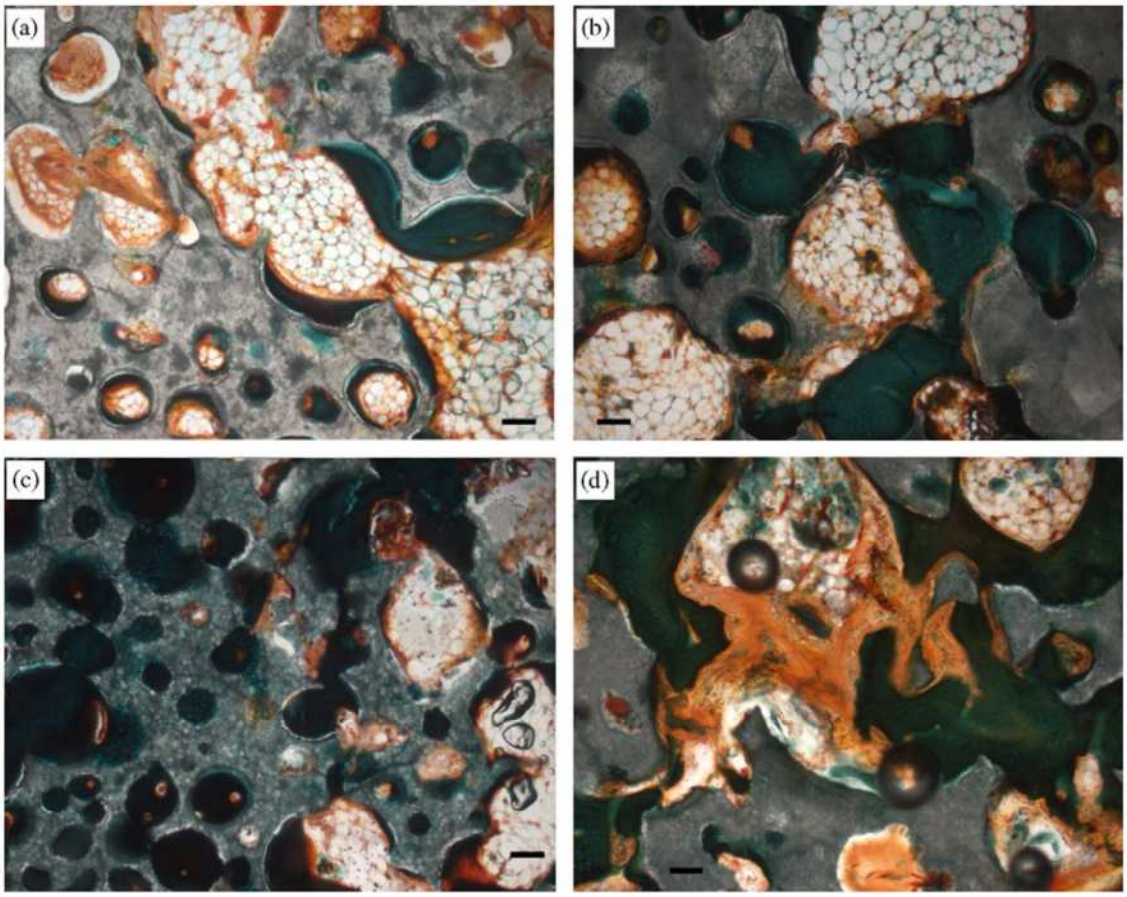

Figure 6-84 Bone morphology at 12 weeks within macroporosity of: (a) PSA02, (b) PSA04, (c) PSA08 and (d) PSA15 (all X50). Bar = 100mm from (Hing *et al*., 2006).

The radial distribution of the bone in the samples shows that at 3 weeks (Figure 6-49) all the samples bar one of the 1.5 samples have either more bone in the centre or in the case of the 0.4 samples has similar bone amounts at edge as at the centre. At 12 weeks (Figure 6-51) only the 0.2 sample has more bone at the edge, while the other samples have a trend for more growth in the middle of the radial distribution. This implies that the amount of silicon substation has an effect on the distribution of the bone within the SBG, perhaps inducing osteoinductive properties.

The change in island number for the SA samples (Figure 6-53) shows that from 3 to 6 weeks both the 0.4 and one of the 1.5 samples increase, and interestingly both the 0.8 and the other 1.5 samples increase in island number from 6 to 12 weeks. The average volume of the bone islands from 3 to 6 weeks shows a similar decrease in volume for the samples of 0.4, 0.8 and the1.5 samples, of a rapid drop. The island data implies that with time the bone from 6 to 12 weeks in SBGs with Silicon substitution of less than or equal to 0.4 wt % is forming into more connected shapes, the higher silicon substitutions are still forming new islands of bone, combining with the volume data this

implies that the 0.8 sample is forming new bone faster than they can join together.

The change in average node size (Figure 6-54) implies that there could be remodelling present in some of the SA samples at 3 to 6 weeks as there is a distinct drop. The average connection size shows that the 0.8 sample appears to follow a similar trend as the 70-20 and 80-10 HA samples with the drop in connection size at 3 weeks before increase afterwards. At 12 weeks the 0.8 sample has the highest connection size being over twice the size of any of the other connections. This is an interesting measurement when combined with the island number measurement, implying that though there are more bone islands at 12 weeks than 6 week, on average the islands are being coming internally more connected, meaning the rate of connection increase is faster than the rate of new bone formation. This higher connection for the 0.8 samples appears to fit with the histology data collected by Hing *et al* with the 0.8 sample showing more well connected bone masses (Figure 6-84).

The contact area between the bone and SBG (Figure 6-48) drops for all the samples from 3 to 6 weeks, and only the 1.5 sample dropping from 6 to 12 weeks. The change in contact area implies a remodelling phase from 3 to 6 weeks for all the samples, with potently the silicon addition inducing enough bone formation so that the new bone out weights the remodelling reduction of bone, except in the case of the 0.8 samples.

The centre of mass of the filled pores (Figure 6-58) shows that the 0.4 sample remains constant while the 0.8 sample shows a large increase from 3 to 6 weeks with the 0.8 then remaining constant from 6 to 12 weeks and the 0.2 samples decreasing from 6 to 12 weeks while the 1.5 samples shows a constant increase. As with the HA data this shift towards the bigger pores for all the samples bar the 0.2, could be a direct effect of the smaller pores being filled faster than the bigger pores.

The pore filled comparison values (Figure 6-59) shows that only 1.5 samples
Shows an increase in pore fill comparison percentage from 3 to 6 and 6 to 12 weeks and only the 0.4 samples shows an increase from 6 to 12 weeks. As with the HA samples the pore filled comparison value could probably be an effect of the smaller pores being filled faster.

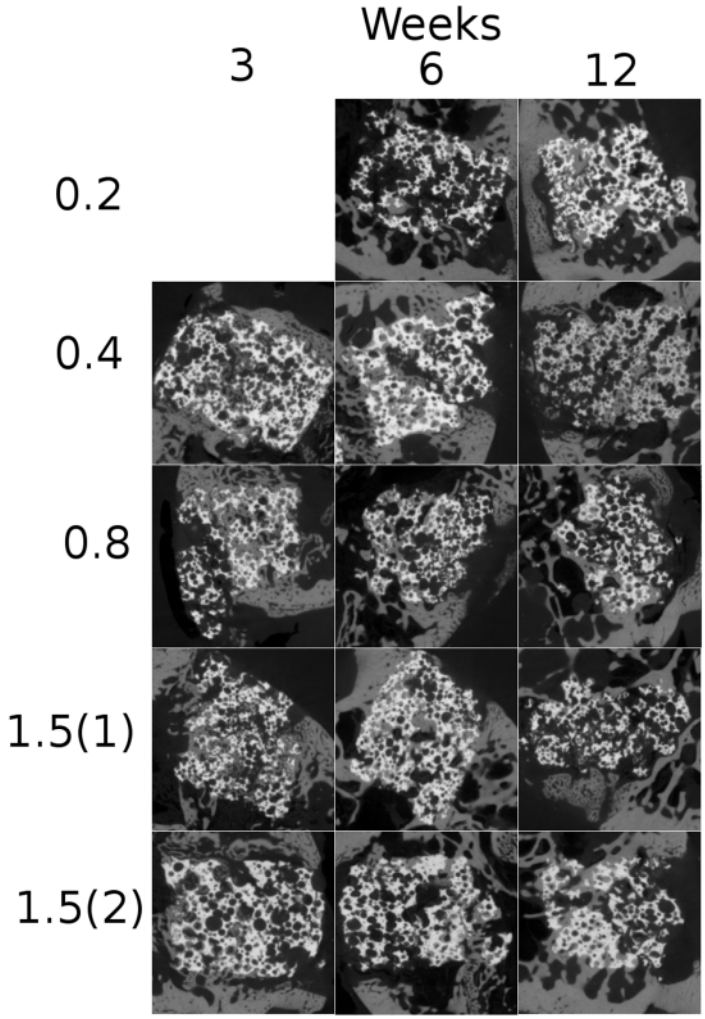

Figure 6-85 CT midway slices of all SA orthotopic samples at all time points for the possible samples.

There is no clear trend of bone remodelling through the SA orthotopic samples, though the contact area change at 6 weeks could imply a change in structure, there is however a similar trend to the HA samples in the 0.8 samples. In general the samples retain a connected network of bone from 3 to 12 weeks in all samples, bone growth generally preferring the centre and middle of the radial distributions than the edge with the exception of the samples of 0.2. The samples with the most bone volume and connectivity are the 0.8 samples; this implies that there is an optimal amount of silicon substitution, in this case 0.8 wt%, with lower and higher substitution amount being inferior. This agrees with the conclusion about 0.8 being the optimal silicon substitution amount asserted by Hing *et al* (Hing *et al*., 2006).

6.3.5.1.C Summary of Orthotopic Samples

In general it appears that the HA samples undergo a clearer remodelling phase than is

seen in the SA samples, with the SA samples all maintaining a larger average connection size with similar sized nodes. This information combined with the measurement of the distributions of bone being more generally closer to the centre in the SA samples than in the HA samples. Which implies that the Silicate substitution has caused a change in how the bone is being formed, with the SA samples seeming to exhibit more osteoconductive (or osteoinductive) qualities than the HA samples with more bone formation in the centre (as defined in the radial distribution). This effect of the silicon in the SBG on the distribution of the bone formation can also be seen in a study by Gibson *et al* with the SA samples (1.2 wt%) shows more bone formation in centre than the HA sample in an orthotopic test at 3 weeks (Gibson, Hing, & Revell, 2001).

The measurements of both the samples types do appear to have the potential to be effected by the SBGs breaking as the SBG is used to define the VOI, with the SA samples seeming to have been effected in this case. While these measurements would affect the volume measurements, the general trends of the distribution and structure of the bone should still be relevant assuming the SBG has not broken into a significant number of pieces.

Comparing the SA sample with the most volume and connectivity (which are the 0.8 samples) to the 70-20 (which has the same porosities as the SA samples) and 80-20 HA samples, it can be seen that at 12 weeks the 0.8 and 80-20 samples have similar bone amounts as aa absolute percentage of the VOI, with the 70-20 having less than both of them. Further to the volume measurements the 0.8 sample has over double the connectivity size but similar node size when compared to the 80-20 or 70-20 samples. Comparing the distribution of the bone between the samples it is at the middle of the radial distribution for the 0.8 sample instead of at the edge for both the 70-20 and 80-20 sample at 12 weeks. Though the 80-20 shows a more uniform radial distribution at 24 weeks than the 70-20 sample. These differences mean that for these 3 samples the 0.8 sample would be the logical choice as the best graft as it has increased connectivity across the sample as well as more evenly distributed bone growth, with the 80-20 being better than the 70-20. If this was done purely on the bone as the absolute percentage of the VOI this would have been a comparison between the 0.8 with 15.7 % 80-20 % with 15.2 and 70-20 with 11.1 %, which while the 0.8 has the highest value, without the

structural and distribution information the decision would not be as clear.

6.3.5.2 Ectopic Samples

The bone volume as an absolute percentage of the VOI (Figure 6-66) shows that there is more volume of both the 35 and 30s samples compared to the 30 samples with of a more difference between the 30 and 35 samples than the 30 and 30s. A study based on samples in a similar ectopic study shows higher bone formation with higher strut porosity than 30 % but interestingly only at 24 weeks not 12 where 32 % and 42 % strut porosity samples have similar amounts of bone formation, though the higher surface contact area with higher strut porosity does agree with the measurements in this study (Chan *et al*., 2012).

The 30 samples have a higher mean number of islands (Figure 6-71) than either the 30s or 35 samples. The average island volume shows the inverse of this relationship with the 30 samples showing a lower mean value and both the 30s and 35 samples showing higher values.

The distribution of the bone in both height and radial distributions (Figure 6-69) is relativity equal, with a slight increase at the edge to the centre. As there is no pre-existing bone, the height distribution is not effected by where there is contact with other bone as seen in the orthotopic samples.

The average node size of the 30 and 30s samples (Figure 6-72) shows significant probability of similarity, while the 35 samples appear to have a larger average node size. With the average connection size showing higher means for both the 30s and 35 samples than the 30 sample.

The contact area between the bone and the SBG (Figure 6-68) for the samples have a higher mean for both the 30s and 35 than the 30 samples implying that both an increase in the surface area and a reduction in distance between the partials forms more bone directly around the SBG partials.

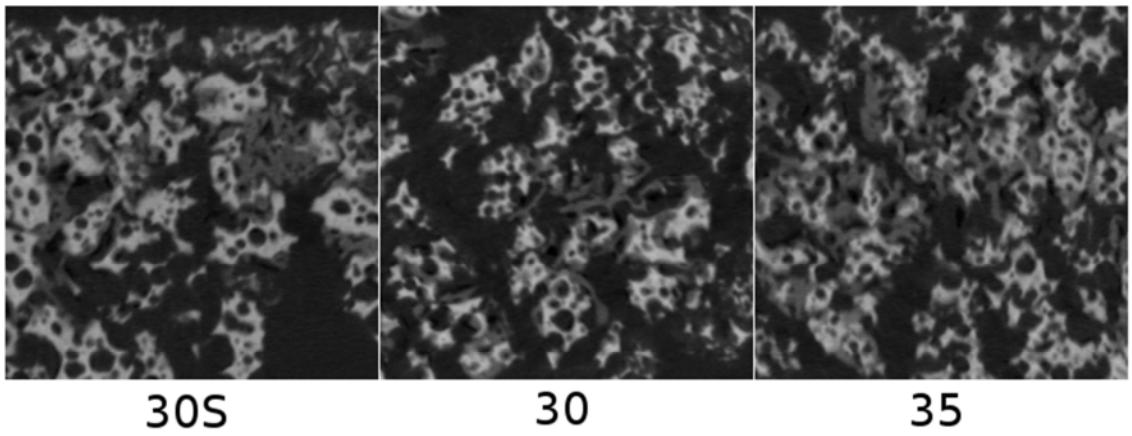

Figure 6-86 CT slices for all ectopic samples types (30s, 30 and 35).

For bone to be formed in the ectopic samples the SBG must be osteoinductive as there is no pre-existing bone for the bone to grow from. Though the remodelling phases cannot be investigated as only one time point is available for the samples if the difference between the 30 and 35 samples are true, the 35 samples are seen to have higher volume and more connected bone both in the VOI and in the size of their connections. This would imply that the increase in strut porosity from 30 to 35 percent does cause either more instances of bone formation or that is speeds up the bone growth. Speeding up the bone appears to be more likely as more instances of bone growth there would be expected to be more islands of bone and the same or smaller average connection sizes; while the 35 samples in fact shows lower number of bone islands with an increase in average connection size when compared to the 30 samples. These trends appear to be confirmed by observation of the SEM and CT images as shown in Figure 6-62, Figure 6-63, Figure 6-64 and Figure 6-86. If the differences between the 30 and 30s samples were in fact shown to be significant, it would imply that the 30s samples had properties in-between that of the 30s and 30 samples, which could be related to the SBG particles being held closer together allowed for a better connected bone network to form as the bone islands had less far to grow to join up.
If 35 samples trends are correct the 35 samples are better at bone formation than the 30 samples. This increase could be due to the surface morphology of the SBG being more suitable for the attachment of osteoblasts, or transportation of one of the associated proteins, possible due to the increase in surface area at the sub-micron scale.
The effect of the addition of a surgical putty and an increase from 30 percentage strut porosity in a previous orthotropic study do not show any significant difference at 8 or 12 weeks and do show signs of bone remodelling in an orthotropic study (Campion *et*

al., 2011). This study by Campion shows a “clear” increase in amount of bone in contact and increase in maturity of the bone network with the higher strut porosity of “46”. With Campion *at al* concluding that the increase in permeability of struts possible increased the physical accessibility of nutrients and an increase in surface area, with the delivery method of either granules or poloaxamer carrier not having as much effect as the increase in strut porosity. These observations by Campion *at al* appear to agree with the observations about the ectopic samples as seen in this study with the apparently faster maturity of the higher strut porosity of samples.

7 Conclusion

This thesis shows the development of automated Method segmentation methods for segmenting out synthetic bone graft (SBG) from bone; the developed colour map overlay method achieves this without ghosting of bone appearing around the SBG, which is present in commonly used threshold based segmentation methods.

As there is no ghosting present around the SBGs, shape and distribution measurements of the bone were developed which allow for more geometric analysis, which would not have been possible with ghosting present in the segmentation. The measurement methods developed measured island size and number, shape, distribution of the bone as well as a measurement of the connections and nodes within bone regions.

These measurements then provides further analysis about how the bone develops in the different SBG, namely the resultant shape, pattern and position of the bone in the SBG, in respect to the position of the SBG, and its implantation site, which is not possible via just volume and surface area measurements. This provides a unique insight into the effect of different SGBs chemistry and structure on the structure of the bone formed within them, as well as importantly how the bone remodels over time while in the SBG.

Also, since this analysis is non-destructive and automated once the calibrations have been determined (which itself is a semi-automated process), it can be performed easily in tandem with other more widely used methods, such as histology, to provide further shape and distribution measurements, with only an increase in time of the study by the CT scan time.

While there are not enough samples measured in this study to provide any statistically significant results about the performance of the investigated SBGs, the measurements from the samples scanned show the possibilities of the conclusions that could be obtained with a larger sample set. Namely the effect of porosity and silicon content on the shape and distribution of the newly formed bone and the bone’s remodelling stages.

This thesis therefore demonstrates methods which can provide further insight into bone growth inside SBGs from CT data, which provide a supplement shape and distribution measurements to currently used analysis methods, such as histology.

7.1 Limitations and Further Work

The colour map overlay segmentation method has limitations, namely the quality of the reference image and the number of possible calibration values. As the calibrations are determined by the validation value of Mn, a further study could be performed, adding further colour map patterns and weighting to measure how much they can lower the Mn value and thus determine if there is an optimal set of test calibrations to run. As this is limited by processing power, this limitation will become less important as computing power increases and its cost decreases.

To reduce human error in the reference images, multiple users could be used to determine the images, possible with a paired histology study to determine if the inter-user error is constant between both the histology measurement and by hand segmentations.

To determine if the trends seen in the bone growth in this thesis are in fact representative, further studies with large sample sets would need to be carried out on at least 6 samples (though more samples would be preferable if smaller differences in means between sample sets are being investigated, *i.e.* < 20 %). This would allow for the general trends of the bone growth over time to be measured for all the samples types. As the HA 80-20 appears to perform better than the 70-20 samples, it would also be of interest to also investigate SA samples with 80-20 porosities. As some of the samples have been shown to break up over time, it is also important to develop a method of identifying the volume of interest independently of the SBG, either via extrapolating the original position of the SBG, or by radio-opaque markers placed at known distances from the implantation site.

It would also be advantageous to be able, instead of having to sacrifice an animal at each time point for each sample, to be able instead to scan *in-situ*, thus not only reducing the number of animals required for the study, but also allowing for actual tracking of the bone growth over time. This could be possible by using a high quality X-ray beam, such as a synchrotron and instead of going for higher resolution than the CT in this study, go for similar resolution with a reduced dose allowing for multiple scans over the time of the study for each animal.

As the main problems in the quantification methods appear to be caused by over and under counting at the boundaries, it would be useful to investigate the possibility of

interpolation of voxels, either before, or during segmentation with the possible addition of edge regions. This of course would require significantly more processing power.

The segmentation technique can also be further validated via testing with different CT systems including synchrotron based ones.

Further studies should also consider different types of bone graft such as autograft and allograft, and SGBs such as bioglass and TCP to identify their effect on the shape and distribution of bone which is formed within them and how that bone remodels over time.

References

Abdou, I., & Pratt, W. (1979). Quantitative design and evaluation of enhancement/thresholding edge detectors. *Proceedings of the IEEE*, *67*(5).

Albee, F. H. (1915). *Bone-graft surgery*. WB Saunders Company.

Albee, F. H. (1920). Studies in Bone Growth: Triple Calcium Phosphate as a Stimulus to Osteogenesis. *Annals of Surgery*, *71*(1), 32–39.

Albrektsson, T., & Johansson, C. (2001). Osteoinduction, osteoconduction and osseointegration. *European Spine Journal*, 96–101.

Athanasou, N. (1996). Current Concepts Review-Cellular Biology of Bone-Resorbing Cells*. *The Journal of Bone & Joint Surgery*, 1096–1112.

Athanasou, N. (2001). Pathological basis of orthopaedic and rheumatic disease. *London: Edward Arnold*.

Ball, M. D., Bonzani, I. C., Bovis, M. J., Williams, A., & Stevens, M. M. (2011). Human periosteum is a source of cells for orthopaedic tissue engineering: a pilot study. *Clinical Orthopaedics and Related Research*, *469*(11), 3085–93. doi:10.1007/s11999-011-1895-x

Barrett, E., Brown, J., & Oleck, S. (1951). Errata: Some Granular Carbonaceous Adsorbents for Sugar Refining (43,640). *Industrial & Engineering Chemistry*, *43*(12), 2956–2956. doi:10.1021/ie50504a613

Barry, P. S. (1975). A comparison of concentrations of lead in human tissues. *British Journal of Industrial Medicine*, *32*(2), 119–39.

Bell, C., & Wyman, J. (1902). *Animal Mechanics*. Printed at The Riverside Press.

Bethge, K., Kraft, G., Kreisler, P., & Walter, G. (2010). *Medical Application of Nuclear Physics*. Springer.

Bi, W., Deng, J. M., Zhang, Z., Behringer, R. R., & de Crombrugghe, B. (1999). Sox9 is required for cartilage formation. *Nature Genetics*, *22*(1), 85–9. doi:10.1038/8792

Bianco, P., Riminucci, M., Majolagbe, a, Kuznetsov, S. a, Collins, M. T., Mankani, M. H., … Robey, P. G. (2000). Mutations of the GNAS1 gene, stromal cell dysfunction, and osteomalacic changes in non-McCune-Albright fibrous dysplasia of bone. *Journal of Bone and Mineral Research : The Official Journal of the American Society for Bone and Mineral Research*, *15*(1), 120–8. doi:10.1359/jbmr.2000.15.1.120

Bilezikian, J. P., Potts, J. T., Fuleihan, G. E.-H., Kleerekoper, M., Neer, R., Peacock, M., … Wells, S. a. (2002). Summary statement from a workshop on asymptomatic primary hyperparathyroidism: a perspective for the 21st century. *The Journal of Clinical Endocrinology and Metabolism*, *87*(12), 5353–61. doi:10.1210/jc.2002-021370

Blitch, E. L., & Ricotta, P. J. (1996). Introduction to bone grafting. *The Journal of Foot and Ankle Surgery*, *35*(5), 458–462. doi:10.1016/S1067-2516(96)80067-6

Boer, H. De. (1988). The history of bone grafts. *Clinical Orthopaedics and Related Research*.

Boivin, G., & Meunier, P. J. (2003). Methodological considerations in measurement of bone mineral content. *Osteoporosis International : A Journal Established as Result of Cooperation between the European Foundation for Osteoporosis and the National Osteoporosis Foundation of the USA*, *14 Suppl 5*, S22–7; discussion S27–8. doi:10.1007/s00198-003-1469-1

Bonewald, L. F. (2007). Osteocytes as dynamic multifunctional cells. *Annals of the New York Academy of Sciences*, *1116*, 281–90. doi:10.1196/annals.1402.018

Borah, B., Ritman, E. L., Dufresne, T. E., Jorgensen, S. M., Liu, S., Sacha, J., … Turner, R. T. (2005). The effect of risedronate on bone mineralization as measured by micro-computed tomography with synchrotron radiation: correlation to histomorphometric indices of turnover. *Bone*, *37*(1), 1–9. doi:10.1016/j.bone.2005.03.017

Bostrom, M. P., Lane, J. M., Berberian, W. S., Missri, a a, Tomin, E., Weiland, a, … Rosen, V. M. (1995). Immunolocalization and expression of bone morphogenetic

proteins 2 and 4 in fracture healing. *Journal of Orthopaedic Research : Official Publication of the Orthopaedic Research Society*, *13*(3), 357–67. doi:10.1002/jor.1100130309

Bourgery, J. B. Ma. (1832). *Traité complet de l'anatomie de l'homme: Anatomie descriptive ou physiologique, appareil de relation, organes de locomotion: ostéologie, syndesmologie*.

Bouxsein, M. L., Boyd, S. K., Christiansen, B. a, Guldberg, R. E., Jepsen, K. J., & Müller, R. (2010). Guidelines for assessment of bone microstructure in rodents using micro-computed tomography. *Journal of Bone and Mineral Research : The Official Journal of the American Society for Bone and Mineral Research*, *25*(7), 1468–86. doi:10.1002/jbmr.141

Boyce, B. F., Yoneda, T., Lowe, C., Soriano, P., & Mundy, G. R. (1992). Rapid Publication to Form Ruffled Borders and Resorb Bone in Mice, *90*(October), 1622–1627.

Brand, R. a. (2010). Biographical sketch: Julius Wolff, 1836-1902. *Clinical Orthopaedics and Related Research*, *468*(4), 1047–9. doi:10.1007/s11999-010-1258-z

Bromage, T. G., Goldman, H. M., McFarlin, S. C., Warshaw, J., Boyde, A., & Riggs, C. M. (2003). Circularly polarized light standards for investigations of collagen fiber orientation in bone. *Anatomical Record. Part B, New Anatomist*, *274*(1), 157–68. doi:10.1002/ar.b.10031

Bronner, F., & Farach-Carson, M. C. (2004). *Bone Formation*. Springer.

Brooks, R. a, & Di Chiro, G. (1976). Beam hardening in x-ray reconstructive tomography. *Physics in Medicine and Biology*, *21*(3), 390–8.

Buie, H. R., Campbell, G. M., Klinck, R. J., MacNeil, J. A., & Boyd, S. K. (2007). Automatic segmentation of cortical and trabecular compartments based on a dual threshold technique for in vivo micro-CT bone analysis. *Bone*, *41*(4), 505–515. doi:10.1016/j.bone.2007.07.007

Burchardt, H. (1983). The biology of bone graft repair. *Clinical Orthopaedics and Related Research*.

Burnell, J. M. (1971). Changes in bone sodium and carbonate in metabolic acidosis and alkalosis in the dog. *The Journal of Clinical Investigation*, *50*(2), 327–31. doi:10.1172/JCI106499

Burr, D. B. (2002). Targeted and nontargeted remodeling. *Bone*, *30*(1), 2–4.

Burr, D. B., Schaffler, M., & Frederickson, R. (1988). Composition of the cement line and its possible mechanical role as a local interface in human compact bone. *Journal of Biomechanics*, (Ii).

Bushberg, J., Seibert, J., Leidholdt, E., & Boone, J. (2012). *The Essential Physics Of Medical Imaging*. Wolters Kluwer.

Byrd, K., Zeng, J., & Chouikha, M. (2007). A Validation model for segmentation algorithms of digital mammography images. *Journal of Applied Science & …*, 41–50.

Cameron, H. U., Pilliar, R. M., & Macnab, I. (1976). The rate of bone ingrowth into porous metal. *Journal of Biomedical Materials Research*, *10*(2), 295–302. doi:10.1002/jbm.820100210

Campion, C. R., Ball, S. L., Clarke, D. L., & Hing, K. a. (2013). Microstructure and chemistry affects apatite nucleation on calcium phosphate bone graft substitutes. *Journal of Materials Science. Materials in Medicine*, *24*(3), 597–610. doi:10.1007/s10856-012-4833-x

Campion, C. R., Chander, C., Buckland, T., & Hing, K. (2011). Increasing strut porosity in silicate-substituted calcium-phosphate bone graft substitutes enhances osteogenesis. *Journal of Biomedical Materials Research. Part B, Applied Biomaterials*, *97*(2), 245–54. doi:10.1002/jbm.b.31807

Canny, J. (1986). A computational approach to edge detection. *IEEE Transactions on Pattern Analysis and Machine Intelligence*, *8*(6), 679–98.

Caplan, a I. (1991). Mesenchymal stem cells. *Journal of Orthopaedic Research : Official Publication of the Orthopaedic Research Society*, *9*(5), 641–50. doi:10.1002/jor.1100090504

Carlisle, E. (1970). Silicon: a possible factor in bone calcification. *Science*, *167*(3916), 279–280.

Carlisle, E. (1986). Silicon as an essential trace element in animal nutrition.

Chambers, T., & Revell, P. (1984). Resorption of bone by isolated rabbit osteoclasts. *Journal of Cell …*, *399*, 383–400.

Chan, O., Coathup, M. J., Nesbitt, a, Ho, C.-Y., Hing, K. a, Buckland, T., … Blunn, G. W. (2012). The effects of microporosity on osteoinduction of calcium phosphate bone graft substitute biomaterials. *Acta Biomaterialia*, *8*(7), 2788–94. doi:10.1016/j.actbio.2012.03.038

Chang, B. S., Lee, C. K., Hong, K. S., Youn, H. J., Ryu, H. S., Chung, S. S., & Park, K. W. (2000). Osteoconduction at porous hydroxyapatite with various pore configurations. *Biomaterials*, *21*(12), 1291–8.

Civitelli, R. (2008). Cell-cell communication in the osteoblast/osteocyte lineage. *Archives of Biochemistry and Biophysics*, *473*(2), 188–92. doi:10.1016/j.abb.2008.04.005

Clark, A. E., Hench, L. L., & Paschall, H. A. (1976). The influence of surface chemistry on implant interface histology: a theoretical basis for implant materials selection. *Journal of Biomedical Materials Research*, *10*(2), 161–174. doi:10.1002/jbm.820100202

Coathup, M. J., Cai, Q., Campion, C., Buckland, T., & Blunn, G. W. (2013). The effect of particle size on the osteointegration of injectable silicate-substituted calcium phosphate bone substitute materials. *Journal of Biomedical Materials Research. Part B, Applied Biomaterials*, *101*(6), 902–10. doi:10.1002/jbm.b.32895

Coathup, M. J., Samizadeh, S., Fang, Y. S., Buckland, T., Hing, K. a, & Blunn, G. W. (2011). The osteoinductivity of silicate-substituted calcium phosphate. *The Journal*

of Bone and Joint Surgery. American Volume, *93*(23), 2219–26. doi:10.2106/JBJS.I.01623

Community Project. (2013). NumPy.

Compston, J. (2006). Bone Quality : What is it and How is it, *50*, 579–585.

Compton, A. H., & Allison, S. K. (1935). *X-rays in Theory and Experiment* (Vol. 18). van Nostrand New York.

Cooper, D., Turinsky, A., Sensen, C., & Hallgrimsson, B. (2007). Effect of voxel size on 3D micro-CT analysis of cortical bone porosity. *Calcified Tissue International*, *80*(3), 211–9. doi:10.1007/s00223-005-0274-6

Currey, J. D. (2002). *Bones Structure and Mechanics*. Princeton.

Currey, J. D. (2011). The structure and mechanics of bone. *Journal of Materials Science*, *47*(1), 41–54. doi:10.1007/s10853-011-5914-9

Curtis, B. F. (1893). Cases of bone implantation and transplantation for cyst of tibia, osteomyelitic cavities and ununited fractures. *Am J Med Sci*, *106*, 30–37.

Damien, E., Hing, K., Saeed, S., & Revell, P. a. (2003). A preliminary study on the enhancement of the osteointegration of a novel synthetic hydroxyapatite scaffold in vivo. *Journal of Biomedical Materials Research. Part A*, *66*(2), 241–6. doi:10.1002/jbm.a.10564

Darwin, C. (1887). *The Life and Letters of Charles Darwin Vol III*. (F. Darwin, Ed.). John Murray.

Davis, G. R., & Elliott, J. C. (2006). Artefacts in X-ray microtomography of materials. *Materials Science and Technology*, *22*(9), 1011–1018. doi:10.1179/174328406X114117

Davis, G. R., Evershed, A. N. Z., & Mills, D. (2012). Recent developments in the MuCAT microtomography facility (Vol. 8506, p. 85060E–85060E–7). doi:10.1117/12.928855

Davison, C. (1916). *Autoplastic bone surgery*. Lea & Febiger.

Dimitriou, R., Tsiridis, E., & Giannoudis, P. V. (2005). Current concepts of molecular aspects of bone healing. *Injury*, *36*(12), 1392–404. doi:10.1016/j.injury.2005.07.019

Ding, M., & Hvid, I. (2000). Quantification of age-related changes in the structure model type and trabecular thickness of human tibial cancellous bone. *Bone*, *26*(3), 291–295. doi:10.1016/S8756-3282(99)00281-1

Dolan, a L., Arden, N. K., Grahame, R., & Spector, T. D. (1998). Assessment of bone in Ehlers Danlos syndrome by ultrasound and densitometry. *Annals of the Rheumatic Diseases*, *57*(10), 630–3.

Donati, D., Zolezzi, C., Tomba, P., & Viganò, A. (2007). Bone grafting: historical and conceptual review, starting with an old manuscript by Vittorio Putti. *Acta Orthopaedica*, *78*(1), 19–25. doi:10.1080/17453670610013376

Ducy, P., Desbois, C., Boyce, B., & Pinero, G. (1996). Increased bone formation in osteocalcin-deficient mice.

Einhorn, T. (1998). The cell and molecular biology of fracture healing. *Clinical Orthopaedics and Related Research*, (355), 7–21.

Epstein, C. (2003). *Introduction To The Mathematics of Medical Imaging*. Pearson.

Eriksen, E. F. (2010). Cellular mechanisms of bone remodeling. *Reviews in Endocrine & Metabolic Disorders*, *11*(4), 219–27. doi:10.1007/s11154-010-9153-1

Evershed, A. N. Z., Mills, D., & Davis, G. (2012). Multi-species beam hardening calibration device for x-ray microtomography (Vol. 8506, p. 85061N–85061N–12). doi:10.1117/12.928933

Fabry, G. (1991). Allograft versus autograft bone in idiopathic scoliosis surgery: a multivariate statistical analysis. *Journal of Pediatric Orthopaedics*.

Favus, M. J. (2010). Bisphosphonates for osteoporosis. *The New England Journal of Medicine*, *363*(21), 2027–35. doi:10.1056/NEJMct1004903

Feldkamp, L., Davis, L., & Kress, J. (1984). Practical cone-beam algorithm. *JOSA A*, *1*(6), 612–619.

Fini, M., Motta, a, Torricelli, P., Giavaresi, G., Nicoli Aldini, N., Tschon, M., … Migliaresi, C. (2005). The healing of confined critical size cancellous defects in the presence of silk fibroin hydrogel. *Biomaterials*, *26*(17), 3527–36. doi:10.1016/j.biomaterials.2004.09.040

Flautre, B., Descamps, M., Delecourt, C., Blary, M. C., & Hardouin, P. (2001). Porous HA ceramic for bone replacement: Role of the pores and interconnections experimental study in the rabbit. *Journal of Materials Science: Materials in Medicine*, *12*(8), 679–682. doi:10.1023/A:1011256107282

Frost, H. M. (1987). Bone "mass" and the "mechanostat": a proposal. *The Anatomical Record*, *219*(1), 1–9. doi:10.1002/ar.1092190104

Frost, H. M. (1998a). Changing concepts in skeletal physiology: Wolff's Law, the Mechanostat, and the "Utah Paradigm." *American Journal of Human Biology*, *605*(July 1997), 599–605.

Frost, H. M. (1998b). From Wolff's Law to the mechanostat: A new "face" of physiology. *Journal of Orthopaedic Science*, *3*(5), 282–286. doi:10.1007/s007760050054

Frost, H. M. (2001). From Wolff ' s Law to the Utah Paradigm : Insights About Bone Physiology and Its Clinical Applications, *419*(February), 398–419.

Frost, H. M. (2003). Bone's mechanostat: a 2003 update. *The Anatomical Record. Part A, Discoveries in Molecular, Cellular, and Evolutionary Biology*, *275*(2), 1081–101. doi:10.1002/ar.a.10119

Frost, H. M., & Turner, C. H. (2000). Toward a Mathematical Description of Bone Biology: The Principle of Cellular Accommodation. *Calcified Tissue International*, *67*(2), 184–187. doi:10.1007/s00223001113

Fukada, E., & Yasuda, I. (1957). On the piezoelectric effect of bone. *Journal of the Physical Society of Japan*, *12*(10), 1158–1162.

Giannoudis, P. V, Dinopoulos, H., & Tsiridis, E. (2005). Bone substitutes: an update. *Injury*, *36 Suppl 3*, S20–7. doi:10.1016/j.injury.2005.07.029

Gibson, I., Hing, K., & Revell, P. (2001). Enhanced in vivo response to silicate-substituted hydroxyapatite. *Key Engineering …*, 2–5.

Gibson, I. R., Best, S. M., & Bonfield, W. (2002). Effect of Silicon Substitution on the Sintering and Microstructure of Hydroxyapatite, *77*, 2771–2777.

Gosain, A., Song, L., & Yu, P. (2000). Osteogenesis in cranial defects: reassessment of the concept of critical size and the expression of TGF-β isoforms. *Plastic and …*, 360–371.

Gray, H. (1977). The Classic Collector's Edition--Gray's Anatomy. *New York: Churehill Livingstone Inc*.

Greenwald, A. S. S., Boden, S. D. D., Goldberg, V. M. M., Khan, Y., Laurencin, C. T. T., & Rosier, R. N. N. (2001). Bone-graft substitutes: facts, fictions, and applications. *The Journal of Bone and Joint Surgery. American Volume*, *83-A Suppl*, 98–103.

Groves, E. (1917). Methods and results of transplantation of bone in the repair of defects caused by injury or disease. *British Journal of Surgery*.

Habibovic, P., Yuan, H., van der Valk, C. M., Meijer, G., van Blitterswijk, C. a, & de Groot, K. (2005). 3D microenvironment as essential element for osteoinduction by biomaterials. *Biomaterials*, *26*(17), 3565–75. doi:10.1016/j.biomaterials.2004.09.056

Hadjidakis, D. J., & Androulakis, I. I. (2006). Bone remodeling. *Annals of the New York Academy of Sciences*, *1092*, 385–96. doi:10.1196/annals.1365.035

Haldeman, K. (1933). The influence of periosteum on the survival of bone grafts. *The Journal of Bone & Joint Surgery*, 302–319.

Hall, B. K. (2005). *Bones and cartilage: developmental and evolutionary skeletal biology*. Academic Press.

Hamburger, V. (1997). Wilhelm Roux: visionary with a blind spot. *Journal of the History of Biology*, *30*(2), 229–238.

Hara, T., Tanck, E., Homminga, J., & Huiskes, R. (2002). The influence of microcomputed tomography threshold variations on the assessment of structural and mechanical trabecular bone properties. *Bone*, *31*(1), 107–109. doi:10.1016/S8756-3282(02)00782-2

Hench, L. L. (2006). The story of Bioglass. *Journal of Materials Science. Materials in Medicine*, *17*(11), 967–78. doi:10.1007/s10856-006-0432-z

Hench, L. L., & Wilson, J. (1993). *An Introduction To Bioceramics*. World Scientific.

Hendricks, S., & Hill, W. (1950). The nature of bone and phosphate rock. … *of the National Academy of Sciences of the …*, *36*(1949), 426–428.

Hermann, G. T. (1980). Image reconstruction from projections. *The Fundamentals of Computerized Tomography*.

Hesaraki, S., Alizadeh, M., Nazarian, H., & Sharifi, D. (2010). Physico-chemical and in vitro biological evaluation of strontium/calcium silicophosphate glass. *Journal of Materials Science: Materials in Medicine*, *21*(2), 695–705. doi:10.1007/s10856-009-3920-0

Hessle, L., Johnson, K. a, Anderson, H. C., Narisawa, S., Sali, A., Goding, J. W., … Millan, J. L. (2002). Tissue-nonspecific alkaline phosphatase and plasma cell membrane glycoprotein-1 are central antagonistic regulators of bone mineralization. *Proceedings of the National Academy of Sciences of the United States of America*, *99*(14), 9445–9. doi:10.1073/pnas.142063399

Hildebrand, T., & Laib, A. (1999). Direct three-dimensional morphometric analysis of human cancellous bone: microstructural data from spine, femur, iliac crest, and calcaneus. *Journal of Bone and …*, *14*(7), 1167<unicode>8211</unicode>1174. doi:10.1359/jbmr.1999.14.7.1167

Hildebrand, T., & Ru, P. (1997). A new method for the model-independent assessment of thickness in three-dimensional images, *185*(November 1995), 67–75.

Hilldore, A. J., Morgan, A. W., Woodard, J. R., & Wagoner Johnson, A. J. (2009). The curve integration method is comparable to manual segmentation for the analysis of bone/scaffold composites using micro-CT. *Journal of Biomedical Materials Research. Part B, Applied Biomaterials*, *88*(1), 271–9. doi:10.1002/jbm.b.31178

Hilldore, A. J., Wojtowicz, A., & Johnson, A. W. (2007). Micro-CT based quantification of non-mineralized tissue on cultured hydroxyapatite scaffolds. *Journal of Biomedical Materials Research Part A*, *82A*(4), 1012–1021. doi:10.1002/jbm.a.31264

Hing, K. a, Annaz, B., Saeed, S., Revell, P. a, & Buckland, T. (2005). Microporosity enhances bioactivity of synthetic bone graft substitutes. *Journal of Materials Science. Materials in Medicine*, *16*(5), 467–75. doi:10.1007/s10856-005-6988-1

Hing, K. a, Best, S. M., Tanner, K. E., Bonfield, W., & Revell, P. a. (2004). Mediation of bone ingrowth in porous hydroxyapatite bone graft substitutes. *Journal of Biomedical Materials Research. Part A*, *68*(1), 187–200. doi:10.1002/jbm.a.10050

Hing, K. a, Buckland, T., & Moseley, P. (2005). Maximising Osseointegration – Unique Bone Grafting Solutions for Different Surgical, 8–13.

Hing, K. a, Revell, P. a, Smith, N., & Buckland, T. (2006). Effect of silicon level on rate, quality and progression of bone healing within silicate-substituted porous hydroxyapatite scaffolds. *Biomaterials*, *27*(29), 5014–26. doi:10.1016/j.biomaterials.2006.05.039

Hing, K. a, Saeed, S., Annaz, B., Buckland, T., & Revell, P. A. (2004). Microporosity Affects Bioactivity of Macroporous Hydroxyapatite Bone Graft Substitutes, *256*, 273–276.

Holden, L. (1887). *Holden's Human osteology*. John Churchill.

Holmes, R., Mooney, V., Bucholz, R., & Tencer, A. (1984). A coralline hydroxyapatite bone graft substitute. *Clinical Orthopaedics and* ….

Horii, C., Bidgood, W. D., & Horii, S. C. (1992). Introduction to the ACR-NEMA DICOM standard. *Radiographics*, *12*(2), 345–355.

Horton, W. A., & Hecht, J. T. (2002). Chondrodysplasias: General Concepts and Diagnostic and Management Considerations. In P. M. Royce & B. Steinmann (Eds.), *Connective Tissue and its Heritable Disorders* (pp. 901–908). John Wiley & Sons.

Hounsfield, G. (1980). Computed medical imaging. *Journal of Computer Assisted Tomography*.

Hubbell, J. H., & Seltzer, S. M. (1996). Tables of x-ray mass attenuation coefficients and mass energy-absorption coefficients. *National Institute of Standards and Technology*.

Hughes, J. M., & Petit, M. A. (2010). Biological underpinnings of Frost ' s mechanostat thresholds : The important role of osteocytes, *10*(April), 128–135.

Huiskes, R. (2000). If bone is the answer, then what is the question? *Journal of Anatomy*, *197 (Pt 2*, 145–56.

Hulbert, S. F., Young, F. A., Mathews, R. S., Klawitter, J. J., Talbert, C. D., & Stelling, F. H. (1970). Potential of ceramic materials as permanently implantable skeletal prostheses. *Journal of Biomedical Materials Research*, *4*(3), 433–456. doi:10.1002/jbm.820040309

Hunter, G. K., & Goldberg, H. a. (1993). Nucleation of hydroxyapatite by bone sialoprotein. *Proceedings of the National Academy of Sciences of the United States of America*, *90*(18), 8562–5.

IBM CORP. (2013). SPSS. IBM Corp.

Ilan, D. I., & Ladd, A. L. (2003). Bone Graft Substitutes, *9*(4), 151–160. doi:10.1053/j.optr.2003.09.003

Itälä, a I., Ylänen, H. O., Ekholm, C., Karlsson, K. H., & Aro, H. T. (2001). Pore diameter of more than 100 microm is not requisite for bone ingrowth in rabbits. *Journal of Biomedical Materials Research*, *58*(6), 679–83.

Jensen, J., Kragskov, J., Wenzel, A., & Sindet-Pedersen, S. (1998). Volumetry of bone grafts by three-dimensional computed tomographic reconstruction: an animal study in the minipig. *Dentomaxillofacial Radiology*, *27*(1), 41–44. doi:10.1038/sj.dmfr.4600319

John, H. (2013). matplotlib.

Jones, A. C., Arns, C. H., Sheppard, A. P., Hutmacher, D. W., Milthorpe, B. K., & Knackstedt, M. a. (2007). Assessment of bone ingrowth into porous biomaterials using MICRO-CT. *Biomaterials*, *28*(15), 2491–504. doi:10.1016/j.biomaterials.2007.01.046

Jones, J. (2005). Scaffolds for tissue engineering. In *Biomaterials, artifical organs and tissue engineering* (pp. 201–214).

Jones, J., Poologasundarampillai, G., Atwood, R. C., Bernard, D., & Lee, P. D. (2007). Non-destructive quantitative 3D analysis for the optimisation of tissue scaffolds. *Biomaterials*, *28*(7), 1404–13. doi:10.1016/j.biomaterials.2006.11.014

Jovanovi, Z., Khan, F., Enzmann, F., & Kersten, M. (2013). Simultaneous segmentation and beam-hardening correction in computed microtomography of rock cores. *Computers & Geosciences*, *56*, 142–150. doi:10.1016/j.cageo.2013.03.015

Judex, S., Boyd, S., Qin, Y., & Miller, L. (2003). Combining high-resolution micro-computed tomography with material composition to define the quality of bone tissue. *Current Osteoporosis …*, *1*(1), 11–19. doi:10.1007/s11914-003-0003-x

Kadler, K. E., Holmes, D. F., Trotter, J. a, & Chapman, J. a. (1996). Collagen fibril formation. *The Biochemical Journal*, *316 (Pt 1*, 1–11.

Kalfas, I. H. (2001). Principles of bone healing. *Neurosurgical Focus*, *10*(4), E1.

Kamitakahara, M., Ohtsuki, C., & Miyazaki, T. (2008). Review paper: behavior of ceramic biomaterials derived from tricalcium phosphate in physiological condition. *Journal of Biomaterials Applications*, *23*(3), 197–212. doi:10.1177/0885328208096798

Kaplan, F. . (1999). Severe orthopaedic complications of Paget's disease. *Bone*, *24*(5), 43S–46S. doi:10.1016/S8756-3282(99)00048-4

Karageorgiou, V., & Kaplan, D. (2005). Porosity of 3D biomaterial scaffolds and osteogenesis. *Biomaterials*, *26*(27), 5474–91. doi:10.1016/j.biomaterials.2005.02.002

Keith, A. (1917). Bone growth and bone repair. *British Journal of Surgery*, 685–693.

Keith, A. (1919). *Menders of the Maimed*. Oxford University Press.

Kern, S., Eichler, H., Stoeve, J., Klüter, H., & Bieback, K. (2006). Comparative analysis of mesenchymal stem cells from bone marrow, umbilical cord blood, or adipose tissue. *Stem Cells (Dayton, Ohio)*, *24*(5), 1294–301. doi:10.1634/stemcells.2005-0342

Khronos Group. (2013). OpenCl.

Klawitter, J. J., Bagwell, J. G., Weinstein, a M., & Sauer, B. W. (1976). An evaluation of bone growth into porous high density polyethylene. *Journal of Biomedical Materials Research*, *10*(2), 311–23. doi:10.1002/jbm.820100212

Klein-Nulend, J., & Plas, A. Van der. (1995). Sensitivity of osteocytes to biomechanical stress in vitro. *The FASEB Journal*, 441–445.

Koch, J. C. (1917). The laws of Bone Architecture, *21*.

Kojimoto, H., Yasui, N., Goto, T., Matsuda, S., & Shimomura, Y. (1988). Bone lengthening in rabbits by callus distraction. The role of periosteum and endosteum. *Journal of Bone & …*, *70*(4).

Kolk, A., Handschel, J., Drescher, W., Rothamel, D., Kloss, F., Blessmann, M., … Smeets, R. (2012). Current trends and future perspectives of bone substitute materials - from space holders to innovative biomaterials. *Journal of Cranio-Maxillo-Facial Surgery : Official Publication of the European Association for Cranio-Maxillo-Facial Surgery*, *40*(8), 706–18. doi:10.1016/j.jcms.2012.01.002

Komori, T., Yagi, H., Nomura, S., Yamaguchi, a, Sasaki, K., Deguchi, K., … Kishimoto, T. (1997). Targeted disruption of Cbfa1 results in a complete lack of bone formation owing to maturational arrest of osteoblasts. *Cell*, *89*(5), 755–64.

Korper, W., Jansen, D. C., Saftig, P., Everts, V., & Delaisse, J. M. (2002). The Bone Lining Cell : Its Role in Cleaning Howship ' s Lacunae and Initiating Bone Formation, *17*(1).

Kubínová, L., Janáček, J., Guilak, F., & Opatrný, Z. (1999). Comparison of several digital and stereological methods for estimating surface area and volume of cells studied by confocal microscopy. *Cytometry*, *36*(2), 85–95. doi:10.1002/(SICI)1097-0320(19990601)36:2<85::AID-CYTO1>3.0.CO;2-3

Kular, J., Tickner, J., Chim, S. M., & Xu, J. (2012). An overview of the regulation of bone remodelling at the cellular level. *Clinical Biochemistry*, *45*(12), 863–73. doi:10.1016/j.clinbiochem.2012.03.021

La Du, B. . (2002). Alkaptonuria. In P. M. Royce & B. Steinmann (Eds.), *Connective Tissue and its Heritable Disorders* (pp. 809–826). John Wiley & Sons.

Lacey, D. L., Timms, E., Tan, H. L., Kelley, M. J., Dunstan, C. R., Burgess, T., … Boyle, W. J. (1998). Osteoprotegerin ligand is a cytokine that regulates osteoclast differentiation and activation. *Cell*, *93*(2), 165–76.

Landis, W. J., Hodgens, K. J., Arena, J., Song, M. J., & McEwen, B. F. (1996). Structural relations between collagen and mineral in bone as determined by high voltage electron microscopic tomography. *Microscopy Research and Technique*, *33*(2), 192–202. doi:10.1002/(SICI)1097-0029(19960201)33:2<192::AID-JEMT9>3.0.CO;2-V

Landis, W. J., Hodgens, K. J., Song, M. J., Arena, J., Kiyonaga, S., Marko, M., … McEwen, B. F. (1996). Mineralization of collagen may occur on fibril surfaces: evidence from conventional and high-voltage electron microscopy and three-dimensional imaging. *Journal of Structural Biology*, *117*(1), 24–35. doi:10.1006/jsbi.1996.0066

Lawler, J., Weinstein, R., & Hynes, R. (1988). Cell attachment to thrombospondin: the role of ARG-GLY-ASP, calcium, and integrin receptors. *The Journal of Cell Biology*, *107*(6).

Le Meng Bao, C., Teo, E. ., Chong, M. S. ., Liu, Y., Choolani, M., & Chan, J. K. . (2013). Advances in Bone Tissue Engineering. In *Regenerative Medicine and Tissue Engineering*.

Lee, S. U., Yoon Chung, S., & Park, R. H. (1990). A comparative performance study of several global thresholding techniques for segmentation. *Computer Vision, Graphics, and Image Processing*, *52*(2), 171–190.

Lemann, J., Litzow, J. R., & Lennon, E. J. (1966). The effects of chronic acid loads in normal man: further evidence for the participation of bone mineral in the defense against chronic metabolic acidosis. *The Journal of Clinical Investigation*, *45*(10), 1608–14. doi:10.1172/JCI105467

Levine, M. D., & Nazif, A. M. (1985). Dynamic measurement of computer generated image segmentations. *Pattern Analysis and Machine Intelligence, IEEE Transactions on*, (2), 155–164.

Li, J., Sarosi, I., Yan, X. Q., Morony, S., Capparelli, C., Tan, H. L., … Boyle, W. J. (2000). RANK is the intrinsic hematopoietic cell surface receptor that controls osteoclastogenesis and regulation of bone mass and calcium metabolism. *Proceedings of the National Academy of Sciences of the United States of America*, *97*(4), 1566–71.

Lim, Y., & Lee, S. (1990). On the color image segmentation algorithm based on the thresholding and the fuzzy c-means techniques. *Pattern Recognition*, *23*(9), 935–952.

Liu, Y., & Thomopoulos, S. (2014). Modelling the mechanics of partially mineralized collagen fibrils, fibres and tissue. *Journal of The Royal Society*, *11*.

Lu, J. X., Flautre, B., Anselme, K., Hardouin, P., Gallur, A., Descamps, M., & Thierry, B. (1999). Role of interconnections in porous bioceramics on bone recolonization in vitro and in vivo. *Journal of Materials Science: Materials in Medicine*, *10*(2), 111–120. doi:10.1023/A:1008973120918

Lu, X., Zhang, H., Guo, Y., Wang, Y., Ge, X., Leng, Y., & Watari, F. (2011). Hexagonal hydroxyapatite formation on TiO2 nanotubes under urea modulation. *CrystEngComm*, *13*(11), 3741. doi:10.1039/c0ce00971g

Machin, D., Campbell, M. J., Tan, S.-B., & Tan, S.-H. (2009). *Sample size tables for clinical studies*. John Wiley & Sons.

Mackie, E. J., Ahmed, Y. a, Tatarczuch, L., Chen, K.-S., & Mirams, M. (2008). Endochondral ossification: how cartilage is converted into bone in the developing skeleton. *The International Journal of Biochemistry & Cell Biology*, *40*(1), 46–62. doi:10.1016/j.biocel.2007.06.009

Mahnama, A., Tafazzoli-Shadpour, M., Geramipanah, F., & Mehdi Dehghan, M. (2013). Verification of the mechanostat theory in mandible remodeling after tooth extraction: animal study and numerical modeling. *Journal of the Mechanical Behavior of Biomedical Materials*, *20*, 354–62. doi:10.1016/j.jmbbm.2013.02.013

Malinin, T. I., & Brown, M. D. (1981). Bone allografts in spinal surgery. *Clinical Orthopaedics and Related Research*, (154), 68–73.

Maquet, P. (1992). Wolff's Law. In *Wolff's Law and Connective Tissue Regulation* (pp. 31–33). Walter De Gruyter.

Martin, D., Fowlkes, C., Tal, D., & Malik, J. (2001). A database of human segmented natural images and its application to evaluating segmentation algorithms and measuring ecological statistics. *Proceedings Eighth IEEE International Conference on Computer Vision. ICCV 2001*, *2*, 416–423. doi:10.1109/ICCV.2001.937655

Martin, R. B. (2000). Does osteocyte formation cause the nonlinear refilling of osteons? *Bone*, *26*(1), 71–8.

McConnell, D. (1962). The crystal structure of bone. *Clin. Orthop*.

Mckibbin, B. (1978). The biology of fracture healing in long bones. *J Bone Joint Surg [Br*.

Meeder, P. J., & Eggers, C. (1994). The history of autogenous bone grafting. *Injury*, *25 Suppl 1*, A2–3.

Meekeren, J. Van. (1668). *Heel En geneeskonstige aanmerkingen*. Amsterdam.

Mehta, A., & Hoffbrand, V. (2013). *Haematology at a Glance*. John Wiley & Sons.

Merrett, K., Kozak Ljunggren, M., Mondal, D., Griffith, M., & Rafat, M. (2012). COLLAGEN TYPE I: A PROMISING SCAFFOLD MATERIAL FOR TISSUE ENGINEERING AND REGENERATIVE MEDICINE. In *Biomaterials - Properties and Devices: Type 1 Collagen:* (pp. 1–45).

Miyaji, F., Kono, Y., & Suyama, Y. (2005). Formation and structure of zinc-substituted calcium hydroxyapatite, *40*, 209–220. doi:10.1016/j.materresbull.2004.10.020

Momose, A. (2005). Recent Advances in X-ray Phase Imaging. *Japanese Journal of Applied Physics*, *44*(9A), 6355–6367. doi:10.1143/JJAP.44.6355

Moore, W., Graves, S., & Bain, G. (2001). Synthetic bone graft substitutes. *ANZ J. Surg*, *71*, 354–361.

Mullender, M. G., & Huiskes, R. (1997). Osteocytes and bone lining cells: which are the best candidates for mechano-sensors in cancellous bone? *Bone*, *20*(6), 527–32.

National Osteoporosis Guideline Group. (2014). Osteoporosis Clinical guideline for prevention and treatment, (March).

Natterer, F. (1986). *The Mathematics of Computerized Tomography*. John Wiley & Sons.

Neuman, W., Toribara, T., & Mulryan, B. (1953). The Surface Chemistry of Bone. VII. The Hydration Shell1. … *of the American Chemical* ….

Nyman, J. S., Roy, A., Shen, X., Acuna, R. L., Tyler, J. H., & Wang, X. (2006). The influence of water removal on the strength and toughness of cortical bone. *Journal of Biomechanics*, *39*(5), 931–8. doi:10.1016/j.jbiomech.2005.01.012

Oldberg, a, Franzén, a, & Heinegård, D. (1988). The primary structure of a cell-binding bone sialoprotein. *The Journal of Biological Chemistry*, *263*(36), 19430–2.

Ooi, C. Y., Hamdi, M., & Ramesh, S. (2007). Properties of hydroxyapatite produced by annealing of bovine bone. *Ceramics International*, *33*(7), 1171–1177. doi:10.1016/j.ceramint.2006.04.001

Otto, F., Thornell, a P., Crompton, T., Denzel, a, Gilmour, K. C., Rosewell, I. R., … Owen, M. J. (1997). Cbfa1, a candidate gene for cleidocranial dysplasia syndrome, is essential for osteoblast differentiation and bone development. *Cell*, *89*(5), 765–71.

Oursler, M., Ott, S., Billard, J., Calvi, L., Chen, D., Hannan, M., … Ralston, S. (2014). ASBMR Bone Curriculum. Retrieved from http://www.asbmr.org/education/bonecurriculum.aspx

Pal, N. R., & Pal, S. K. (1989). Entropic thresholding. *Signal Processing*, *16*(2), 97–108.

Paley, W., Brougham, H., & Bell, C. (1836). *Paley's Natural Theology Vol:II*.

Parfitt, A., Mathews, C., Villanueva, A., Kleerekoper, M., Frame, B., & Rao, D. (1983). Relationships between Surface , Volume , and Thickness of Iliac Trabecular Bone in Aging and in Osteoporosis, *72*(June), 1396–1409.

Parker, J. (2010). *Algorithms for image processing and computer vision*. John Wiley & Sons.

Polak, M., Zhang, H., & Pi, M. (2009). An evaluation metric for image segmentation of multiple objects. *Image and Vision Computing*, *27*(8), 1223–1227. doi:10.1016/j.imavis.2008.09.008

Polak, S. J., Candido, S., Levengood, S. K. L., & Wagoner Johnson, A. J. (2012). Automated segmentation of micro-CT images of bone formation in calcium phosphate scaffolds. *Computerized Medical Imaging and Graphics*, *36*(1), 54–65. doi:10.1016/j.compmedimag.2011.07.004

Porter, a, Patel, N., Brooks, R., Best, S., Rushton, N., & Bonfield, W. (2005). Effect of carbonate substitution on the ultrastructural characteristics of hydroxyapatite implants. *Journal of Materials Science. Materials in Medicine*, *16*(10), 899–907. doi:10.1007/s10856-005-4424-1

Posner, A. (1969). Crystal chemistry of bone mineral. *Physiological Reviews*, *49*(4), 760–92.

Posner, A. (1985). The mineral of bone. *Clinical Orthopaedics and Related Research*.

Pyeritz, R. ., & Dietz, H. C. (2002). The Marfan Syndrome and Other Microfibrillar Disorders. In P. M. Royce & B. Steinmann (Eds.), *Connective Tissue and its Heritable Disorders* (pp. 585–626). John Wiley & Sons.

Python Software Foundation. (2013). Python 2.7.3.

Quain, J. (1849). *Human Anatomy* (Vol. 1). Lea and Blanchard.

Radon, J. (1917). über die Bestimmung von Funktionen durch ihre Integralwerte längs gewisser Mannigfaltigkeiten. *Classic Papers in Modern Diagnostic Radiology*.

Ramachandran, G., & Chandrasekharan, R. (1968). Interchain hydrogen bonds via bound water molecules in the collagen triple helix. *Biopolymers*, *6*(250), 1649–1658.

Rawadi, G., Vayssière, B., Dunn, F., Baron, R., & Roman-Roman, S. (2003). BMP-2 controls alkaline phosphatase expression and osteoblast mineralization by a Wnt autocrine loop. *Journal of Bone and Mineral Research : The Official Journal of the*

American Society for Bone and Mineral Research, *18*(10), 1842–53. doi:10.1359/jbmr.2003.18.10.1842

Ray, R., Degge, J., Gloyd, P., & Mooney, G. (1952). BONE REGENERATION An Experimental Study of Bone-Grafting Materials. *The Journal of Bone & Joint …*, *32*(3), 638–647.

Reddy, S., Kurihara, N., Menaa, C., & Roodman, G. D. (2001). Paget's disease of bone: a disease of the osteoclast. *Reviews in Endocrine & Metabolic Disorders*, (151), 195–201.

Reinholt, F. P., Hultenby, K., Oldberg, a, & Heinegård, D. (1990). Osteopontin--a possible anchor of osteoclasts to bone. *Proceedings of the National Academy of Sciences of the United States of America*, *87*(12), 4473–5.

Rho, J., Kuhn-Spearing, L., & Zioupos, P. (1998). Mechanical properties and the hierarchical structure of bone. *Medical Engineering & Physics*, *20*(2), 92–102.

Rho, J., Tsui, T. Y., & Pharr, G. M. (1997). Elastic properties of human cortical and trabecular lamellar bone measured by nanoindentation. *Biomaterials*, *18*(20), 1325–30.

Rho, J., Zioupos, P., Currey, J. D., & Pharr, G. M. (1999). Variations in the individual thick lamellar properties within osteons by nanodentation. *Bone*, *25*(3), 295–300.

Riggs, B. L., Wahner, H. W., Seeman, E., Offord, K. P., Dunn, W. L., Mazess, R. B., … Melton, L. J. (1982). Changes in bone mineral density of the proximal femur and spine with aging. Differences between the postmenopausal and senile osteoporosis syndromes. *The Journal of Clinical Investigation*, *70*(4), 716–23.

Ritman, E. L. (2004). Micro-computed tomography-current status and developments. *Annual Review of Biomedical Engineering*, *6*, 185–208. doi:10.1146/annurev.bioeng.6.040803.140130

Roach, H. (1994). Why Does Bone MAtrix Contain Non-Collagenous Proteins? The Possible Roles of Osteocalcin, Osteonectin, Osteopontin and Bone Sialoprotein In Bone Mineralisation And Resorption. *Cell Biology International*, *18*(6), 617–628.

Roentgen, W. (2005). A new kind of rays. *Resonance*, 89–95.

Roesler, H. (1987). The history of some fundamental concepts in bone biomechanics. *Journal of Biomechanics*, *20*.

Rojbani, H., Nyan, M., Ohya, K., & Kasugai, S. (2011). Evaluation of the osteoconductivity of α-tricalcium phosphate, β-tricalcium phosphate, and hydroxyapatite combined with or without simvastatin in rat calvarial defect. *Journal of Biomedical Materials Research. Part A*, *98*(4), 488–98. doi:10.1002/jbm.a.33117

Roodman, G. (1995). Osteoclast function in Paget's disease and multiple myeloma. *Bone*, *17*(2), 57–61.

Rose, A. (1973). *Vision Human and Electronic*. Plenum Press.

Roux, W. (1881). *Der Kampf Der Theili Im Organimus*. Leipzig.

Roy, D., & Linnehan, S. (1974). Hydroxyapatite formed from coral skeletal carbonate by hydrothermal exchange. *Nature*.

Ruff, C., Holt, B., & Trinkaus, E. (2006). Perspectives Who ' s Afraid of the Big Bad Wolff ? : "' Wolff ' s Law "' and Bone Functional Adaptation, *498*(September 2005), 484–498. doi:10.1002/ajpa

Ruppel, M. E., Burr, D. B., & Miller, L. M. (2006). Chemical makeup of microdamaged bone differs from undamaged bone. *Bone*, *39*(2), 318–24. doi:10.1016/j.bone.2006.02.052

Sahoo, P. ., Soltani, S., & Wong, a. K. . (1988). A survey of thresholding techniques. *Computer Vision, Graphics, and Image Processing*, *41*(2), 233–260. doi:10.1016/0734-189X(88)90022-9

Sanan, A., & Haines, S. (1997). Repairing holes in the head: a history of cranioplasty. *Neurosurgery*, *40*(3), 588–603.

Schett, G. (2004). Bone Turnover. In D. A. Isenberg (Ed.), *Oxford Textbook of Rheumatology*.

Scheuer, L., & Black, S. (2004). *The juvenile skeleton*. Academic Press.

Schindelin, J., Cardona, A., Longair, M., & Schmid, B. (2011). Fiji Is Just ImageJ.

Secret Labs AB. (2009). Python Imaging Libary.

Sela, J., & Bab, I. (2012). *Principles of Bone Regeneration*. Boston, MA: Springer. doi:10.1007/978-1-4614-2059-0

Shen, H.-C., Peng, H., Usas, A., Gearhart, B., Fu, F. H., & Huard, J. (2004). Structural and functional healing of critical-size segmental bone defects by transduced muscle-derived cells expressing BMP4. *The Journal of Gene Medicine*, *6*(9), 984–91. doi:10.1002/jgm.588

Simkiss, K. (1975). *Bone and Biomineralization*. Edward Arnold.

Simonet, W. S., Lacey, D. L., Dunstan, C. R., Kelley, M., Chang, M. S., Lüthy, R., … Boyle, W. J. (1997). Osteoprotegerin: a novel secreted protein involved in the regulation of bone density. *Cell*, *89*(2), 309–19.

Singer, C. (1952). Galen's elementary course on bones. *Proceedings of the Royal Society of Medicine*, 25–34.

Singh, I. (1978). The architecture of cancellous bone. *Journal of Anatomy*, *127*(Pt 2), 305–10.

Skedros, J. G., & Brand, R. a. (2011). Biographical sketch: Georg Hermann von Meyer (1815-1892). *Clinical Orthopaedics and Related Research*, *469*(11), 3072–6. doi:10.1007/s11999-011-2040-6

Skedros, J. G., Holmes, J. L., Vajda, E. G., & Bloebaum, R. D. (2005). Cement lines of secondary osteons in human bone are not mineral-deficient: new data in a historical perspective. *The Anatomical Record. Part A, Discoveries in Molecular, Cellular, and Evolutionary Biology*, *286*(1), 781–803. doi:10.1002/ar.a.20214

Smith, D. M., Khairi, M. R., & Johnston, C. C. (1975). The loss of bone mineral with aging and its relationship to risk of fracture. *The Journal of Clinical Investigation*, *56*(2), 311–8. doi:10.1172/JCI108095

Smith, R., Wordsworth, B. P., & others. (2005). *Clinical and biochemical disorders of the skeleton*. Oxford University Press Oxford.

Smith, S. (1921). Fractures Occuring In Bone Grafts. *The Journal of Bone & Joint Surgery*, 270–276.

Snyder, W., Cook, M., & Nasset, E. (1974). Report of the task group on reference man. *International Commission of …*.

Spath, S.-S., Andrade, A. C., Chau, M., & Nilsson, O. (2011). Local Regulation of Growth Plate Cartilage. In C. Camacho-Hubner, O. Nilsson, & L. Savendahl (Eds.), *Cartilage and Bone Development and its Disorders* (pp. 23–29). KARGER.

Stevens, M. M., Qanadilo, H. F., Langer, R., & Shastri, V. P. (2004). A rapid-curing alginate gel system : utility in periosteum-derived cartilage tissue engineering. *Biomaterials*, *25*, 887–894. doi:10.1016/j.biomaterials.2003.07.002

Stevenson, A. (Ed.). (2010). *Oxford dictionary of English*. Oxford University Press.

Stout, S., & Crowder, C. M. (2012). Bone Remodeling, Histomorphology, and Histomorphometry. In *Bone Histology* (pp. 1–22).

Strasters, K. C., & Gerbrands, J. J. (1991). Three-dimensional image segmentation using a split, merge and group approach. *Pattern Recognition Letters*, *12*(5), 307–325. doi:10.1016/0167-8655(91)90414-H

Strong, R. (1919). Adaptation In Bone Architecture. *The Scientific Monthly*, *8*(1), 71–80.

Su, X., Sun, K., Cui, F. ., & Landis, W. . (2003). Organization of apatite crystals in human woven bone. *Bone*, *32*(2), 150–162. doi:10.1016/S8756-3282(02)00945-6

Subburaj, K., Ravi, B., & Agarwal, M. (2009). Automated identification of anatomical landmarks on 3D bone models reconstructed from CT scan images. *Computerized Medical Imaging and Graphics : The Official Journal of the Computerized Medical Imaging Society*, *33*(5), 359–68. doi:10.1016/j.compmedimag.2009.03.001

Sundaram, K., Senn, J., & Reddy, S. V. (2013). SOCS-1/3 participation in FGF-2 signaling to modulate RANK ligand expression in paget's disease of bone. *Journal of Cellular Biochemistry*, *114*(9), 2032–8. doi:10.1002/jcb.24554

Sweeney, S. ., & Martin, C. . (2003). Pore size distributions calculated from 3-D images of DEM-simulated powder compacts. *Acta Materialia*, *51*(12), 3635–3649. doi:10.1016/S1359-6454(03)00183-6

Tariq, F., Haswell, R., Lee, P. D., & McComb, D. W. (2011). Characterization of hierarchical pore structures in ceramics using multiscale tomography. *Acta Materialia*, *59*(5), 2109–2120. doi:10.1016/j.actamat.2010.12.012

Teitelbaum, S. L. (2000). Bone Resorption by Osteoclasts. *Science*, *289*(5484), 1504–1508. doi:10.1126/science.289.5484.1504

Termine, J. D., Kleinman, H. K., Whitson, S. W., Conn, M., Mcgarvey, M. L., & Martin, G. R. (1981). Osteonectin, A Bone-Specific Protein Linking Mineral to Collagen, *26*(October), 99–105.

Thacher, T., Fischer , P., Pettifor, J. M., Lawson, J., Isichei, C., James, R., & Chan, G. (1999). A comparison of calcium, vitamin D, or both for nutritional rickets in Nigerian children. … *England Journal of* …, 563–568.

The GIMP Development Team. (2013). Gimp.

Thordarson, D. (1995). Important Advances in Clinical Medicine. *WJM*, *1463*(6), 565–566.

Tomes, J., & Morgan, C. de. (1853). Observations on the structure and development of bone. *Philosophical Transactions of the Royal Society of …*, *143*(1853), 109–139.

Tomkinson, a, Reeve, J., Shaw, R. W., & Noble, B. S. (1997). The death of osteocytes via apoptosis accompanies estrogen withdrawal in human bone. *The Journal of Clinical Endocrinology and Metabolism*, *82*(9), 3128–35. doi:10.1210/jcem.82.9.4200

Toriwaki, J., & Yonekura, T. (2002). Euler number and connectivity indexes of a three dimensional digital picture. *FORMA-TOKYO-*, 183–209.

Townsend, P. R., Rose, R. M., & Radin, E. L. (1975). Buckling studies of single human trabeculae. *Journal of Biomechanics*, *8*(3-4), 199–201.

Trussell, H., & Vrhel, M. (2008). *Fundamentals of Digital Imaging*. Cambridge University Press.

Tsuji, K., Bandyopadhyay, A., Harfe, B. D., Cox, K., Kakar, S., Gerstenfeld, L., … Rosen, V. (2006). BMP2 activity, although dispensable for bone formation, is required for the initiation of fracture healing. *Nature Genetics*, *38*(12), 1424–9. doi:10.1038/ng1916

Turner, C. H. (1999). Toward a mathematical description of bone biology: the principle of cellular accommodation. *Calcified Tissue International*, *65*(6), 466–71.

Turner, C. H., Rho, J., Takano, Y., Tsui, T. Y., & Pharr, G. M. (1999). The elastic properties of trabecular and cortical bone tissues are similar: results from two microscopic measurement techniques. *Journal of Biomechanics*, *32*(4), 437–41.

Udagawa, A., Sato, S., Hasuike, A., Kishida, M., Arai, Y., & Ito, K. (2013). Micro-CT observation of angiogenesis in bone regeneration. *Clinical Oral Implants Research*, *24*(7), 787–92. doi:10.1111/j.1600-0501.2012.02458.x

Ulrich, D., van Rietbergen, B., Laib, A., & Rüegsegger, P. (1999). The ability of three-dimensional structural indices to reflect mechanical aspects of trabecular bone. *Bone*, *25*(1), 55–60.

Urist, M. (1953). Physiologic basis of bone-graft surgery., with special reference to the theory of induction. *Clinical Orthopaedics*.

Urist, M., & Nilsson, O. (1987). Bone regeneration under the influence of a bone morphogenetic protein (BMP) beta tricalcium phosphate (TCP) composite in skull trephine defects in dogs. … *and Related Research*.

US National Library of Medicine. (2013). Bone Papers Search 2012/01/01-2013/01/01. Retrieved from http://www.ncbi.nlm.nih.gov/pubmed

Väänänen, H. K., Karhukorpi, E. K., Sundquist, K., Wallmark, B., Roininen, I., Hentunen, T., … Lakkakorpi, P. (1990). Evidence for the presence of a proton pump of the vacuolar H(+)-ATPase type in the ruffled borders of osteoclasts. *The Journal of Cell Biology*, *111*(3), 1305–11.

Van Der Plas, A., & Nijweide, P. . (1992). Isolation and Purification of Osteocytes. *Journal of Bone and Mineral Research*, *7*(4), 389–396.

Van Oers, R. F. M., Ruimerman, R., Tanck, E., Hilbers, P. a J., & Huiskes, R. (2008). A unified theory for osteonal and hemi-osteonal remodeling. *Bone*, *42*(2), 250–9. doi:10.1016/j.bone.2007.10.009

Vanovschi, V. (2013). Parallel Python.

Varshavskii, V. I., Vorontsova, I. P., Chandrasekaran, B., Shen, D. W. C., Norman, M. F., Shapiro, I. J., … Haven, N. (1983). Histogram Concavity Analysis as an Aid in Threshold Selection (K , h (K)), (3), 231–235.

Verberckmoes, S. C., Behets, G. J., Oste, L., Bervoets, A. R., Lamberts, L. V, Drakopoulos, M., … Haese, P. C. D. (2004). Effects of Strontium on the Physicochemical Characteristics of Hydroxyapatite, 405–415. doi:10.1007/s00223-004-0260-4

Von Meyer, G. H. (2011). The classic: The architecture of the trabecular bone (tenth contribution on the mechanics of the human skeletal framework). *Clinical Orthopaedics and Related Research*, *469*(11), 3079–84. doi:10.1007/s11999-011-2042-4

Wagermaier, W., Gupta, H. S., Gourrier, a, Burghammer, M., Roschger, P., & Fratzl, P. (2006). Spiral twisting of fiber orientation inside bone lamellae. *Biointerphases*, *1*(1), 1. doi:10.1116/1.2178386

Wang, L., Wang, Y., Han, Y., Henderson, S. C., Majeska, R. J., Weinbaum, S., & Schaffler, M. B. (2005). In situ measurement of solute transport in the bone lacunar-canalicular system. *Proceedings of the National Academy of Sciences of the United States of America*, *102*(33), 11911–6. doi:10.1073/pnas.0505193102

Wang, X., Shen, X., Li, X., & Agrawal, C. M. (2002). Age-related changes in the collagen network and toughness of bone. *Bone*, *31*(1), 1–7.

Warbasse, J. P. (1916). Book review of Albee and Davison. *Annals of Surgery*, *63*(4), 504.

Ward, F. . (1838). *Outlines of human osteology*. London : H. Renshaw.

Weber, J., White, E., & Lebiedzik, J. (1971). New porous biomaterials by replication of echinoderm skeletal microstructures.

Wehr, M., Richards, J., & Adair, T. (1984). *Physics of The Atom*. Assison-Wesley.

Weiner, S., Arad, T., Sabanay, I., & Traub, W. (1997). Rotated plywood structure of primary lamellar bone in the rat: orientations of the collagen fibril arrays. *Bone*, *20*(6), 509–14.

Weiner, S., & Traub, W. (1992). Bone structure: from angstroms to microns. *The FASEB Journal*, 879–885.

Weiner, S., & Wagner, H. D. (1998). The Material Bone: Structure-Mechanical Function Relations. *Annual Review of Materials Science*, *28*(1), 271–298. doi:10.1146/annurev.matsci.28.1.271

Wenger, M. P. E., Bozec, L., Horton, M. a, & Mesquida, P. (2007). Mechanical properties of collagen fibrils. *Biophysical Journal*, *93*(4), 1255–63. doi:10.1529/biophysj.106.103192

Wenger, M. P. E., Horton, M. a, & Mesquida, P. (2008). Nanoscale scraping and dissection of collagen fibrils. *Nanotechnology*, *19*(38), 384006. doi:10.1088/0957-4484/19/38/384006

Werb, Z. (1997). ECM and Cell Surface Proteolysis :, *91*, 439–442.

White, R., Weber, J., & White, E. (1972). Replamineform: a new process for preparing porous ceramic, metal, and polymer prosthetic materials. *Science*, *176*.

Wolff, J. (1986). *The Law of Bone Remodeling (translation of the German 1892 edition)*. New York, NY: Springer.

Wolff, J. (2010). The classic: on the inner architecture of bones and its importance for bone growth. 1870. *Clinical Orthopaedics and Related Research*, *468*(4), 1056–65. doi:10.1007/s11999-010-1239-2

Wolff, J. (2011). The classic: On the significance of the architecture of the spongy substance for the question of bone growth: a preliminary publication. 1869. *Clinical Orthopaedics and Related Research*, *469*(11), 3077–8. doi:10.1007/s11999-011-2041-5

Wuelling, M., & Vortkamp, A. (2011). Chondrocyte Proliferation and Diffentiation. In C. Camacho-Hubner, O. Nilsson, & L. Savendahl (Eds.), *Cartilage and Bone Development and its Disorders*. Karger.

Wyman, J. (1857). On the cancellated structure of some of the bones of the human body. *Boston Journal of Nautral History*, *6*, 125–140.

Xiang, A., Kanematsu, M., Kumar, S., Yamashita, D., Kaise, T., Kikkawa, H., … Kinoshita, M. (2007). Changes in micro-CT 3D bone parameters reflect effects of a potent cathepsin K inhibitor (SB-553484) on bone resorption and cortical bone formation in ovariectomized mice. *Bone*, *40*(5), 1231–1237. doi:10.1016/j.bone.2007.01.010

Yaffe, M. J., & Rowlands, J. a. (1997). X-ray detectors for digital radiography. *Physics in Medicine and Biology*, *42*(1), 1–39.

Yasnoff, W., & Bacus, J. W. (1984). Scene-segmentation algorithm development using error measures. *Analytical and Quantitative Cytology*, *6*(1), 45–58.

Yasnoff, W., Mui, J., & Bacus, J. (1977). Error measures for scene segmentation. *Pattern Recognition*.

Yasuda, H., Shima, N., Nakagawa, N., Mochizuki, S. I., Yano, K., Fujise, N., … Higashio, K. (1998). Identity of osteoclastogenesis inhibitory factor (OCIF) and osteoprotegerin (OPG): a mechanism by which OPG/OCIF inhibits osteoclastogenesis in vitro. *Endocrinology*, *139*(3), 1329–37. doi:10.1210/endo.139.3.5837

Yasuda, H., Shima, N., Nakagawa, N., Yamaguchi, K., Kinosaki, M., Mochizuki, S., … Suda, T. (1998). Osteoclast differentiation factor is a ligand for osteoprotegerin/osteoclastogenesis-inhibitory factor and is identical to TRANCE/RANKL. *Proceedings of the National Academy of Sciences of the United States of America*, *95*(7), 3597–602.

Young, R. (1975). Biological apatite vs hydroxyapatite at the atomic level. *Clinical Orthopaedics and Related Research*.

Youssef, S., Maire, E., & Gaertner, R. (2005). Finite element modelling of the actual structure of cellular materials determined by X-ray tomography. *Acta Materialia*, *53*(3), 719–730. doi:10.1016/j.actamat.2004.10.024

Zhang, A., Gertych, A., & Liu, B. (2007). Automatic bone age assessment for young children from newborn to 7-year-old using carpal bones. *Computerized Medical Imaging and Graphics*, *31*(45), 299–310. doi:10.1016/j.compmedimag.2007.02.008

Zhang, J., Yan, C.-H., Chui, C.-K., & Ong, S.-H. (2010). Fast segmentation of bone in CT images using 3D adaptive thresholding. *Computers in Biology and Medicine*, *40*(2), 231–6. doi:10.1016/j.compbiomed.2009.11.020

Zhang, Y. (1996). A survey on evaluation methods for image segmentation. *Pattern Recognition*, *29*(8), 1335–1346.

Zhang, Y. J., & Gerbrands, J. J. (1994). Objective and quantitative segmentation evaluation and comparison. *Signal Processing*, *39*(1), 43–54.

Zimmermann, G., & Moghaddam, A. (2011). Allograft bone matrix versus synthetic bone graft substitutes. *Injury*, *42 Suppl 2*, S16–21. doi:10.1016/j.injury.2011.06.199

Ziv, V., Sabanay, I., Arad, T., Traub, W., & Weiner, S. (1996). Transitional structures in lamellar bone. *Microscopy Research and Technique*, *33*(2), 203–13. doi:10.1002/(SICI)1097-0029(19960201)33:2<203::AID-JEMT10>3.0.CO;2-Y

Zurutuza, L., Muller, F., Gibrat, J. F., Taillandier, a, Simon-Bouy, B., Serre, J. L., & Mornet, E. (1999). Correlations of genotype and phenotype in hypophosphatasia. *Human Molecular Genetics*, *8*(6), 1039–46.

Appendix

Table 0-1 Table of Bone volume in mm^3, SBG volume in mm^3. Bone as percentage of VOI, Normalised Bone volume, Bone surface area in mm^2 and Bone/SBG contact area in mm^2 for the orthotopic samples.

Sample ID	Weeks	Bone Volume mm^3	SBG Volume mm^3	Absolute volume of Bone as % of VOI	Normalised Bone Volume	Bone Surface Area mm^2	SBG Surface Area mm^2	Bone/SBG Contact Area mm^2
60-20	3	4.95	77.48	5.18	27.59	542.55	782.84	266.70
60-20	6	4.41	78.21	4.55	23.53	509.29	760.25	241.48
60-20	12	4.71	76.22	5.23	33.92	457.40	777.33	253.95
60-20	24	4.90	72.42	5.40	26.70	471.07	855.40	246.28
70-10	3	8.35	62.59	9.40	31.80	812.64	1256.54	411.36
70-10	6	7.03	59.06	9.01	37.05	716.18	1036.53	394.61
70-20	3	10.44	49.09	15.59	58.38	699.38	1632.43	415.87
70-20	6	4.77	52.12	6.48	22.21	538.04	805.09	254.57
70-20	12	9.49	63.48	11.12	43.30	749.40	1524.99	416.61
70-20	24	12.48	55.77	14.48	41.05	952.29	1991.76	500.82
80-10	3	12.25	43.98	17.76	48.95	755.99	1992.75	387.96
80-10	6	3.63	37.75	6.28	18.16	333.62	772.33	141.54
80-10	12	8.32	59.39	10.60	43.64	668.69	1377.71	376.67
80-20	3	9.85	44.61	13.84	37.09	795.39	1545.94	404.79
80-20	6	7.74	39.36	13.19	40.09	587.95	1307.74	309.22
80-20	12	11.10	51.83	15.25	52.93	789.32	1822.12	452.19
80-20	24	13.51	44.88	19.42	54.68	876.34	2174.97	504.96
0.2	6	5.11	42.46	8.05	24.33	425.15	928.13	204.07
0.2	12	6.91	53.58	10.14	47.35	528.83	1169.04	301.33
0.4	3	12.22	70.50	12.84	49.56	872.26	1944.87	479.43
0.4	6	11.89	64.36	13.92	56.40	679.77	2090.51	351.45
0.4	12	9.88	46.22	13.78	38.80	769.59	1603.41	391.90
0.8	3	11.00	42.67	17.71	56.52	644.60	1869.42	364.00
0.8	6	8.14	41.57	13.05	39.11	604.06	1376.83	309.11
0.8	12	11.15	46.28	15.73	45.28	659.97	2000.27	315.14
1.5 (1)	3	9.29	48.70	13.48	45.94	712.37	1489.53	395.87
1.5 (2)	3	8.24	58.47	9.98	34.28	658.84	1375.21	317.48
1.5 (1)	6	6.79	58.25	9.14	42.45	520.79	1169.43	289.03
1.5 (2)	6	8.06	52.72	10.60	34.59	548.39	1428.98	254.94
1.5 (1)	12	3.92	37.70	6.70	18.83	439.73	777.53	188.72
1.5 (2)	12	7.84	51.80	11.34	45.23	530.57	1381.04	281.86

Table 0-2 Table of Bone/SBG contact area as percentage of the SBG's surface area, Bone KCubic value, Bone Island number, Average Bone island volume in mm^3, Average Bone connection size in mm, Average Bone node size in mm for the orthotopic samples.

Sample ID	Weeks	Bone/SBG Contact Area as % of SBG Surface Area	Bone Kcubic	Bone Island Number	Average Bone Island Volume mm^3	Average Bone Connection Size mm	Average Bone Node Size mm
60-20	3	34.07	30.22	1039	0.005	0.030	0.090
60-20	6	31.76	31.41	1376	0.003	0.000	0.075
60-20	12	32.67	19.96	779	0.006	0.030	0.108
60-20	24	28.79	20.16	710	0.007	0.030	0.106
70-10	3	32.74	35.62	690	0.012	0.030	0.130
70-10	6	38.07	34.38	576	0.012	0.030	0.124
70-20	3	25.48	14.52	289	0.036	0.030	0.280
70-20	6	31.62	31.68	886	0.005	0.000	0.094
70-20	12	27.32	21.62	503	0.019	0.030	0.194
70-20	24	25.14	25.67	249	0.050	0.060	0.237
80-10	3	19.47	13.32	290	0.042	0.046	0.341
80-10	6	18.33	13.06	747	0.005	0.000	0.101
80-10	12	27.34	20.01	436	0.019	0.030	0.193
80-20	3	26.18	24.02	629	0.016	0.030	0.193
80-20	6	23.65	15.71	456	0.017	0.030	0.219
80-20	12	24.82	18.48	491	0.023	0.050	0.228
80-20	24	23.22	17.06	280	0.048	0.068	0.310
0.2	6	21.99	13.63	611	0.008	0.030	0.139
0.2	12	25.78	14.34	513	0.013	0.057	0.177
0.4	3	24.65	20.57	407	0.030	0.033	0.273
0.4	6	16.81	10.29	612	0.019	0.062	0.217
0.4	12	24.44	21.63	488	0.020	0.041	0.196
0.8	3	19.47	10.24	330	0.033	0.096	0.313
0.8	6	22.45	15.38	356	0.023	0.046	0.234
0.8	12	15.76	10.70	512	0.022	0.142	0.254
1.5 (1)	3	26.58	19.39	436	0.021	0.072	0.244
1.5 (2)	3	23.09	19.51	559	0.015	0.030	0.187
1.5 (1)	6	24.72	14.20	541	0.013	0.047	0.164
1.5 (2)	6	17.84	11.75	487	0.017	0.030	0.225
1.5 (1)	12	24.27	25.57	712	0.006	0.030	0.093
1.5 (2)	12	20.41	11.25	411	0.019	0.064	0.231

Table 0-3 Table of Connectivity Factor, Structural Factor, Largest node size in mm, Normalised Connectivity Factor, shape factor, weighted height distribution as a percentage and weighted radial distribution as a percentage for the orthotopic samples.

Sample ID	Weeks	Connectivity Factor	Structural Factor	Largest Node mm	Normalised Connectivity Factor	Shape Factor	% Weighted Height distribution	% Weighted Radial distribution
60-20	3	0.030	1081	0.303	0.100	0.062	47	51
60-20	6	0.000	1376	0.413	0.000	0.054	46	50
60-20	12	0.030	897	0.414	0.071	0.058	60	49
60-20	24	0.030	949	0.621	0.048	0.059	54	58
70-10	3	0.030	1067	0.561	0.053	0.071	46	51
70-10	6	0.030	892	0.532	0.056	0.076	58	44
70-20	3	0.030	405	0.666	0.045	0.099	47	50
70-20	6	0.000	886	0.443	0.000	0.068	37	51
70-20	12	0.030	626	0.650	0.045	0.086	39	53
70-20	24	0.089	630	0.591	0.150	0.102	57	54
80-10	3	0.030	394	0.847	0.036	0.091	44	49
80-10	6	0.000	747	0.590	0.000	0.056	78	53
80-10	12	0.030	568	0.532	0.056	0.084	46	50
80-20	3	0.030	740	0.575	0.053	0.076	54	45
80-20	6	0.030	479	0.590	0.050	0.079	41	45
80-20	12	0.030	538	0.621	0.048	0.096	27	53
80-20	24	0.148	486	0.709	0.208	0.102	57	47
0.2	6	0.030	626	0.680	0.043	0.066	54	66
0.2	12	0.030	605	0.768	0.038	0.073	57	53
0.4	3	0.030	571	0.739	0.040	0.084	54	49
0.4	6	0.030	696	1.033	0.029	0.087	51	45
0.4	12	0.030	626	0.975	0.030	0.089	47	50
0.8	3	0.030	356	0.885	0.033	0.095	47	45
0.8	6	0.059	472	0.590	0.100	0.082	51	48
0.8	12	0.030	520	0.946	0.031	0.090	41	48
1.5 (1)	3	0.030	474	0.620	0.048	0.085	59	45
1.5 (2)	3	0.030	649	0.620	0.048	0.075	55	53
1.5 (1)	6	0.030	644	0.885	0.033	0.073	40	41
1.5 (2)	6	0.030	513	0.738	0.040	0.075	36	56
1.5 (1)	12	0.030	778	0.355	0.083	0.065	47	46
1.5 (2)	12	0.030	459	0.916	0.032	0.080	54	49

Table 0-4 Table of Height Distribution of bone as percentage of the VOI in fifths and Radial Distribution of bone as a percentage of the VOI in fifths for the orthotopic samples.

		Height Distribution of Bone as % of VOI					Radial Distribution of Bone as % of VOI				
Sample ID	Weeks	1/5	2/5	3/5	4/5	5/5	1/5	2/5	3/5	4/5	5/5
60-20	3	6.63	5.06	4.17	4.56	6.13	4.15	5.00	5.72	5.57	5.67
60-20	6	6.15	4.18	4.37	4.28	4.45	5.03	4.53	4.73	4.82	5.25
60-20	12	4.65	3.87	4.43	6.46	7.35	5.91	5.25	5.62	5.70	5.79
60-20	24	6.18	4.23	4.35	6.76	6.14	3.39	3.91	5.67	6.03	6.72
70-10	3	9.01	10.78	7.78	6.76	14.41	8.66	9.13	10.03	11.02	9.94
70-10	6	5.32	7.13	10.39	11.88	11.19	9.32	10.52	9.82	9.28	6.76
70-20	3	10.94	18.03	20.27	16.37	9.51	14.61	15.39	18.65	18.79	16.29
70-20	6	7.58	9.23	6.38	4.20	3.99	5.96	6.33	6.36	6.77	7.22
70-20	12	11.31	16.76	10.21	9.28	8.28	10.54	10.02	10.28	12.70	13.08
70-20	24	11.25	13.06	12.99	20.58	15.17	12.83	13.17	12.56	15.35	17.69
80-10	3	10.43	22.80	25.67	12.59	11.45	19.91	16.44	16.89	18.44	20.42
80-10	6	3.26	0.56	2.82	4.52	8.38	5.63	5.09	5.00	6.05	7.30
80-10	12	9.21	13.43	10.45	9.54	10.07	10.26	10.50	10.25	11.47	11.54
80-20	3	20.60	11.18	9.62	15.88	15.31	14.42	16.78	15.22	14.26	13.75
80-20	6	11.55	18.08	16.61	9.62	7.60	14.62	15.64	15.12	14.13	13.65
80-20	12	19.76	15.98	10.11	3.74	19.39	11.69	13.31	17.11	17.92	17.22
80-20	24	14.12	15.34	21.15	26.04	18.66	21.15	22.89	19.70	20.61	21.29
0.2	6	5.33	7.39	9.36	10.66	7.78	4.00	3.87	6.24	10.59	11.58
0.2	12	5.93	8.84	11.10	14.77	9.70	9.70	8.42	10.24	11.38	12.22
0.4	3	7.50	11.74	18.45	18.57	8.06	13.55	14.59	13.10	14.00	14.49
0.4	6	6.70	17.26	17.80	10.99	5.94	13.56	19.01	17.72	15.60	14.31
0.4	12	9.10	16.57	17.17	13.41	10.37	12.19	13.29	16.68	14.61	13.87
0.8	3	12.73	18.82	26.44	17.15	9.92	22.55	20.79	21.14	18.43	18.82
0.8	6	9.45	12.64	15.07	14.27	11.98	14.20	12.81	13.19	14.23	14.30
0.8	12	10.06	20.90	15.80	8.02	15.57	14.71	17.08	18.55	18.15	15.99
1.5 (1)	3	6.11	10.10	16.05	21.67	10.92	17.95	13.91	13.35	14.87	14.54
1.5 (2)	3	5.78	8.23	13.42	13.15	8.55	9.46	8.86	9.51	10.91	11.75
1.5 (1)	6	7.00	14.89	10.33	6.56	6.66	14.98	11.01	9.15	9.63	10.23
1.5 (2)	6	11.95	17.88	11.35	9.06	5.57	7.34	7.60	10.86	12.67	12.98
1.5 (1)	12	6.66	5.39	8.36	7.14	4.25	8.22	7.23	6.89	7.54	7.01
1.5 (2)	12	7.14	9.71	14.31	13.76	10.38	12.01	12.39	12.34	11.84	12.94

Table 0-5 Table of Cumulative mean pore Diameter in mm, Cumulative Mean Filled Pore Diameter in mm, Pore comparisons a percentage, Connectivity Index based on number and Connectivity Index based on Diameter for the orthotopic samples.

Sample ID	Weeks	Cumulative Mean pore Diameter mm	Cumulative Mean Filled Diameter mm	Pore comparison %	index (number)	index (diameter)
60-20	3	0.061	0.030	50	0.316	0.265
60-20	6	0.059	0.030	50	0.311	0.278
60-20	12	0.059	0.030	50	0.254	0.229
60-20	24	0.059	0.030	50	0.293	0.281
70-10	3	0.089	0.059	66.66667	0.227	0.283
70-10	6	0.059	0.030	50	0.154	0.167
70-20	3	0.061	0.030	50	0.165	0.188
70-20	6	0.059	0.030	50	0.156	0.187
70-20	12	0.177	0.118	66.66667	0.313	0.371
70-20	24	0.089	0.059	66.66667	0.231	0.265
80-10	3	0.151	0.121	80	0.308	0.392
80-10	6	0.118	0.059	50	0.210	0.282
80-10	12	0.148	0.089	60	0.331	0.386
80-20	3	0.091	0.061	66.66667	0.202	0.254
80-20	6	0.148	0.059	40	0.192	0.222
80-20	12	1.182	0.059	5	0.182	0.209
80-20	24	0.059	0.059	100	0.198	0.238
0.2	6	0.089	0.059	66.66667	0.205	0.248
0.2	12	0.059	0.030	50	0.171	0.199
0.4	3	0.059	0.059	100	0.215	0.243
0.4	6	0.531	0.059	11.11111	0.259	0.285
0.4	12	0.089	0.059	66.66667	0.179	0.236
0.8	3	0.059	0.059	100	0.190	0.223
0.8	6	0.384	0.148	38.46154	0.368	0.391
0.8	12	1.359	0.148	10.86957	0.313	0.316
1.5 (1)	3	0.059	0.030	50	0.204	0.219
1.5 (2)	3	0.148	0.059	40	0.343	0.384
1.5 (1)	6	0.089	0.030	33.33333	0.211	0.224
1.5 (2)	6	0.148	0.089	60	0.268	0.297
1.5 (1)	12	0.118	0.030	25	0.208	0.239
1.5 (2)	12	0.236	0.148	62.5	0.415	0.447

Table 0-6 Table of Bone volume in mm^3, SBG volume in mm^3. Bone as percentage of VOI, Normalised Bone volume, Bone surface area in mm^2 and Bone/SBG contact area in mm^2 for the ectopic samples.

Sample ID	Weeks	Bone Volume mm^3	SBG Volume mm^3	Bone as % of VOI	Normalised Bone Volume	Bone Surface Area mm^2	SBG Surface Area mm^2	Bone/SBG Contact Area mm^2
20	12	146.84	671.99	8.19	13.09	16591.54	21126.17	5944.90
20	12	101.36	794.34	6.42	12.93	11010.38	14575.23	4254.71
20	12	71.25	417.17	7.33	12.84	8615.64	10150.75	3216.56
30	12	33.52	260.42	5.44	9.44	4156.09	5294.57	1439.69
30	12	119.26	381.33	9.71	14.08	10559.62	19124.44	3444.20
30	12	51.62	269.29	7.70	12.87	5807.17	7985.33	2093.33
35	12	149.64	639.81	8.39	13.09	13158.73	23384.32	4710.22
35	12	202.80	760.94	8.88	13.32	20984.90	29704.63	7827.88
35	12	55.72	240.88	8.72	14.00	6162.16	8250.68	2279.83
35	12	167.57	441.84	13.61	21.22	13969.31	25312.82	5555.31
30s	12	172.46	641.22	9.35	14.33	16980.36	25969.33	6106.92
30s	12	112.26	682.56	8.28	16.69	10745.72	16376.47	4465.49
30s	12	67.45	275.32	9.37	15.18	6619.21	10487.24	2412.87
30s	12	276.35	1075.11	8.97	13.77	30763.51	39655.62	11391.10
30s	12	9.86	66.64	6.53	11.69	1192.05	1775.48	407.53

Table 0-7 Table of Bone/SBG contact area as percentage of the SBG's surface area, Bone KCubic value, Bone Island number, Average Bone island volume in mm^3, Average Bone connection size in mm, Average Bone node size in mm for the ectopic samples.

Sample ID	Weeks	Bone/SBG Contact Area as % of SBG Surface Area	Bone KCubic	Bone Island Number	Average Bone Island Volume mm^3	Average Bone Connection Size mm	Average Bone Node Size mm
20	12	28.14	980.60	8004	0.018	0.030	0.112
20	12	29.19	601.47	14028	0.007	0.030	0.100
20	12	31.69	583.28	6014	0.012	0.030	0.088
30	12	27.19	295.75	13436	0.002	0.000	0.069
30	12	18.01	383.25	8085	0.015	0.030	0.162
30	12	26.21	340.20	8562	0.006	0.030	0.094
35	12	20.14	471.05	11065	0.014	0.030	0.160
35	12	26.35	1040.21	7869	0.026	0.032	0.142
35	12	27.63	348.86	9996	0.006	0.030	0.090
35	12	21.95	449.47	5414	0.031	0.043	0.202
30s	12	23.52	762.09	10652	0.016	0.030	0.134
30s	12	27.27	455.82	10904	0.010	0.030	0.138
30s	12	23.01	295.11	7084	0.010	0.030	0.127
30s	12	28.73	1764.95	6657	0.042	0.045	0.118
30s	12	22.95	80.67	5965	0.002	0.000	0.062

Table 0-8 Table of Connectivity Factor, Structural Factor, Largest node size in mm, Normalised Connectivity Factor, shape factor, weighted height distribution as a percentage and weighted radial distribution as a percentage for the ectopic samples.

Sample ID	Weeks	Connectivity Factor	Structural Factor	Largest Node mm	Normalised Connectivity Factor	Shape Factor	% Weighted Height distribution	% Weighted Radial distribution
20	12	0.030	16043	0.450	0.067	0.102	53	48
20	12	0.030	18045	0.540	0.056	0.068	51	50
20	12	0.030	11618	0.300	0.100	0.093	47	51
30	12	0.000	13436	0.210	0.000	0.046	49	45
30	12	0.030	10308	0.750	0.040	0.081	49	49
30	12	0.030	11167	0.420	0.071	0.061	43	48
35	12	0.030	14156	0.750	0.040	0.075	50	51
35	12	0.060	16381	0.660	0.091	0.104	53	51
35	12	0.030	13760	0.390	0.077	0.057	43	41
35	12	0.090	10551	0.690	0.130	0.092	48	49
30s	12	0.030	16953	0.600	0.050	0.090	54	45
30s	12	0.030	13893	0.602	0.050	0.068	46	47
30s	12	0.030	9409	0.600	0.050	0.066	42	53
30s	12	0.060	23495	0.390	0.154	0.144	47	50
30s	12	0.000	5965	0.210	0.000	0.035	51	41

Table 0-9 Table of Height Distribution of bone as percentage of the VOI in fifths and Radial Distribution of bone as a percentage of the VOI in fifths for the ectopic samples.

		Height Distribution of Bone as % of VOI					Radial Distribution of Bone as % of VOI				
Sample ID	Weeks	1/5	2/5	3/5	4/5	5/5	1/5	2/5	3/5	4/5	5/5
20	12	6.09	7.92	8.35	9.06	8.33	7.64	6.74	6.58	6.87	7.06
20	12	6.34	6.37	5.89	6.05	7.64	4.98	5.50	5.62	5.90	5.93
20	12	6.91	7.69	8.18	7.06	6.04	6.72	7.25	7.55	7.83	7.71
30	12	4.17	5.86	5.84	5.57	5.08	6.64	6.97	6.41	6.08	5.54
30	12	9.50	10.04	9.04	9.61	10.52	9.19	8.86	9.15	9.31	9.06
30	12	10.59	7.33	7.67	6.88	6.02	8.65	8.84	8.00	8.31	7.98
35	12	7.57	8.03	9.60	8.19	7.69	6.10	5.11	5.36	6.11	6.26
35	12	8.23	8.38	8.79	9.97	9.73	6.51	7.56	7.72	7.98	7.99
35	12	12.00	9.01	7.30	7.72	8.41	13.84	10.34	8.90	8.99	9.29
35	12	13.05	14.68	14.05	12.69	13.63	14.25	14.63	14.90	14.48	14.69
30s	12	8.10	8.16	9.11	10.47	10.15	9.27	8.74	8.11	7.82	8.06
30s	12	9.50	8.26	7.74	7.80	8.96	8.60	7.82	7.80	8.04	7.46
30s	12	9.25	9.72	9.45	8.92	7.36	7.65	7.90	8.67	9.37	9.98
30s	12	9.79	9.57	8.41	8.63	8.62	7.43	8.18	8.43	8.47	8.75
30s	12	6.59	5.91	6.34	6.62	7.60	8.42	7.27	6.79	6.47	5.55